Universidade de Coimbra

Faculdade de Ciências e Tecnologia

Study of the Reflectance Distributions of Fluoropolymers and Other Rough Surfaces with Interest to Scintillation Detectors

Dissertação de Doutoramento em Física
Especialidade de Física Experimental
apresentada à Faculdade de Ciências e Tecnologia da
Universidade de Coimbra

Cláudio Frederico Pascoal da Silva

Coimbra, 2009

.

Acknowledgements

Abstract

Gaseous and liquid xenon particle detectors are being used in a number of applications including dark matter search and neutrino-less double beta decay experiments. Polytetrafluoroethylene (PTFE) is often used in these detectors both as an electrical insulator and as a light reflector to improve the efficiency of detection of scintillation photons. However, xenon emits in the vacuum ultraviolet (VUV) wavelength region ($\lambda \simeq 175$ nm) where the reflecting properties of PTFE are not sufficiently known.

In this work we report on extensive measurements of PTFE reflectance, including its angular distribution, for the xenon scintillation light. Various samples of PTFE, manufactured by different processes (extruded, expanded, skived and pressed) have been studied.

The data were interpreted with a physical model comprising three components: a specular spike, a specular lobe and a diffuse lobe. The model was successfully applied to describe the reflectance of xenon scintillation light ($\lambda = 175$ nm) by PTFE and other fluoropolymers. The measured data favours a Trowbridge-Reitz distribution function of ellipsoidal micro-surfaces. The intensity of the coherent reflection increases with increasing angles of incidence, as expected, since the surface appears smoother at grazing angles. The relative intensity of the specular spike was found to follow a law $\exp(-K \cos\theta_i)$ where θ_i is the angle of incidence and K is a constant proportional to the roughness of the surface.

This simulation describes fairly well the observed reflectance of the PTFE and other polymers for the entire range of angles.

The reflectance distributions were integrated to obtain the hemispherical reflectances. At normal incidence the hemispherical reflectance of PTFE in vacuum is between 47% and 75% depending of the manufacturing process and surface finishing.

The reflectance model was implemented and coded as a class of Geant4. This new class was used to describe the reflectance processes in a liquid xenon chamber.

The reflectance of the PTFE in the liquid will be larger than in the gas. In this case the reflectance is estimated to be between 76% and 90%

Resumo

Os detectores de xenon, gasoso e líquido, são utilizados em diversas experiências no domínio da detecção de eventos raros, particularmente em experiências de procura de matéria negra, experiências de decaimento duplo de radiação beta. O politetrafluoroetileno (PTFE) é usualmente escolhido como isolador eléctrico e reflector melhorando a eficiência de detecção da cintilação do xénon. No entanto, o xénon cintila na região do ultravioleta do vácuo, nessa região do espectro electromagnético as propriedades reflectoras do PTFE não são suficientemente bem conhecidas.

Neste trabalho é medida a distribuição angular do PTFE para a luz de cintilação do xénon. Diferentes amostras de PTFE produzidas de modo distinto foram estudadas. O estudo também incluiu os copolímeros ETFE, FEP e PFA, na eventualidade de poderem ser usados como substituto do PTFE.

Os dados são descritos por um modelo físico composto por três componentes distintas, lobo especular, lobo difuso e pico especular. Os dados observados indicam uma distribuição das microfaces baseada no modelo de Trowbridge-Reitz. Este modelo assume que a superfície pode ser descrita por uma distribuição de alturas dada por um elipsoide de revolução. A intensidade do pico especular cresce, como esperado com o ângulo de incidência. Assim a superfície parece mais espelhada para direcções de visionamento afastadas da normal da superfície.

O modelo for introduzido no Geant4 podendo ser utilizado em simulações e análise de dados dos detectores de cintilação.

A reflectância obtida para o PTFE situa-se entre 47% e 75% para a luz de cintilação do xénon. No entanto este valor é baixo quando comparado com a reflectância no visível. Por isso realizaram-se medidas no visível que mostraram que a reflectância cresce no visível para os níveis esperados.

Numa câmara de xénon líquido a reflectância observada é maior sendo estimada entre 76% e 90%.

Contents

Introduction

Liquid/gaseous xenon detectors based on scintillation are being used (or developed) for several applications, in particular dark matter search, neutrino experiments or medical imaging [1]. The response of such detectors depends of the properties of the liquid/gas (namely absorption and Rayleigh scattering) but also of the reflectance of the container surfaces. This response is of extreme importance for the optimization of the scintillation detectors and particularly as an input for the Monte Carlo simulations. However, since the scintillation light is in vacuum ultraviolet (VUV) at $\lambda \simeq 175$ nm, the absorption in air is high, making the measurement of the reflectance difficult.

The aim of this work is to measure the angular distributions of the xenon scintillation light reflected by materials which are used in the container surfaces of the liquid/gas xenon chambers, especially polytetrafluoroethylene(PTFE) which is most often applied in the inner walls of liquid/gas containers [2].

The PTFE, also known as Teflon®, is a polymer produced from the tetrafluoroethylene $((C_2F_4)_n)$ in which the strong bound between the carbon and fluorine atoms leads to a high chemical stability in a wide range of temperatures. This stability makes the PTFE suitable to be used in scintillation detectors. However, the main reason for the use of this material is its high reflectance which is about $\simeq 99\%$ for wavelengths in the range from 350 to 1800 nm [3]. For the xenon scintillation light the reflectance distribution is not well known, although some results suggest that it is placed between 50% and 70% (Kadhkhoda, 1999 [4]).

The PTFE can be produced by different industrial processes (namely molded, skived, extruded and expanded). In all these cases PTFE is obtained by suspension polymerization from the tetrafluoroethylene, reduced to a fine powder and agglomerated in small pellets, to be then: i) compressed in a mold, ii) extruded, iii) skived and iv) expanded by air injection, respectively, to produce the types aforementioned.

The PTFE belongs to a class of polymers known as fluoropolymers, which includes also materials as for example ETFE, FEP and PFA. The ETFE is also known as Tefzel®,

or Fluon®, is used in certain applications as a replacement of the glass due its high transparency for visible light. The FEP or Fluorinated ethylene propylene is translucent for the visible light. The PFA is used as an isolator. Owing to the fact that all these materials belong to the same family of polymers, they can be used as a replacement for the PTFE.

The measurement of the reflectance distribution requires a angle resolution system, also called goniometer, to obtain the scattered intensity at different angles. The goniometer used was conceived and mounted in our laboratory and due the absorption of the light by the oxygen molecules it was placed inside a air tight chamber filled with argon gas. The source of VUV light is a small cylindrical proportional counter filled with xenon gas at about about one bar and emitting light with a wavelength of 175 nm. The charge signal taken from the central anode is used for triggering thus reducing the background signal. The light is collimated with two iris diaphragms and strikes in a sample mounted in a structure that can rotate about the vertical axis allowing the angle of incidence to be changed accordingly. The light detector (a photomultiplier) is mounted on a moving stem allowing to change the viewing direction. The photons are detected in single photon mode, both the signals of the charge and light are digitalized and carried to a coincidence unit. The components of the system are aligned with a He-Ne laser beam, namely the positions of pin holes, the PMT slit and the inclination of the samples relatively to the plane of reflection. The measurements are performed in the plane of incidence but can be performed in other planes as well, as far as the sample is inclined relative to the rotation axis.

The measured reflectance corresponds to the ratio between the observed intensity and the incident flux. The incident flux is measured with the sample raised, letting the light go straight to the PMT, then the sample is lowered and the intensity is measured for several positions of the sample and photomultiplier.

The collected data needs to be interpreted using a reflectance model. Usually for a perfectly smooth sample the reflectance is fully described using the Fresnel equations which are dependent of only two parameters: the index of refraction, n, and the extinction coefficient, κ. However, the surfaces have usually at least some roughness and the reflection can no longer be considered purely specular. Also the light that is transmitted to the bulk of the material can suffer multiple refraction producing a diffuse reflectance pattern. More generally the reflection is described by a bidirectional reflectance function ϱ defined for the incident (θ_i, ϕ_i) and viewing directions (θ_r, ϕ_r). This quantity is however purely conceptual and can not be measured directly with the goniometer. Thus it is necessary to modelling the reflectance distribution of the material.

The bidirectional reflectance of rough surfaces can be modeled by a superposition of a diffuse plus a specular reflection. Much less, however, is known for wavelengths $\lambda \simeq 175$ nm concerning both the reflectance and the angular distribution of the reflected light. Consequently, the Monte Carlo simulations usually assume *a priori* that the surface is purely lambertian [5]. In the lambertian model the surface looks equally bright

independently of the viewing angle. In inhomogeneous dielectrics the diffuse component arises from subsurface multiple scattering of the light due to inhomogeneities in the material [6]. However, there are some situations where variations relatively to the lambertian model have been observed, specially for small viewing grazing angles. Thus new models have been proposed including the effect introduced by the interface between the gas/liquid and the material (Wolff model) and the effect introduced by the roughness of the surface (Oren-Nayar model).

The roughness of the surface, which has effect on both diffuse and specular reflections, can be generically described by a function of heights and a correlation function between two different points of the surface. The computation of the scattered electromagnetic wave results in i) a coherent field corresponding to the average field and yielding a spike at the direction of specular reflection and ii) a fluctuating field leading to the specular lobe of reflection.

However, in many situations, when the wavelength of the incident light is larger comparatively to the dimensions of the surface the roughness characterization can be approximated to an ensemble of micro-surfaces randomly oriented in space, following a certain probability distribution function related to the surface structure [7]. At low grazing angles the quantity of the reflected light is reduced due effects of shadowing and masking that occur at the surface, this effect is introduced using a geometrical attenuation factor.

For the rougher samples three parameters suffice to describe the observed reflectance, namely: i) the index of refraction, ii) the albedo of the surface and iii) a roughness parameter. The reflectance distributions of the samples were measured both in and out of the plane of incidence. It was found that smoother surfaces are better described if a specular reflection spike is also included to account for coherent reflection at the surface average plane.

The reflectance models were applied to describe the reflectance distribution in metals (copper and gold), crystals (quartz), glass and the fluoropolymers. The reflectance of the PTFE was measured for different manufacturers, different manufacture methods and for polished and unpolished surfaces. Then the results can be integrated for all viewing or/and incident directions to obtain the hemispherical reflectances.

This study is not restricted to the xenon scintillation light. It is possible measure the reflectance at any wavelength in the visible and U.V. spectra. In this work the reflectance of the PTFE was also studied for larger wavelengths using light emitting diodes. The same procedure can be followed to study other scintillation detectors.

The reflectance models currently in use in the Geant4 toolkit are not suitable to reproduce the observed reflectance distribution. They usually assume constant weight factors for the reflection components, independent of the incident and viewing directions which does not correspond to the reality. This is not observed in our experiment, thus a new reflectance model was introduced in the Geant4.

The model introduced in the Geant4 can be applied directly to a liquid xenon cham-

ber. The index of refraction of the liquid xenon is larger than the index of refraction of the PTFE, thus when the PTFE is immersed in the liquid the reflectance increases due the larger probability of reflection in the interface liquid/PTFE and the lower probability of reflection in the interface PTFE/liquid.

On the Liquid/Gas Xenon Scintillation Detectors

The gaseous/liquid xenon detectors are being used today in many experiments in the field of particle physics. We can identify dark matter experiments [8], neutrinoless double-beta decay searches [9] or rare decays such as $\mu \to e\gamma$ [10]. These detectors are also relevant for medical imaging applications and more generally in systems aiming at detect very small energy depositions or/and a very low event rate. The liquid xenon is a good medium to detect these phenomena due its high mass and high density which provides a high stopping power for the ionizing radiation.

The liquid xenon detectors work by measuring the scintillation produced from the xenon excimers or collecting the charge emitted by the ionized xenon atoms, the excimers and ions are produced by the passage of charged particles in the medium. E.g., the charged particle can be a recoil of a xenon nucleus caused by an incident neutral particle (e.g. a neutron or other neutral particle such as a neutralino), a recoil from an electron produced in a photoelectric process due an incident gamma ray. Among the rare gases detectors the xenon has the highest scintillation and ionization yield comparatively to the other rare gases.

The detection of small amounts of energy or a low event rate require a very good control of the background which involves a good knowledge of the detector, not only of the properties of xenon as scintillation and detector medium but also of the reflecting properties of the surrounding surfaces. The aim of this work is the study of the reflectance of the interior surfaces. The types of the surfaces that are used in the liquid/gaseous xenon can be crystals (ex. quartz and fused silica), metals (ex. copper and stainless steel) and plastics. One plastic that is used today in many of the liquid/gas xenon experiments is the polytetrafluoroethylene (PTFE). It has good mechanical and thermal properties, can be used in a high range of temperatures, is a good electric insulator and has a low natural radioactivity being suitable to be used in the scintillation

detectors. It has also a high reflectance (at least above 200 nm), which is a good characteristic to detect small amounts of energy deposition. However, the reflectance of the PTFE is not well known for the wavelength of the scintillation of the xenon (at 175 nm) and a detailed study of this phenomenon is needed.

1.1 Physics of the Liquid/Gas Xenon Detectors

The physical and optical properties of the xenon makes it a good candidate to be used in rare event experiments. Properties such as its high density of the liquid phase (ρ_{Lxe}=2.953g/cm^3 [11]) and high atomic number of the xenon atom (Z=54, A=131.29) provides a high event rate and makes the xenon very efficient to stop the incident radiation [12] (see table I). Comparatively to argon and krypton, xenon has the highest boiling point (about $-104°$C) and the highest liquid density.

The basic mechanism of the rare gaseous/liquid detectors is the conversion of the energy of the incident particle to photons of scintillation and charge carriers. The xenon is a good scintillator having the largest light yield comparatively to the other rare gaseous detectors. The scintillation produced has the highest wavelength (175 nm) relatively to the other rare gas detectors. Although it belongs to the vacuum ultra violet region (VUV), thus absorbed by the air and some materials as glass, it can be detected by photomultipliers (PMT's) equipped with quartz windows.

The xenon has about nine stable isotopes, about 48% of them have odd mass numbers, either as ^{129}Xe or ^{131}Xe. These nuclei have a nuclear spin different from zero, thus it is possible to use these nuclei to observe spin dependent intereactions. The xenon does not have long live radioactive isotopes which it is an essential requirement in low event experiments. It can be however contaminated with ^{85}Kr in the process of the xenon extraction from the air. It is usually removed from the xenon using processes of distillation and absorption .

Table I: Physical properties of the noble gas and noble liquid detectors

	Neon	Argon	Krypton	Xenon
Atomic number Z	10	18	36	54
Atomic weight A	20.1797	39.948	83.798	131.30
Boiling Point (T_B) at 1 atm (K)	27.102	87.26	119.74	169
Triple Point (K, bar) [13]	(25; 0.434)	(84; 0.67)	(116; 0.72)	(161; 0.80)
Gas density at 1 atm (g/l) [14]	0.8881	1.7606	3.696	5.8971
Liquid density at T_B (g/ml)	1.204	1.399	2.403	3.100

Mechanism of scintillation

The scintillation observed in a rare gas detector is emitted by the dimmer molecule, Xe_2 for the xenon. The process of formation of the molecule is represented in the figure 1.1 for the xenon. As shown, the ionized particle (e.g., electron, alpha particle, xenon atom) traveling through the xenon loses energy through ionization ($Xe \rightarrow Xe^+$) or excitation ($Xe \rightarrow Xe^*$) of the neighbour atoms. The excited atom Xe^* will form in some picoseconds the metastable excimer molecule Xe_2^* [15]. In the ionization the ions of Xe^+ combine with a xenon atom to form Xe_2^+ as it has $\sim$1 eV less than both Xe^+ and Xe separated. The electrons created in the ionization process lose energy in the medium by creating more excitons Xe^*, ionizing more atoms Xe^+ or emitting phonons. If there is no electric field applied then they will recombine with the ion Xe_2^+ producing the exited state Xe^{**} and a xenon atom which decays to Xe^* in a non-radiative process producing another excimer molecule Xe_2^* [16].

The photons of scintillation in xenon are produced in the transition between the singlet $\left({}^1\Sigma_u^+\right)$ or the triplet $\left({}^3\Sigma_u^+\right)$ and the ground state $\left({}^1\Sigma_g^+\right)$ of the dimmer molecule Xe_2^*. In the gas the emission spectra is dependent of the pressure. For a gaseous pressure below 0.1 bar the emission is dominated by the first continuum which corresponds
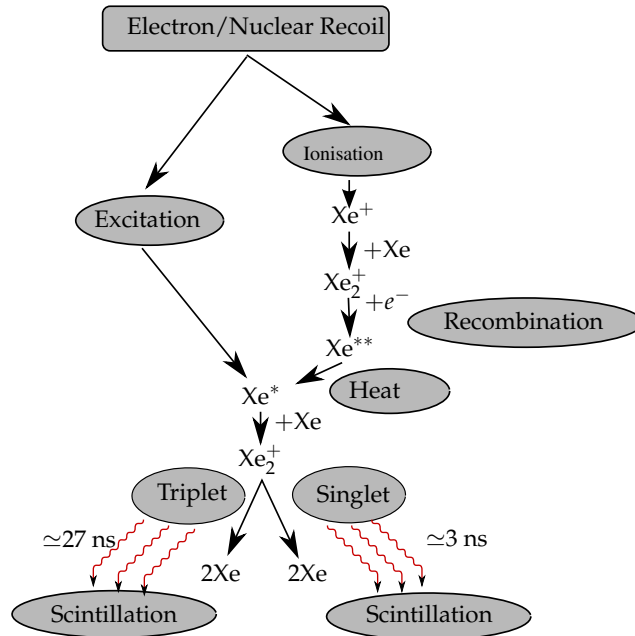
Figure 1.1: Mechanism of scintillation in xenon. There are two main channels for the production of VUV scintillation, ionization and excitation. In both situations a photon of scintillation is produced in the radiative decay of the molecule Xe_2.
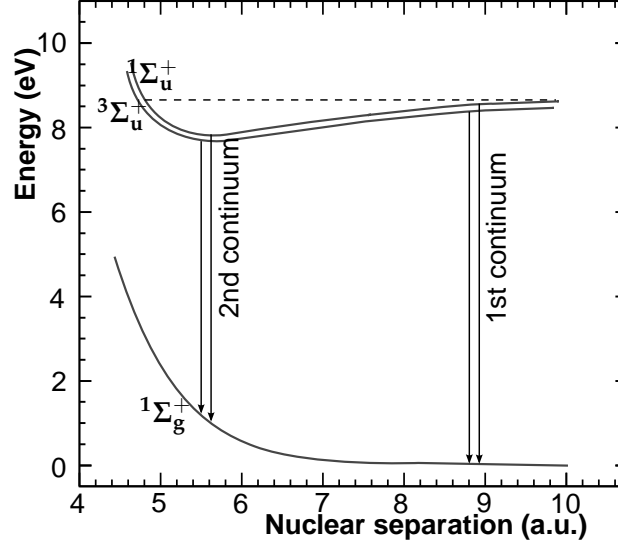
Figure 1.2: Potential curve of the lowest Xe_2 states and the transitions of the 1st and 2nd continua, 1 a.u.= 0.053 nm (from [18])

to a decay from a high vibrational level to the ground state. This emission is highly dependent of the pressure and placed around 150 nm [17]. The second continuum is attributed to transitions from the lower vibrational levels of the same electronic states. It appears at a pressure of about 0.05 bar and becomes dominant over the first continuum above a pressure of 0.2 bar. Above 0.5 bar the second continuum is highly suppressed and only the second continuum is generally observed [44]. The potential curves of the states of the molecule Xe_2 and the two continua are shown in the figure 1.2.

The wavelength of the emitted scintillation for the second continuum is about the same both states of the excimer and is peaked at 175 nm in the gaseous xenon and is slightly red shifted in the liquid ($\simeq$ 178 nm). The width of the emission spectra in the gas is larger comparatively to the liquid and solid (see figure 1.3). The peak of emission for the different rare gases in the liquid and gas states is shown in the table II. As shown the peaks have relatively the same value in gas and in the liquid expect for the krypton. It is also observed that the wavelength of the scintillation generally increases with the increasing of the atomic number of the element.

The decay time of the excited molecule Xe_2^* is dependent of the molecular state of the excimer, in the liquid xenon it is about 3 ns for the singlet $^1\Sigma_u^+$ and about 27 ns for the triplet state $^3\Sigma_u^+$. For the gaseous state the decay time of the singlet decreases with increasing of the gas pressure, approaching to the values of the liquid at high pressures [19]. This corresponds to the lowest decay times relatively to the other rare gases [20] (see table II) providing a time resolution comparable to the plastic scintillators.

The decay times do not depend strongly with the type and energy of the incident
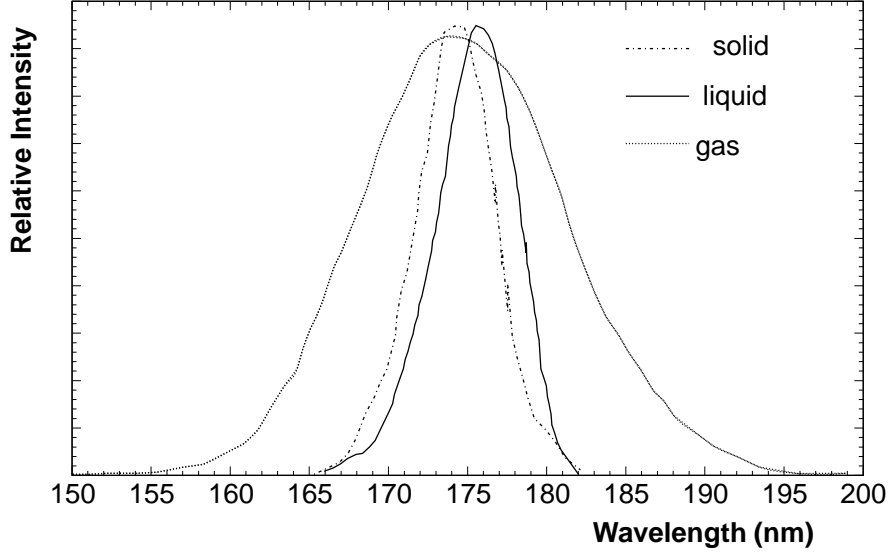
Figure 1.3: The emission spectra for the liquid (full line), solid (dashed line) and gaseous (dotted line) xenon. These results were obtained by [37] at a pressure of 1 bar.

particle [28]. However, these values are increased by recombination time which is dependent of the incident radiation. For electronic recoils the recombination time is about 15 ns, for alpha particles recoils the time of recombination is very short because the linear energy transfer LET (dE/dx) is much higher that in the electrons. Moreover, the ratio between the intensities of the singlet state, I_1, and triplet state, I_3, is different. In a recoil from an electron the scintillation is originated mainly from the triplet state, in contrast with a nuclear recoil for which the singlet state is stronger. Thus the analysis of the pulse shape can be used to discriminate between a recoil from an electron and a recoil from a nuclei.

The ionization and scintillation yields

In a scintillation detector the light detected in the photo-sensors need to be related with the type, energy and position of interaction of the incoming particle. This however requires a deep knowledge of the detector and the physical processes involved. The liquid xenon has a higher ionization and scintillation yield than the other rare gases being more efficient to produce both scintillation and ionization.

9

Table II: Scintillation and ionization characteristics of the argon, krypton and xenon detectors

		Argon		Krypton		Xenon	
		Gas	Liquid	Gas	Liquid	Gas	Liquid
Scintillation Properties							
Second continuum (nm)		130±8 [21]	129±5 [21]	148±6 [21]	177±6 [21]	175±7 [21]	178±7 [21]
First continuum (nm)		† 108 [22]		125 [22]		149 [22]	
$^1\Sigma_u^+ \to {}^1\Sigma_g^+$ τ_1 (ns)	at 1.5 bar at 10 bar	25 [19] 4.2 [19]	5.0±0.2 [27]		2.1±0.3 [27]	15.3±3 [19] 5.5 [19]	2.2±0.3 [27]
$^3\Sigma_u^+ \to {}^1\Sigma_g^+$ τ_3 (ns)		3,200±300 [19]	860±30 [27]		80±3 [27]	96±5 [19]	27±1 [27]
I_1/I_3	(electron) (alpha recoils) (fission frag.)		0.3 [28] 1.3 [28] 3 [28]				0.05[28] 0.45±0.07 [28] 1.6±0.2 [28]
Refractive index n ‡			1.38 [23]††	1.0006548 [24]	1.51 [23]††	1.0011867 [24]	1.69 [25] [23] ††
Rayleigh scattering length (estimated) L_r (cm)			90 [23]	-	60 [23]		30 [23]
Attenuation Length (measured) (cm)			66±3 [26]		82±4 [26]		29±2 [26]
Ionization Properties							
W_i (eV)	at 1.5 bar at 10 bar	26.4±0.5 [30] 26.7±0.5 [30]	23.6±0.3 [31]	24.0±0.5 [30] 23.8±0.5 [30]	18.4±0.3 [31]	20.9±0.4 [30] 21.0±0.4 [30]	15.6±0.3 [31]
N_{ex}/N_i		0.52 [30]	0.26 [15]	0.55 [30]	0.10 [15]	0.60 [30]	0.06[15]
Scintillation Yield W_{ph} (eV)							
Relativistic Electrons			25.1±2.5 [26]				23.7±2.4 [26] ††
α-particles (in the gas at 1-2 bar)		50.6±2.6 [34]	27.5±2.8 [26]	42.0±3.0 [34]		49.6±1.1 [35] 34.3±1.6 [34]	19.6±2.1 17.1±1.4 [36]
α-particles at high pressure (10 bar)		25.3±1.1 [34]		22.3±0.8 [34]		14.6±0.5 [34]	
α-particles with an applied electric field						59.4±2.4 [30]	
Nuclear recoil							14.7±1.5 ††
L_β/L_α *			1.11±0.05 [31]				0.87 [32]

† Only observed for low pressures of gas (typically below 0.1 bar)
‡ At the scintillation wavelength of the second continuum
†† *Estimated*
* Ratio between the scintillation produced in an electronic recoil and recoil from an α-particle

When a particle interacts with the atom of xenon it deposits a certain amount of energy E under excitation or ionization. The energy balance equation for this process is given by

$$E_0 = N_i E_i + N_e E_e + N_i \epsilon \tag{1.1}$$

where N_{ex} and N_i are respectively the number of excited and ionized atoms by the incident radiation, E_i and E_e are the average expended energy for the ionization and excitation and ϵ corresponds to the average energy of the sub-excitation electrons.

The ionization yield is given by E_0/W_i where E_0 corresponds to the deposited energy and W_i is defined as the average absorbed energy required for the production of the electron-ion pair. This value is almost independent of the energy and type of the incident particle, therefore it is a characteristic of the medium. It is about 21.0 eV for the gas and 15.6 eV for the liquid [31] (these values are shown in the table II and compared with the other rare gases).

The measurement of the ionization is performed by applying an electric field to the liquid or gas which inhibits the recombination of the electrons with the xenon ions. When the ionization density is low (e.g. an electronic recoil or a recoil in a low pressure gaseous detector) the electrons can be collected using a weak electric field. For heavily ionizing particles, such as a recoil from an alpha particle, large part of the electrons recombine with the xenon ions even when a large electric field is applied. For an alpha recoil in a liquid xenon detector only 10% of the charge is collected for an applied field of 20 kV/cm [29]. Due the lower density the charge collection efficiency is usually higher for the krypton and argon

In the same manner the scintillation yield is E/W_{ph} where W_{ph} is the average absorbed energy required for the production of a photon [38]. In the absence of photon reduction processes W_{ph} is related with W_i through

$$W_{ph} = W_i / (1 + N_{ex}/N_i) \tag{1.2}$$

However, it is observed deviations relatively to the equation 1.2, and generally the value W_{ph} is dependent of the linear energy transfer (LET) of the recoiled particle, the amount of energy deposited by the recoiled particle per unit of length path. The value of W_{ph} increases for small LET (<10 MeV· cm^2/g) and higher LET (>1 GeV·cm^2/g) [39] of the particle that is recoiled.

In the low LET region, such as a recoil from a relativistic electron, the value of W_{ph} is higher because some electrons do not recombine immediatly due the low ionization density. They lose their energy in successive elastic scattering with the atom (thermalization) and do not recombine in an extended period of time.

In the high LET region, recoils of the heavier particles usually a nuclear recoil, the reduced light yield is caused by the so-called quenching effect. The ratio between the the scintillation yield by the nuclear recoil and the scintillation yield by an electron recoil of the same energy is called called the relative scintillation efficiency L_{eff} [40]. The quenching is usually assumed to be caused by energy transfer from the recoiled particle

to the translational motion of the atoms (atomic quenching described by the Lindhard theory [41], [42]). However, the quenching observed for the rare gases is larger than the predicted by the Lindhard theory. Hitachi proposed the collision between two excitons producing one photon instead of two as the cause for the electronic quenching [43] ($Xe^* + Xe^* \rightarrow Xe^+ + e^-$). Due to its large atomic mass the quenching for the xenon atom is larger relatively to the other rare gases. The measured value for the quenching factor shows that the value changes with the energy of the incident atom, however it is almost flat for a xenon nuclear recoil with energy between 20 keV and 200 keV being about 0.19±0.02 [44].

The values obtained for W_{ph} for the alpha and electrons are shown in the table II for the gas and the liquid and compared with other rare gases. As shown the value of W_{ph} is smaller relatively to the other rare gases being the xenon more effective to produce scintillation photons.

Photon interactions in the liquid xenon detectors

In a liquid/gas xenon detector, the light can change their direction between the hit position and the photo-detector window(e.g. a photomultiplier), due the scattering in the inner surfaces of the detector, Rayleigh scattering, or be absorbed in the surfaces or in the liquid/gas bulk. A description of these phenomena is necessary to relate the light observed in the photo-detectors with the deposited energy. The xenon is considered to be transparent to their own wavelength scintillation, the energy of absorption band is above of the energy of the emission band, however the photons can be absorbed by impurities that exist in the bulk, particularly water vapor and oxygen [45]. Thus, this value is dependent of the purification of the liquid or gas, being usually necessary to control the purification during the experimental procedure. The Rayleigh scattering should have a assignable effect in the liquid. The estimated Rayleigh scattering length is about 30 cm [23], however this value was not measured experimentally. It is experimentally difficult to distinguish the Rayleigh scattering from absorption, therefore what is usually reported is the attenuation length d_{at} given by a combination of both effects

$$\frac{1}{L_{at}} = \frac{1}{L_r} + \frac{1}{L_{ab}} \tag{1.3}$$

L_r is the Rayleigh scattering length and L_{ab} is the absorption length. The values reported for the attenuation length are 29±2 cm [46], 36.4±1.8 [25]. These values are very similar even when different purification systems are used, thus the main contributor for the attenuation length should be the Rayleigh scattering. The reported values of the attenuation length for the xenon are lower comparatively to the liquid argon or krypton where the attenuation reported is greater than 60 cm [46]. This reduces the position/energy resolution of the liquid xenon relatively to the other rare gases. However, mixtures between argon or krypton and liquid xenon (3%) have attenuations length reported greater than 1 m being the emitted photons peaked at 174 nm similarly to the

pure liquid xenon [26].

Concerning to the reflection in the interior surfaces of the scintillation detectors there is poor knowledge of the reflecting properties of most materials that are used. Because the index of refraction of the gas ($n \simeq 1$) and of the liquid ($n \simeq 1.69$, [25]) are far apart, the reflectance in the interior surfaces will be different. Moreover, liquid and xenon detectors usually work at different temperatures which can change the optical constants of the materials involved.

A deep knowledge of the reflection processes is essential for a good data analysis (e.g. simulation and position reconstruction) and also for the design of new detectors. Whenever the number of photons produced is very low a high reflectance is required for the interior surfaces which means using materials such as PTFE or alike enhancing the properties that are desirable to a specific experiment. For example when the recoil energies are very low the number of photons produced is very low, this requires a high reflectance of the interior surfaces and use a material such as the PTFE.

The two-phase detectors

The most interesting mode of operation of liquid noble gases detectors is in the two phase mode. This type of detectors are composed by a liquid phase plus a gaseous phase (saturated vapour) in which both the scintillation and the ionization are measured. A high and constant electric field is applied in three distinctive regions, the liquid, the vapour and the liquid/gas interface. Due the electric field applied the electrons created by the primary ionization in the liquid phase that do not recombine are pushed to surface of the liquid and extracted to the vapour phase. In the vapour they produce more light, electroluminescence or secondary scintillation (often abbreviated to S2), proportional to the primary ionization. The light signal from the excitation and recombination is called primary scintillation (abbreviated to S1). Both signals from primary and secondary scintillation are detected by VUV sensitive photodetectors such as photomultipliers that can be located in the gas or in the liquid. The two signals are strongly anti-correlated because the presence of an electric field leads to the suppression of the recombination [47], decreasing the signal of the primary scintillation.

The advantage of the two phase detectors is the increased power of discrimination between an electron and a nuclear recoil. An incident beta or gamma ray will produce mainly electroluminescence because the recombination is highly suppressed, whereas the recoils due to incident alphas or nuclei will produce mainly direct scintillation (S1). Thus the ratio between primary and secondary scintillation will be different in the two situations. Another advantage comes from the 3D position sensitivity resolution that is achieved with the detection of both signals. The signal from the electroluminescence provides a good spacial resolution in the x-y plane, also the delay of this signal relatively to the S1 signal is caused by the drift time of the electrons in the liquid, giving information about the depthness of the interaction in the liquid.

1.2 Experiments Using Scintillation Gas/Liquid Xenon Detectors

Several experiments seeking fundamental physics use of liquid/gas detectors. Generally they are aimed at observing rare events such as the interaction of dark matter, double beta decay or other rare decays such as $\mu \rightarrow e\gamma$ decay. It worths mention the fact that concurrent experiments using liquid/gas detectors are being used to measure the same phenomena (e.g. dark matter or double β decay searches). The active mass of these experiments has been increased in recent years and there are projects to experiments with active masses that can reach one ton.

The application of xenon detectors is not restricted to fundamental physics, they have also been projected to be used in medical imaging and gamma ray telescopes [50].

The detectors use mainly dual phase detectors measuring both light and charge thus the particle identification is easier. To increase the efficiency in the light collection the materials in contact with the xenon should have a high reflection, thus the use of PTFE as a vessel material is common.

Dark matter searches

The existence of dark matter is required by various cosmological evidences. The primary cosmological evidence is the observation of the rotation curves of the galaxies, i.e. the circular velocity of the stars as function of the distance to the centre of the galaxy. The matter observed is not enough to explain the rotation curves observed using the newtonian dynamics, therefore a halo of exotic matter is usually assumed [55]. Moreover, the barionic density inferred from the primordial nucleosynthesis is not able to explain the formation on large scales and extra-galactic dynamics [51, 52].

One of the diverse possibilities of dark matter is the existence of weakly interactive massive particles (WIMP) [8]. A good candidate is the neutralino, the lightest and stable particle of the supersymmetric model [53],[54].

The high mass of the Xe nucleus provides both a good kinematics match for WIMPs in the energy range between 10 and 1000 GeV and a high event rate comparatively to the other rare gas detectors. The coherent cross section between the WIMP particle and the nucleus is proportional to A^2, where A is the atomic mass of the nucleus [55]. Nevertheless the expected rate of collisions in the liquid is still very low (between 0.1 and 0.0001 events/kg/day in a liquid xenon detector [56]) which implies reducing the background to extremely low levels. The event rate of one of those detectors is typically $\simeq 10^6$ lower than the ambient background rate due the radioactivity from the detector and shielding structures and muon cosmic rays. Thus these experiments need to be placed in deep underground facilities such as mines or mountainous tunnels. Also in the construction of the detector is necessary to use low radioactive materials and implement an active veto system for background rejection in addition to a passive shielding structures for neutrons and gammas background.

1.2 Experiments Using Scintillation Gas/Liquid Xenon Detectors

Currently there are four major collaborations searching for dark matter collisions [49]: i) the ZEPLIN collaboration working at the Palmer Laboratory in a potash salt mine in United Kingdom, ii) the XENON collaboration operating in the Laboratori Nazionale del Gran Sasso in Italy, the LUX collaboration in Stanford Deep Underground Laboratory at the Homestake Mine, South Dakota and the XMASS collaboration in Mozumi Mine in Kamioka, Japan.

The ZEPLIN II experiment conducted by the ZEPLIN collaboration was a two phase detector with a 31 kg of liquid xenon. The volume was viewed with seven photomultipliers placed above the liquid in the gas phase. The volume was defined by a thick PTFE tapered annulus with a conical frustum [56], [59]. This experiment excluded WIMP-nucleon collisions with a cross section above 7×10^{-2} pb for a WIMP mass of 65 GeV/c^2. In the simulation studies of this detector, the PTFE was assumed to be a perfectly diffused surface with an albedo of 0.9 [5].

The ZEPLIN III experiment is currently in operation, it uses a 12 kg two-phase xenon time projection chamber, with 31 photomultipliers viewing the liquid from the bottom. The liquid is surrounded by a copper reflector where the bottom surface has been lapped and left highly polished [60]. In the simulation studies the reflectance of the copper was set to be 15% with a gaussian smearing of 20° around the specular direction [61]. The results from the first science run have excluded a WIMP-nucleon elastic scattering spin-independent cross section above 8.1×10^{-8} pb at 60 GeV/c^2 with a 90% confidence limit [62].

A cross section view of the ZEPLIN II and ZEPLIN III detectors is shown in the figure 1.4.

The XENON10 experiment from the XENON collaboration has a 15 kg of fiducial mass, two sets of PMT's that are placed above and below the liquid, the lower set of PMT's is placed in the liquid detecting the light that is oriented to the bottom of the chamber, the top array is placed in the gas detecting mainly the proportional scintillation light [57]. The active volume is defined by a cylinder of PTFE with an inner diameter of 20 cm and a height of 20 cm. The first results are already published [64] and show an upper limit for the WIMP placed at about 8.8×10^{-8} pb for a WIMP mass of 100 GeV/c^2.

The XENON100 is an improvement over XENON10 aiming to increase the sensibility by a factor of 100. The active volume has a mass of about 70 kg and it is enclosed in a PTFE cylinder of 15 cm radius and 30 cm height [58].

The LUX collaboration will be a 350 kg active mass two-phase xenon experiment, whose active volume is viewed by 120 PMT's. It aims to achieve a sensitivity better than $\sim7\times10^{-9}$ pb in one year of operation [31]. PTFE is being considered for the vessel inner walls.

The XMASS experiment (Xenon detector for Weakly Interacting Massive Particles) is being constructed in the mine of Kamioka and was designed as a multi-purpose experiment. The detector will be spherical in shape and uses 800 kg of liquid xenon

1. ON THE LIQUID/GAS XENON SCINTILLATION DETECTORS
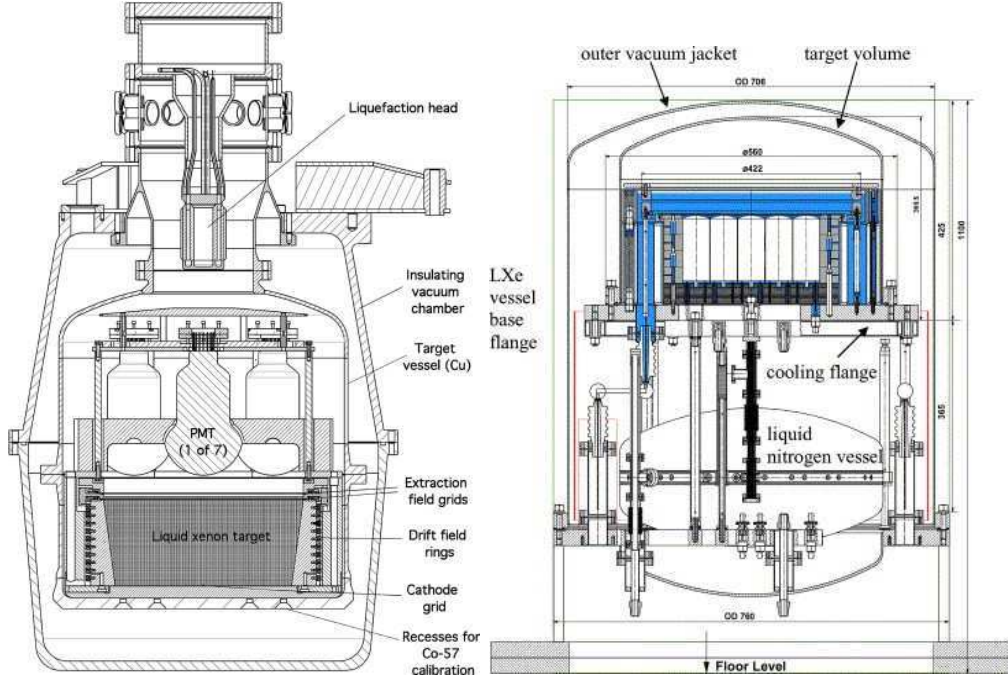
(a) Schematic of the ZEPLIN-II detector. The liquid xenon volume is viewed from above by 7 quartz-window photomultipliers and surround by a PTFE wall [63].

(b) Cross-sectional view of the ZEPLIN-III detector showing the key sub-system components. The liquid xenon volume is viewed by 31 photomultipliers, the bulk of the parts are made of copper [60].

Figure 1.4: Cross section view of the two ZEPLIN detectors

that are completely surrounded by 642 hexagonal PMT's [65]. A prototype with about 100 kg has already demonstrated the feasibility and working principle. It is the only collaboration to use a single-phase detector.

Neutrino-less double-beta decay

The double-beta decay consists in the simultaneous emission of two beta rays by a nucleus. It is the rarest known nuclear process, with the longest half life (in the order of $\simeq 10^{18} - 10^{21}$ years). It is only observable when the single beta decay is forbidden or strongly suppressed. According to the Standard Model the conservation of the lepton number requires also the emission of two anti-neutrinos [9]

$$A\left(Z, N\right) \to A\left(Z + 2, N - 2\right) + 2e^{-} + 2\bar{\nu} \tag{1.4}$$

The zero neutrino double beta decay ($0\nu2\beta$) is not possible according to the Standard Model as the lepton number is not conserved. Nevertheless this decay can exist if
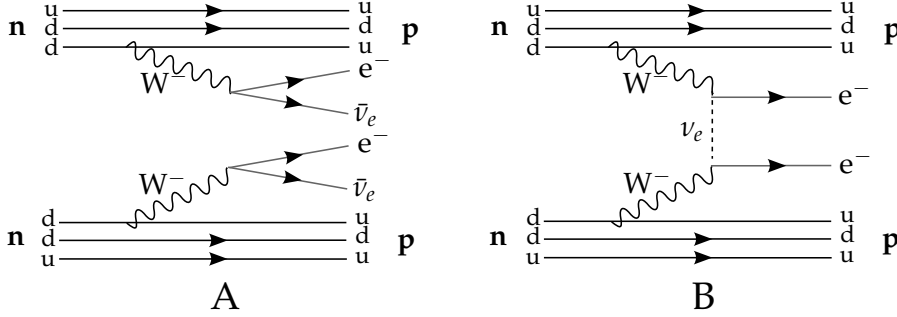
Figure 1.5: Feynman diagram of the double-beta decay with the emission of two neutrinos (A) and the neutrinoless emission (B).

the neutrino has non zero mass and it is a Majorana particle (the neutrinos and antineutrinos are the same particle). The emission will occur at a single well-defined energy, Q, which corresponds to the total energy emitted in the process. The mass of the neutrino can be measured as it is proportional to the square of the event rate [31]. The Feynman diagrams of the double beta decay with/without neutrino emission are shown in the figure 1.5

In a xenon detector the double beta decay can occur for the xenon isotopes ^{124}Xe, ^{134}Xe, ^{136}Xe thus the detectors need to be enriched in these isotopes. The energy released in the process of double beta decay of ^{136}Xe is about $Q = 2479$ keV. The lifetime is larger than 10^{22} yr for the $2\beta2\nu$ decay [66]. Such a rare process requires that the background of the experiment to be highly reduced and under control. Two detectors are being projected for the detection of this decay, the EXO and the NEXT experiment.

The EXO experiment ("Enriched Xenon Observatory") is a two-phase detector enriched to 80% of the isotope ^{136}Xe that will be assembled in the WIPP (Waste Isolation Pilot Plant) in New Mexico [67]. Two different detectors will be constructed; EXO-200, a 200 kilogram prototype aims to provide a competitive limit in the neutrinoless beta decay. The knowledge acquired in this prototype will be used in the next phase, a ton scale experiment. In the EXO-200 detector the scintillation light is read by 258 bare large area avalanche photo-diodes. The liquid is surrounded by thin PTFE sheets supported by acrylic pillars.

The NEXT experiment ("Neutrino Experiment with Xenon TPC") is being projected as a time projection chamber with 10 kg of xenon pressurized at 5-10 bar. The chamber will be assembled at the Laboratorio Subterraneo de Canfranc (LSC) in Huesca (Spain) [68]. It is possible that this experiment will make use of PTFE in its interior surfaces[1].

---

[1]Private communication

1. ON THE LIQUID/GAS XENON SCINTILLATION DETECTORS

Charged lepton flavour violation

The charged lepton flavour violation corresponds to the decay of a more massive charged lepton into a less massive charged lepton with no conservation of the lepton number. This process is only possible for a massive neutrino, however according to the Standard Model the branching ratio of these decays is very small ($\simeq 10^{-50}$) and cannot be observed within the current experimental limits [10]. Nevertheless, the supersymmetric theories predict a much greater branching ratio ranging between $10^{-11} - 10^{-14}$, meaning that $\mu \to e\gamma$ could be observed within the current experimental limit.

The MEG (Muegamma) experiment, currently in preparation, aims to search for the decay $\mu \to e\gamma$ [69]. A 900 liter liquid xenon detector equipped with 846 PMT's placed around the active volume is being projected [70]. The photomultipliers are embedded in an aluminum structure. It will use the DC muon beam of the Paul Scherrer Institut (PSI) in Zurich, Switzerland. The key requirement for this detector is a high energy resolution of the gamma rays. The construction of this detector has been completed and data taken in 2008 have yield an upper limit in the branching ratio $\mu^+ \to e^+\gamma \leq 3.0 \times 10^{-11}$ (90% C.L.) [71], additional improvements are being made aimed to lower this value.

Gamma ray telescopes

A gamma ray telescope capable to observe and study the several gamma ray sources that exist in the universe such as supernovas, star formation, the distribution black holes or the nucleosynthesis. It requires a detector with a large field of view, large effective area, low background and good discrimination due to the small cross-section of the gamma rays, small source fluxes and lack of focusing optics [72].

The LXeGRIT (liquid xenon gamma-ray imagine telescope) is a time projection chamber with about 10 liters of liquid xenon to image gamma ray emissions between 0.15 and 10 MeV. The detector measures both scintillation and charge produced in the interaction of the γ rays with the liquid and is able to measure the position and energy of the event [73]. The interior surfaces of the detector are in stainless steel, except for the four ceramic rods supporting the TPC structure.

The LXeGrit was tested in balloon flights in 2000 measuring the background and sensitivity of the instrument and demonstrating the principle of working [50].

Medical imaging

Liquid xenon detectors can also be used as gamma detectors in positron emission tomography (PET). This imaging technique uses radio active labeled molecules to image *in vivo* the biological processes to the medical diagnosis. Typical radio-tracers are ^{11}C, ^{13}N, ^{15}O and ^{18}F. The emitted positrons annihilate generating two back to back gamma rays. These gamma rays are then detected by a structure that surrounds the

patient. The resolution of these systems in real time is typically some millimeters. The measurement of the time of flight increases further the resolution of the system being possible to know exactly the position of interaction measuring the difference between the arrival of both gamma rays [74].

1.3 Fluoropolymers and their Properties

The structural units of fluoropolymers have as rely on the fluorine carbon bound (CF). The fluorine atom is more electronegative than the carbon atom and the electrons are pulled toward the fluorine, making it the strongest bound in organic chemistry endowing these materials with a strong chemical resistivity. The simplest fluoropolymer is PTFE (polytetrafluoroethylene), which corresponds to a chain of carbon atoms each bounded with two fluorine atoms. Other fluoropolymers (perfluoroalkoxy, ethylenetetrafluoroethylene and fluorinated ethylene propylene) have other molecules attached as hydrogen and oxygen. The chemical structure of some fluoropolymers referred to above is depicted in figure 1.6.

The polytetrafluoroethylene (PTFE)

The PTFE (Polytetrafluoroethylene) is a polymer produced from the Tetrafluoroethylene with a chemical structure given by C_nF_{2n} (figure 1.6). It was first synthesized by Roy Plunkett at the DuPont's Jackson Laboratory in 1938. It is also known as Teflon®, a trademark of DuPond registered in 1944. It is characterized by a chain of carbon atoms completely surrounded by fluorine atoms. The molecule has a helix form requiring 13 to 15 units of CF_2 to complete a 180° twist of the molecule (figure 1.7) [76].
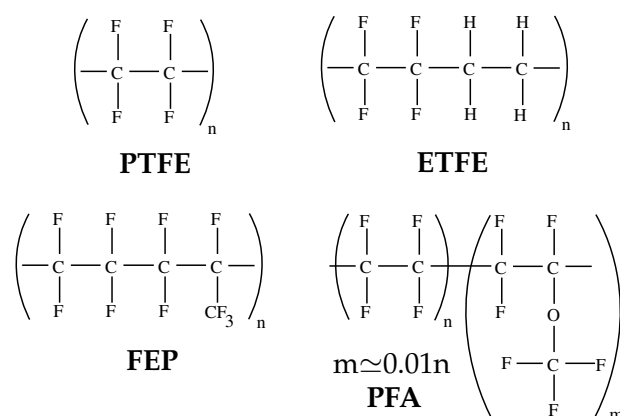
Figure 1.6: The chemical structure of the monomers (structural units) of the fluoropolymers, PTFE, ETFE, FEP and PFA

Table III: Properties of the fluoropolymers taken from the manufacturer specifications sheets.

Manufacturer	ASTM∗	PTFE Fluoroseals®	PTFE GoodFellow®	PFA Dupond®	FEP Dupond®	ETFE Dupond®
Refractive index	D542	-	1.38	1.350	1.341-1.347	1.407[78]
Solar transmission (%)	E424			96	96	95
Density (g/cm^3)	D792	2.13-2.18	2.20	2.100	2.12-2.17	1.71
Tensile strength (MPa) †	D1457	21-34		25	23	40-46
Flexural modulus (GPa) ‡	D790		0.3-0.8	0.70	0.655	1.2
Coefficient of friction ††	D1894	0.07	0.05-0.2	0.1-0.3	0.3-0.4	
Melting point (°C)	D3418	325-335		302-310	260-280	255-280
Maximum temperature of service (°C)	UL746	260		260	205	150
Water absorption 24h (%)	D570	0.01	0.01	<0.03	<0.01	0.007
Water contact angle (°) ‡‡		120 [79]	120 [79]	106 [80]	114[81]	96 [82]

∗ Standards defined by the American Society for Testing and Materials, the definition of the standards used here can be found in [77]

† Indicates the maximum of the stress-strain curve

‡ The material is subjected to three-point bending. The specimen is deflected until it either breaks or the outer fiber strain reaches 5%.

†† Static coefficient of friction measured in steel.

‡‡ Angle in which the water droplet meets the surface, angles larger than 90° indicate an hydrophobic material.
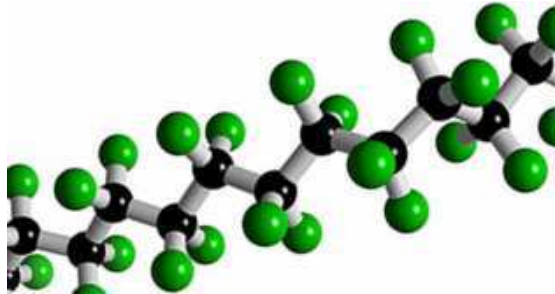
Figure 1.7: 3D representation of a PTFE molecule. Black spheres represent the carbon atom, the green spheres represent the the fluorine atom (from [75]).

Table III contains the optical, thermal and mechanical characteristics of the PTFE and other fluoropolymers. As the properties of the PTFE can change with the manufacture, two producers are shown for the PTFE (Fluoroseals® and GoodFellow®). Some of the properties that make the PTFE an exceptional plastic for use in scintillation detectors are:

a) *High density:* the PTFE has a density of 2.15 g/cm^2 which is higher than the majority of the plastics whose value is usually placed between 0.9 and 1.4 g/cm^2.

b) *Low coefficient of friction:* it is the lowest of any polymer known being an attractive material to be used in lubrication of sliding materials such as gaskets, rings and bearing for vacuum insulation [83].

c) *High temperature resistance:* it can be operated in a wide range of temperatures between -200°C and -260°C, the melting point is about 330°C, higher than the majority of the plastics and can be used until 200°C without losing its chemical and physical properties. The thermal conductivity is very low thus the PTFE can be used as a thermal insulator.

d) *Chemical resistance:* the PTFE is insoluble against almost all chemical solvents known, acids or bases, due to the strong inter-atomic bounding. However, alkaline metals as the sodium or liquid ammonia react with the PTFE extracting the fluorine atoms of the molecule leaving a black surface finish [84].

e) *Low water absorption and low outgassing:* it is less than 0.01% in mass in 24h, a value that is small compared to the majority of plastics, (for example the water absorption of the POM is about 0.3% in 24h). This is associated with the hydrophobic nature of the PTFE molecule due to its fluorine atoms. In fact this is very convenient, as in the experiments less water will be present to contaminate the system.

Table IV: Typical levels of radioactive contaminants in the PTFE.

Element	Concentration in mass
^{40}K	$(1.65 \pm 0.17) \times 10^{-9}$
^{232}Th	$< 0.35 \times 10^{-12}$
^{238}U	$< 0.35 \times 10^{-12}$

Measurements to the PTFE TE-6472, a PTFE developed by Dupont with a high purity standard (measurements performed by the EXO collaboration [67]).

f) *Low adhesion:* PTFE has an extremely low adhesion as shown by its high contact angle with the water [85]. This effect is increases when the roughness of the material increases [86]. This is an important property in a xenon detector to obtain a clean surface.

g) *High reflectance:* Due their high reflectance the PTFE has been used as coating layer in integrating spheres and calibration standard for on-board sensors on satellites in remote sensing [87]. Both the PTFE and the human skin are mainly diffuse materials. Thus the PTFE has been used in biological studies as a probe for the study of the diffuse reflectance of the skin [88, 89].

h) *Low radioactivity:* PTFE shows very low level of long-lived radioactivity, particularly ^{232}Th, ^{238}U and ^{40}K. When the cosmic rays interact with the PTFE and other plastics they generally will not produce long-lived radioactive isotopes as in many of the metals. Table IV summarizes the level of radioactivity for the PTFE measured by the EXO collaboration [67].

The use of PTFE in the scintillation chambers brings however some disadvantages relatively to other materials such as metals.

a) *Non electrical conductivity:* Due its low conductivity in the double-phase configuration it can trap some ions reducing their mobility and thus decreasing the effectiveness of the charge collection. In the ZEPLIN II experiment it was observed an unexpected population of events due the migration of the radon daughters to the surface of the detector. Small energy deposits of some keV that occur in the PTFE can mimic a nuclear recoil increasing the background of the measurement [63].

b) *Radiation resistance:* The PTFE is sensitive to ionizing radiation, as it is able to break the PTFE chains reducing its molecular weight [90].

c) *Production:* the PTFE cannot be produced by melt-process techniques because the melted PTFE has a high viscosity (about 10 GPa·s). Alternative processes are used however they are more expensive.

d) *Wear Resistance:* the PTFE is plastic relatively soft having a poor wear[1] resistance. This can cause leakage in the seals thus effectively reducing the vacuum quality [91] .

The structure of the PTFE

PTFE is a two-phase system composed of crystalline and amorphous domains [92]. In the crystalline domains the PTFE chains are ordered, they are folded back into themselves and stacked in lamella as depicted in the figure 1.8. In the amorphous phase the PTFE chains have no particular orientation. The degree of crystallinity, defined as the ratio between the crystalline and the amorphous domains, depends of the manufacture of the PTFE and affects the mechanical and optical characteristics of the PTFE.

The PTFE shows a low index of refraction due the high fluorine content inducing a low polarizability in the material. For a totally amorphous PTFE the index of refraction in the visible spectra is about 1.29 [94]. This corresponds to one of the lowest refractive indexes of the organic polymers. However, the crystalline domain has a larger value of 1.4 [95]. Thus the index of refraction of the PTFE depends generally of the degree of crystallinity of the material. Usually it is not possible to inhibit the crystallization of the PTFE completely and values between 1.325 [96] and 1.38 [97] are reported for the index of refraction in the visible spectra.

In the visible spectra the index of refraction is weakly dependent of the wavelength. As observed by [98] for a PTFE layer of 1 μm the index of refraction decreased from 1.38 to 1.37 when the wavelength increased from 350 nm to 1000 nm.
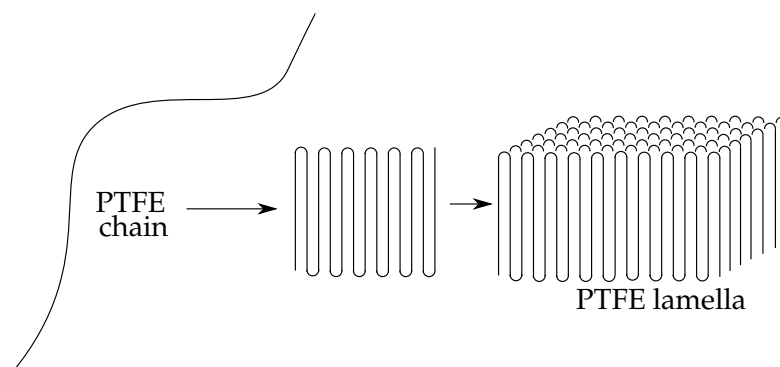

PTFE
chain

PTFE lamella

Figure 1.8: Structure of a crystalline domain in a polymer (adapted from [93])

---

[1]Erosion of the material by the action of another surface

The index of refraction of the PTFE is also dependent of the thickness of the PTFE layer, for the thicker materials it is observed a larger index of refraction [98].

Production of PTFE

There are two methods of production to obtain the PTFE from the fluoroethylene (TFE), the suspension polymerization used to produce granular PTFE and the dispersion polymerization [99, 100], "in which" resulting PTFE is a milky paste used to produce dispersion and fine power used in coatings [101]. In both cases the PTFE is polymerized in water in the presence of an initiator.

Suspension Polymerization   In the suspension polymerization process the gaseous TFE is piped into a reaction chamber filled with water, an initiator (ex. ammonia) and also a very small amount of a dispersion agent (ex. perfluoroalkanoic acid salts) [99]. The solution is vigorously agitated, the TFE will polymerize into PTFE and form solid grains in the surface of the liquid that are collected.

The product obtained, called granular PTFE, has a high molecular mass and a high crystallinity level (about 92-98%) [102]. The processing of the PTFE is more difficult than in the majority of the materials, above 320°C the PTFE becomes gel like, it is highly viscous and melt process techniques cannot be used. At temperatures above 400°C the bound C-F starts fracturing and the material decomposes.

Dispersion Polymerization   In the dispersion polymerization the concentrations of the initiator and reaction agent are much higher than in the suspension process. The agitation comparatively to the suspension process in usually milder. The result is a milky paste having grain dimensions much smaller than obtained by the suspension method. This form of PTFE is usually used for coating and cannot be molded.

The PTFE finishing

The granular PTFE produced by suspension polymerization is then converted in the final product that is available commercially which can be sheets rods, tubs or tapings etc. In principle, these processes can result in different optical properties of the final product.

Molded process   The molded process consists of three different steps, performing, sintering and cooling. In the first step the material is introduced in a mold and then loaded into a hydraulic press, the typical pressures applied range from 200 to 300 bar [103]. Then it is introduced in a sintering oven and is heated above the crystalline melting point of the PTFE (360-380°C) [103], the PTFE particles coalesce resulting into a strong homogeneous structure. The cooling determines some of the properties of the PTFE.

Table V: Domain size of the PTFE cooled at different cooling rates

Cooling Rate (°C/min)	Crystallinity (%)	Domain Size [†] (nm)	Density (g/cm^3)
Quenched in ice water	45	111±33	2.138
2	53	160±49	2.146
0.48	58	144±50	2.156
0.12	65	185±84	2.192
0.02	68	259±204	2.205

This table was adapted from [92].

[†] The domain size corresponds to the approximate size of the crystallites.

The crystallinity, the domain size and the density of the material increase when the cooling rate decreases (see table V). At a cooling rate of 4°C/min the crystallinity obtained is minimized and does not decrease for higher cooling rates. The crystallinity of the material also changes with the stress applied during the manufacturing, decreasing with increasing the strain applied.

Skived PTFE   The skived process consists in cutting the billets produced in the molded process with a sharp cutting tool into small thin layers or the desired thickness. The layers produced with this process have a typically thickness ranging from 25 *μm* to 3 mm [102].

Extruded PTFE   In the extrusion process the PTFE powder is blended with a lubricant and then pre-compressed at about 0.7-2.0 MPa. It is then placed in the extrusion cylinder and pushed slowly through a heated die with a cylindrical form. The effect of temperature and pressure generates a continuum extrudate with a rod or tube form [104].

This process can in principle introduce different reflecting properties (specifically index of refraction) along direction of extrusion and across the direction of extrusion.

Expanded PTFE   Expanded PTFE is produced by injecting air during the manufacturing process. This produces a soft and very flexible material with mechanical characteristics remarkably different from the PTFE produced with other processes. The expanded sample has a porous micro-structure that is about 50% air by volume. This product can be used in gaskets, membranes etc. [105]. It has a special use in biomedical applications because it has mechanical properties compatible with the biological tissues and is inert [106].

1. ON THE LIQUID/GAS XENON SCINTILLATION DETECTORS

Filled PTFE compounds   The addition of particles during the PTFE production, fillers, improves some physical qualities of the PTFE such as reducing the creep and wear rate of the material [107]. Some of the common fillers that are added to the PTFE are glass, carbon and bronze. The glass is added to the PTFE in quantities ranging from 5% to 40% of the total mass reducing the creep and compressibility of the material. The carbon fiber reduces creep, increases hardness and thermal conductivity of the PTFE.

The copolymers (PFA, ETFE, FEP)

The PTFE is part of the large family of fluoropolymers. The PTFE is a homopolymer as it has only one repeating molecule, the tetrafluoroethylene. The copolymers have at least two different types of constituent species, monomers, that are joined together to form the molecule of the polymer. The copolymers that are refereed here (FEP, ETFE, PFA) are all produced by melt processing techniques. They all are transparent when they are illuminated by visible light, the ETFE has the largest optical clarity and can be used as replacement of the glass.

The fluorinated ethylene propylene (FEP)   The fluorinated ethylene propylene (FEP) is produced from the tetrafluoroethylene and hexafluoropropylene. The FEP was produced as an alternative to the PTFE as it can be manufactured by melt processing techniques [76]. It has however a reduced thermal stability and a lower temperature of service, this is caused by the introduction of the methyl group which acts as a defect in the crystallinity of the material and reduced the melting point [102]; it reduces also the index of refraction relatively to the PTFE. It is a relatively soft thermoplastic with lower tensile strength, wear resistance, and creep resistance than many other engineering plastics. FEP is also known to have a good resistance against the UV radiation [108].

The perfluoroalkoxy (PFA)   The PFA (perfluoroalkoxy) also known by the trade-name of Teflon®, can be produced by melt-processing and has the same upper temperature of service as the PTFE. It is a copolymer formed from the tetrafluoroethylene and fluoroacetylene ($CF_2CFOC_3F_7$). However these two mers are not added in the same ratio. For each fluoroacetylene there is about 100 tetrafluoroethylenes.

The ethylene-tetrafluoroethylene (ETFE)   The ethylene-tetrafluoroethylene (ETFE) is a copolymer formed from the tetrafluoroethylene and ethylene. It is known by the trademark Tefzel®, of DuPont. It is a mechanically stronger polymer relatively to the PTFE, however due the presence of the hydrogen molecule it has a lower chemical resistance, lower temperature of service and higher coefficient of friction. They have also a poor resistance to crack at higher temperatures. The ETFE is an amorphous material, however the presence of the hydrogen molecule in the polymer increases the refractivity of the material [92], [109].

1.4 The Reflectance of the PTFE - Summary of the Published Measurements

The PTFE has a high reflectance at the visible light, this is mainly caused by diffuse reflection. This corresponds to the light that is transmitted to the PTFE, scattered in the material inhomogeneities and transmitted back to the first medium. For diffuse materials, such as the PTFE, the method usually used to measure the reflectance are the hemispherical methods (appendix A). These methods make use of a total integrating sphere coated with a "perfect" diffuse material used to gather the light into the photo-detector. As we can observe from the figure 1.9 two openings are necessary , one for the beam entrance and another for the sample [110]. The coating that is usually used due its high reflectance in the visible spectra is the PTFE [111].

This is the best method to measure the directional-hemispherical reflectance at fore-hand without the need to introduce any model to perform the integration. However it is not possible to obtain with this method the BRIDF (bidirectional reflectance intensity distribution function, see appendix A), which is the basic quantity to describe the reflection distribution. Even with a light trap is not possible to separate the specular from the diffuse reflection due the broadening of the specular component in samples with some level of roughness. Moreover, below 200 nm the reflectance characteristics of most materials that are used as coatings in the integrating spheres, including the PTFE, are not well known.
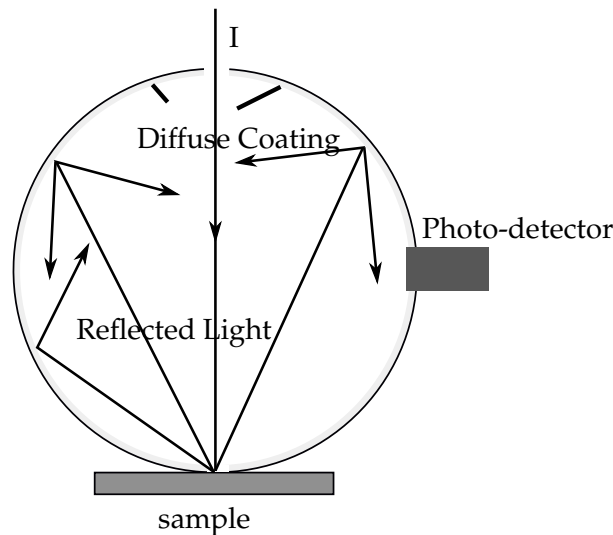
Figure 1.9: Schematics of a total integrating sphere [112, 113]. The light (I) enters through an opening and is scattered by the sample. The diffuse coating collects the light into the photo-detector shown in the figure.

Detector

H

V

Position A

Sample

ϕ

θ_i θ_r

n

Position B

Collimator
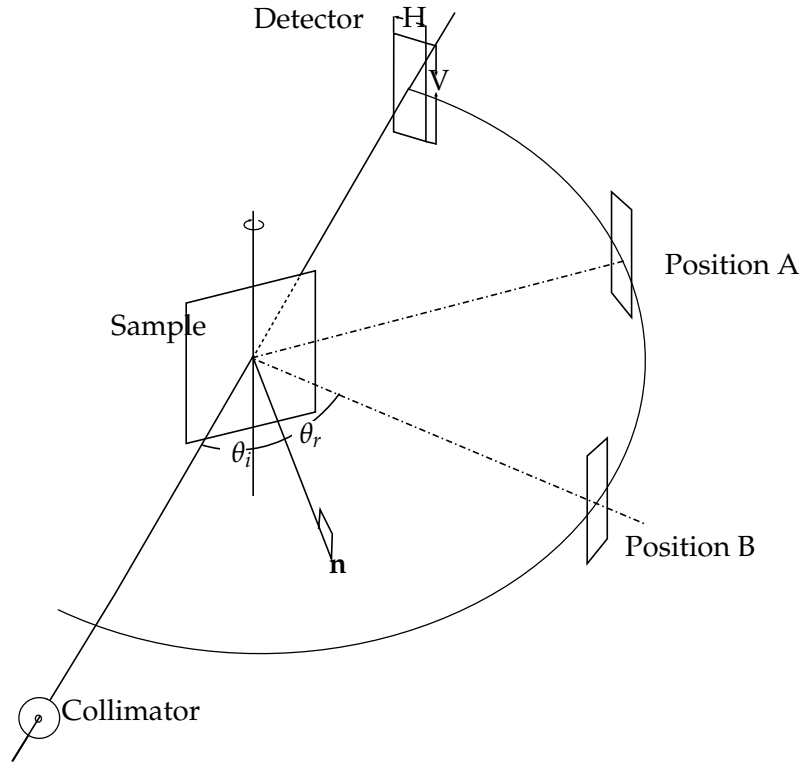
Figure 1.10: Schematics of an angle-resolution scattering system. The photo-detector is placed at different positions where the reflected flux is measured. The incident beam is measured either raising the sample or using a beam splitter.

Thus instead of a hemispherical method a bi-conical method (also called angle-resolution scattering method, ARS) will be used. Such a system is exemplified in the figure 1.10. In this method both the sample and the detector rotates changing the angles θ_i and θ_r. For each angle of incidence of reflectance the reflected intensity is measured. The incident flux is measured by either removing the sample or using a beam splitter [113]. The ratio between both quantities corresponds to the bi-conical reflectance.

Measurements over 200 nm

The reflectance of pressed PTFE powder was exhaustively studied by the Optical Technology Division of the National Institute of Standards and Technology (NIST) [3],[115] with the aim to use this material as a diffuse reflectance standard. The hemispherical reflectance of pressed PTFE powder was measured for wavelengths between 200-2500 nm. These measurements were performed in several laboratories in two different rounds. In the first round-robin it was observed that the PTFE is affected by the
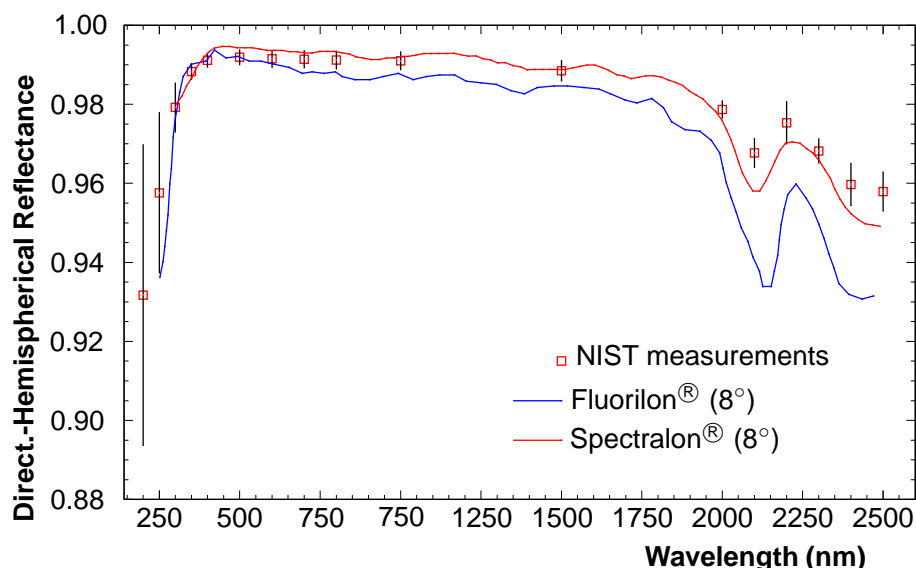
Figure 1.11: Pressed PTFE power directional hemispherical-reflectance (6°) as a function of the wavelength for the NIST measurements [115]. The directional hemispherical reflectance (8°) of two reflectance standards Spectralon®[116] and Fluorilon® [117] is also shown in full lines.

density of the pressed powder. The maximum of reflectance was obtained for densities between 0.8 and 1.2 g/cm^3 [3].

In the second round-robin the density of the samples was restricted to 0.80-1.08 g/cm^3. The directional-hemispherical reflectance (θ_i=6°) obtained as a function of the wavelength is shown in figure 1.11. Each point is the average of the reflectance of 16 samples measured in nine different laboratories. The results show the high reflectance of the PTFE (about 99%) for light of wavelength between 350 nm and 1500 nm. The reflectance decreases in the ultraviolet, not withstanding the fact that the uncertainties increase. At 200 nm reflectance of the PTFE is about (93 ± 4)%, suggesting even smaller values in the VUV region. The results also show a decreasing in the reflectance at wavelengths larger than 1500 nm, however this effect is smaller than the decreasing observed in the ultraviolet region.

Addicionaly, in the figure 1.11 it is also shown the reflectances for two reflectance standards Spectralon® and Fluorilon® as function of the wavelength.

The Labsphere's Spectralon® is a special pressed PTFE designed to have a high reflectance, it has the highest hemispherical reflectance of all materials known in the visible light. The value of the hemispherical reflectance is above 99% from 400-1500 nm although it decreases however significantly in the UV. Another special PTFE grade known for its high reflectance is the Fluorilon®. The blue curve in the figure 1.11 rep-

resents the hemispherical reflectance of the Fluorilon® [117], it has a good reflectance (about 99%), however smaller than the results obtained by the NIST. Both Spectralon® and Fluorilon® are used as standards in reflection measurements.

Measurements in the VUV region

The Alvensleben Laser Zentrum Hannover has measured the reflectance of the PTFE between 120 and 220 nm using a total integrating sphere [4]. The results obtained are shown in the figure 1.12 for the Spectralon PTFE and for a type of PTFE not specified. As shown the reflectance decreases slowly between 220 and 175 nm for both samples of PTFE, then it decreases sharply due the absorption edge of the PTFE.

The hemispherical reflectance at the wavelength of the scintillation of xenon is about 73% for the Spectralon, and 56% for the PTFE. These values are even smaller comparatively to the visible light.

These authors also measured the bi-conical measurements for an angle of incidence of 5° and they observed that both the PTFE samples show a lambertian behaviour only above the absorption edge.

The absorption spectra of the PTFE is shown in figure 1.13. The PTFE has a strong absorption at 161 nm, at lower wavelengths it is observed a rising structure with fine structure at 133 nm, 124 nm and 115 nm [118]. A weak absorption tail is observed between 175 nm and 240 nm which explains the decreasing of the reflectance of the
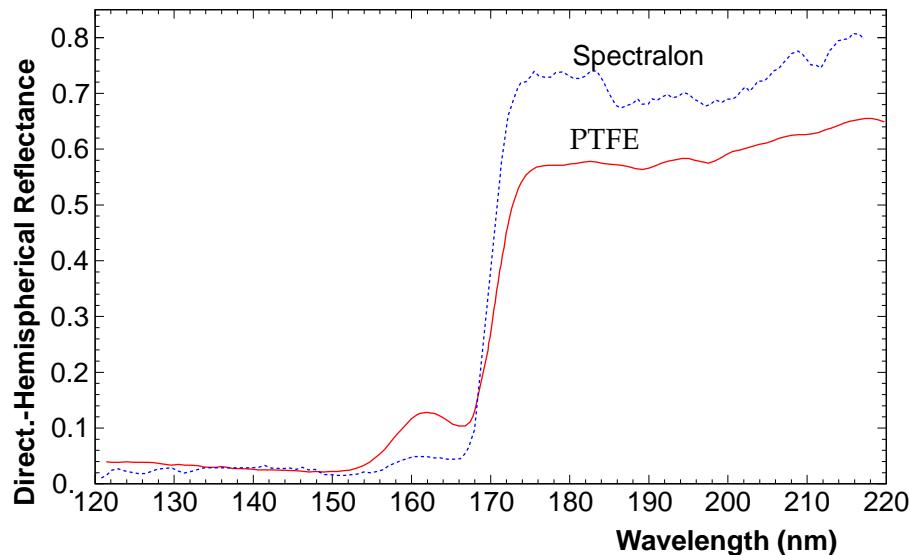
Figure 1.12: Hemispherical reflectance of the PTFE and of the Spectralon® in the VUV region of the spectrum (results obtained by [4]).

1.4 The Reflectance of the PTFE - Summary of the Published Measurements
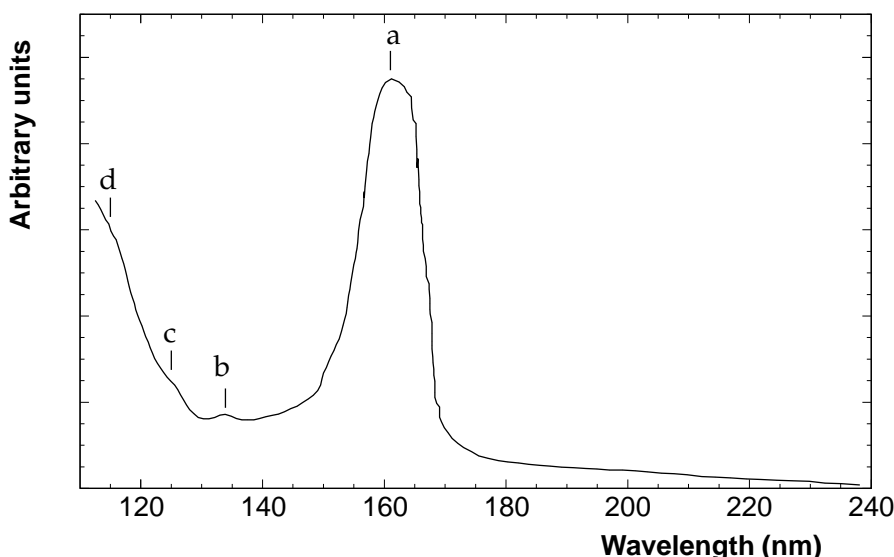
Figure 1.13: VUV Absorption spectra for the PTFE measured using a H_2 discharge lamp. The values obtained are only relative. The resolution of the system is 0.96 nm. The spectra has a absorption peak at 161 nm and fine structures at lower wavelengths (b-d). The data taken by [118].

PTFE mentioned above.

The reflectance distribution of the PTFE was reported by S. Bricola *et al* [119] for an angle of incidence of 45° at 172 nm. They observed both a specular and a diffuse component with the root mean square of the specular lobe being about 14°. Nevertheless the intensities of both components were not reported.

The study of the fluorescence

It is well reported that the PTFE can show some fluorescence when it is illuminated by ultra-violet radiation [120]. When the material is heated at moderate temperatures (90°C) and kept in vacuum conditions the fluorescence decreases [121], thus the fluorescence is not caused by the material itself but from contaminants. These contaminants can be added during the manufacturing or by exposing the material to contaminants after-wards. As spectroscopic analysis of the PTFE fluorescence showed to be compatible with polycyclic aromatic hydrocarbonets, these substances can be absorbed by the PTFE and like the PTFE fluorescence they show an absorption band between 200 nm and 300 nm and an emission band between 250-400 nm. The fluorescence of the PTFE has a large effect in a integrating sphere where the light can be reflected several times within the sphere. Thus the integrating spheres with PTFE are not usually used below

300 nm.

In scintillation detectors these substances have also another undesirable effect, they can contaminate the gas or liquid affecting its efficiency. Thus to clean the PTFE the material should be heated at about 90°C and kept in vacuum (10^{-6} mbar) during about two days [122]. We do not have any information about how the material behaves at higher temperatures. If the detector cannot be heated at these temperatures, this procedure should be done first before the assembly of the detector, then it should be kept in a air tight vessel such a glass vessel. Plastic containers are not recommended as they can contaminate the PTFE.

VUV degradation

It is also known that the reflectance of the PTFE decreases significantly when it is exposed under intense ultra-violet radiation. This is more significant at lower wavelengths. At 200 nm it was observed a decreasing of about 15% when the PTFE was exposed under intense VUV radiation during about 90 h [123]. This is caused by the carbonification of the surface layers of the PTFE films. The carbonification occurs due the removal of the chemical bond between the carbon and fluorine atoms, thus increasing the groups CCF and CCF_2 [124]. A special care should be taken when mercury or a xenon discharge lamp are used in a detector with PTFE. It was also observed that the reflectance of the PTFE decreases even under low-level radiation when the material has been stored during long time [125], this effect mainly occurs in the short wavelength range.

The Goniometer for the Reflection Measurements

Many materials exhibit both specular reflectance concentrated along the specular direction and a diffuse component arising from the internal scattering in the material. This component is usually weakly dependent of the viewing directions. We should be able to measure these two components with a single apparatus, however they have different experimental requirements, a larger field of view detector for the diffuse component and a small field of view detector for the specular component. A goniometer to measure the reflectance is in principle a good compromise to detect efficiently both components enabling to measure the BRIDF over different incident and viewing directions. A detailed description of the goniometer constructed to the reflection measurements is described in this chapter.

The scintillation light used in the reflection measurements is produced in a proportional counter filled with gaseous xenon that was placed inside a vacuum chamber. The emitted light is collimated in its way to the sample, where it is reflected/refracted and eventually detected by a photomultiplier (see figure 2.3). The observed background is effectively reduced using the charge signal collected in the proportional counter as the trigger signal. The photon intensity is measured in a photon counting mode. Both the sample and the photomultiplier can be positioned independently, thus changing the angle of incidence and reflectance, respectively. Both the data acquisition and the positioning of the PMT and the sample are automated by means of a computer program.

The xenon scintillation light is highly attenuated by an oxygen atmosphere, thus a vacuum chamber large enough to include both the goniometer and the light source was constructed providing a controlled environment to the experiment.

The description of the set-up described in this chapter was published in NIM-A [126].

2.1 The Chamber

The scintillation from the xenon (second continuum) is placed in the vacuum ultra violet region. This region is placed below 205 nm where the light starts to be absorbed by the oxygen. Between 175 nm and 205 nm the absorption is dominated by the Schumman-Runge band system. These bands correspond to the transition between two triplet states of the oxygen molecule O_2, $X^3\Sigma_u^2 \rightarrow B^3\Sigma_g^-$ [127]. At these wavelengths the absorption cross section is highly dependent of the wavelength as observed in the figure 2.1. The Schumann-Runge continuum starts at 175 nm and extends up to 125 nm. In this region the light is highly attenuated by the oxygen. For the xenon scintillation wavelength the absorption coefficient in the atmosphere is highly variable and can change between 0.1 cm^{-1} and 100 cm^{-1}. Thus the experiment needs to be placed in a controlled environment without oxygen.

Hence, to study the reflection of this light we designed and built an air tight chamber which provides the controlled environment needed for the measurements. The top
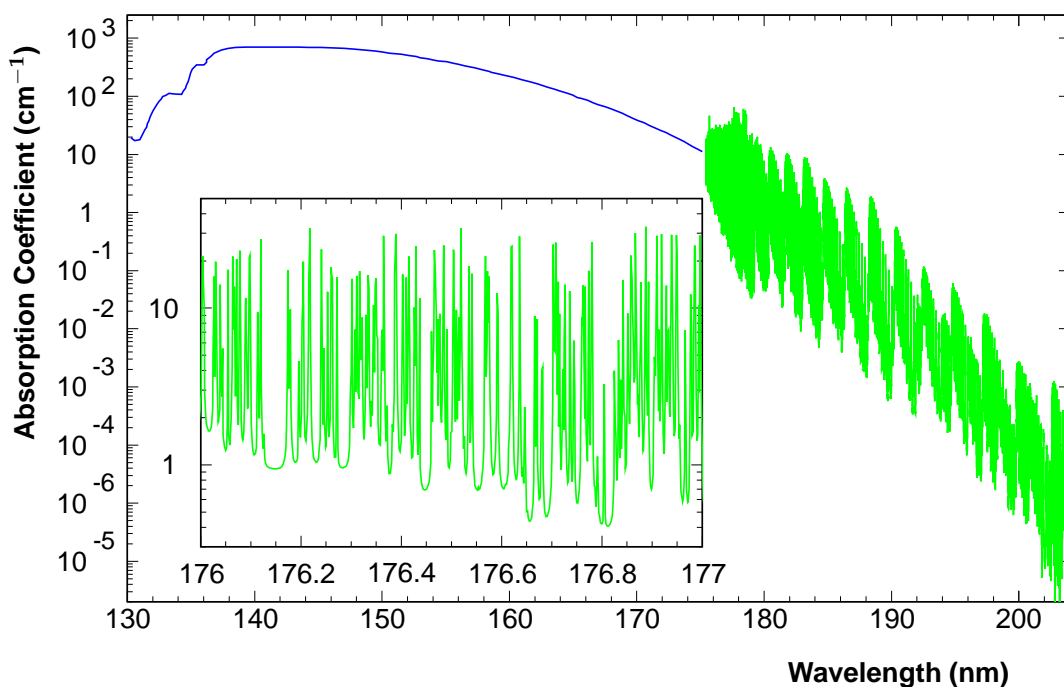
Figure 2.1: Dependence of the absorption coefficient in air with the wavelength for the temperature of 300 K and pressure of 1 bar. The Schumann-Runge bands were calculated using a polynomial fit obtained by K. Minschwaner *et al* 1992 [128], the values for the Schumann-Runge continuum were obtained by K. Yoshino *et al* 2005 [129].
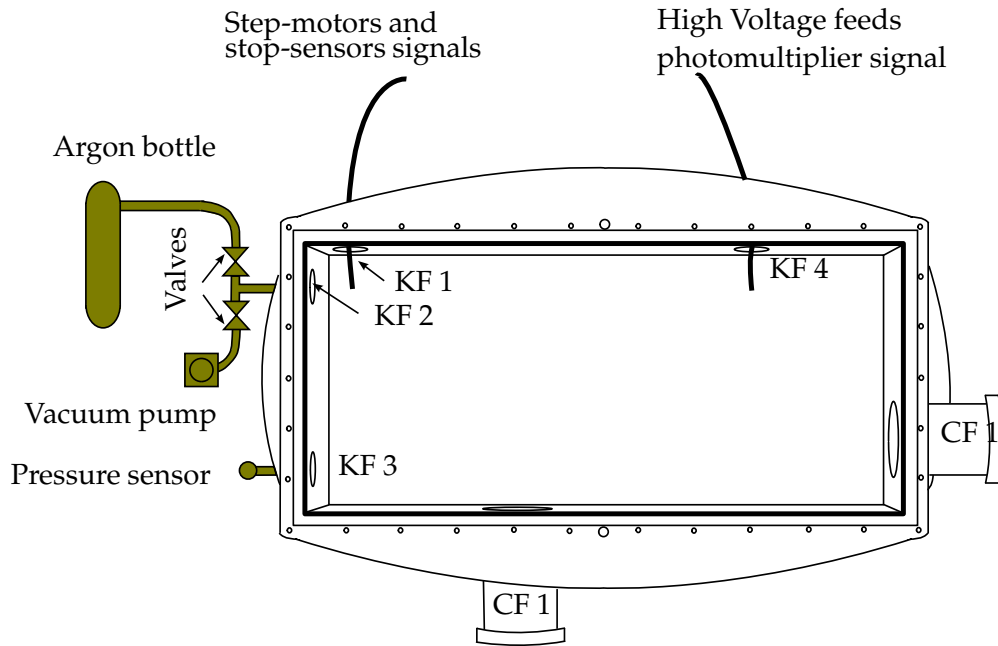
(a) Plane view of the vacuum chamber. The gas system is also shown.
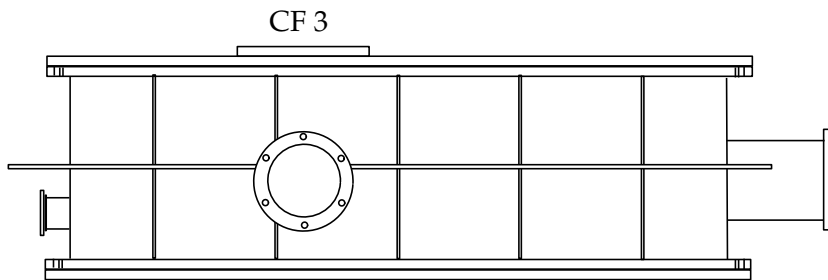
(b) Front elevation view of the vacuum chamber

Figure 2.2: The layout of the chamber used in the measurements viewed from the top a) and bottom b). CF and KF stands for ConFlat and *Klein Flange* respectively.

2. THE GONIOMETER FOR THE REFLECTION MEASUREMENTS
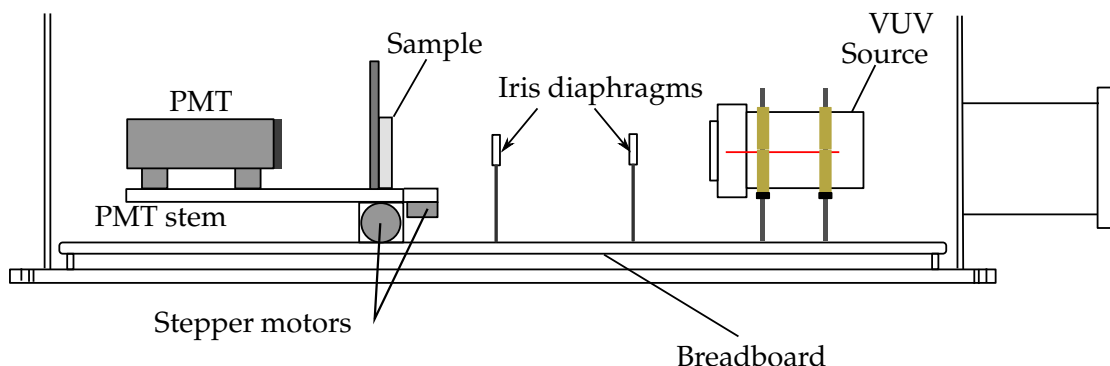
Figure 2.3: Cross sectional view of the chamber showing the breadboard and the optical system (goniometer) fitting inside.

and front views of this chamber are shown in the figure 2.2. The chamber has inner dimensions $820 \times 370 \times 226$ mm^3 (length$\times$width$\times$height) so that the optical system (goniometer) can fit inside.

The chamber walls are made of 5 mm thick stainless steel reinforced with a lateral structure to increase its mechanical resistance. The top and bottom are made of aluminum 14.5 mm thick for easier handling. The joints of the cover and bottom of the chamber and of the flanges are sealed with a O-rings.

The chamber is equipped with 4 KF flanges (all with an inner diameter of 35 mm) and 3 CF flanges (figure 2.2(a)). The KF-2 is used to connect to the gas system, i.e. to extract gas from the chamber with a vacuum pump and to introduce argon in the chamber's volume. An electrical feed-through with 4 pins was passed through the flange KF-4. It carries i) the high voltage to the proportional counter; ii) the high voltage to the PMT and iii) the signal from the PMT. The signals to the step-motors and from the stop sensors pass through the flange KF-1. The flange KF-3 was to connect a pressure sensor (Convectorr E-type).

Two of the CF flanges placed in the lateral walls have 92 mm of inner diameter. The flange CF-1 is placed right in front of the sample and was equipped with a polyethylene fitting to monitor the status of the experiment, so that in a case of a problem inside the chamber it would be possible to identify the cause without having to open it. The flange CF-2 was included to permit the coupling of a monochromator. However this was not used along this work.

The flange CF-3 placed at the top of the chamber has 100 mm inner diameter and was placed right above the surface sample and whereabouts. It is used to have access to the chamber without removing the cover of the chamber.

An aluminum breadboard 5 mm thick with dimensions $810 \times 360 \, \mathrm{mm}^2$ was introduced at the chamber's bottom. This board was perforated with tapped holes and inserted in a squared grid with a pitch of 35 mm. All the optical elements are assembled
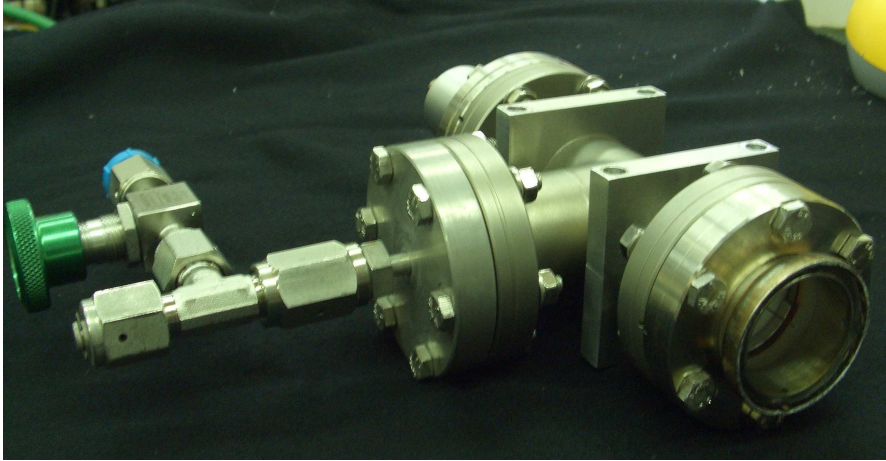
(a) VUV Light Source placed outside the vacuum chamber
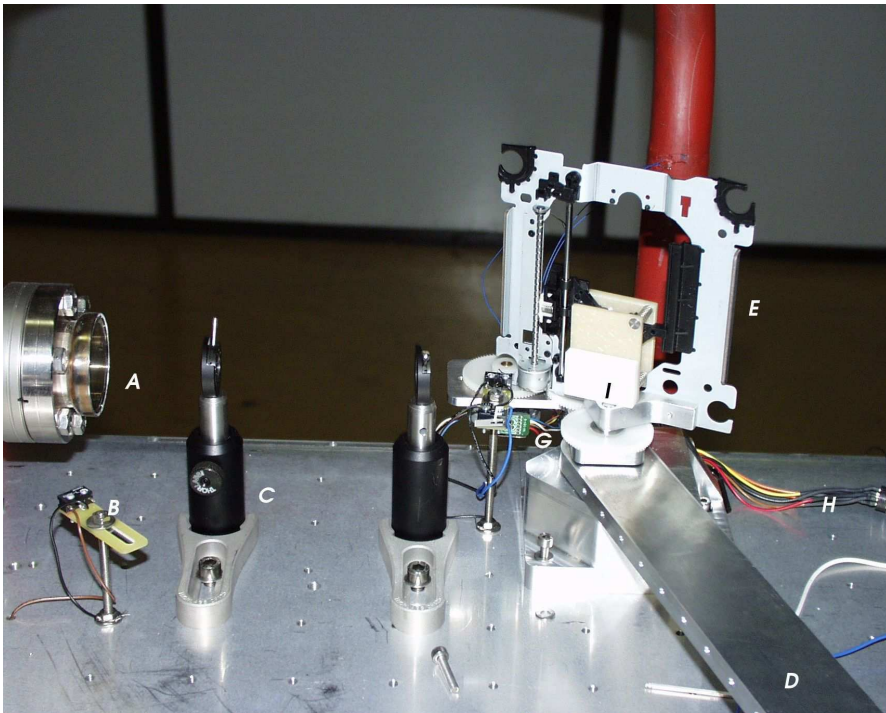
(b) Optical elements assembled to the breadboard without the black paper cover: A VUV light source, B stop sensor, C iris diaphragm, D PMT stem, E surface support, G stepper motor, I PTFE Sample

Figure 2.4: Pictures of the optical components placed inside the chamber. a) the proportional counter used to produce VUV light and b) some optical elements as indicated above.

2. THE GONIOMETER FOR THE REFLECTION MEASUREMENTS
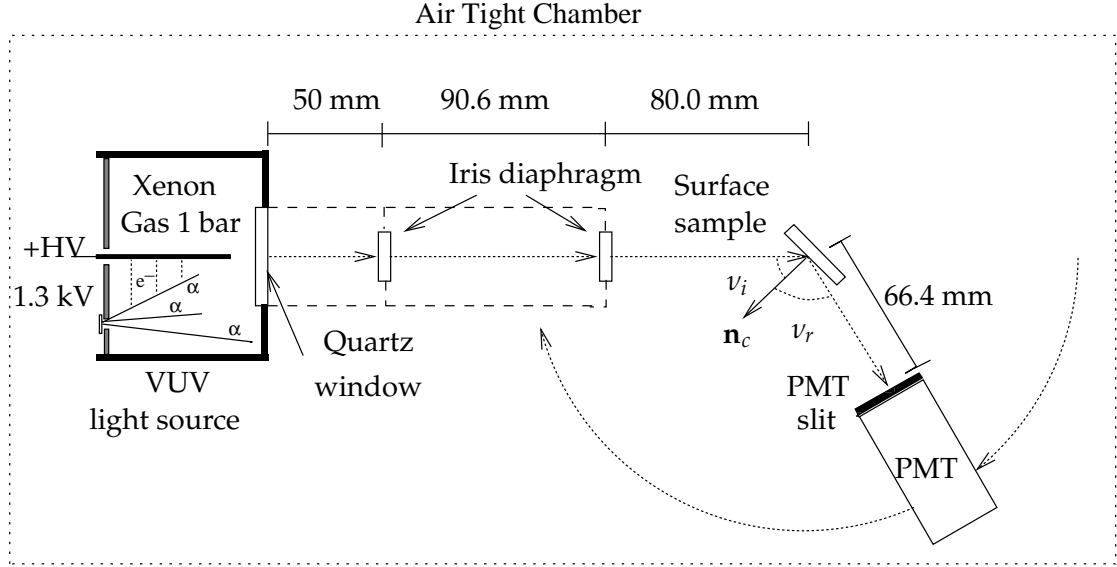
Figure 2.5: Top view of the optical system used in the experiment placed inside the vacuum chamber.

in this breadboard. The board is supported by four legs 1 cm above the floor, disposed symmetrically on the bottom vacuum chamber but not attached to it (see figure 2.3). Thus, the distortions of the chamber caused by vacuum or high pressures are not transmitted to the optical system assembled in the board. All the wires that are needed pass between the board and the bottom of the chamber and do not interfere with the measurement.

To reduce the random light background, the inner walls of the chamber and most of the pieces of equipment were covered with black flocked self-adhesive paper with low reflectivity (Thorlabs BFP1) . Due to its textured matte black surface this material was found to be a better light trap than applying a black paint directly to the surface. For incident angles near 90° relative to the normal the light is absorbed due the flocked nature of the material [130]. Being self-adhesive this paper can be easily removed if it is needed. The fibers of the paper do not shed, dust or lint thus it is possible to use a vacuum pump and maintain the chamber cleanness.

The optical system which was attached to the breadboard is depicted in figure 2.5. Figure 2.4(b) shows the optical system during the assembling, still without the black paper cover and the PMT. The details of the optical system will be given in the next sections.

2.2 The VUV Light Source

The VUV light of the xenon is produced in a small cylindrical proportional counter with an internal diameter of 40.0 mm and a titanium anode with diameter 0.5 mm, filled with gaseous xenon at 1.1 bar. The central anode is separated from the cathode wall by a 5 mm thick slab of PTFE. A picture of the proportional counter is shown in the figure 2.4(a) and the working principle is depicted in the figure 2.6.

An ^{241}Am source with an activity of 0.74 GBq (20μ Ci) is placed in the PTFE base, at a distance of 15 mm from the central anode. The source has a circular shape with a diameter of 2 mm. It emits 5.48 MeV α-particles with an half-life of 432.6 years [131] along the counter volume. The flux of α-particles is collimated by a 1 mm diameter hole across the PTFE reducing the rate of alpha particles that can be detected to about 1 kBq. These alphas are emitted almost parallel relatively to the anode of the VUV source and loose energy through excitation and ionization of the gas atoms yielding primary scintillation and electron-ion pairs. The range of the particles at 1 bar and 20 °C is
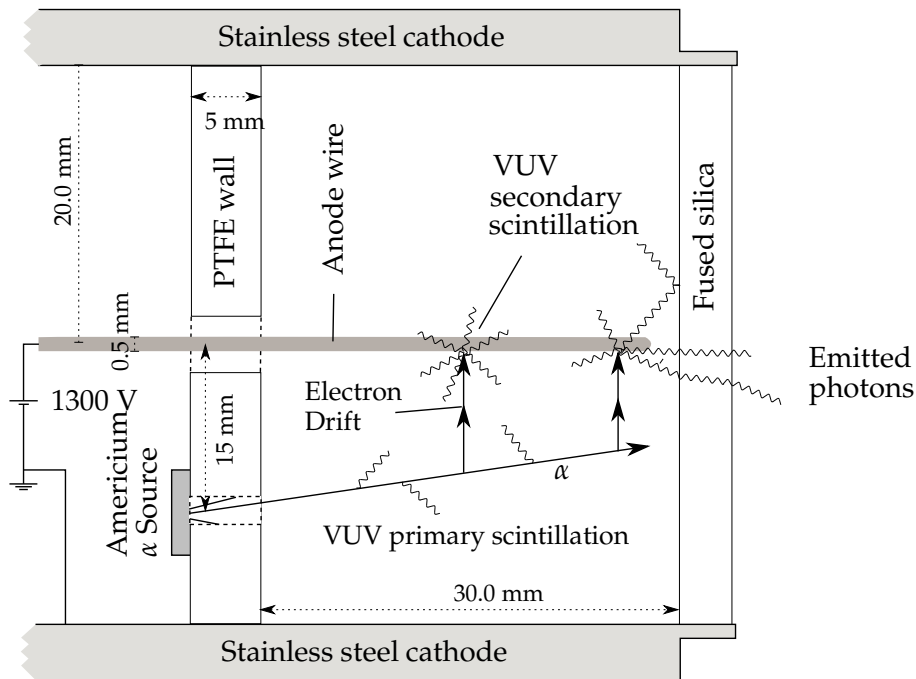
Figure 2.6: Light emission process inside the VUV Light Source. The α particles are emitted by an americium source and are collimated by a hole of 1 mm diameter perforated in the PTFE. The α particles lose energy by producing charge (electrons) and primary scintillation. The electrons produced along the alpha track drift under a cylindrical field towards the anode emitting secondary scintillation.

2. THE GONIOMETER FOR THE REFLECTION MEASUREMENTS

about 24 mm deposited mainly at the end of the particle's path ($dE/dx \propto E^{-1}$, [132]). The number of photons created in the primary scintillation is given by E_α/W_{ph} where $E_\alpha$ is the energy of the alpha particle and W_{ph} the average energy to produce a photon of scintillation. Given that $W_{ph} \simeq$35-50 eV for the gas at 1 bar and without electric field, the number of photons produced in the primary scintillation per each alpha particle is between 100,000 and 150,000 [35].

Under an applied voltage between the anode and the cathode, the electrons in the gas are extracted from the α-tracks and do not recombine. They drift along the field lines, accelerate and produce secondary scintillation by the anode wire. The electric field is axial and varies according to

$$E = \frac{V}{\ln\frac{r_c}{r_a}}\frac{1}{\rho}\,\text{V/cm/bar} \simeq \frac{V}{4.4\rho}\,\text{V/cm/bar} \tag{2.1}$$

where ρ is the axial coordinate, r_c =20.0 mm is the internal radius of the proportional counter and r_a =0.25 mm is the radius of the anode. The typical voltage applied between the anode and the cathode is about 1350 V.

The xenon gas has a low efficiency for the multiplication of the charge comparatively to the other rare gases. The charge multiplication is only observed for fields larger than 6 kV/(cm·bar) and only significant for fields larger than 14 kV/(cm·bar) [133, 134]. The electric field over the anode surface (at $\rho = 0.25$ mm) for an applied voltage of 1350 V is about 12 kV thus the charge multiplication can be neglected.

The charge collected by the anode was measured for different potentials applied to the VUV source. The histogram for the charge collected by the anode is shown in the figure 2.7 for three different voltages. At 1350 V the distribution is peaked at 50,000 electrons with a FWHM of 11,000 electrons. This value increases slightly for larger fields being about 52,000 for 2000 V. The observed increasing can be attributed to charge multiplication near the anode. The value obtained for the ionization yield is $W_i \simeq 110$ eV which is significantly higher comparatively to the expected value of 21 eV shown in table II of the chapter 1.

Although the electric field changes with ρ, the electron drift velocity remains fairly constant. For an applied voltage of 1350 the drift velocity is $\simeq$0.8 mm/μs for ρ=1.5 cm and $\simeq$1.3 mm/μs for ρ=0.1 cm, thus the electrons take about 20 μs to arrive to the anode. All the electrons drift almost the same distance due the fact that the alpha track is parallel with the anode, thus they arrive to the anode almost at the same time.

According to the several measurements ([135], [136]) of the secondary scintillation of xenon the scintillation is only produced for a reduced field larger than 800 V/(cm·bar) at 1 bar, which for an applied voltage of 1350 V corresponds to a region less than 4.0 mm from the anode wire. The number of photons created by single primary electron per unit path ($dn/d\rho$) is proportional to the electric field [137], following the semi-empirical formula

$$\frac{dn}{d\rho} = \frac{1}{P}\left(aE - b\right)\quad\text{photons} \tag{2.2}$$
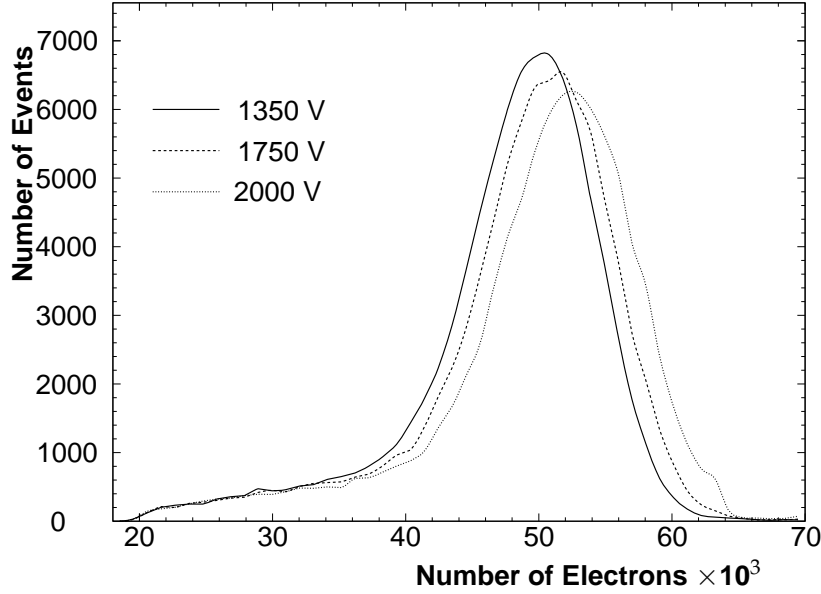
Figure 2.7: Number of electrons collected by the anode wire per alpha particle for three different voltages applied.

where E is the electric field in kV/cm and P the pressure of the gas in bar. a and b are the parameters of the linear regression, there exist some disagreement in these parameters attributed to different gas purity levels. The measured values for a range from 70 to 140 photons/kV and for b are between 56-116 photons/kV (a detailed review of these measurements can be found in [138]). The light gain g is given by the integral

$$g = \int_{r_a}^{r_t} \frac{\mathrm{d}n}{\mathrm{d}\rho}\mathrm{d}\rho \tag{2.3}$$

where r_t is the distance from the anode where the light starts to be emitted and is given by $r_t = V/\log\left(r_c/r_a\right)$. This integral is solved using the equation 2.1 resulting in a light gain between between 40 and 80 for a voltage of 1350 V.

The photons emitted by this proportional counter exit through a 5 mm thick fused silica window with an internal diameter of 40 mm. According to the manufacturer (Neyco®) the light starts to be attenuated at about 200 nm [139] and below 160 nm the light is highly attenuated by the view port. Thus, it is expected that part of the light produced in the proportional counter is absorbed at the exit window.

The photons created inside the light source are refracted into the fused silica window and then refracted into the chamber volume, reducing the light intensity in about 13%. Only the paraxial photons pass throw the two iris diaphragms placed in front of the window. Thus the light beam should remain unpolarized even after the two
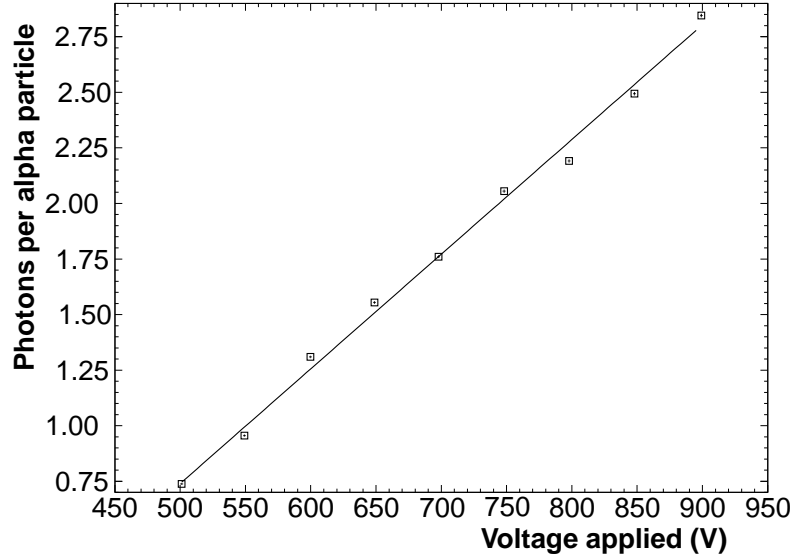
Figure 2.8: Number of photons per alpha particle emitted by the VUV source as function of the voltage applied. The light source is placed outside the chamber in front of the photomultiplier. Between the photomultiplier and the source we have introduced a collimator with a diameter of 1 mm.

refractions.

The anode signal is used to generate a gate in coincidence with the photons and only those collected during this period of time are considered for further analysis. The amount of charge signals in a certain time interval is proportional to the activity of the americium source. The number of these signals was about $N \simeq 1,000/s$.

Figure 2.8 shows the number of photons per alpha particle detected by a photomultiplier placed at about 5 mm from the window of the proportional counter. The emitted light is collimated with a pin-hole with 0.5 diameter. It was observed that the secondary light starts to be observed for an applied voltage of 350 V, and increases linearly with the increasing of the applied voltage.

2.3   The Beam Collimation

To assess the bidirectional reflectance (see appendix A) one needs to know the direction of the incoming light. As previously mentioned the light is produced isotropically all along the anode wire of the proportional counter. The collimation of this light is achieved through two iris diaphragms placed along the light beam between the source and the sample to be illuminated, at about 80 mm from the sample and at about 50 mm
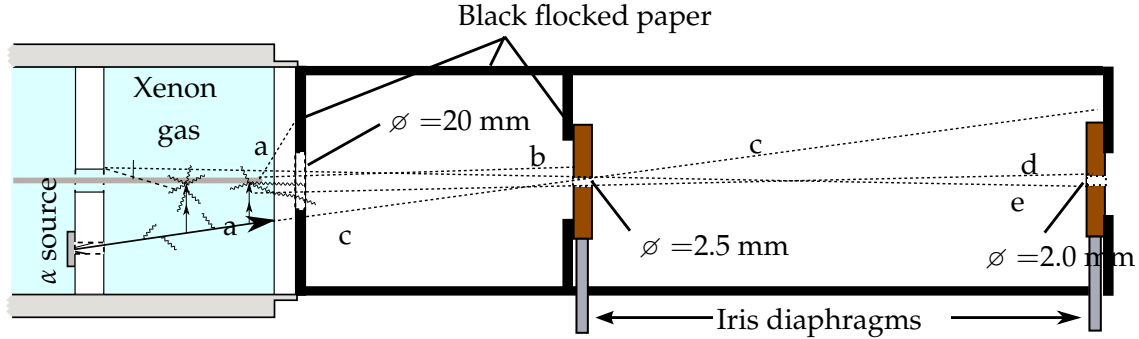
Figure 2.9: Collimation of the light emitted by the proportional counter. The two iris are placed between the sample and the VUV light source. The dashed lines represent some possible directions of the emitted photons from primary and secondary scintillation. a) the light is absorbed by the pin hole in front of the VUV light source b) the light has not the right direction to pass through the first pin hole c) the light emitted by the primary scintillation does not have the right direction to pass though the second iris d) the light is emitted to far from the anode and does not have the right direction to pass through the second iris e) the light reflected by the PTFE diffuser does not have the right direction to pass through the second iris. Only the photons emitted at a distance from the anode below 3.2 mm are able to pass through both iris.

from the proportional counter respectively (see figure 2.5).

Each iris has an external diameter of 1.20 in and aperture variable between a minimum of $\varnothing 0.8$ mm and a maximum of $\varnothing 12$ mm. The aperture of the iris near the proportional counter was about $\simeq 2.5$ mm. As for the aperture for the iris near the sample we used a smaller hole (between 0.8-2.0 mm).

The light can be reflected in any surface and be detected by the photomultiplier, not necessarily at the wanted sample. To prevent this to happen a tube covered with black flocked paper (inside and outside) was placed between the view port of the proportional counter and the second iris diaphragm (see figure 2.9), so that the light could only escape to the chamber through the second iris diaphragm. Additionally the exit window was covered with black paper with a 20 mm diameter hole at the window centre.

Figure 2.10 shows the intensity of the light beam as function of the applied voltage. The dependence is no longer linear as observed in the figure 2.8. When the applied voltage is increased the light starts to be emitted further away from the anode wire. For values larger than a certain distance from the anode (at about 3.2 mm assuming an aperture of the iris diaphragms shown in the figure 2.9) the light is no longer able to pass through both pin holes. The dashed line corresponds to the estimated efficiency of detection as function of the applied voltage. This efficiency is defined as the ratio between

2. THE GONIOMETER FOR THE REFLECTION MEASUREMENTS
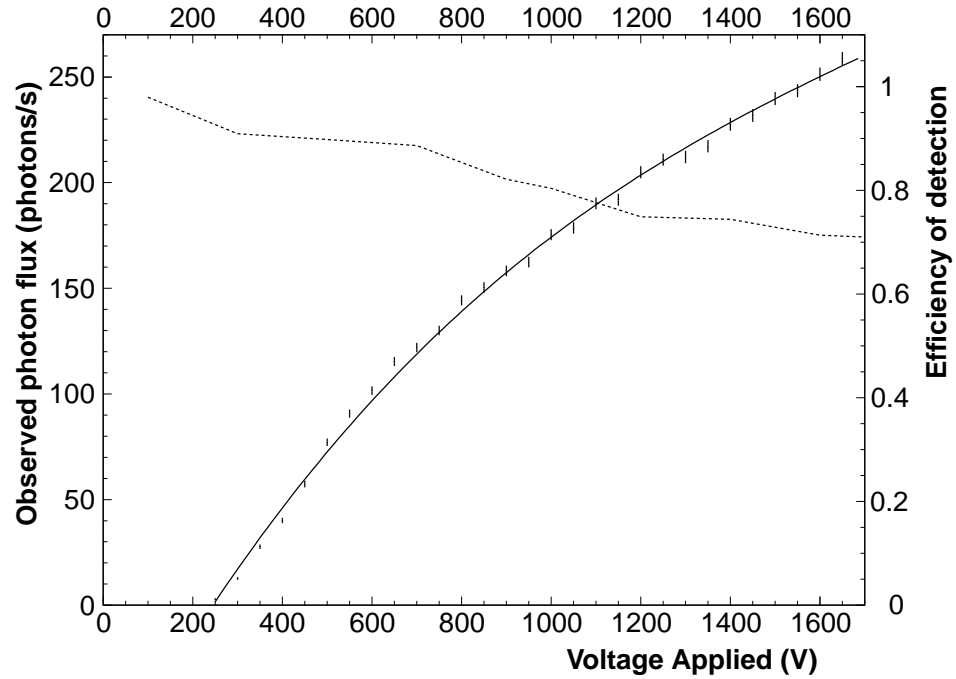
Figure 2.10: Incident flux as function of the voltage applied in the proportional counter. The PMT is placed inside the chamber in front of the incident beam. The apertures of the iris diaphragms are 2.5 mm diameter for the iris near the proportional counter and 2.0 mm diameter for the iris near the sample. The dashed line represents the efficiency of the photon detection, for a specific applied voltage. The efficiency ($E = 1$) is obtained when all the photons are generated in the anode at a radius of $\rho = 0$. For higher fields the photons that are generated far from the needle and can not be detected. To compute this effect it is assumed the empirical law $dn/d\rho = 70E - 56$ (kV/(cm·bar)) to generate the photons. The distance from the anode in which the photons start to be emitted is also shown as function of the applied voltage.

number of photons emitted in the electron drift that pass though both pin holes and the number of photons passing though both pin holes assuming that all photons were emitted at $\rho = 0$. This ratio was computed assuming that the number of photons produced per unit path is proportional to the reduced field ($dn/d\rho = 70E - 56$ kV/(cm·bar)) and that the emission only occurs for reduced fields larger than 800 V/(cm·bar).

The light from the primary scintillation (represented as c in the figure 2.9) is produced at about 15 mm from the anode and does not have the right direction to pass through both pin holes, thus can not be detected.

2.4 The positioning of the Sample and of the Photomultiplier

The beam light impinges the sample with a certain angle of incidence, which hopefully can be changed automatically during the experimental procedure. To accomplish this objective the sample is mounted in a movable structure adapted from a CD player (figure 2.11). Attached to the structure there is a geared stepper motor with 8000 steps per revolution which corresponds to $0.045°$ per step. A drive-shaft transmits the movement to a tooth wheel system which is able to rotate the structure that supports the sample (figure 2.11). The position of the structure is bounded by two stop sensors, when the structure arrives to such position a motion sensor stops the movement. The positions of the stop sensors are such that it is possible to measure angles of incidence from $0°$ to $90°$.

The stepper motor from the CD player is used to lift and lower the sample. Thus the collimated light can pass through the structure or otherwise be reflected by the sample. This vertical movement is also controlled by motion sensors.

The sample is supported by three screws for fine tuning of the surface inclination. With these screws it is possible to change the angle of inclination of the sample, ψ, relative to the plane of movement. This structure has been carefully designed to avoid having any material behind the sample, as this might disturb the measurement of partial or totally transparent materials (e.g. quartz).

The VUV photons are detected by a photomultiplier (PMT) mounted on a moving stem that can be rotated horizontally around the axis of the sample (see fig. 2.11). The stem is 235 mm long and is attached to the breadboard with a ball bearing. The stem was machined in aluminum to reduce its weight though ensuring its strength. The
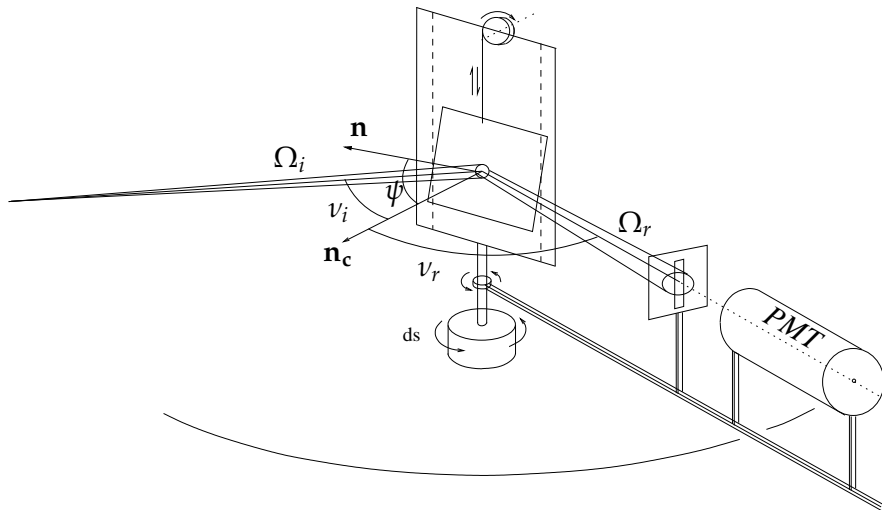
Figure 2.11: Schematics of the positioning of the sample and PMT.

movement is controlled by a geared stepper motor with 1480 steps per revolution and is limited by two stop sensors.

The photomultiplier used in this work is from the R1668 series from the Hammamatsu$^{®}$. It has a bi-alkaline photo-cathode with a diameter of 25 mm and a quartz window. The dark current has a special importance in this experiment as we need to detect a low number of photons. Thus several PMT's of the series R1668 were tested and the PMT with the lowest dark current (with reference ZH2512) was chosen. The manufacturer did not produce the quantum efficiency curve specific for this photomultiplier. Nevertheless similar PMT's of the same series have quantum efficiencies of about 23% at 175 nm. Since we are concerned measuring relative values of intensity, the quantum efficiency is not a critical parameter of this study. The photomultiplier is fed with a supply voltage of +1400 V between the anode and the photocathode, thus the photocathode is at 0 V.

In front of the PMT we placed a cylindrical collimator made of black Polyoxymethylene (POM), 17 mm long and 13 mm in diameter attached to a rectangular slit of 2×13 mm^2 that reduces the solid angle of observation.

2.5 The Electronic System

The electronic system can be divided in three main frames, the signal processing of the charge and light, the stepper motor system control and the data acquisition system.

The signal processing

The diagram of the electronics for the signal processing used in the experiments is represented in figure 2.12.

The PMT was operated in the photon counting mode, i.e. the PMT signals were digitalized through a discriminator and counted. The discriminator rejects the low intensity noise, increasing the signal-to-noise ratio. This mode of operation is more stable relatively to the analog mode because a small change in the photoelectron's amplitude does affect the signal observed. However, it is limited by the PMT resolution and subsequent electronics. The resolution of the PMT used has one photoelectron pulse duration of about 20 ns.

The signals from the PMT are fed into the fast filter amplifier Ortec 579 (integration constant τ_i=20 ns, differentiation constant τ_d=20 ns, amplification A=125). The signal is divided and discriminated by a low level discriminator (LLD) and an upper level discriminator (ULD). The LLD eliminates signal amplitudes below a certain threshold. The threshold is adjusted at the single photoelectron amplitude. Then the signal is digitalized yielding a rectangular pulse $\sim$ 20 ns long. The upper level discriminator (ULD) was introduced to remove the gliches from the power supply. These signals are very rare however they are too large and are interpreted by the system as several
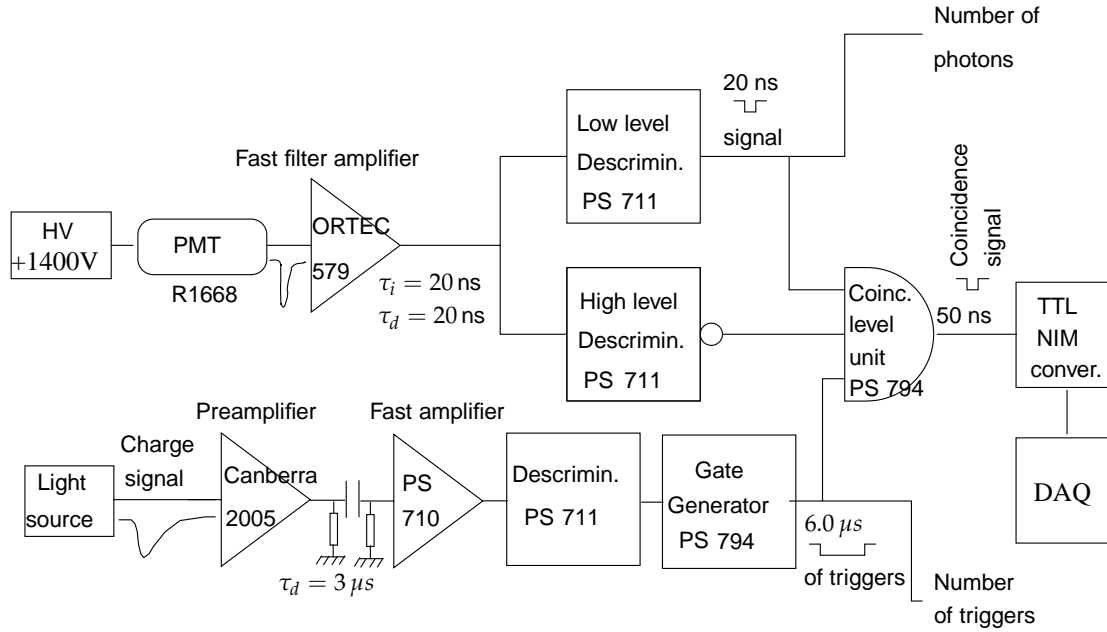
Figure 2.12: Diagram of the signal processing for the PMT and the charge used in the experiment. PS stands for Phillips Scientific.

photons. Therefore the ULD yields a negative rectangular pulse with $1\mu s$ long which is fed into the coincidence unit. The ULD pulse inhibit the formation of the coincidence signal.

The charge signal from the ionization of the xenon proportional counter is pre-amplified by a Canberra 2005 pre-amplifier with an integration 50 μs. It is then differentiated using a RC=3.3 μs and amplified by a fast amplifier Phillips Scientific 710. This signal once discriminated generates a gate 6.0 μs wide and with average rate of about 1000 Hz. The light and charge signals are fed into a coincidence unit generating a digital output 50 ns wide. This unit generates as many outputs as input pulses received within the gate length, as long as they are separated by more than 50 ns. This coincidence signal is fed into a DAQ system and recorded in the computer disk.

Figure 2.13 shows the typical signals observed for the light taken directly from the PMT and for charge after the preamplifier. In this case the PMT is placed at about 6 cm away from the window of the proportional counter, hence the number of photons detected is much higher than when measuring the reflectance. It is possible to observe that the secondary scintillation appears about 3.5 μs after the primary scintillation and is emitted during about 3 μs.

The photon counting mode does not work under a strong light intensity. The discrimination of the photons in the figure 2.13 would lead clearly to photon loss because there are photons being detected in the same time frame. The system is limited by

2. THE GONIOMETER FOR THE REFLECTION MEASUREMENTS
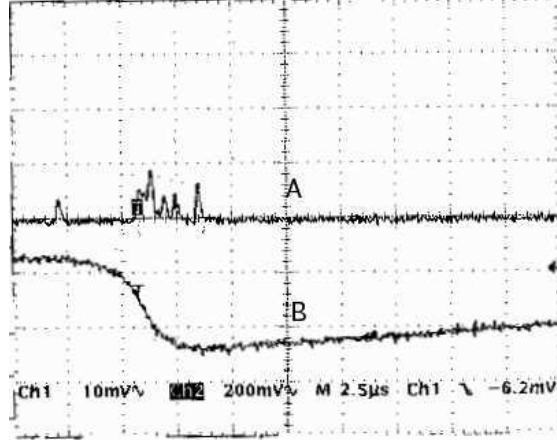
Figure 2.13: Signal from the photomultiplier before amplification and inverted (A) and the charge collected at the anode of the proportional counter (B) after pre-amplification. The PMT is placed outside the vacuum chamber at about 6 cm from the proportional counter.

the time of resolution of the signals that are detected. Let m be the measured count rate (photons/s) and τ the time of resolution, the real count rate n is approximated as follows [140, 141]

$$n = \frac{m}{1 - m\tau} \tag{2.4}$$

where m corresponds to the measured rate. However, in this work whenever measuring the reflectances the number of photons per coincidence signal is actually low enough (about 0.7 photons per coincidence). When the PMT is aligned with the incident beam the difference between the real count rate and the measured count rate is about 0.35% assuming a time of resolution of 50 ns which corresponds to the width of the signal sent to the DAQ system. For larger values of photon counting the equation 2.4 would have to be applied to obtain the real number of photons.

Because of the delays introduced by the discrimination of both the photomultiplier's signal and the charge signal some photons (secondary photons) appear before the charge signal and are rejected by the trigger system. This is caused by the delay of the trigger signal relatively to the photon signal. However, the delay is not larger than 100 ns and has no effect in the measurements as we are performing relative measurements and the same fraction of light is lost in measuring both the incident and the reflected beams. When the photons are counted (the PMT signal after the discriminator, see figure 2.12) instead of the coincidences it is observed that this number is about 50% larger than the number of coincidences observed. Nevertheless the trigger system should be used in the signal processing because it reduces significantly the observed background. In fact it was observed that the background for the number of photons is

100 times larger than the background for the number of coincidence signals.

The output of the coincidence unit is read by a computer program through a data acquisition card from National Instruments. As the data acquisition is only able to accept TTL (transistor-transistor logic) signals, the NIM (nuclear instrumentation module) signals needed to be converted first. It was observed that the number of photons was not altered in this conversion.

Position control system

To obtain the reflectance distributions it is necessary to change the incident and viewing direction, which means changing the positions of the photomultiplier and of the sample. The PMT stem, the sample position and the sample axis are moved by stepper motors. The stepper motors are very precise as they move in discrete steps rather than continuously. The position of each step is related with the internal windings of the motor and do not change with their use. Table I shows some characteristics for each stepper motors used.

Both the stepper motor of the PMT stem and of the surface structure make use of a geared system attached to the rotor to increase the precision. These two motors are both unipolar. The stepper motor which lifts and lowers the sample is a bipolar stepper motor. They differ in the fact that the unipolar stepper motor has a central tap in each two windings and the bipolar has no central tap. As a result the direction of the movement in unipolar motors can be easily changed without having to change the direction of the current, whereas the bipolar motors require the current to be reversed to change the direction of movement, however a bipolar motor has a larger torque comparativelly to a unipolar motor with the same weight.

Each stepper motor is controlled by a specific drive (UCN5804B from Allegro® for the bipolar stepper motor and MC3479 from Onsemi® for the unipolar stepper motor).

Table I: Characteristics of the different stepper motors used in the control of the sample and of the PMT

	Type	Steps per Revolution	Geared Ratio[†]	*Torque* N·cm
Sample rotation	Unipolar	8000	125:1	27.6
PMT position	Unipolar	1440	25:1	80
Sample position	Bipolar	12	-	-

[†] The geared ratio corresponds to the number of revolutions performed by the stepper motor after the geared system and the number of revolutions performed by the rotor.

2. THE GONIOMETER FOR THE REFLECTION MEASUREMENTS

A micro-controller PIC 16873N was programed to produce the signals needed to these drivers. Each drive receives the following signals a) the supply voltage for the winding of the stepper motor (about 5 V for the bipolar stepper motor and 12 V for the unipolar stepper motor) , b) a squared signal with the desired frequency for the stepper motor, c) the direction of movement (clockwise or counterclockwise), d) enabling the half-step option and e) enabling the output of the stepper-motor. The half-step option was turned off because the positioning with this option was observed to be not very precise. The windings of the stepper motor are connected at the exits of the of each driver.

The movements inside the chamber are stopped by mechanical switches positioned in predefined positions at the course end. The mechanical switch associated to the sample is activated when the sample is completely lowered, this ensures that the sample is correctly positioned for the measurement. The reproducibility of the movement of the PMT and structure was tested and tuned by performing several revolutions around their axis. Eventually the system can "lost" one step, although this occur very rarely and it is caused mainly by the mechanical switches.

The PIC receives the signal from five mechanical switches, two associated to the PMT stem, two associated to the rotation of the sample and one associated with the vertical positioning of the sample, when the switch is activated the PIC disables the output of the driver and the respective stepper motor stops.

The slow control and data acquisition systems

A Lab-Windows/CVI program from the national instruments controls both the movement of the PMT and the sample, the data acquisition system and all the measurement procedure which is previously programmed. The principle of working is depicted in the figure 2.14.
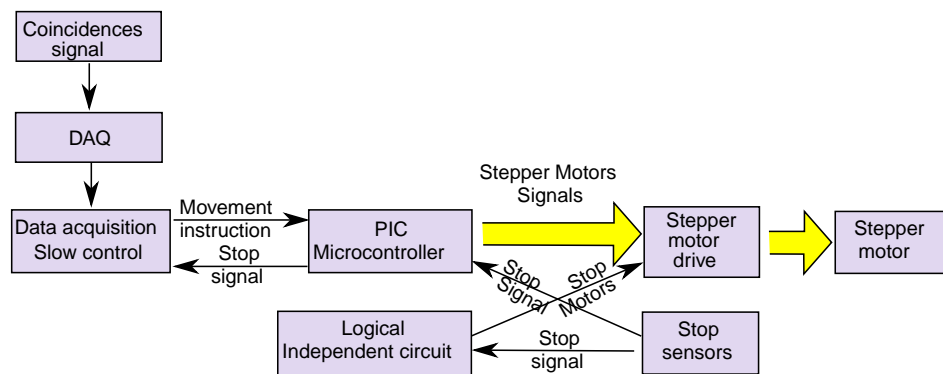
Figure 2.14: Schematics of the slow control implemented in the experiment. The coincidences signal is passed to a Lab-Windows computer program which controls both the data acquisition system and the stepper motors.
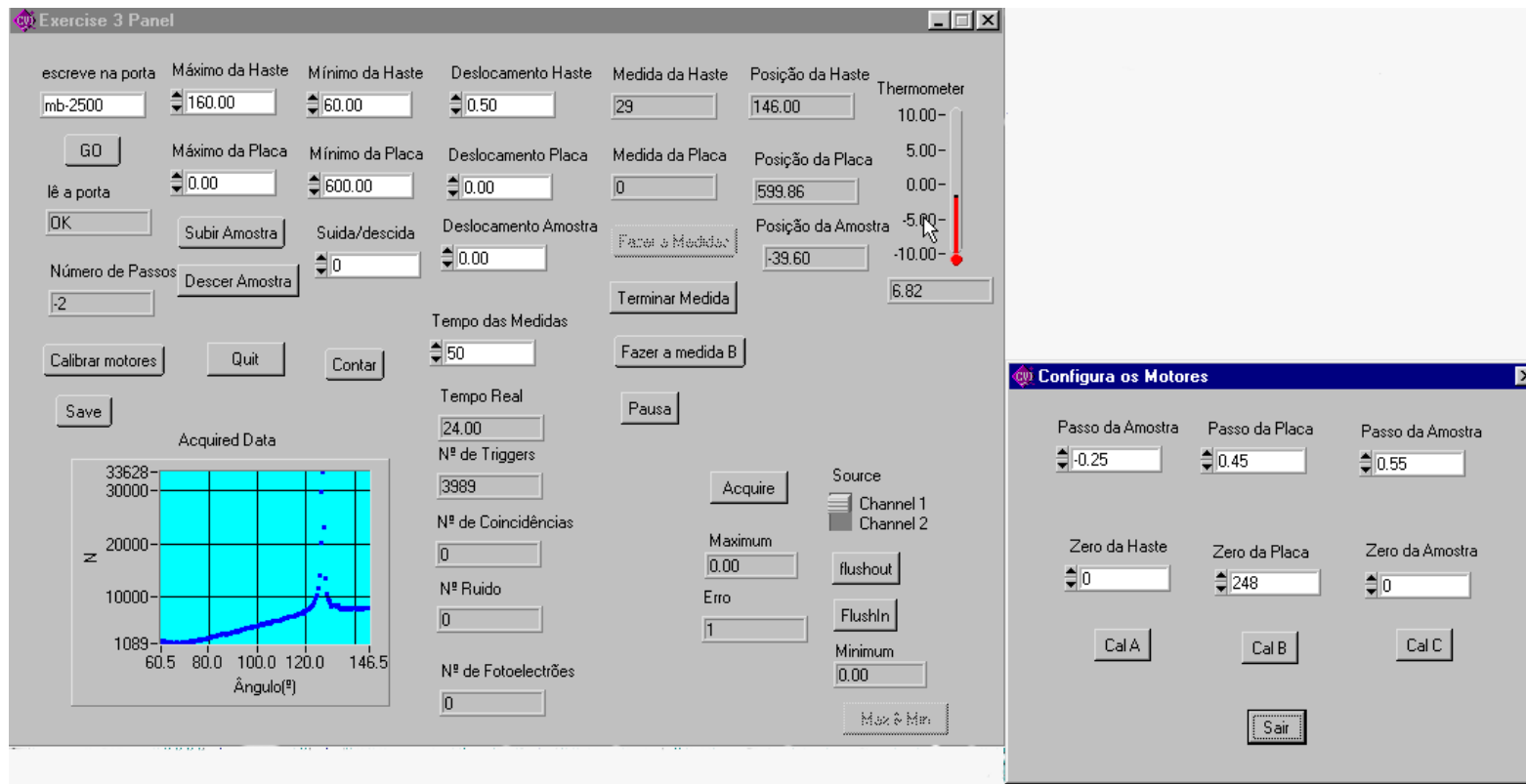
Figure 2.15: Display of the data acquisition control panels that was implemented for this work. The main panel and the motor configuration panel are shown. The plot of the collected data shown to monitor the status of the experiment. The quality of the run can be assessed namely by the live quality of the acquired data, as shown.

2. THE GONIOMETER FOR THE REFLECTION MEASUREMENTS

The program counts the number of pulse signals received by the DAQ board during a certain amount of time introduced by the user.

The program communicates with the micro-controller through a serial port RS-232 informing which stepper should be moved and for how many steps. Thus, the system is only able to move a stepper motor at a time. When a stop sensor is activated an information appears on the display. A logical circuit working independently of the PIC stops all the stepper motors when a stop sensor is activated in case of error, ensuring that the system works properly. Both the stepper motor of the PMT stem and of the surface structure make use of a geared system attached to the rotor to increase the precision.

The control panels of the Lab-Windows program which controls the measurement procedure are shown in the figure 2.15. When measuring the reflection distribution the user is required to introduce: i) the initial and ii) final position of the PMT, thus defining the PMT course, iii) the angle of displacement of the PMT between measurements, iv) the angle of incidence ν_i, v) the data taking period and vi) the sample position (lifted or lowered). The measurement starts by moving the PMT to the initial position and the sample to the correct position, the number of coincidences are counted during the time introduced by the used. Then the PMT advances the number of steps that corresponds to the angle of displacement introduced by the user. This is done repeatedly until the PMT arrives to the end course.

In the motor configuration panel the angles ν_i and ν_r are calibrated. The used introduces the angle between a calibrated position defined by the user (e.g. the position in which the PMT or samples are aligned with the light beam) and the respective stop sensor. Then the photomultiplier or the samples are moved to the position of reference. The angles used in the experimental procedure are measured relatively to this position.

The program is also able to calibrate the angles ν_i and ν_r. The user needs to introduce the off-set angles between the PMT or sample and the stop sensors.

2.6   The Alignment of the Optical System

The optical system, specifically the photo-detector (PMT), the VUV source, the iris diaphragms and the positioning of the sample need to be correctly aligned before the measurement. A 100 mW He-Ne laser was used to perform the alignment

The alignment is done in two steps. First, the centres of the PMT, the iris diaphragms, the anode wire of the proportional counter and the sample need to be placed in the plane of measurement (figures 2.16). The angles ν_i and ν_r are measured in this plane and it is the plane of reference to measure the surface's inclination ψ (see figure 2.16(a)). The laser was placed at the PMT position and the iris diaphragms were aligned in line with the anode of the proportional counter (figure 2.16(a)). The PMT was again put in place and the laser positioned at the exit of the proportional counter (see figure 2.16(b)).

(a) Alignment of the VUV source and of the iris diaphragms. The He-Ne laser is placed in the position of the PMT and the iris and VUV source are aligned.

(b) Alignment of the PMT and the iris diaphragms. The He-Ne laser is placed in the position of the VUV source

Figure 2.16: Alignment of the VUV source, iris diaphragms and PMT

The VUV source is fixed with a system of screws and can be removed without compromising the alignment.

The second step concerns the alignment of the sample (figures 2.17). To perform this operation the laser is placed in the position of the VUV source. The sample is placed parallel to the laser beam and the surface is aligned with the beam using the three screws placed behind the sample. A rotation around its own axis is performed to verify if the alignment is correct (figure 2.17(a)). If the sample is correctly aligned half of the laser beam should hit the border of the sample, the other half should pass directly to the PMT. This should occur in both the positions of the sample at $v_i = 0$ and $v_i = 180$.

To verify the inclination of the sample relative to the optical plan a small mirror was fixed in front of the sample (figure 2.17(b)). The sample was rotated and reflected in the walls of the chamber. The surface is correctly aligned if the spot in the walls of the chamber describes an horizontal line at the same height from the breadboard for all angles of incidence v_i. This procedure is repeated until all the components were completely aligned. Once the optical system and the sample are in place and aligned, the chamber is closed and the air is evacuated.

Below 180 nm the absorption coefficient in air is above 0.1 cm^{-1} and the light is absorbed. Therefore the measurement cannot be carried out in air. The air is removed using a low-vacuum pump up to a pressure of $\sim 10^{-3}$ mbar during about 10 hours. This vacuum is also limited by the sealing of the chamber and the outgassing of the
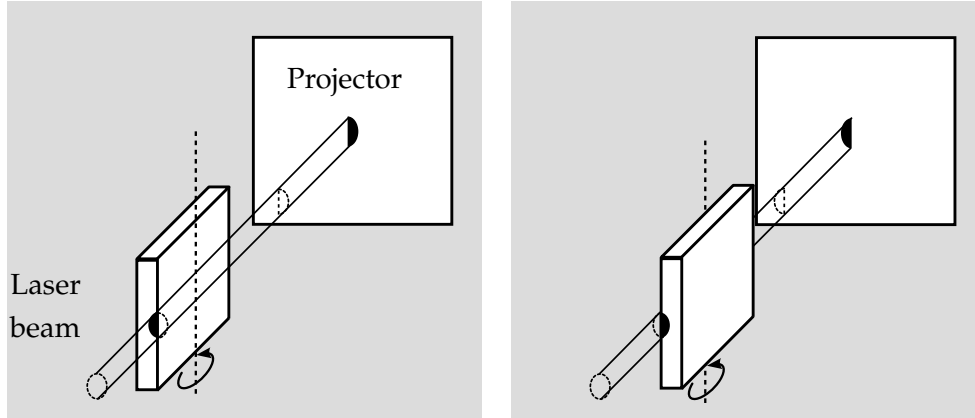
(a) Alignment of the sample with the incident beam. The sample is placed parallel with the laser beam and turned around itself. In both situations half of the laser beam should be blocked and the other half should be observed in the projector.
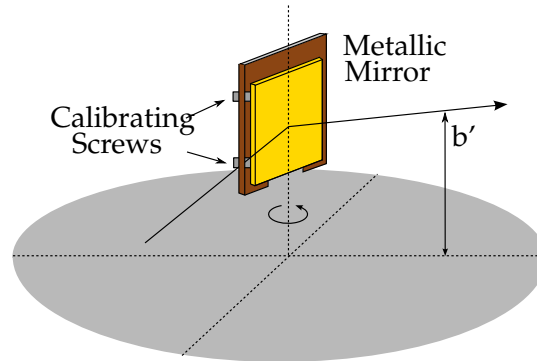
(b) Alignment of the sample with the optical plan. The light emitted by the laser is reflected by a mirror placed above the sample. The reflected light is projected in the walls of the sample and the height b' is measured.

Figure 2.17: Alignment of the sample with the optical system

interior materials. The air pumping is limited by the dust present in the chamber. The dust can scatter the incident VUV light (Mie scattering) increasing the stray light of the detector. Then the chamber is filled with argon until it reaches a pressure of 1.1 bar. The measurements can now be performed.

The Measurement of Radiometric Quantities

In this chapter it is described the procedure to measure the different radiometric quantities, solid angles, incident and reflected fluxes and intensities and the BRIDF for both metals and diffuse dielectrics using the goniometer described in the previous section. The calibration of the angles of incidence and reflectance is performed *in situ* without opening the chamber. Several tests to the experimental procedure are also described.

Figure 3.1 represent different experimental settings used to measure the radiometric quantities. The intensity of the incident beam is measured with the sample raised, letting the light go straight to the photomultiplier (PMT) (figure 3.1 a), in this position it is calibrated the PMT position which defines the angle of incidence. Then, the sample is lowered and the position of the sample and reflectance angle are calibrated putting the sample perfectly parallel to the incident beam (figure 3.1 b). The intensity observed is defined for each position of PMT as the ratio between the flux observed and the solid angle subtended by the slit placed in front of the PMT (figure 3.1 d). To this value it is subtracted the background measured with the sample raised (figure 3.1 e).

The reflectance is then given by the ratio between the observed intensity in the PMT and the incident flux. This quantity is an experimental quantity and does not correspond directly to bidirectional reflectance because both the directions of incidence and reflectance are not unidirectional.

The light emitted by the xenon proportional counter was studied by measuring the light spectra for wavelengths larger than 220 nm, measuring the emitted light with the chamber filled with air and introducing an interference filter.
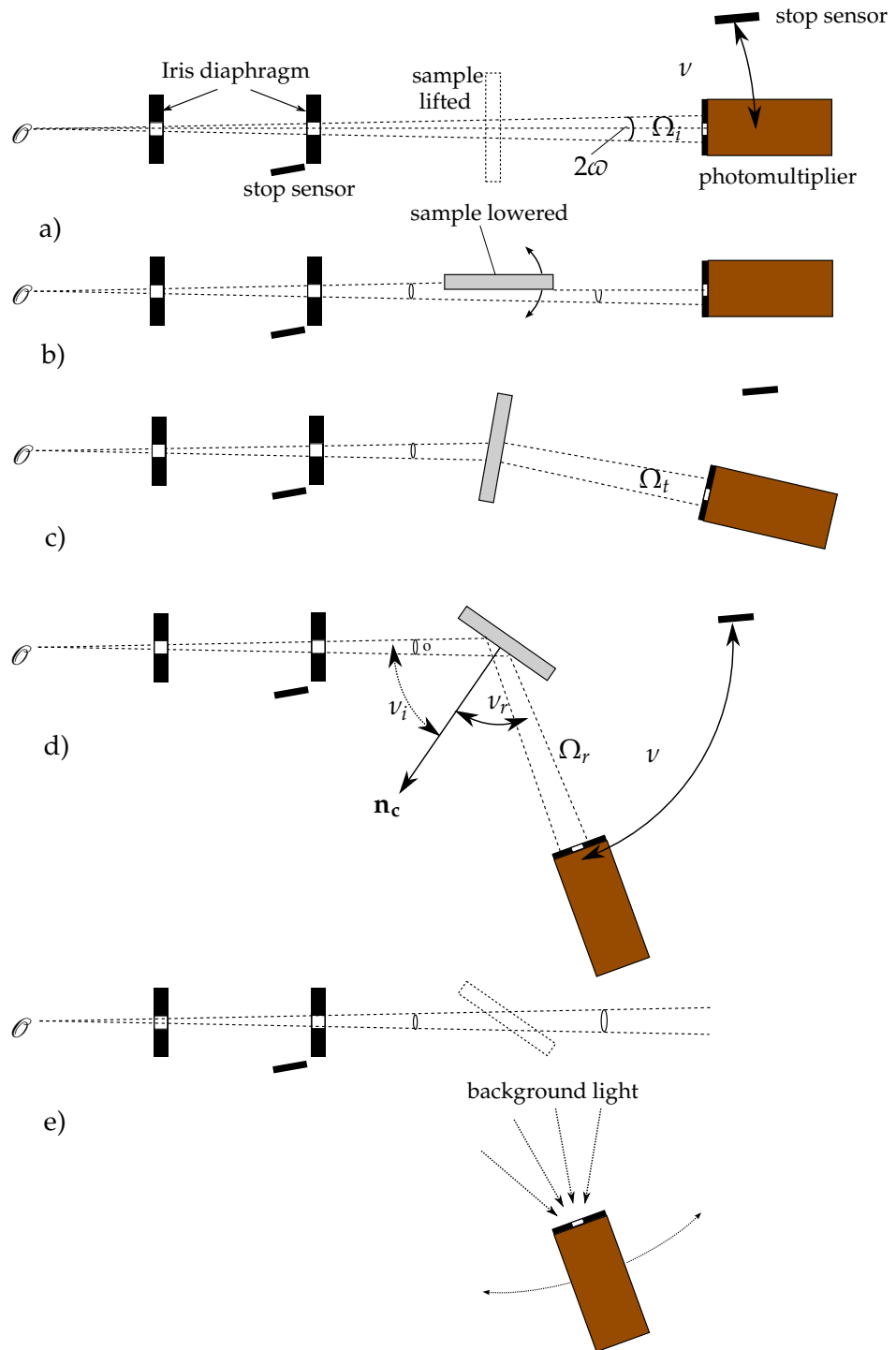
Figure 3.1: Different experimental settings used to measure the, a) Incident beam, b) angle of incidence, c) transmitted beam, d) reflected beam and e) the background.

3.1 The Incident Beam Flux

The incident beam is measured with the sample raised and the structure placed perpendicularly to the incident beam (figure 3.1 a)). In this situation the light is transmitted through the structure without any interference. The PMT is then moved around to sample the entire beam spot. From these measurements we extracted: a) the incident flux on the sample, b) the direction of maximum intensity (thus calibrating the position of the PMT arm) and c) the opening aperture of the incident beam. In fact, the slit placed in front of the PMT window is narrow enough for the beam spot have to be sampled at various angles. The incident flux is given by the integral of these measurements. The PMT is, therefore, moved in successive steps from its initial position, near the end course, up to the point where the incident beam has been completely sampled. Each position is defined by the angle ν defined between the PMT position and the position of reference given by the motion sensor (see fig. 3.1 a)). The data taking time at each position is between 25 s and 50 s, the longer times are used at positions where the slice of incident beam has already low intensity. The integration can be performed only in ν as the vertical dimension of the slit is sufficient to encompass the entire beam spot.

In the computation of the incident beam it is assumed that the light beam spot viewed by the PMT is homogeneous. This corresponds to consider that the light is produced in a fixed point in front of the proportional counter and that it is distributed uniformly within the incident solid angle. Actually the light is not produced in a specific position in the proportional counter but created along the anode of the proportional counter (about 20 mm long), however this distance is much smaller than the distance between the proportional counter and the PMT (about 287 mm). The light starts to be emitted at a certain distance from the anode, however due the fact that the number of electrons produced is proportional to the electric field the majority of the photons will be emitted near the anode.

The light is emitted inside a conical solid angle with an apex angle ϵ measured relative to the position $\mathscr{O}$ of the light source. However the axis of rotation of the photomultiplier is placed in the position of the sample, therefore the incident flux will be observed within a larger solide angle, defined as ϖ in the figure 3.2. This angle is very small ($\varpi < 0.025$ rad), therefore the observed beam spot Ω_i^S is still homogeneous and can be approximated to a circle with a radius ϖ

$$\Omega_i^S = 2\pi \left(1 - \cos \varpi\right) \simeq \pi \varpi^2 \tag{3.1}$$

The angle, ϵ, is related with the angle ϖ that is observed by the relation (see figure 3.2):

$$\epsilon = \arctan \left(0.231 \tan \varpi\right) \tag{3.2}$$

The incident flux is given by the integral of the intensity observed over the solid angle Ω_i^S. The intensity (I) observed by the PMT at each position ν is given by the integral over the sampled strip of the beam spot (fig. 3.3). The integral limits are defined

3. THE MEASUREMENT OF RADIOMETRIC QUANTITIES
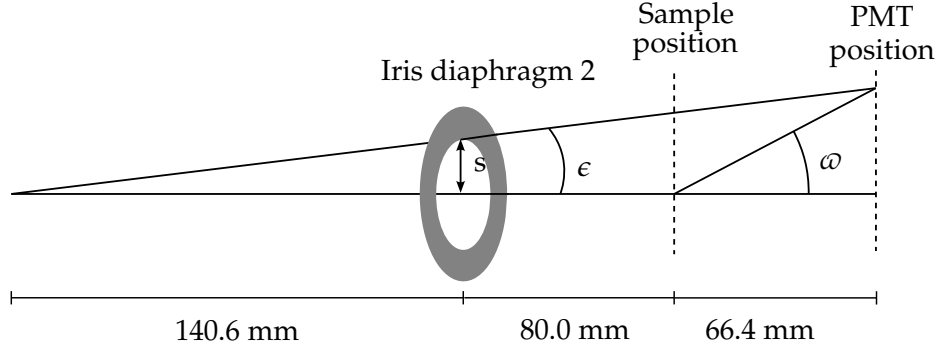
Figure 3.2: Relation between the observed aperture angle ϖ, the half apex angle of the incident beam ϵ and the aperture of the second iris diaphragms (the aperture of the iris diaphragm is exaggerated for clarity).

by the slit width H placed in front of the PMT. Thus, thus the intensity at certain position, ν, is given by

$$I = \frac{\Phi_i}{\pi\varpi^2} \int_{\nu-\eta}^{\nu+\eta} 2\sqrt{\varpi^2 - \nu'^2} d\nu' \tag{3.3}$$

Φ_i is the incident flux that strikes the surface and $\eta = \arctan\{(H/2)/p_o\}$ where H is the horizontal dimension of the slit in front of the photomultiplier and p_o the distance between the photomultiplier and the sample. The normalization factor, $\pi\varpi^2$, corresponds to the area of the beam spot. The angle ν is related with the angle ν_0, defined between the PMT position and the position of the stop sensor, through

$$\nu = \nu_0 - \nu_{\max} \tag{3.4}$$

where $\nu_{\max}$ is the angle between the position of the maximum intensity of the incident beam and the position of the stop sensor.

The integral 3.3 yields

$$I(\Phi_i, \varpi, \nu) = \Phi_i \left[\nu\sqrt{\varpi^2 + \nu^2} + \varpi^2 \arctan\left(\frac{\nu_{\max}}{\sqrt{\varpi^2 - (\nu + \Delta)^2}}\right) \right]_{\nu-\eta}^{\nu+\eta} \tag{3.5}$$

which is a function of three parameters (Φ_i, ϖ and $\nu_{\max}$). From it we can extract i) the beam aperture, ϖ, ii) the angle of maximum intensity, $\nu_{\max}$, and the incident flux Φ_i. The values obtained from the fit to different flux intensities are shown in the table I.

The solid angle defined by the incident beam Ω_i with apex angle of 2ϵ is given by

$$\Omega_i = 2\pi(1 - \cos\epsilon) \qquad [\text{sr}] \tag{3.6}$$

the aperture of the second iris diaphragm was set to

$$s = 140.6 \tan\epsilon \qquad [\text{mm}] \tag{3.7}$$
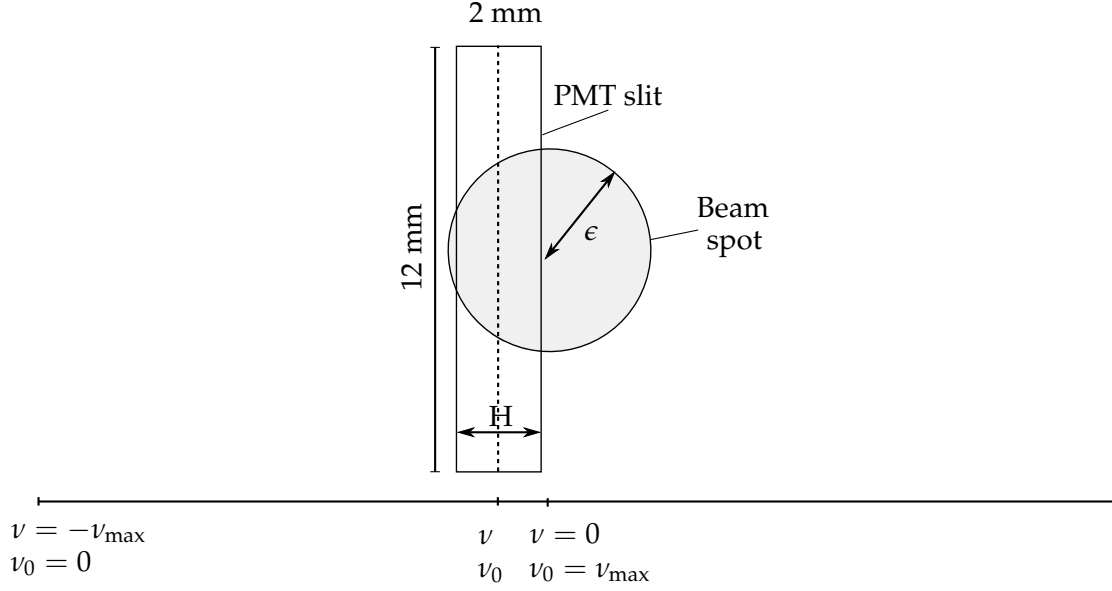
Figure 3.3: Measurement of the incident beam. The integral is performed to a part of the beam that is viewed by the PMT in a certain position ν. H corresponds to the horizontal dimension of the slit.

Table I: Typical parameters of the beam obtained from the fit to its intensity profile (see figure 3.4).

Φ_i (ph/s)	ν_{max} (deg)	ϖ (deg)	ϵ (deg)	Ω_i (μsr)	s (mm)	E (Φ_i/Ω_i) (ph/(s·μsr))
246±2	4.024±0.005	0.923±0.009	0.214±0.004	44±2	0.524±0.010	5.7±0.2
578±3	4.925±0.004	1.340±0.005	0.310±0.005	92±3	0.761±0.013	6.3±0.2
728±3	5.132±0.003	1.400±0.002	0.324±0.005	101±3	0.795±0.013	7.3±0.2
1008±4	5.254±0.003	1.728±0.005	0.400±0.006	153±5	0.981±0.016	6.7±0.2
1456±4	5.536±0.003	1.946±0.004	0.450±0.007	194±5	1.105±0.018	7.5±0.2

The voltage applied to the proportional counter was 1350 V in all the measurements shown in this table.

The values for ϵ, Ω_i, s, derived from ϖ are shown in the table I for different photon fluxes. The incident beam intensity E (Φ_i/Ω_i) is also shown. This value should not change significantly with the angle of incidence. The values in the table I lie between 5.7 and 7.5 ph·s$^{-1}\mu$sr^{-1}. This difference may be due to the non-uniformity of the incident beam.

The value obtained for the incident flux is difficult to be compared with the ex-

3. THE MEASUREMENT OF RADIOMETRIC QUANTITIES

pected value as it is the result of several factors that are not well known, specifically the quantum efficiency of the photomultiplier at the xenon scintillation wavelength and the light gain in the secondary scintillation. Nevertheless the flux can be estimated using the following equation

$$\Phi_i \simeq n_p g E_{\text{col}} R_{\text{quartz}} (1 - A_{\text{quartz}})(1 - A_{\text{air}}) q_{\text{PMT}} E_{\text{trigger}} \frac{\Omega_i}{4\pi} \qquad (3.8)$$

where,

n_p	Number of primary electrons (measured in fig. 2.7)	50,000 (for 1350 V)
g	Light gain in the secondary scintillation per primary electron	40-80 (for 1350 V)
E_{col}	Collimator efficiency (calculated from fig. 2.10)	0.6-0.8 (for 1350 V)
R_{quartz}	Transmission probability, namely at the interface xenon gas quartz and quartz chamber (for $n_{\text{quartz}} = 1.7$ at 175 nm)	$\simeq 87\%$
A_{quartz}	Absorption in the window of the proportional counter	$\simeq 0.0$
A_{air}	Absorption by oxygen molecules	$\simeq 0.0$
q_{PMT}	Quantum efficiency of the PMT	0.1-0.3
E_{trigger}	Trigger efficiency	0.6-0.7
Ω_i	Solid angle	40-200 μsr

Assuming that $\Omega_i \simeq 40 \,\mu$sr, a collimation efficiency and trigger efficiencies of 0.7, a quantum efficiency of the photomultiplier of 0.2 and a light gain in the secondary scintillation of 40 photons per electron, thus the predicted flux is about 1.6 photons per alpha particle or 1300 photons/s. This value is similar to the flux measured (see table I).

The intensity observed in the PMT for different angles ν is shown in the figure 3.4 for two different slit widths (1 mm and 2 mm). The solid lines represent the fitted function $I(\Phi_i, \epsilon, \nu)$ of equation 3.5. Gaussian fits are also shown for comparison (dotted lines), using as free parameters the amplitude of the distribution Φ_{max}, the standard deviation, σ, and ν_{max} the angular position of maximum intensity relative to the stop sensor ν_{max}. In this case the incident flux is given by

$$\Phi_i = \frac{\sqrt{2\pi}\sigma\Phi_{\text{max}}}{\arctan(H/574)} \qquad (3.9)$$

The values obtained for the incident flux differ less than 1% and are never greater than 2%. The gaussian fit overestimates the points at the maximum amplitude and the fit with the equation 3.4 underestimate the points with maximum amplitude. Nevertheless the χ^2 of the fit with the equation 3.5 is usually smaller than with the gaussian
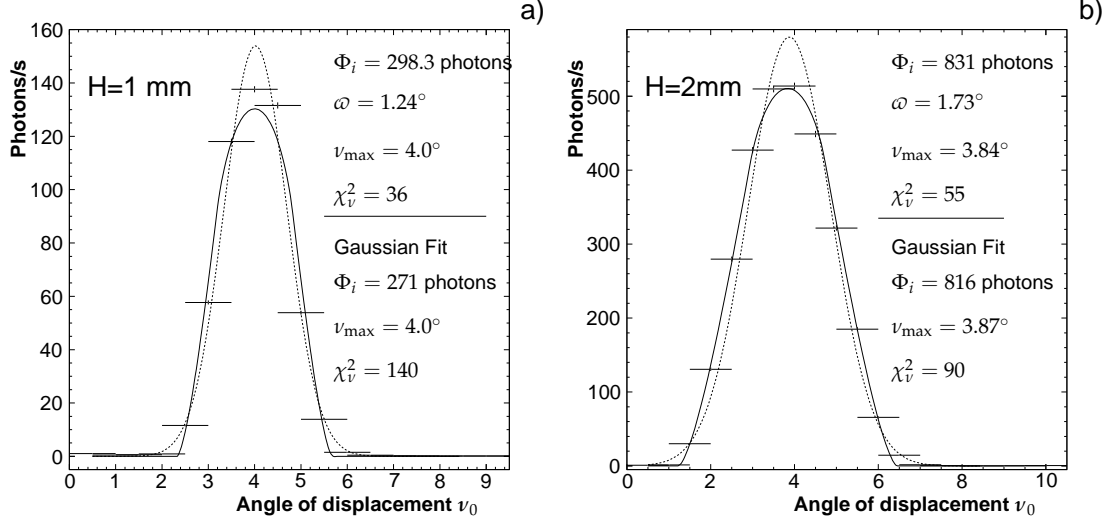
Figure 3.4: The incident flux measured with two PMT slit widths, H=1 mm (a) and H=2 mm (b). The solid lines represent fits of the equation 3.5 (solid lines) and Gaussian fits (dashed lines) are also shown for comparison. The error bars correspond to angular uncertainties of 0.5 degrees.

distribution and the tails of the observed data are better described with this distribution. In both minimizations the reduced chi-square is too large, therefore the errors of the parameters obtained in the minimization do not have statistical meaning. Hence, the uncertainties are taken from the error of the parameters it is used instead the root mean square of the several measurements made to the incident beam.

Light source stability

The light source should be stable during the measurements to ensure that the incident flux in the samples remain the same. The evolution of the incident light flux (Φ_i) with time (since the closure of chamber, in hours) is shown in figure 3.5, for a high voltage of 1350 V. Three different apertures of the iris diaphragms are shown. As can be seen the flux is very stable of a time period of more than 100 h. Though, continuous decreasing of about 0.5 photons/hour is observed at high intensities which might be caused by the outgassing of different materials inside the chamber, increasing the level of oxygen, and consequently the VUV absorption. A typical measurement of the reflected light flux for a specific angle of incidence lasts between eight and twenty hours. During this time the incident flux decreases in about 4 to 10 photons, in whichever case it corresponds to a value below 1% of the incident light flux.
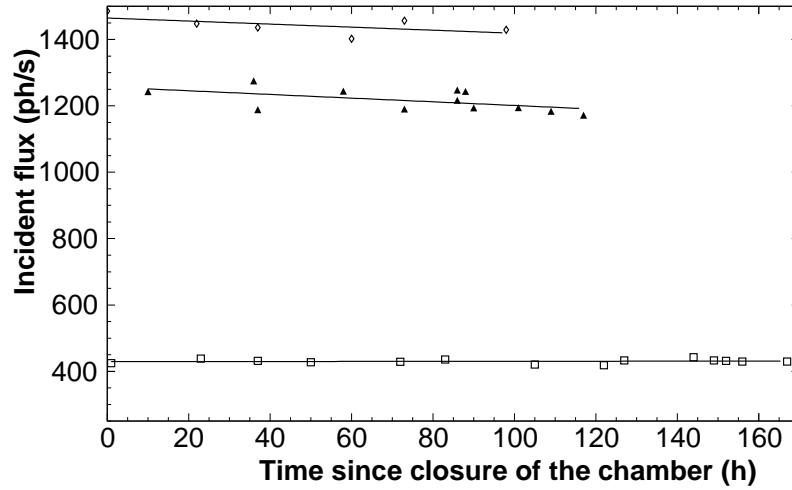
Figure 3.5: Incident flux observed as function of time since the closure of the chamber for three different beam intensities.
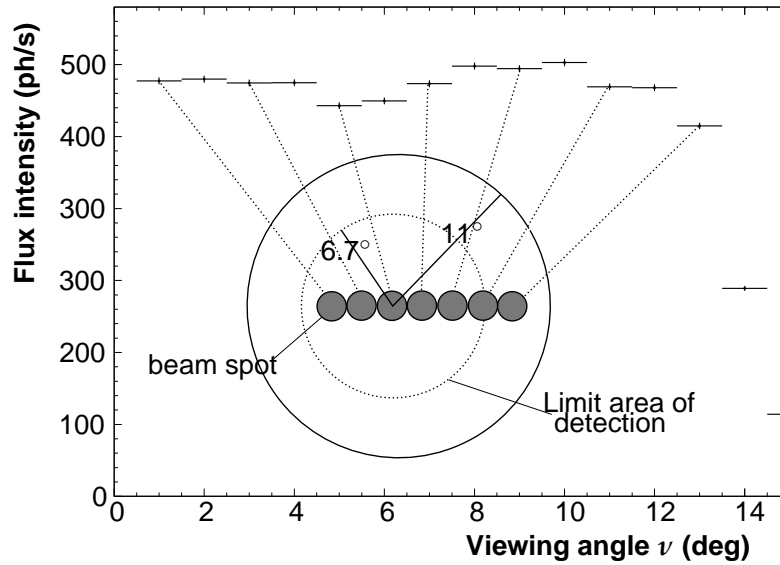
Figure 3.6: Test to the uniformity of the photo-cathode of the photomultiplier. The slit in front of the PMT was removed and the PMT directed to the incident beam. The outer circle represents the PMT window. Only the central region marked by the dotted line, was used for detection. The beam spot is also shown at different positions over the photocathode along with the corresponding beam flux. The non-uniformity of the photocathode is about 3.5 (r.m.s.).

Non-uniformity of the photo-cathode

The type of measurements performed require the area of the photomultiplier to be uniform. Therefore, the uniformity of the photomultiplier was checked without the slit normally placed in front of the PMT window. The incident beam was collimated to about $\varpi = 1.2°$ measured relatively to the sample and the incident flux was measured at different positions of the PMT, ν.

The intensity observed in the photomultiplier as function of the position, ν, is shown in the figure 3.6, different regions of the photocathode are illuminated in each case, as shown in this figure. The zone delimited by the dotted circle corresponds to the zone of the PMT that can observe photons, the outer annulus is masked by the slit placed in front of the PMT. The difference between the largest and smallest measured flux is less than 10.0% and the r.m.s. obtained is 3.3% of the observed intensities. Therefore the non-uniformity pose no problem to the reflectance measurements, namely because the slit is kept in place across all bunch of measurements.

The vertical calibration

The vertical calibration aims to measure and check for any residual vertical displacement of the incident beam relative to the photomultiplier axis. This calibration was done routinely in between experiments. To perform this operation the slit that is in front of the PMT is placed in an oblique position. We used an inclination of 22.62° with the horizontal instead of 90° (figure 3.7 b and c). Any displacement will show up when sampling the beam spot as above. The beam is measured for several positions of the
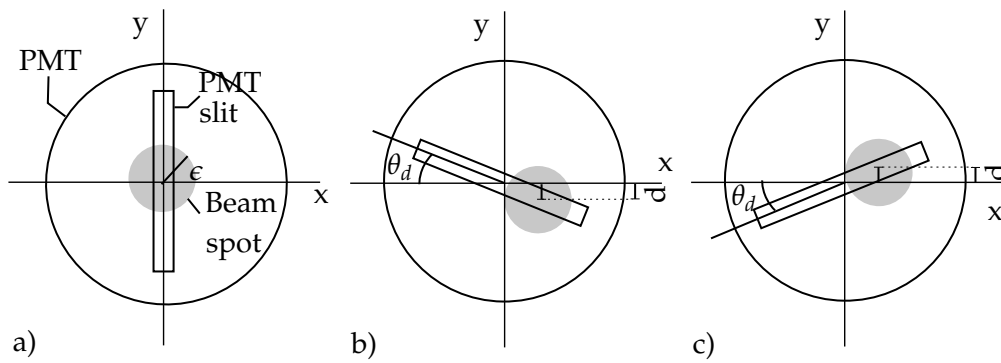
Figure 3.7: Calibration of the incident beam relative to the PMT axis a) for the incident beam correctly aligned; b) if the incident beam is centered below the PMT axis, c) if the incident beam is placed above the PMT axis. By turning the slit a certain angle is possible to evaluate the position of displacement of the beam spot, d, at the PMT window.

PMT. If the beam is correctly aligned the position of the maximum of intensity will be right at the same position as the maximum intensity observed having the slit vertical, at 90°. In the event of any misalignment it can be corrected further during the data analysis. For the majority of the measurements performed the correction introduced is of 0.5 mm.

3.2 Calibration of the Angle of Incidence

The angle of incidence ν_i is calibrated after the position of maximum intensity. The PMT is positioned in line-of-sight with the source (Figure 3.1 b)). The sample is lowered and oriented until being nearly parallel to the incident beam. The sample is then rotated successively in small steps (of about 0.18°) and the flux of photons observed in the PMT is recorded. A typical ν_i calibration curve is showed in figure 3.8.

The angles are all measured relative to the position of the reference point given by the motion sensor. The position of intersection between both lines, $\nu_{\text{sample}}^{\text{max}}$, corresponds to the maximum flux observed and is given by $\nu_{\text{sample}}^{\text{max}} = (a_2 - a_1) / (m_1 - m_2)$. In this position the sample is parallel with the incident beam. Due the geometry of the experiment m_1 and m_2 should be similar. When the sample is correctly aligned with
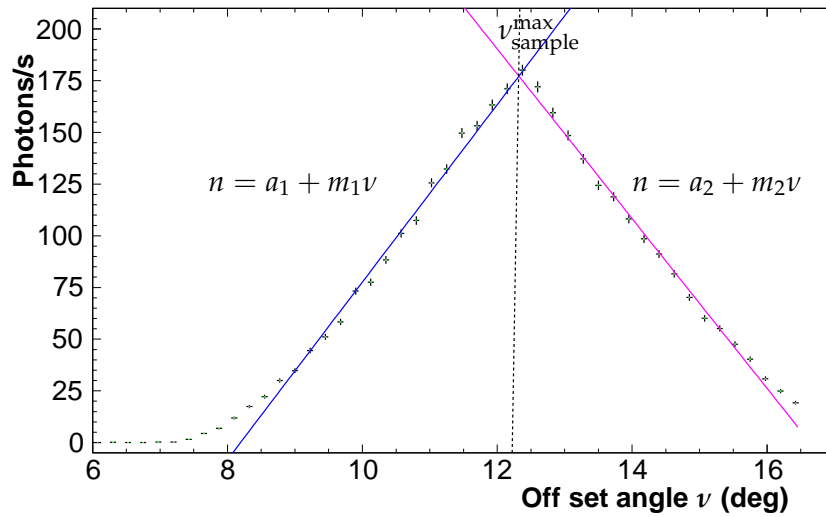
Figure 3.8: Calibration of the angle of incidence, the PMT is placed aligned with the beam and the sample position changed according to the angle ν measured between the sample and the stop sensor. The lines correspond to inear fits to the data at left and right of the position of maximum intensity. The position $\nu_{\text{sample}}^{\text{max}}$ corresponds to the angle of incidence $\nu_i = 90°$

the incident beam the intensity observed at the position $v^{\max}_{\text{sample}}$ should be half of the intensity of the beam. At this position the angle of incidence is $v_i = 90°$. The angle between this position and the stop sensor of the structure that supports the sample is about 12° as can be seen in figure 3.8.

3.3   Measuring the Reflected Light Flux

After the measurement and calibration of the angle of incidence, the sample can be positioned at whatever angle of incidence. When the sample is illuminated at the normal incidence the diameter d of the beam spot produced in the sample is $d = 2p_s \tan \epsilon$ mm where p_s is the distance between the proportional counter and the sample ($p_s \simeq$ 220.6 mm). When the angle of incidence, θ_i, is increased the beam is stretched in the horizontal direction and the size of the beam is now given by

$$d = 2p_s \tan \epsilon / (\cos \theta_i) \qquad [\text{mm}] \tag{3.10}$$

The samples used have horizontal dimensions of 30-35 mm, thus it is not possible to measure the reflectance at very low grazing angles. The width of the beam spot at the normal direction and at $\theta_i = 80°$ is shown in table II for different apertures of the iris diaphragms. The maximum angle that can be measured assuming a sample with a horizontal dimension of 30 mm is also shown.

To check that no light goes beyond the sample limits, the sample is positioned at specific angle of incidence, the photomultiplier is moved as if it was measuring the incident beam, but for the fact that the sample is now lowered. In this situation if all goes well we should only observe the background signal. At angles larger than $\theta^{\max}_i$ (defined in the table II) part of the light does not strike in the sample and is transmitted directly to the PMT.

Table II: Horizontal size of the beam spot produced in the sample for different aperture angles and for different angles of incidence. The maximum angle of incidence ($\theta^{\max}_i$) that can be observed for a sample with horizontal dimensions of 35 mm is also shown.

ϵ (deg)	d ($\theta_i = 0°$) (mm)	d ($\theta_i = 80°$) (mm)	($\theta^{\max}_i$) (deg)
0.214	1.65	9.49	87
0.310	2.38	13.7	85
0.324	2.50	14.4	85
0.400	3.08	17.7	84
0.450	3.47	20.0	83

3. THE MEASUREMENT OF RADIOMETRIC QUANTITIES
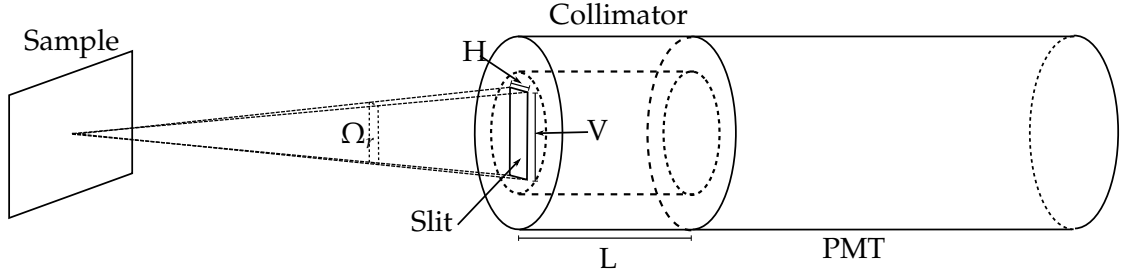
Figure 3.9: Definition of the solid angle Ω_r defined by the slit with dimensions HV placed in front of the PMT.

With the sample in place the reflect light is measured moving the PMT in successive steps all along its course (figure 3.1 d). The angles near the specular direction are sampled in small steps (0.5° or 1°) most of the light is concentrated in a narrow band of angles near the specular direction. As for the other directions the reflectance is sampled in steps of 2°.

The time of data taking Δt is between 125 and 250 s for the angles near the specular direction and 750-1500 s otherwise. The intensity observed for angles far from the specular direction is small thus requiring longer data taking periods. The time required for the measurement of each angle of incidence is between 8 h ($\nu_i = 0°$) and 20 h ($\nu_i = 80°$).

The reflection angle ν_r is derived from the angle ν_{max} (which was obtained from the fit to the incident beam) as

$$\nu_r = 180° - \nu_i - \nu + \nu_{max} \tag{3.11}$$

where ν is the position of the PMT relative to the end course sensor. It should be noted that, as defined, ν_r is negative whenever $\nu > 180° - \nu_i + \nu_{max}$.

The angle between the two stop sensors is 162°, thus the minimum value for ν_r that can be observed by the PMT is

$$(\nu_r)_{min} = 18 + \nu_{max} - \nu_i \tag{3.12}$$

Hence, for a typical value of $\nu_{max} \simeq 4°$ (see figure 3.4), to observe the specular lobe or eventually the specular spike, the incident angle ν_i needs to be larger than 11°.

The viewing solid angle Ω_r

The solid angle subtended by the light detector, Ω_r, is defined by the slit placed in front of the PMT window (figure 3.9). This solid angle is pyramidal with apex angles θ_V and θ_H given by

$$\theta_V = \arctan\left(\frac{V}{d_{po}}\right), \quad \theta_H = \arctan\left(\frac{H}{d_{po}}\right)$$

Table III: Apex angles and solid angles for the slits used during the experimental procedure

	H (mm)	V (mm)	d_{po} (mm)	θ_H (deg)	θ_V (deg)	Ω_r (msr)
Slit A	1.0±0.1	13.0±0.1	73.4±0.1	1.72±0.04	11.1±0.5	5.8±0.3
Slit B	2.0±0.1	12.0±0.1	66.4±0.1	0.86±0.02	10.2±0.5	2.67±0.07

H and V are the dimensions of the slit. θ_H and θ_V are the apex angles of the viewing solid angle Ω_r (see also figure 3.9).

where V is the height of the slit and H the width. d_{po} is the distance between the slit and the sample. Thus the viewing solid angle is given by

$$\Omega_r = 4 \arcsin\left(\sin\frac{\theta_H}{2} \sin\frac{\theta_D}{2} \right) \tag{3.13}$$

The values of θ_V, θ_H and Ω_r are shown in the table III for the two slits used. In both cases we have $\Omega_r \gg \Omega_i$.

The measurement of the solid angles is affected by large uncertainties. This can be solved using a reflectance standard such as the Fluorilon® 99 or the Spectralon® 99. These reflectance factors are not appropriated to be used below 200 nm, nevertheless light with larger wavelength can also be used [4].

Measuring the reflectance of smooth surfaces

The light reflected by a polished or very smooth surface with no diffuse reflection is clustered within a solid angle similar to the incident beam. Therefore, to measure the reflected light is necessary to sample the reflected beam in successive steps, following the procedure described in 3.1. For a certain angle of incidence, v_i, the PMT is placed some angles before the specular direction. The measurements are taken in successive steps of 0.5° until the reflected beam has been totally sampled. The observed flux is then fitted with the function 3.5 and the values for the parameters Φ_r, v_r and ϵ, the reflected flux, peak angle of incidence and apex angle respectively are extracted. If the system is correctly aligned the peak should be positioned at $v_i = v_r$. The incident beam direction will correspond in principle to several incident directions. The aperture angle observed for the reflected beam will be exactly the same ad the aperture observed for the direct beam as suggested in figure 3.10.
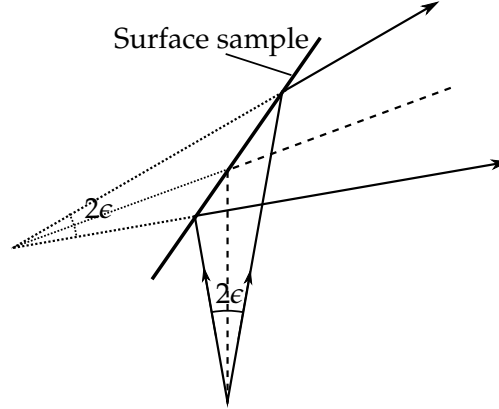
Figure 3.10: The reflected ray for a perfectly specular beam. The aperture of the reflected beam ϵ is equal to the aperture observed in the photomultiplier when pointing directly to the beam. The aperture of the incident beam is exaggerated for effects of visualization.

3.4 The Background Measurement

The background is measured regularly as a function of the angle of incidence. The sample is lifted off, the beam of light and the PMT are moved normally sampling all around as if it was measuring the reflectivity of a surface (figure 3.1 e).

These measurements showed that the background is between 0.12 and 0.20 photons/s along the PMT course. The background observed has two primary sources, i) the electronic noise of the PMT and ii) the light scattered in the interior surfaces of the detector. The electronic noise of the PMT is caused by thermalized electrons in the photocathode that are amplified and produce noise pulses. Some of these pulses are sufficiently large to be detected. The background caused by the electronic noise can be evaluated counting the number of photons with the light source turned off. The number observed is about 10 photons per second without trigger and $\simeq 0.1$ photons/second if looking at coincidences with the trigger signal. This value amounts to the majority of the observed background.

The background was observed to be independent of the angles ν_i, ν_r and the inclination of the sample, ψ, as can be judged from the analysis of the figure 3.11. It is low enough ($\simeq 0.15$ ph/s), to permit the observation of the diffuse reflection, which in the cases analysed amounts to about 0.9 ph/s at $\theta_r \simeq 0°$. In this case the signal/noise ratio is about 6.

There are, however, two main problems concerning this measurement procedure: a) given that the light that might pass through the sample is eventually reflected at the walls of the chamber, the background is artificially increased and b) the light that is reflected by the sample can be reflected by nearby surfaces and reach eventually the
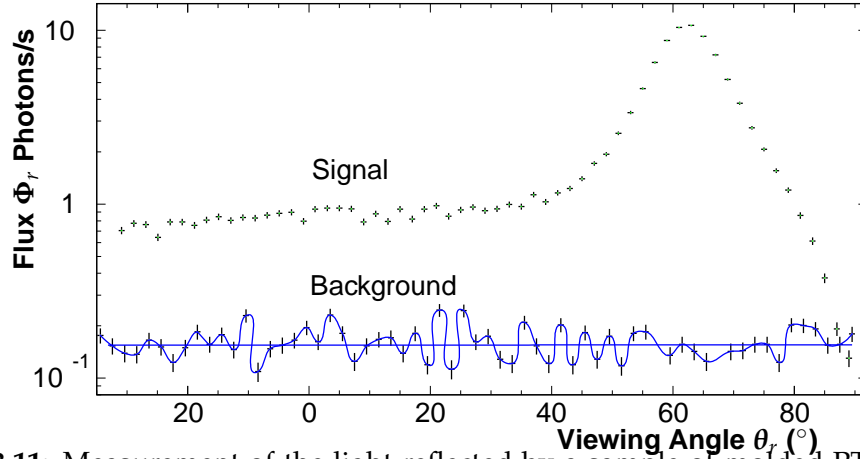
Figure 3.11: Measurement of the light reflected by a sample of molded PTFE (signal) illuminated at $\nu_i = 65°$. The measured background is shown in the same scale. As can be seen, the background is low enough to allow the observation of the reflection at angles far from the specular direction. The solid line corresponds to the average value of the background, and the curved line is to guide the eye.
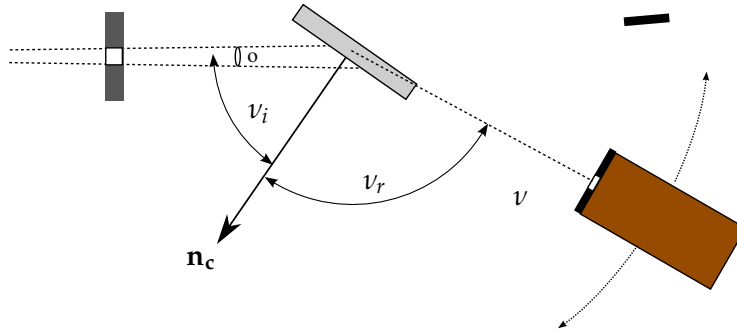
Figure 3.12: The background measurement with the sample lowered, the PMT is placed at an angle of reflectance larger than $90°$ to measure the background. This procedure assumes that the background in the chamber is uniform.

PMT. This light should amount to the background and its effect cannot be measured with the procedure described above. These two issues can be addressed by measuring the background with the sample lowered and the PMT placed at reflectance angles larger than $\nu_r > 90°$, as shown in figure 3.12. With this configuration the light reflected by the sample cannot reach the PMT directly, it can, however, be scattered by the nearby surfaces and be detected by the PMT. However, this procedure requires the background to be uniform along the PMT course.
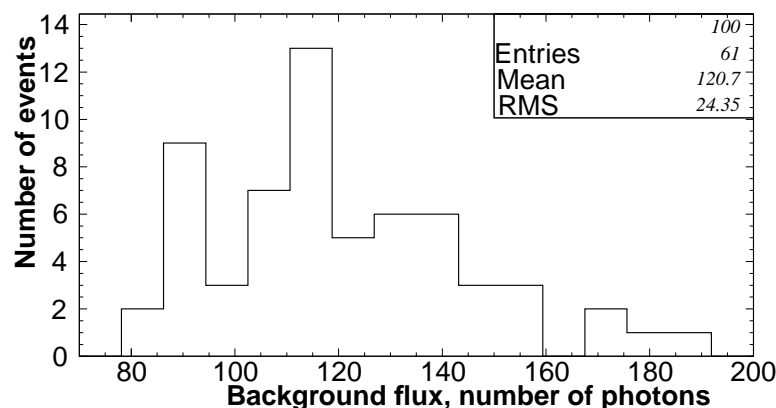
Figure 3.13: The distribution of the number of photons observed in the background measurements for the results shown in the figure 3.12. The data taking time was 750 s.

A histogram of the background measurements is shown in the figure 3.13. The root mean square obtained (0.032) is significantly higher than the error obtained with a Poisson distribution (0.018).

3.5 Tests with Wavelength Filters

Various tests were carried out to ensure that the observed light is effectively VUV scintillation light coming from the xenon proportional counter and not from something else. To be certain that the light beam originated from the xenon proportional counter has no light other than the expected scintillation we placed an interference filter after the last iris diaphragm. The interference filter that has been used is a dielectric-metal filter from S. A. Matra® whose transmittance efficiency is 12% at 172 nm, according to the manufacture. The transmission curve has a FWHM of 17 nm. The filter was positioned at the last iris diaphragm to ensure that all the light that strikes the surfaces passes through the filter near the normal.

In figure 3.14 we compare the reflection distribution obtained for the PTFE with and without the VUV filter. The amount of light obtained after the filter is very small, hence the comparison is only done for angles close to the specular direction. The ratio of the areas of the reflection lobes with and without the filter is 13.7% (see table IV), a value comparable to the manufacturer's figure. Therefore, we conclude that the beam is of VUV light.

Another hint comes from the beam attenuation in air. The intensity is attenuated to about 1/200 when air is introduced in the chamber. At 175 nm the absorption coefficient for the atmosphere is larger than 1 cm^{-1} (fig. 2.1), thus no light can be observed by the photomultiplier. However the emission spectra for the xenon shows that 15% of the

70

Figure 3.14: Comparison between the reflectance distributions obtained with and without the Fabry-Perot interference filter at ν_i=65° for a sample of PTFE. As can be seen the filter reduces the amount of light but not the shape of the distribution. This is clearly seen when the two distribution are normalized to each other (right panel).

Table IV: The parameters of the gaussian fits of the PTFE reflectance in the specular lobe region for $\nu_i = 65°$ with and without the filter (see text).

	Amplitude (ph/s)	σ (deg.)	$\sigma \cdot A$
without filter	11.2 ± 0.1	11.6 ± 0.1	2.27
with filter	1.67 ± 0.04	10.6 ± 0.4	0.31
ratio (filter/no filter)	0.149 ± 0.004	1.09 ± 0.04	0.137 ± 0.003

emitted light is above 182 nm. For these wavelengths the absorption coefficient can be as low as 0.01 cm^{-1}, which means that it can be detected.

No light is observed when a piece of glass is placed between the PMT and the VUV source. This test was performed to several types of glasses with different thicknesses. One of the glasses used is transparent for wavelengths larger than 270 nm. When the proportional counter is placed at a distance of 10 cm from the photomultiplier in air the number of photons observed without the glass is 3113 photons/min and with the glass 164 photons/min. The measured background observed was at about 164 photons/min. Thus if any light above ∼300 nm is emitted by the proportional counter it should be
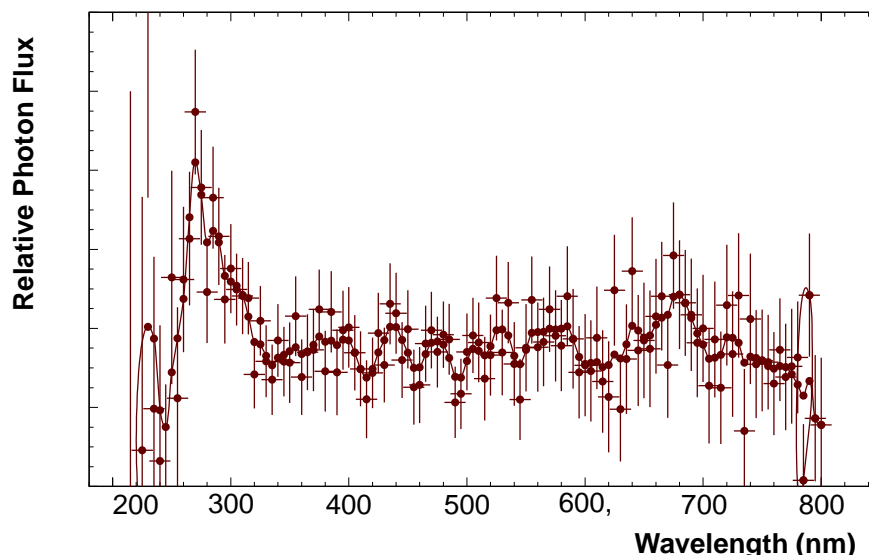
Figure 3.15: The emission spectrum of the light emitted by the proportional counter between 200 and 800 nm for an applied voltage in the proportional counter of 1750 V. The background was removed from each data point. The resolution of the spectrometer is 9 nm and the time of each measurement was 300 s.

very small, without any statistical significance.

Furthermore, the proportional counter was coupled to a monochromator to measure the spectra of the emitted light between 220 nm and 800 nm for high voltages of 1350 V and 1700 V. The spectra was measured with steps of 5 nm with a resolution of 9 nm. The time of each measurement was about 1000 s. The background was subtracted for each wavelength and the result obtained was corrected by the diffraction grid efficiency and the photomultiplier quantum efficiency. Above 340 nm no emission was observed as expected and the collected data is comparable with the measured background. However, between 240 and 340 nm the proportional counter produces light (see figure 3.15) with the distribution is peaked at about 280-290 nm. The observed signal is very small corresponding to about one photon per second and a signal to noise ratio of 0.18 but it was not possible to compare the intensity of this signal with the intensity of the second continuum.

The origin of this light could not be identified and it is still unknown. It can be caused by impurities. However impurities such as XeF_2 ($\simeq$ 350 nm), O_2 ($\simeq$ 558 nm), N_2 ($\simeq$ 337 nm) and water OH ($\simeq$ 306 nm) do not have this spectral characteristics and were discarded. This emission can also be associated to the so-called third continuum which is placed between 200 nm and 400 nm [142]. As observed by E. Robert *et al* [143] this emission is quite broad and at 1 bar it starts at about 220 nm, has a maximum at

270-290 nm and extends up to 500 nm. These characteristics are shared by the observed data. The origin of the third continuum in rare gases is uncertain, some hypothesis for this emission are given by A. M. Boichenko (2000, [142]) and Pierre Milet (1979, [18]).

3.6 The Reflectance Quantities

The intensity for a specific position $\{v_i, v_r, \psi\}$, is given by the ratio between the photon flux observed in the PMT with the background measured subtracted and the
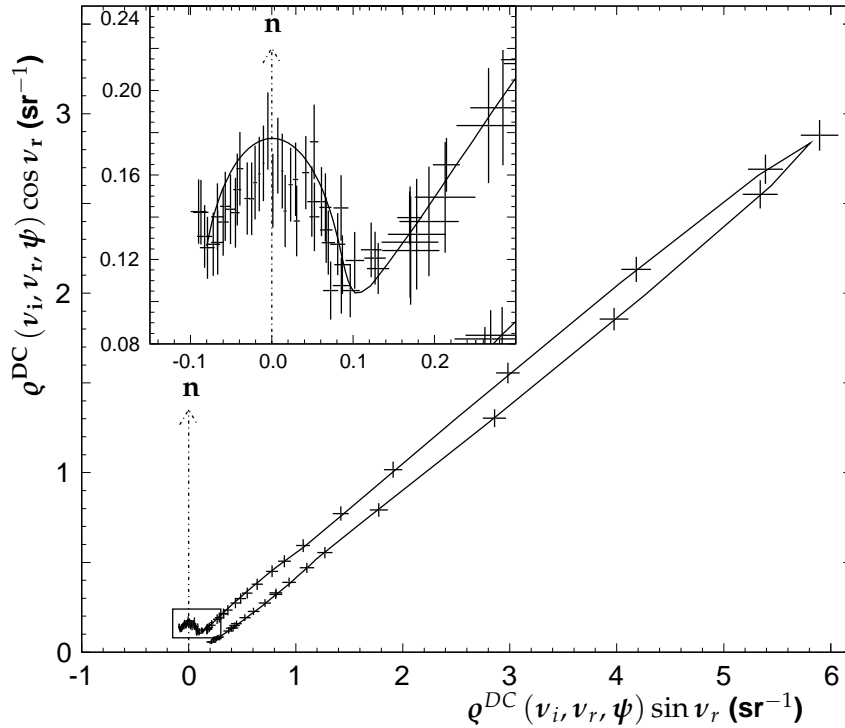
Figure 3.16: The Reflectance distribution of a sample of PFA in polar coordinates, measured at an angle of incidence $v_i = 65°$ and for $\psi = 0°$ (for the definition of the angles see figure 2.11 of chapter 2). The reflectance shows a directional contribution peaked at the specular direction plus a diffuse component distributed around the normal **n** to the surface which is typically lambertian. The data are well described by the fitted function ϱ which will be treated further in the next chapter. The error bars are given by the equation 3.17.

3. THE MEASUREMENT OF RADIOMETRIC QUANTITIES

solid angle Ω_r,

$$I_r = \frac{\Phi_r}{\Omega} = \frac{\frac{n_{ph}}{\Delta t} - B}{\Omega_r} \tag{3.14}$$

n_{ph} is the number of photons measured by the PMT during the time Δt and B is the background flux.

The measurements performed corresponds to a bi-conical reflectance. However, the incident solid angle Ω_i is usually very small comparatively to Ω_r, therefore we opted by the directional-conical reflectance (see appendix A) to represent our data.

The directional-conical reflectance is given by the ratio between the intensity observed in the PMT and the flux incident on the sample. This is in general a function of both the incident and the reflectance direction

$$\varrho^{DC}(v_i, v_r, \psi) = \frac{I_r}{\Phi_i} \tag{3.15}$$

In a perfectly smooth surface the directional-hemispherical reflectance for a certain angle of incidence θ_i can be calculated directly by the ratio of the total reflected and incident fluxes

$$R(\theta_i) = \frac{\Phi_r}{\Phi_i} \tag{3.16}$$

The uncertainties of each reflectance measurement can be obtained by error propagation of the quantities n_{ph}, B, Ω_r and Φ_i. The number of photons of the signal is assumed to follow a Poisson law, thus $\sigma_{n_{ph}} = \sqrt{n_{ph}}$, the error for reflectance is given by

$$\sigma_\varrho^{DC} = \varrho \sqrt{\frac{\frac{n_{ph}}{(\Delta t)^2} + \sigma_B^2}{\left(\frac{n_{ph}}{\Delta t} - B\right)^2} + \frac{\sigma_{\Omega_r}^2}{\Omega_r^2} + \frac{\sigma_{\Phi_i}^2}{\Phi_i^2}} \tag{3.17}$$

The reflectance distribution is shown in figure 3.16 for $v_i = 65°$ for a sample of PFA. This polar plot shows the presence of both a specular lobe along the specular direction, and a distribution in $\cos v_r$ characteristic of a lambertian surface. Although the directional reflectance seems to be strong, the data was taken exclusively in the plane of reflection but the light is diffused all around, especially the lambertian component. A modelling of the reflectance is necessary to obtain the reflectance outside this plane and to obtain the hemispherical reflectances. The curve represents the best fit to the measured data using such a model function $\varrho(v_i, v_r, \psi)$. The modelling of the reflection will be discussed in the next chapter.

Modelling the Reflection

It is not practical to describe, compare or even predict reflectances using the large amount of data that was collected with the goniometer. Also the data are restricted to a part of the hemisphere and the reflectance measured does not correspond exactly to the BRIDF (bidirectional reflected-radiance-distribution function , see appendix A). This factors render necessary an effective modelling of the reflectance, thus using a restrict number of parameters physically motivated to describe the reflectance properties of an interface. These models and the results obtained with them can be used in detector physics, particularly in the understanding of the detector and the development of simulations and the data analysis.

The modelling can be performed using two different methods, an analytical method in which the bidirectional reflectance function ϱ is computed at every point of the hemisphere or a Monte-Carlo method where the photons are tracked and the direction of reflection is obtained by the sampling the function ϱ. Here, we are mainly focused in the analytical method, a Monte-Carlo method will be used further in the chapter 6.

A surface corresponds generically to the frontier between two materials with different optical characteristics. The reflectance of a polished surface with no internal scattering can be fully characterized by the laws of reflection and refraction (Snell-Descartes) and the Fresnel equations. These equations are dependent of the optical properties of the materials of the two media that meet at the surface namely the indexes of refraction and the extinction coefficients. However, most surfaces are at least slightly rough, characterized by vertical deviations of the surface points relatively to a perfectly smooth plane, rougher surfaces will have larger and more frequent deviations. Apart from these effects it is also frequent to have internal scattering of the light in the bulk. Therefore, the reflection usually involves three different components: i) a specular spike, ii) a specular lobe and a iii) diffuse lobe. The diffuse lobe is associated to an internal scatter-

4. MODELLING THE REFLECTION

ing of the light in the volume of the material beneath the surface and yields a reflection distribution which is mostly independent of the direction of the incident light. The specular lobe is centered along the specular reflection direction and has a width and distribution directly proportional to the roughness of the surface. Finally, the specular spike corresponds to mirror like reflection which can be attributed to a coherent reflection at the mean plane of the surface. As the surface becomes rougher so does the intensity of the specular lobe, at expenses of the specular spike which decreases.

The specular components are dependent of the roughness of the surface. The roughness can be described using two different models, the height distribution model and the slope distribution model. The first model characterizes the surface using a height distribution with certain a correlation function between two every points of the surface. Usually, two parameters are needed to characterize the surface: the root mean square of the heights and a correlation length. The model of slopes, on the other hand, describes the surface irregularities by a collection of micro-surfaces randomly oriented whose slopes follow a certain probability distribution function. The height distribution model is usually used in smooth samples namely whenever the physical dimensions of the irregularities are important to describe the optical behaviour of the surface

The scattered electromagnetic wave that is generated at the rough interface has two different components corresponding to the coherent and incoherent superposition of the fields. The coherent field corresponds to the average field and yields a spike right at the direction of specular reflection. The incoherent field corresponds to the fluctuating field and leads to the specular lobe of reflection. The two fields are computed through the integration of the Helmholtz equations. Usually it is necessary to consider some approximations when computing the integrals, such as the small slope approximation and the tangent plane approximation which corresponds to consider the surface locally flat.

If the roughness is large enough, such that the physical dimensions of the irregularities are much larger than the wavelength of the incident light, then a geometrical approximation can be used instead. The specular lobe is then well described by a distribution of micro-facets. This approximation, however, cannot describe the coherent field as it is intrinsically a wave phenomenon.

In dielectrics the diffuse reflection arises from internal scattering in the subsurface layers. It usually presumed this reflection has constant radiance according to the Lambertian model. However, the diffuse reflected light is refracted twice at the surface plus one or more internal reflections. Therefore, the radiance is found to have some angular dependency. These effects are accounted for by the Wolff model of reflection [6]. Moreover, there is a geometrical effect introduced by the roughness of the surface. When the viewer direction approaches to the direction of incidence it is observed an increasing in the observed radiance of the surface, this effect is described here by the Oren-Nayar model [144]. Associated to the internal scattering of the light it is possible to observe a coherent backscattering of photons that corresponds to a photon self-interference with
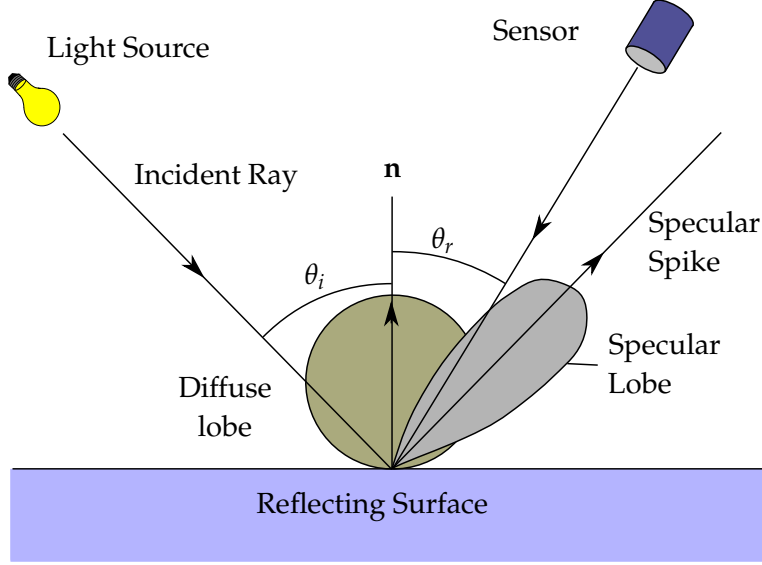
Figure 4.1: Polar representation of the three components of the reflection. The diffuse lobe is centered around the surface normal and the specular components are centered around the specular direction.

an enhance intensity cone in the backscattering direction [145]. Although this a very interisting phenomenon because it is directly related with the mean path of the light in the disordered media it has usually a very small effect in the reflection distribution.

Figure 4.1 depicts the typical reflection distribution at a rough surface with the three reflection components referred to above: the diffuse lobe, the specular lobe and the specular spike. The angle of incidence, θ_i, is defined between the normal to the plane of the surface and the incident direction whereas the viewing angle, θ_r, refers to the angle between the normal to the plane and the direction towards which the reflected light is being viewed.

The BRIDF ($\varrho(\theta_i, \phi_i, \theta_r, \phi_r) = \frac{\mathrm{d}\Phi_r/\mathrm{d}\Omega_r}{\Phi_i}$, see appendix A) should be given by the sum of these three contributions:

$$\varrho = \varrho_D + \varrho_S + \varrho_C \tag{4.1}$$

where ϱ_D, ϱ_S, ϱ_C are the contributions for the total BRIDF of the diffuse lobe, the specular lobe and the specular spike (coherent) respectively.

These components usually assumes that the light is scattered only once at the surface (or twice as in the diffuse component). However, if the surface is rough enough, then some parts of the surface can hide or be hidden by other parts of the surface. Here the light can be multiple reflected at different parts of the surface (a part from the diffuse component which by its nature is a multi-scattering phenomenon). This effect is called shadowing-masking and should be included when attempting to describe the
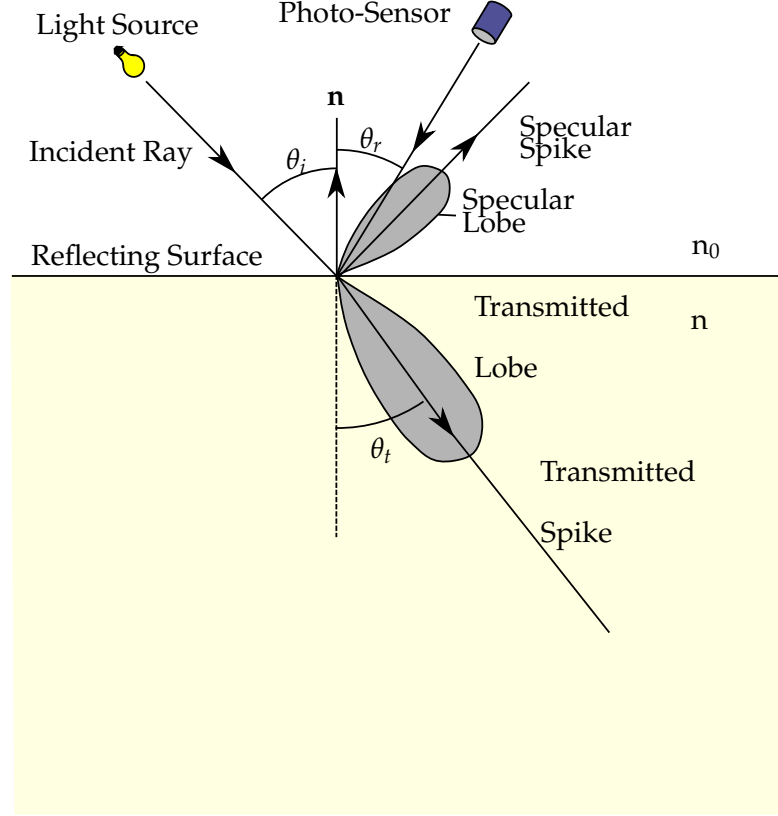
Figure 4.2: The reflected and transmitted components in a interface between two different media with indices of refraction n_0 and n. The intensity of the transmitted components is usually larger than the specular components. It is considered that no internal reflection occurs in the transmitted medium.

reflectance distribution of a surface.

To describe light that is not reflected, but otherwise transmitted into the other side of the interface it is also necessary to consider various contributions namely the specular lobe and coherent spike. In this case the BTIDF (bidirectional transmitted intensity distribution function) ϱ^t is given by

$$\varrho^t = \varrho_S^t + \varrho_C^t \tag{4.2}$$

where ϱ_S^t described the transmitted lobe and ϱ_C^t the transmitted spike. It is assumed that no multiple scattering occurs in the second medium, or else it should be necessary to describe the scattering process that occurs inside the medium.

Figure 4.2 represents the scattering of an electromagnetic wave, considering both a lobe and a spike for both the reflection and transmition processes. The angle θ_t corresponds to the transmitted angle obtained using the Snell's law.

The majority of the models that are addressed in this chapter are not restricted to the scattering of electromagnetic waves but can be adapted to the reflection of other type of waves such as acoustic waves [146] or seismic waves [147].

4.1 Reflection and Refraction of a Plane Wave

An electromagnetic plane wave that reaches a boundary between two homogeneous media with different optical properties is split into two parts, a reflected wave and a transmitted wave, towards directions given by the laws of reflection and refraction

$$\theta_r = \theta_i \qquad \text{(reflection)} \tag{4.3a}$$

$$n_0 \sin\theta_i = n \sin\theta_t \qquad \text{(refraction)} \tag{4.3b}$$

where n and n are the indices of refraction in the incoming and transmitted medium. When a wave propagates from an optical denser (higher index of refraction) medium into one optically less dense it can occur total internal reflection for angles larger than $\sin\theta_i > n_0/n$.

The index of refraction of an absorbing medium is a complex number given by $\tilde{n} = n + i\kappa$. The intensity of the transmitted electromagnetic wave decreases in this according to the exponential $I(z) = I_0 \exp\left(-z/\zeta\right)$, where ζ is the attenuation length of the electromagnetic wave in the material. This attenuation length is related with the extinction coefficient, κ, of the medium and the wavelength in the vacuum, λ, through the relation

$$\kappa = \frac{\lambda}{4\pi\zeta} \tag{4.4}$$

This length is dependent of the material itself and the wavelength of the radiation.

For significative values of k the equations 4.3a and 4.3b cannot be directly applied.

The Fresnel formulæ

The equations of Fresnel relate the amplitudes of the reflected and transmitted waves at a given interface between two different media. These equations are usually written separately for each polarization components, parallel (p) and perpendicular (s) to the plane of incidence. For an interface between a non-absorptive medium and an absorptive medium [148], the ratio of the amplitudes of the electric field is squared

$$F_s = \frac{\left(n_\theta - \cos\theta_i\right)^2 + \kappa_\theta^2}{\left(n_\theta + \cos\theta_i\right)^2 + \kappa_\theta^2} \tag{4.5a}$$

$$F_p = F_s \left[\frac{\left(n_\theta - \sin\theta_i \tan\theta_i\right)^2 + \kappa_\theta^2}{\left(n_\theta + \sin\theta_i \tan\theta_i\right)^2 + \kappa_\theta^2} \right] \tag{4.5b}$$

where n_θ and κ_θ are given by:

$$n_\theta^2 = \frac{1}{2}\left[\sqrt{\left(n^2 - \kappa^2 - \sin^2\theta_i\right)^2 + 4n^2\kappa^2} + \left(n^2 - \kappa^2 - \sin^2\theta_i\right)\right]^2 \tag{4.6a}$$

$$\kappa_\theta^2 = \frac{1}{2}\left[\sqrt{\left(n^2 - \kappa^2 - \sin^2\theta_i\right)^2 + 4n^2\kappa^2} - \left(n^2 - \kappa^2 + \sin^2\theta_i\right)\right]^2 \tag{4.6b}$$

where n and κ are the index of refraction and extinction coefficient of the second medium. For the normal incidence $n_\theta = n$ and $\kappa_\theta = \kappa$.

The transmission coefficient, the fraction of light that is refracted to the new medium, is obtained using the relations:

$$F_s + T_s = 1 \quad \text{and} \quad F_p + T_p = 1 \tag{4.7}$$

The equations 4.5a and 4.5b can be simplified when $\kappa \ll 1$ and in this case the reflection and transmission coefficients are given by [149]

$$F_p = \left(\frac{n\cos\theta_i - \sqrt{1 - \frac{1}{n^2}\sin^2\theta_i}}{n\cos\theta_i + \sqrt{1 - \frac{1}{n^2}\sin^2\theta_i}}\right)^2 \tag{4.8a}$$

$$F_s = \left(\frac{\cos\theta_i - n\sqrt{1 - \frac{1}{n^2}\sin^2\theta_i}}{\cos\theta_i + n\sqrt{1 - \frac{1}{n^2}\sin^2\theta_i}}\right)^2 \tag{4.8b}$$

$$T_p = \frac{\sin 2\theta_i \sin 2\theta_t}{\sin^2(\theta_i + \theta_t)\cos^2(\theta_i - \theta_t)} \tag{4.8c}$$

$$T_s = \frac{\sin 2\theta_t \cos 2\theta_i}{\sin^2(\theta_i + \theta_t)} \tag{4.8d}$$

For the normal incidence ($\theta_i = \theta_t = 0$ and $\kappa_\theta = \kappa$, $n_\theta = n$), the distinction between perpendicular and parallel equations disappears and we have

$$R = \frac{(n-1)^2 + \kappa^2}{(n+1)^2 + \kappa^2} \qquad T = \frac{4n}{(n+1)^2 + \kappa^2} \tag{4.9}$$

4.2 Models of the Surface Structure

The way the light is reflected in a rough surface is dependent of the microscopic shape of the surface, the roughness. The origin of the roughness of a surface is diverse and can have many causes. It includes random scratches surviving in the surface after polishing, any irregularities in result of machine cut, etc...[150]. The roughness is usually an undesirable effect increasing the wear and friction of the material. Moreover, in result of this roughness the light is scattered other than in the specular direction and in general leads to a specular lobe. Thus it is necessary to describe or somehow model the surface structure so to be able to describe the reflectance distribution in the surface.

The roughness measurements

There are different methods to measure the roughness of a surface. Among these methods are stylus profilometers (SP), the optical profilometers (OP), the scanning electron microscopic (SEM) methods, the scanning tunneling microscopy (STM) or an atomic force microscopy (AFM) [151]. The intrinsic resolution of these systems, vertical and horizontal, is shown in the figure 4.3. As shown these systems have usually larger resolutions in the vertical spacing than in the horizontal spacing.

In the SP measurement a stylus is loaded into the surface and moved to obtain the height variation of the surface. A SP is not convenient in a soft materials such as the PTFE or pure metals because the stylus usually will scratch the surface [152]. In such situations the optical profilometers have the advantage to be non-destructive and can be used for any rough surfaces [153]. There are different optical methods such interferometry techniques or the proper scattering of light in a surface. These techniques are however very model dependent and restricted to specific surface's profilers. They are described in detail in Jean M. Bennett (1976, [154]).

The STM microscopy measures the tunneling current between a sharp tip and the surface. When the distance between the tip and the surface decreases so does the tunneling current increases, being possible to measure the roughness of the surface. This is the most precise method but it is limited to the analysis of conductors.

In AFM measurement the tunneling tip is replaced by a force sensor which measures the force between the tip and the surface [155]. This force has different contributions from Van der Waals, electrostatic and magnetic forces. Unlike STM the AFM technique is not limited to conducting materials and can be used in soft dielectric materials such as the PTFE.

The measurement of the roughness of the samples used in this work was limited to the observation with a optical microscope. More precise methods were not used because we do not have direct access to these instruments. Nevertheless it is highly recommendable to do such measurement in the near future.

Usually the roughness is a very complex feature and only rarely can be described in detail. Thus the roughness measurements are usually expressed by a series of statistical parameters. A detailed description of the different roughness parameters can be found in [157].

The height distribution

In the height distribution model the surface structure is approximated by a distribution of heights. This model of the surface expresses the roughness by a random variation from an ideal smooth plane that represents ideally a smooth surface. The surface profile is then given by the height function $h(x,y)$ of the surface in the (x,y) plane. This function is defined such that $\langle h(x,y) \rangle = 0$. The root mean square of this distribution is
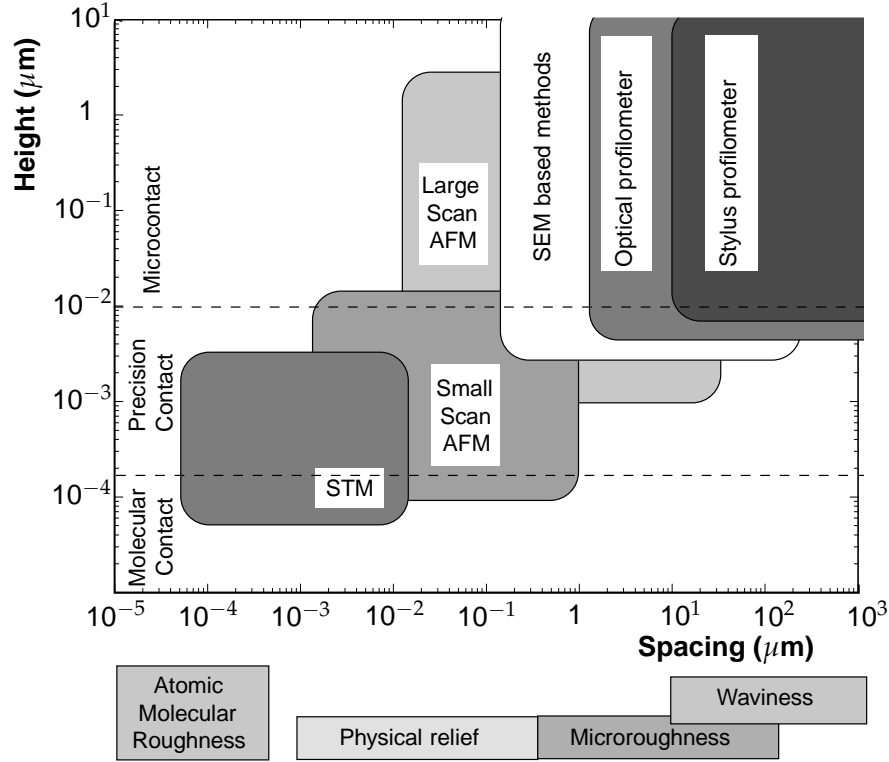
Figure 4.3: Vertical and lateral resolution of different methods of measuring the roughness of the surface. STM stands for scanning tunneling microscope, SEM for scanning electron microscope and AFM atomic force telescope (adapted from [156]).

given by

$$\sigma_h = \sqrt{\frac{1}{S} \int_S h^2 (x,y) \, \mathrm{d}x \mathrm{d}y} \rightarrow \sqrt{\frac{1}{N} \sum_{i=0}^{N} h^2 (x,y)} \tag{4.10}$$

where S is the area of the surface under consideration. This parameter measures in fact the deviations relatively to the smooth plane and it is usually used to describe the finishing/roughness of the surface. It can be measured experimentally by measuring the height of several points of the surface.

Given the impossibility of knowing precisely the function $h(x,y)$, it is associated to this function a probability distribution $P_z(h)$, defined as the probability to find in the vicinity of the point (x,y) an height in the interval [h, h+dh]. This probability distribution must reproduce the height distribution of the surface irregularities.

Figure 4.4 shows the profiles of two different surfaces, they have the same σ_h and probability function P_z, but different spacing. The profiles are significantly different be-
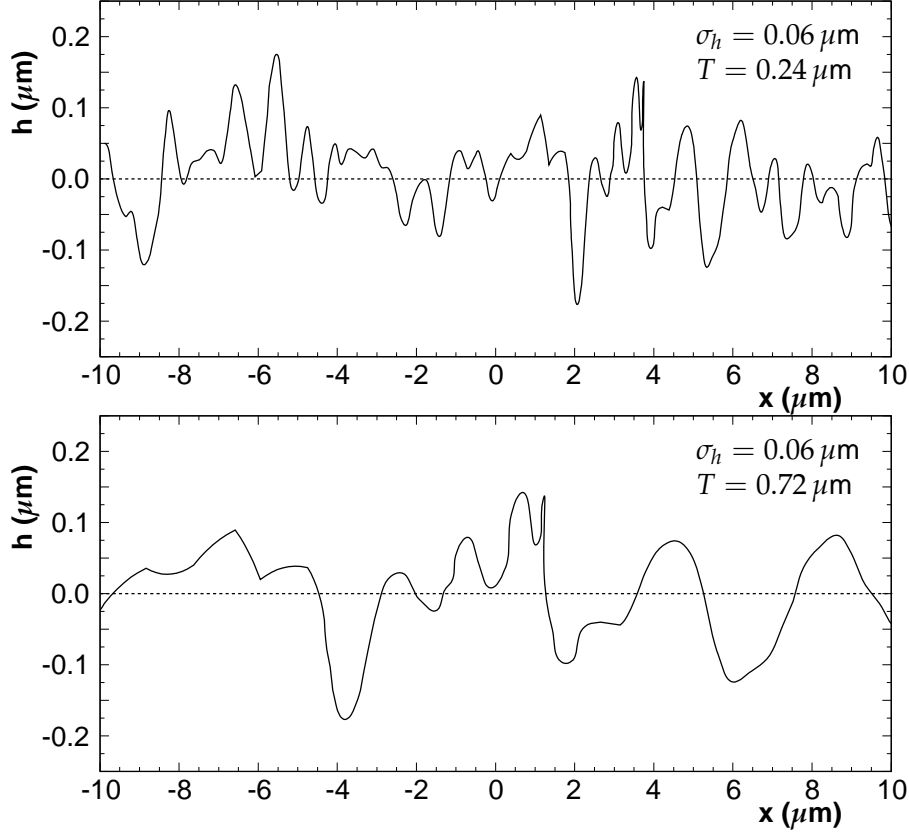
Figure 4.4: Profile for two different rough surfaces with the same roughness parameter σ_h=0.24 μm and different correlations lengths, The surface with the smaller correlation length is considered rougher (graphic taken from [158]).

cause neither σ_h nor P_z give information about the lateral distribution of surface heights. This means that we have to pay attention to the correlation function between separated points of the surface, defining a correlation function such that

$$\langle h\left(x_1,y_1\right),h\left(x_2,y_2\right)\rangle = \sigma_h^2 C\left(x_2 - x_1, y_2 - y_1\right) \tag{4.11}$$

where $C\left(x_2 - x_1, y_2 - y_1\right) = C\left(r\right)$ is the correlation function of the surface. This function constrains the variation of the function h across the surface as function of the distance between the two points.

For an unknown surface profile or for a surface roughness that is produced by truly
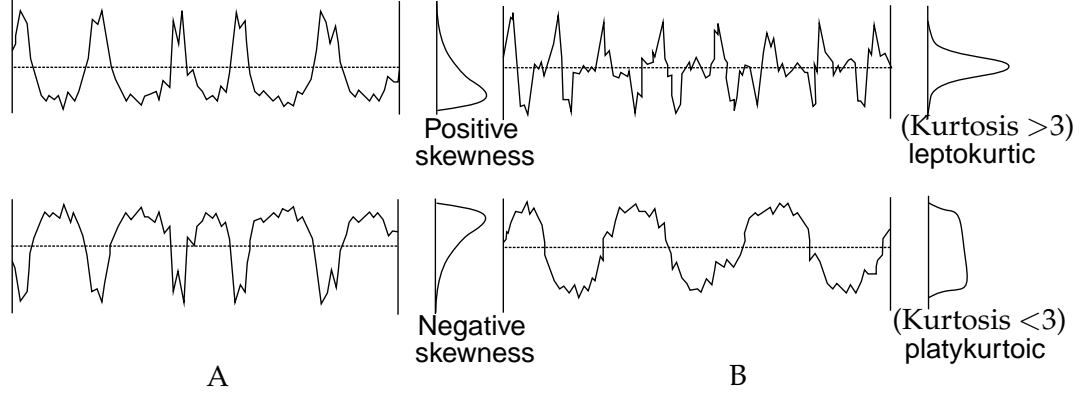
Figure 4.5: Definition of skewness (A) and kurtosis (B). The surface profiles shown have different levels of skewness and kurtosis (adapted from [157]). The function P_z is represented for each surface profile.

random processes it is usually assumed a gaussian distribution for both distributions:

$$P_z(z) \quad = \quad \frac{1}{\sqrt{2\pi}\sigma_h} \exp\left(-z^2/2\sigma_h^2\right) \tag{4.12a}$$

$$C(r) \quad = \quad \exp\left(-r^2/T^2\right) \tag{4.12b}$$

where T is a correlation length that is defined as the average distance that the correlation function $C(T)$ falls to $1/e$. The correlation function is normalized in such a way that $C(0) = 1$, A gaussian distribution of heights was observed in different surfaces such as the lunar soil [159], rubber [160], metallic deposits [161], fused quartz and machined copper [154].

However, some surfaces are not produced in a truly random process, thus different height and correlation functions have to be considered. An exponential distribution for both P_z and $C(r)$ is also common [162]

$$P_z(z) \quad = \quad \frac{1}{\sqrt{2}\sigma_h} \exp\left(-\sqrt{2}\,|z|\,/\sigma_h\right) \tag{4.13a}$$

$$C(r) \quad = \quad \exp\left(-\,|r|\,/T\right) \tag{4.13b}$$

The surface profiles described by the probability functions 4.12a and 4.13a are symmetric relatively to the surface average plane. However some surfaces have an asymmetric profile to measure this property we use the skewness of the surface which is given by

$$S_h = \frac{1}{\sigma_h^3} \frac{1}{S} \int_S h^3(x,y)\,\mathrm{d}x\mathrm{d}y \tag{4.14}$$

Positive values for the skewness means that the positive values of the function $h(x,y)$ are more disperse than the negative values. In this case the surface is characterized by

pronounced and narrow peaks and wide valleys (glacier type). On the other hand when $S_h < 0$ the surface is characterized by large plateau and narrow valleys (coombs). Surfaces with deep scratches or with the peaks removed have usually negative skewness. Profiles with negative and positive skewness are shown in the figure 4.5-A.

The fourth momentum of the height distribution corresponds to the kurtosis. It measures the heaviness of the tails of the probability distribution function of heights and is given by

$$K_h = \frac{1}{\sigma_h^4} \frac{1}{S} \int_S h^4 (x, y) \, \mathrm{d}x \mathrm{d}y \qquad (4.15)$$

The kurtosis is usually referred to the gaussian distribution for which $K_h = 3$. Distributions with higher kurtosis (also called leptokurtic distributions) will have a more pronounced peak of P_z, the exponential distribution is a leptokurtic distribution with $K_h = 6$. Distributions with smaller kurtosis relatively to the gaussian distribution are called platykurtotic distributions. Surface profiles with different kurtosis are shown in the figure 4.5-B.

The slope distribution

When the physical dimensions of the surface are not relevant for the observed reflection distribution the slope distribution is a very good approximation to fully describe the roughness of the surface. In the slope distribution the surface is described by a collection of small micro-facets each having a local normal $\mathbf{n}'$ distributed around the the global normal of the surface $\mathbf{n}$. The slope of a certain elementary surface, α, is defined by the angle between $\mathbf{n}'$ and $\mathbf{n}$. Given that $\mathbf{n} \cdot \mathbf{n}' > 0$ then α is defined between 0 and $\frac{\pi}{2}$.

Two sets of coordinates are at work when considering the reflection at a rough surface: i) a global set $\{\theta_i, \theta_r, \phi_i, \phi_r\}$ relative to the global normal to the surface $\mathbf{n}$ and ii) a local set, $\left\{\theta_i', \theta_r', \phi_i', \phi_r'\right\}$ which is defined relative to the local normal $\mathbf{n}'$, at a given point of the surface (see fig. 4.6). The angles θ are polar angles, defined between 0 and $\frac{\pi}{2}$ whereas the angles ϕ are azimuthal angles defined between 0 and 2π. Under the assumption that the roughness is isotropic, i.e. that there is no preferable direction across the surface, then the ϕ_i can be set to zero without loss of generality.

When the light is specularly reflected the law of reflection can be directly applied to the local variables and $\theta_r' = \theta_i' = \theta'$. In this case θ' and α are computed by the relations

$$\cos 2\theta' = \cos \theta_r \cos \theta_i - \sin \theta_r \sin \theta_i \cos \phi \qquad (4.16a)$$

$$\cos \alpha = \frac{\cos \theta_i + \cos \theta_r}{2 \cos \theta'} \qquad (4.16b)$$

The angles α between $\mathbf{n}$ and $\mathbf{n}'$ should be distributed according to a probability distribution function $P(\alpha)$, called the micro-facet distribution function, in such a way that the function $P(\alpha) \, \mathrm{d}\Omega_\alpha$ gives the probability that the micro-facet with normal $\mathbf{n}'$ lies
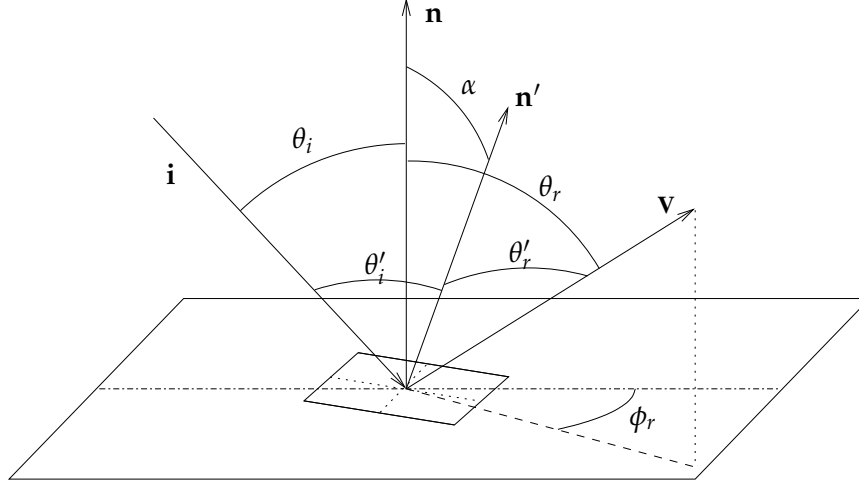
Figure 4.6: The system of coordinates in the slope distribution model: **i** represents the direction of incidence of the photons, **v** is the viewing direction, and **n** and **n**′ are surface normal vectors, of the global (macroscopic) surface and of a local micro-surface. Primed angles are measured relatively to the local normal **n**′.

within the solid angle $d\Omega_\alpha$. More generally, for non-isotropic surfaces, the function P should be written as $P(\alpha, \phi_\alpha)$, where ϕ_α is the azimuthal angle about **n** [163].

The probability distribution function $P(\alpha)$ should respect the following normalization condition[1]

$$\int_{-\pi}^{+\pi} \int_{0}^{\frac{\pi}{2}} P(\alpha) \cos\alpha \sin\alpha \, d\alpha \, d\phi_\alpha = 1 \tag{4.17}$$

such that the projected area in the average plane be the area of the plane surface itself.

There are different expressions for the slope distribution function that correspond to different modellings of the surface. The most used distribution is perhaps the normal distribution (Torrance-Sparrow) [7]. Here we report also the Trowbridge-Reitz distribution [164].

The Torrance-Sparrow and Cook-Torrance distributions

The micro-facets model of Torrance-Sparrow [7] models the surface roughness as a collection of mirror like micro-surfaces symmetrically distributed about the surface normal, with a normal distribution

$$P(\alpha, \sigma) = \frac{1}{\sigma_\alpha \sqrt{2\pi}} \exp\left(-\frac{\alpha^2}{2\sigma_\alpha^2}\right) \tag{4.18}$$

---

[1]Some authors use a slightly different normalization with this integral equalized to π. Therefore, the factors π in the Cook-Torrance and the Trowbridge-Reitz distributions should be removed in this case.

where σ_α is the standard deviation of the angle α. This parameter measures in fact the surface roughness.

If the heights distribution (P_z) and correlation function ($C(r)$) are assumed both gaussian then the parameters σ_h, T and σ_α, are related by [165]

$$\frac{\sigma_h}{T} = 0.5 \tan\left(\sqrt{2}\sigma_\alpha\right) \tag{4.19}$$

The function $P(\alpha, \sigma_\alpha)$ of equation 4.18 is normalized as $\int_{-\infty}^{+\infty} P(\alpha, \sigma)\, d\alpha = 1$ which is in contradiction with the normalization condition 4.17. Thus, in this case, it is necessary to introduce an artificial weighting factor to account for the difference between the two normalizations.

Cook and Torrance have corrected the original Torrance-Sparrow hypothetical distribution so that it is normalized according to the expression 4.17, thus avoiding the need of including arbitrary normalization factors [166]. They arrived to the following equation:

$$P_{CT}(\alpha, m) = \frac{1}{\pi m^2 \cos^4 \alpha} \exp\left(-\frac{\tan^2 \alpha}{m^2}\right) \tag{4.20}$$

where m ($m \simeq \sqrt{2}\sigma$) represents the roughness of the surface. For low values of roughness the Cook-Torrance and Torrance-Sparrow distributions are similar apart from a factor of $\sqrt{\pi}$.

The Trowbridge-Reitz distribution

The Trowbridge-Reitz formulation ([164]) assumes that the surface is composed by an ensemble of micro-areas randomly oriented and randomly curved. This ensemble can be represented by an average ellipsoid surface irregularity optically smooth surface symmetric relatively to the macro-surface normal. This average surface should have the effect of reflecting the radiation in the same direction as the original rough surface, thus producing the same reflection distribution . Therefore, the surface profile can be represented by a large number of small identical average irregularities.

For the average irregularity Trowbridge and Reitz have proposed an ellipsoid of revolution or spheroid (see figure 4.7). The two semi-axis of this spheroid are coplanar with the average plane of the surface and and have the same length.

The distribution of heights of the spheroid is given statistically by (see fig. 4.7)

$$\frac{h^2}{a^2} + \frac{r^2}{b^2} = 1 \quad \text{i.e.} \quad h = \pm a \sqrt{\left(1 - \frac{r^2}{b^2}\right)} \tag{4.21}$$

$r = \sqrt{x^2 + y^2}$ corresponds to the radius of the spheroid over the plan. The following relation holds between α and the ellipsoid parameters,

$$-\frac{dh}{dr} = \tan \alpha \tag{4.22}$$

4. MODELLING THE REFLECTION
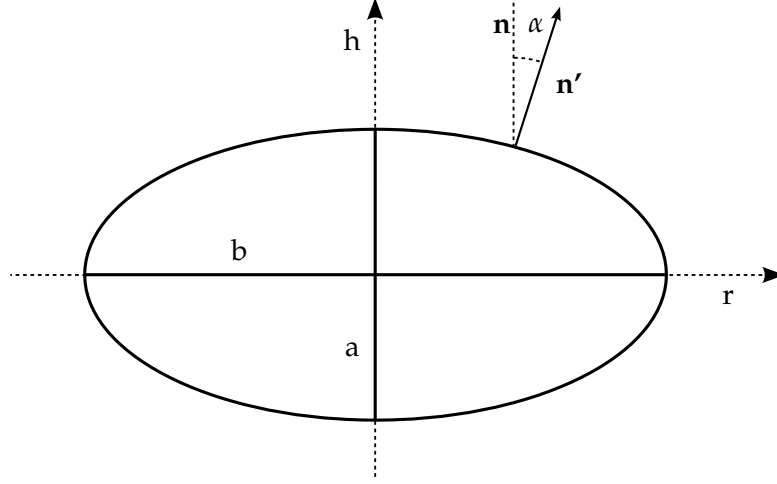
Figure 4.7: The average surface irregularity used in the Trowbridge-Reitz-Model is given by an ellipsoid of revolution with semi-axis a and b.

The two solutions in the equation 4.21 correspond to convex (+ sign) and concave (-sign) surfaces with the same probability distribution for the angle α. The computation of the probability-distribution function of the angle α for the height distribution function of the equation 4.21 results in [164]

$$P_{\text{TR}}(\alpha, \gamma) = \frac{\gamma^2}{\pi \left(\gamma^2 \cos^2 \alpha + \sin^2 \alpha\right)^2} \tag{4.23}$$

The parameter $\gamma = a/b$ is the oblateness of the surface and it corresponds to the ratio between the semi-axis of the ellipsoid, for $\gamma = 1$ we would have a sphere. It should be stressed that the function 4.23 is sole dependent of the shape parameter γ and not of the size of the spheroid. The parameter γ controls the width of the distribution, when this parameter increases the spheroid becomes more prolate and the roughness of the surface increases. The table I shows typical values for the γ for some common materials measured by [164].

The function 4.23 is correctly normalized according to the condition 4.17 thus the values given by this distribution are absolute. This function resembles a Cauchy-Lorentz distribution with $\gamma \simeq \Gamma$. Figure 4.8 compares this distribution function with the corresponding function of Cook and Torrance referred to above. As shown the Trowbridge-Reitz function has a more pronounced peak and larger tails in comparison to the Cook-Torrance function distribution.

The shape used by Trowbridge-Reitz is very similar to the shape of biological cells, thus this function is useful for the modelling of the reflection from that type of surfaces. It has been used specifically to modelling the reflection from leaves and bark and also of the stratum corneum cells of the human skin [167].

Table I: Value for the oblateness of the roughness for some materials.

	γ
Concrete cement	0.5-1.0
Semi-glossy dark paint	0.05-0.1
Wood	0.5
Grass	1.6

(values taken from Trowbridge and Reitz, 1965 [164].)
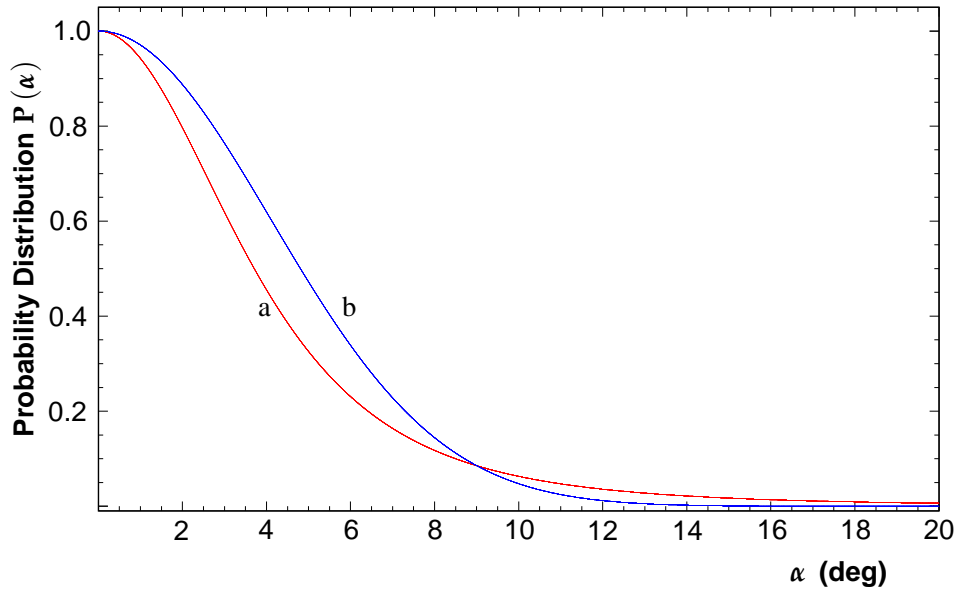
Figure 4.8: Comparison between the micro-facet distributions of Trowbridge-Reitz (a) and of Cook-Torrance (b), for a roughness $m = \gamma = 0.1$ respectively. They are both normalized to $P\left(\alpha = 0\right) = 1$. As can be seen the Trowbridge-Reitz function function has longer tails producing larger angles of scattering.

4.3 The Scattering of Electromagnetic Waves at a Rough Surface

The inhomogeneities of the surface are randomly distributed and are described by the probabilities distribution of heights, slopes or the correlation function as discussed above as discussed above. Thus, the scattering of an electric field in the surface will be a

4. MODELLING THE REFLECTION

probabilistic problem. This problem is usually treated for a conductor/dielectric interface. In this case the light cannot be transmitted from the dielectric into the conductor and the electric field can be approximated to zero at the surface. We are, however, interested in solving the scattering of an electromagnetic wave for a dielectric/dielectric interface.

The scattering equations

When an electromagnetic wave arrives at the surface that separates two different media it will be either scattered back or transmitted into the new medium. The general expression for the scattered field E^{scat} is generally obtained by solving the Maxwell equations for a space free of charges and currents at the surface, satisfying the appropriate Dirichelet and Neumann boundary conditions .

Let it be an electromagnetic plane wave propagating thought a specific medium, monocromatic and defined by the following scalar

$$E_0 = \exp\left[(\mathbf{k}_i \cdot \mathbf{r} - \omega t)\right] \tag{4.24}$$

whose wave vector is $\mathbf{k_i}$ arriving at the point B defined by the vector $\mathbf{r}'$, at the surface (see figure 4.9). The surface between the two media is rough by hypothesis. The media are both considered homogeneous and isotropic and to have different indexes of refraction n_0 and n. The directions of reflectance and transmittance are given by the wave vectors $\mathbf{k}_r$ and $\mathbf{k}_t$. Using the coordinate system defined in the figure 4.9 the wave vectors are defined by:

$$\mathbf{k}_i \quad = \quad \frac{2\pi n_0}{\lambda}\left(\sin\theta_i\cos\phi_i\hat{\mathbf{e}}_\mathbf{x} + \sin\theta_i\sin\phi_i\hat{\mathbf{e}}_\mathbf{y} - \cos\theta_i\hat{\mathbf{e}}_\mathbf{z}\right) \tag{4.25a}$$

$$\mathbf{k}_r \quad = \quad \frac{2\pi n_0}{\lambda}\left(\sin\theta_r\cos\phi_r\hat{\mathbf{e}}_\mathbf{x} + \sin\theta_r\sin\phi_r\hat{\mathbf{e}}_\mathbf{y} + \cos\theta_r\hat{\mathbf{e}}_\mathbf{z}\right) \tag{4.25b}$$

$$\mathbf{k}_t \quad = \quad \frac{2\pi n}{\lambda}\left(\sin\theta_t\cos\phi_t\hat{\mathbf{e}}_\mathbf{x} + \sin\theta_t\sin\phi_t\hat{\mathbf{e}}_\mathbf{y} - \cos\theta_i\hat{\mathbf{e}}_\mathbf{z}\right) \tag{4.25c}$$

where n_0 is the index of refraction of the first medium, n the index of refraction of the second medium and λ corresponds to the wavelength of the light in vacuum. The angles θ_i, θ_r and θ_t are those of figure 4.9 and ϕ_i, ϕ_r and ϕ_t the respective azimuthal angles.

The roughness is described by the height function $h(x,y)$. A point in the space (x,y,z) belongs to the medium 0 if $z > h(x,y)$ and to medium 1 if $z < h(x,y)$.

In what follows we consider the radiation to be monochromatic and unpolarized.

In both sides of the surface the Helmholtz equation holds [168]:

$$\nabla^2 E\left(\mathbf{r}\right) + k_0^2 E\left(\mathbf{r}\right) \quad = \quad 0, \quad z > h\left(x,y\right) \tag{4.26a}$$
$$\nabla^2 E\left(\mathbf{r}\right) + k^2 E\left(\mathbf{r}\right) \quad = \quad 0, \quad z < h\left(x,y\right) \tag{4.26b}$$

where $k_0 = \frac{2\pi n_0}{\lambda}$ and $k = \frac{2\pi n}{\lambda}$, and $E(\mathbf{r})$ corresponds to the electric field in a specific point of the space defined by the vector $\mathbf{r}$. We are mainly focused in the reflection mode, thus only the first equation will be considered. The calculation of the transmitted field is however similar and can be found here [168, 169].

The application of the Maxwell equations to the surface results in the following Dirichlet and Neumann boundary conditions, respectively

$$E(\mathbf{r})\,|_{z=h^+(x,y)} \;=\; E(\mathbf{r})\,|_{z=h^-(x,y)} \tag{4.27a}$$

$$\left[\frac{\partial E(\mathbf{r})}{\partial \mathbf{n}'}\right]_{z=h^+(x,y)} \;=\; \left[\frac{\partial E(\mathbf{r})}{\partial \mathbf{n}'}\right]_{z=h^-(x,y)} \tag{4.27b}$$

with h^+ and h^- representing the surface function when approached from above or from below the surface, respectively. $\mathbf{n}'$ is the outward normal to the surface given by

$$\mathbf{n}' = \gamma^{-1}\left(-h'_x\hat{\mathbf{e}}_\mathbf{x} - h'_y\hat{\mathbf{e}}_\mathbf{y} + \hat{\mathbf{e}}_\mathbf{z}\right) \tag{4.28}$$

where $h'_x = \frac{\partial h(x,y)}{\partial x}$, $h'_y = \frac{\partial h(x,y)}{\partial y}$ and $\gamma = \sqrt{1 + (h'_x)^2 + \left(h'_y\right)^2}$. The derivatives $\frac{\partial}{\partial \mathbf{n}'} = \mathbf{n}' \cdot \nabla$.

The Helmholtz equation is solved by using the Green's theorem yielding the following result [146, 170]

$$E(\mathbf{r}) = \frac{1}{4\pi}\oint_S \mathrm{d}S\left[G(\mathbf{r},\mathbf{r}')\,\nabla E(\mathbf{r}') - E(\mathbf{r}')\,\nabla G(\mathbf{r},\mathbf{r}')\right] \tag{4.29}$$

G is the Green function satisfying the same continuity requirements ad the field E and $\mathbf{r}'$ points to any point in the surface. The closed surface S is the limiting surface of the volume in the upper plane V_0 and can divided in two parts, the upper half sphere of infinite radius S^∞ and the rough surface S' described by the roughness function $z = h(x,y)$

$$\oint_S \mathrm{d}S = \int_{S^\infty} \mathrm{d}S^\infty + \int_{S'} \mathrm{d}S' \tag{4.30}$$

The integral in S^∞ results in the incident field $\mathbf{E}_0$. Thus we have for the total field

$$E(\mathbf{r}) = E_0(\mathbf{r}) + \frac{1}{4\pi}\int_{S'} \mathrm{d}S'\left[G(\mathbf{r},\mathbf{r}')\frac{\partial E(\mathbf{r}')}{\partial \mathbf{n}'} - E(\mathbf{r}')\frac{\partial G(\mathbf{r},\mathbf{r}')}{\partial \mathbf{n}'}\right] \tag{4.31}$$

where the integral term of the equation 4.31 corresponds to the scattered field E^{scat}. In a perfect conductor the electric field in the surface is zero $E(\mathbf{r}') = 0$ and only the second term of the integral remains. However this approximation is not suitable for the case of dielectric-dielectric interfaces.

The Green's function is usually represented by a spherical wave [171]:

$$G(\mathbf{r},\mathbf{r}') = \frac{\exp(ik_0|\mathbf{r} - \mathbf{r}'|)}{4\pi|\mathbf{r} - \mathbf{r}'|} \tag{4.32}$$

4. MODELLING THE REFLECTION
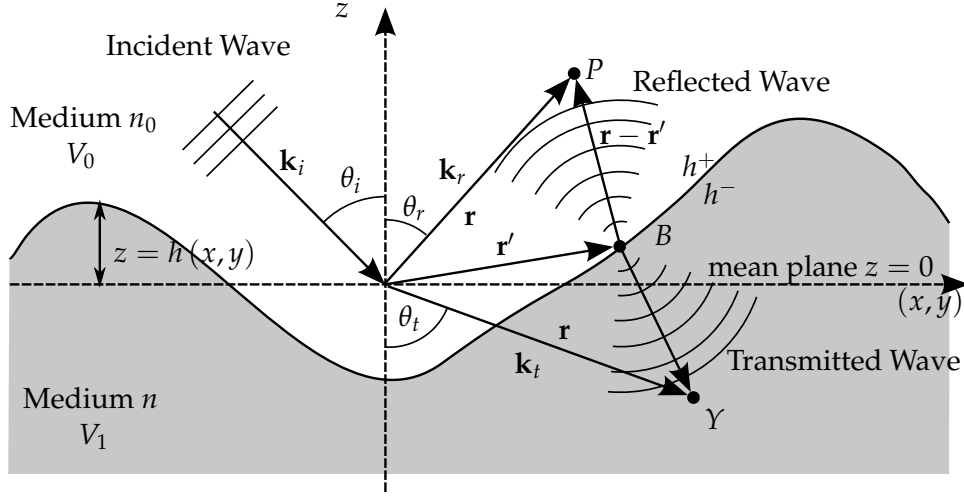
Figure 4.9: System of coordinates used to derive the intensity of the scattered waves (transmitted and reflected).

Given that the spherical light is measured at a great distance from the surface (in comparison with λ) thus the far field approximation ($k_0 \mathbf{r} \gg 1$), or the Fraunhofer diffraction limit, is valid and the following approximation holds [172]

$$\frac{\exp\left(ik_0|\mathbf{r}-\mathbf{r}'|\right)}{|\mathbf{r}-\mathbf{r}'|} \simeq \frac{\exp\left(ik_0\sqrt{r^2+r'^2-2\mathbf{r}\cdot\mathbf{r}'}\right)}{r} \simeq \frac{\exp\left(ik_0 r - i\mathbf{k}_r \cdot \mathbf{r}'\right)}{r} \tag{4.33}$$

the derivative of the Green function is given by:

$$\frac{\partial G\left(\mathbf{r},\mathbf{r}'\right)}{\partial \mathbf{n}'} = \mathbf{n}' \cdot \nabla G\left(\mathbf{r},\mathbf{r}'\right) = -i\mathbf{n}' \cdot \mathbf{k}_r \frac{\exp\left(ik_0 r - i\mathbf{k}_r \cdot \mathbf{r}'\right)}{r} \tag{4.34}$$

thus we have for the scattered electric field,

$$E^{\text{scat}} = \frac{\exp\left(ik_0 r\right)}{4\pi r} \int_{S'} dS' \left\{ \left[i\mathbf{k}_r \frac{\partial \mathbf{r}'}{\partial \mathbf{n}'} \right] E\left(\mathbf{r}'\right) + i\frac{\partial E\left(\mathbf{r}'\right)}{\partial \mathbf{n}'} \right\} \exp\left(-i\mathbf{k}_r \cdot \mathbf{r}'\right) \tag{4.35}$$

where r is the magnitude of the vector $\mathbf{r}$.

The Kirchhoff approximation

The integral in eq. 4.35 cannot be solved analytically in most cases due the complexity of the function $h\left(x,y\right)$. It is however possible to solve this integral numerically [158, 173], these methods provide rigorous solution. However these methods are computationally expensive in time and memory and more practical approximations to the integral are usually performed. One solution is to use a perturbation approach [174].

4.3 The Scattering of Electromagnetic Waves at a Rough Surface

In this method the reflected field is the sum of the solution from a smooth surface plus a small perturbation due to the roughness effect. This approach is however restricted to smoother surfaces.

Another more convenient approximation is the Kirchhoff approximation also known as the tangent plane approximation. This approximation assumes that each point of the surface has the same optical properties of its tangent plan defined by the local normal $\mathbf{n}'$ [175]. Thus, the scattered field is given by the sum of the reflected field originating at each local plane as given by the Fresnel equations. This approximation requires the radius of curvature of the roughness to be small enough in comparison with the wavelength of the light, thus requiring the surface to be locally flat. Assuming as above that the incident field is plane wave, $E_0(\mathbf{r}') = \exp(i\mathbf{k}_i \cdot \mathbf{r}')$, then the field and field derivatives $(\partial E(\mathbf{r}')/\partial \mathbf{n}')$ are given by [176]:

$$E(\mathbf{r}') = E_0(\mathbf{r}') + E^{\text{scat}}(\mathbf{r}') = (1+R)\exp(i\mathbf{k}_i \cdot \mathbf{r}') \tag{4.36a}$$

$$\frac{\partial E(\mathbf{r}')}{\partial \mathbf{n}'} = \frac{\partial E_0(\mathbf{r}')}{\partial \mathbf{n}'} + \frac{\partial E^{\text{scat}}(\mathbf{r}')}{\partial \mathbf{n}'} = i\mathbf{n}' \cdot \mathbf{k}_i (1-R)\exp(i\mathbf{k}_i \cdot \mathbf{r}') \tag{4.36b}$$

where $R = E/E_0$ is proportional to the amplitude of the reflected electromagnetic field, as given by the Fresnel equations, for unpolarized light. This factor has to be calculated at every local tangent plane to obtain the reflected wave [169]. A similar approximation can be performed for the transmitted wave [177].

Inserting 4.36a and 4.36b into the equation 4.35 we obtain for the scattered field [171]

$$E^{\text{scat}}(\mathbf{r}) = \frac{i\exp(iik_0 r)}{4\pi r} \int_{S'} dS' \left[(1-R)\mathbf{k}_i + (1+R)\mathbf{k}_r\right] \cdot \mathbf{n}' \exp(i\mathbf{k} \cdot \mathbf{r}') \tag{4.37}$$

where $\mathbf{k} = \mathbf{k_i} - \mathbf{k_r}$ is the variation of the wave vector after reflection [178] (see equations 4.25)

$$\mathbf{k} = k_0 \left\{ (\sin\theta_i \cos\phi_i - \sin\theta_r \cos\phi_r)\,\hat{\mathbf{e}}_\mathbf{x} + (\sin\theta_i \sin\phi_i - \sin\theta_r \sin\phi_r)\,\hat{\mathbf{e}}_\mathbf{y} - \right. $$
$$\left. (\cos\theta_i + \cos\theta_r)\,\hat{\mathbf{e}}_\mathbf{z} \right\} \tag{4.38}$$

In the small slopes approximation the local normal of the surface $\mathbf{n}'$ not far from the global normal ($\alpha \simeq 0$, $h'_x \simeq 0$ and $h'_y \simeq 0$). Hence, in this approximation we can define the following identity

$$\mathcal{F}(\mathbf{n}', \mathbf{k}_i, \mathbf{k}_r) = \left[(1-R)\mathbf{k}_i + (1+R)\mathbf{k}_r\right] \cdot \mathbf{n}' \tag{4.39}$$

which can be approximated to $\mathcal{F}(\mathbf{n}, \mathbf{k}_i, \mathbf{k}_r)$. The integral 4.37 is then given by

$$E^{\text{scat}}(\mathbf{r}) = \frac{i\exp(ik_0 r)}{4\pi r} \mathcal{F} \int_{S'} dS' \exp[i\mathbf{k} \cdot \mathbf{r}] \tag{4.40}$$

which gives the field reflected wave in a more manageable form.

4. MODELLING THE REFLECTION

The intensity of the electromagnetic field

The roughness of the surface means that the electric field **E** scattered at the surface will be correlated with its roughness. The electric is a random function of the position and is given by an average field $\langle E \rangle$, the so called coherent field, plus a fluctuating field F usually referred to as the incoherent field [177]:

$$E(\mathbf{r}) = \langle E \rangle + F(\mathbf{r}) \tag{4.41a}$$

$$\langle F(\mathbf{r}) \rangle = 0 \tag{4.41b}$$

The coherent field contributes only in the specular direction whereas the incoherent field contributes in all directions. In the limiting case of a flat surface the scattered intensity consists only in the coherent field.

The intensity of the scattered electromagnetic wave field is $I = E(\mathbf{r}) E^*(\mathbf{r})$. We have

$$EE^* = \langle E \rangle \langle E^* \rangle + \langle E \rangle F^* + \langle E^* \rangle F + FF^* \tag{4.42}$$

The average intensity can be written as the sum of the coherent and incoherent contributions

$$\langle I \rangle = I_C + I_D \tag{4.43a}$$

$$I_C = \frac{\epsilon}{2} |\langle E \rangle|^2 \tag{4.43b}$$

$$I_D = \frac{\epsilon}{2} \langle |F|^2 \rangle = \frac{\epsilon}{2} \langle |E|^2 \rangle - \frac{\epsilon}{2} |\langle E \rangle|^2 \tag{4.43c}$$

The factor $\frac{\epsilon}{2}$ will be further omitted for convenience.

The coherent reflection

The integral 4.40 will be computed over a rectangular region with dimensions A and B in x and y respectively. The product $\mathbf{k} \cdot \mathbf{r}$ can be written as $\mathbf{k} \cdot \mathbf{r} = k_x x + k_y y + k_z h(x, y)$, thus we have for the integral in equation 4.40

$$J \equiv \int_{S'} dx dy \exp\left[ik_x x + ik_y y\right] \exp\left[ik_z h(x, y)\right] \tag{4.44}$$

The average field of the illuminated area is given by

$$\langle E \rangle = \frac{i \exp(ik_0 r)}{4\pi r} \langle J \rangle \tag{4.45}$$

The surface is supposed to be isotropic thus the average does not depend of the coordinates x and y being only performed in z, thus,

$$\langle J \rangle = \int_{S'} dx dy \exp(ik_x x + ik_y y) \langle \exp[ik_z h(x, y)] \rangle \tag{4.46}$$

The average in the integral corresponds to the characteristic function of $h(x,y)$, which is determined by the probability distribution function. Thus [176]

$$\chi_1 \equiv \langle \exp(ik_z h(x,y)) \rangle = \int_{-\infty}^{\infty} dz P_z(z) \exp(ik_z z) \tag{4.47}$$

which means that χ_1 is in fact the inverse Fourier transform of the probability distribution function, P_z [178].

Assuming that the dimensions of the illuminated area S are much larger than the wavelength of the light λ we have [1]

$$\langle J \rangle = \chi_1 4\pi^2 \delta(k_x) \delta(k_y) \tag{4.48}$$

Therefore[2]

$$\langle |J| \rangle^2 = 4\pi^2 S |\chi_1|^2 \delta(k_x) \delta(k_y) \tag{4.49}$$

where S is the illuminated area. Both k_x, k_y were defined in equation 4.38. The delta functions can be put in the form [176] [3]

$$\delta(k_x) \delta(k_y) = \frac{\delta(\theta_i - \theta_r) \delta(\phi_r)}{k_0^2 \sin\theta_i \cos\theta_i} \tag{4.50}$$

Therefore, the coherent field intensity is given by

$$I_C = \frac{(\exp(ik_0 r))^2 \mathcal{F}^2}{16\pi^2 r^2} \langle |J| \rangle^2 = \frac{|E_0|^2}{4r^2} S \mathcal{F}^2 |\chi_1|^2 \frac{\delta(\theta_i - \theta_r) \delta(\phi_i - \phi_r)}{k_0^2 \sin\theta_i \cos\theta_i} \tag{4.51}$$

where $|E_0|^2 = (\exp(ik_0 r))^2$ corresponds to the intensity of the incident field.

The coefficient $\mathcal{F}^2$ can further simplified. At the specular direction $\theta_i = \theta_r$ and $\phi_i = \phi_r$ and thus $\mathbf{k}_i = \frac{2\pi}{\lambda}(\sin\theta_i \hat{\mathbf{e}}_x + -\cos\theta_i \hat{\mathbf{e}}_z)$ and $\mathbf{k}_r = \frac{2\pi}{\lambda}(\sin\theta_r \hat{\mathbf{e}}_x + \cos\theta_r \hat{\mathbf{e}}_z)$ then we have:

$$\mathcal{F}^2 = 4k_0^2 R^2 \cos^2\theta_i \tag{4.52}$$

R^2 corresponds to the factor F defined in the equations 4.8a and 4.8b. Finally

$$I_C = \frac{(\exp(ik_0 r))^2 \mathcal{F}^2}{16\pi^2 r^2} \langle J \rangle^2 = \frac{(\exp(ik_0 r))^2}{r^2} S \cos\theta_i F \Lambda \frac{\delta(\theta_i - \theta_r) \delta(\phi_r)}{\sin\theta_i} \tag{4.53}$$

where $\Lambda = |\chi_1|^2$ corresponds to the relative intensity of the specular spike. We conclude from the above equations that the average field is only observed at the specular direction where the reflected waves are all in phase. This is in fact the specular spike that is observed in the data.

---

[1]The identity $\delta(x) = \frac{1}{2\pi} \int_{-\infty}^{+\infty} \exp(ixu) du$ was used

[2]where we have $\frac{1}{2\pi} \int_{x_{\min}}^{x_{\max}} dx \exp(ik_x) \delta(k_x) = (x_{\min} - x_{\max}) \delta(k_x)$ and $\frac{1}{2\pi} \int_{y_{\max}}^{y_{\min}} dy \exp(ik_y) \delta(k_y) = (y_{\max} - y_{\min}) \delta(k_y)$

[3]Note that $\delta(g(x)) = \sum \frac{1}{|g'(x)|} \delta(x - x_i)$ with $g(x_i) = 0$

4. MODELLING THE REFLECTION

The intensity of the coherent field needs to be related with the radiometric quantities, namely the bidirectional reflectance function ϱ_C (appendix A) The function ϱ_C is given by (equation A.14)

$$\varrho_C = \frac{d\Phi_r}{d\Omega\Phi_i} \tag{4.54}$$

where Φ_i is the light flux impinging on the surface that is given by

$$\Phi_i = |E_0|^2 S \cos\theta_i \tag{4.55}$$

and $S\cos\theta_i$ corresponds to the projected viewing area of the surface.

The Dirac delta function can be written as[1][179]

$$\delta\left(\mathbf{r} - \mathbf{i}'\right) = \frac{1}{r^2 \sin\theta_i}\delta\left(\theta - \theta'\right)\delta\left(\phi_i - \phi_r\right) \tag{4.56}$$

$\mathbf{i}'$ corresponds to the symmetric vector of $\mathbf{i}$ relative to the plane defined by the surface. It is given by $\mathbf{i}' = \mathbf{i}_\parallel - \mathbf{i}_\perp = \mathbf{i} - 2\left(\mathbf{i}\cdot\mathbf{n}\right)\mathbf{n}$.

Thus we arrive at the following BRIDF function

$$\varrho = F\left(\theta_i; n, \kappa\right)\Lambda\left(\theta_i; \lambda, \sigma_h\right)\delta\left(\mathbf{r} - \mathbf{i}'\right) \tag{4.57}$$

where the delta function ensures that this component is present only at the specular direction.

The intensity of the coherent reflection is decreased by a factor Λ relative to the corresponding perfectly polished surface. This factor is dependent of the height distribution function P_z of the surface. Usually, a gaussian distribution (equation 4.13b) is assumed for the probability distribution function P_z. In such a case, it can be shown that

$$\Lambda = \exp\left\{-g\right\} \quad \text{with} \quad g = \left(\frac{4\pi n_0 \sigma_h \cos\theta_i}{\lambda}\right)^2 \tag{4.58}$$

thus the intensity of the specular spike decreases when the decreasing of the wavelength of the incident light. Therefore, in the rare gaseous scintillation detectors a surface appears to be rougher than if it is illuminated with visible light. The description of the roughness of the surface can be consequently an important issue. The intensity of the specular spike is also dependent of the angle of incidence θ_i. If the angle of incidence is increased the surface looks more polished.

---

[1]If the set of coordinates of $\mathbf{u}$ is related with the cartesian coordinates via $u_i = u_i\left(x_1, x_2, ..., x_n\right)$ with $i = 1, ..., n$ then we have for the delta function

$$\delta(\mathbf{x} - \mathbf{x}') = \frac{1}{J}\delta\left(\mathbf{u} - \mathbf{u}'\right)$$

J is the jacobian given by $J = \det\left[\frac{\partial x_i}{\partial u_i}\right]$

When the surface is illuminated at the normal incidence ($\cos \theta_i = 1$), the intensity of the specular spike is reduced to

$$\Lambda = \exp\left(-g\right) = \exp\left[-\left(\frac{4\pi n_0 \sigma_h}{\lambda}\right)^2\right] \tag{4.59}$$

This equation is known as the total integrated scatter (TIS) formula and it is used as a standard method to measure the roughness of a metal [180, 181, 182].

In many situations the height distribution of the surface does not follow a gaussian distribution function P_z. It generally depends how the surface has been produced. The assumption that the distribution function is exponential is also common and written as

$$P_z = \frac{1}{\sqrt{2}\sigma_h} \exp\left(-\frac{\sqrt{2}\,|z|}{\sigma_h}\right) \tag{4.60}$$

For this distribution the characteristic function Λ can now be computed [186]

$$\Lambda = \left[\frac{1}{(1+g/2)^2}\right]^2 \tag{4.61}$$

where g follows the same definition of the equation 4.58.

The coherent transmission

The intensity of the transmitted coherent field is computed in a similar manner as for the reflected component. For a gaussian distribution, P_z, the intensity of the transmitted coherent field is given by [171, 176]

$$I_C^{(t)} = F \exp\left[-\left(\frac{4\pi}{\lambda}\cos\theta_i\sigma_h\left(n - n_0\right)\right)^2\right] \tag{4.62}$$

this equation is very similar to the equation of the reflected field with the index of refraction of the first medium replaced by the difference between indices of refraction. For the majority of interfaces of interest we have $(n - n_0) < n_0$, therefore the relative contribution of the coherent transmission relativelly to the transmitted light will be larger than the relative contribution of the coherent reflection for the reflected light, i.e. the effect of the roughness will be smaller for the transmitted wave.

The incoherent intensity

The intensity of the incoherent field I_D is computed through the equation

$$I_D = \frac{|E_0|^2}{16\pi^2 r^2}\mathcal{F}^2\left(\left\langle|J|^2\right\rangle - |\langle J\rangle|^2\right) \tag{4.63}$$

4. MODELLING THE REFLECTION

the $|\langle J\rangle|^2$ was computed previously and is given by the equation 4.48. The term $\langle |J|^2\rangle$ requires the introduction of the correlation function $C(r)$.

The derivation of the intensity of the incoherent field is not shown explicitly here, however it can be found in [176, 183, 184, 185]. We only show the expression for the coherent intensity/specular lobe when the surface is described by both a gaussian distribution function of heights and a gaussian correlation function. The reader can find more details in [187]. Therefore we have for the specular lobe

$$\varrho_S = \frac{1}{4\cos\theta'}\exp\left(-g\right)FDPG \tag{4.64}$$

were g is given by the equation 4.58 with $4\cos\theta_i$ replaced by $2\left(\cos\theta_i + \cos\theta_r\right)$, F is the Fresnel factor. P is given by the following geommetric series and D is a geometric factor

$$P = \frac{\pi^2 T^2}{4\lambda^2}\sum_{m=1}^{\infty}\frac{g^m}{m!m}\exp\left[-\left(k_x^2 + k_y^2\right)T^2/4m\right] \tag{4.65a}$$

$$D = \frac{1}{\cos^4\alpha}\left(\cos\theta_i + \cos\theta_r\right)^2 \tag{4.65b}$$

where T corresponds to the correlation length, defined in 4.12b. G corresponds to the shadowing-masking term, the nature of this term will be discussed in 4.4.

Using the local coordinates defined in section 4.2 the equations 4.65a and 4.65b can be written as

$$DP = \frac{\varsigma}{\pi\cos^4\alpha}\sum_{m=1}^{\infty}\frac{g^m}{m!m}\exp\left[-\tan^2\left(\alpha\right)\varsigma/m\right] \tag{4.66}$$

where the function ς is the effective correlation given by:

$$\varsigma = \left(k_0\frac{T}{2}\left[\cos\theta_i + \cos\theta_r\right)\right]^2 \tag{4.67}$$

The coherent field for the Trowbridge-Reitz surface profile

In the original paper of Trowbridge-Reitz [164] no coherent component was considered, the calculations are shown below.

In the Trowbridge-Reitz function the height distribution is defined *a priori*, thus the intensity of the specular spike can be computed using the average function defined in the equation 4.47. This average function can be expanded in the following sum of integrals

$$\Lambda = \left|\frac{1}{S}\int_S \exp\left[ik_z h(x)\right]dxdy\right|^2 = \left|\frac{1}{S}\int_S \cos\left[k_z h(x)\right]dxdy\right|^2 + \left|\frac{1}{S}\int_S \sin\left[k_z h(x)\right]dxdy\right|^2 \tag{4.68}$$

where S is the assembled area and $S \gg k_z h\left(x,z\right)$. For symmetric profiles, the second integral is zero.

Table II: Statistical properties for surfaces described by a spheroid (ellipsoid of revolution) and a elliptic cylinder.

		Spheroid	Elliptic cylinder
Average height $\langle |h| \rangle$	A_h	(2/3)a	$(\pi/4)$a
Root mean square	σ_h	0.235a	0.224a
Skewness	S_h	-0.58	-1.14
Kurtosis	K_h	2.4	3.5

Let us consider the height distribution defined by Trowbridge-Reitz

$$h(r) = \pm a \sqrt{\left(1 - \frac{r^2}{b^2}\right)} \tag{4.69}$$

One important feature of this profile is that it has concave and convex shape according to the sign $\pm$. This profile is dependent of r, which is a cylindrical coordinate $r^2 = x^2 + y^2$, thus the differential $dxdy$ should be replaced by rdr.

This integral was solved numerically for different dimensions of the axis of the spheroid, a and b[1]. However, we observed that the intensity of the specular spike (Λ) was independent of b, thus it is independent of the shape of the spheroid. The results for Λ are shown in the dashed curve in the figure 4.10, as function of $4\pi a/\lambda$. The results show that the intensity of the specular spike is a periodic function of the dimension of the oblate. This periodicity is a consequence of the imposition of a upper and lower limit to the height distribution function.

Many materials are composed by ellipsoids that are packed together producing an asymmetric surface profile. This is especially true for biological materials such the leaves or the human skin. In this situation, only the upper level of the spheroid is visible and used in for the reflection of the light. We will call to this surface hemispheroid. The height distribution of this surface is given by

$$h(r) = a \sqrt{\left(1 - \frac{r^2}{b^2}\right)} - \frac{2}{3}a \tag{4.70}$$

the second term forces the condition $\langle h(x) \rangle = 0$. The relevant statistical properties of this distribution are displayed in the table II. We observe that the standard deviation of the height distribution 4.70 is only dependent of the axis a of the hemispheroid. The skewness of the surface is independent of a and b, the value is negative meaning that

---

[1]a is collinear with the axis of revolution of the spheroid.
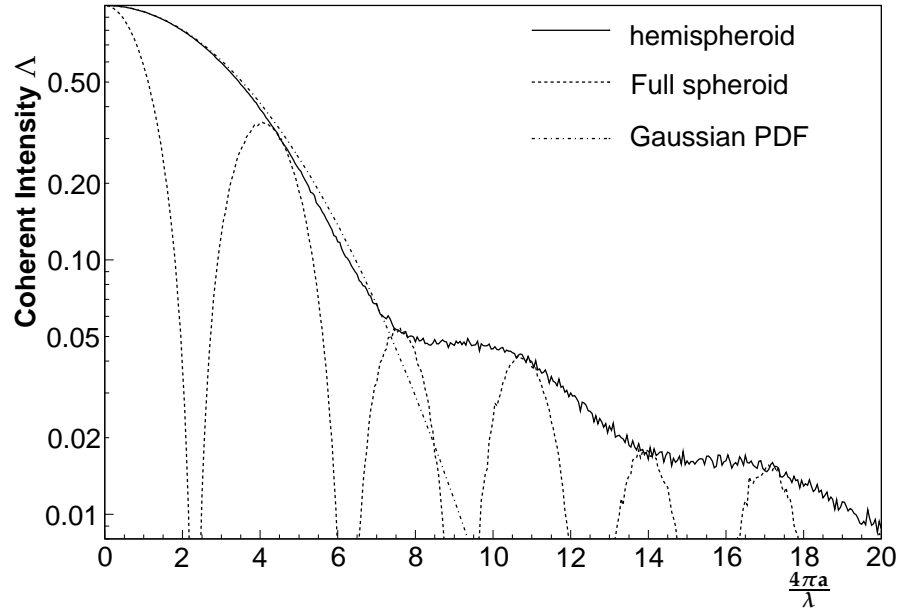
Figure 4.10: Intensity of the specular spike component as function of $4\pi a/\lambda$ for the spheroid surface. For the gaussian PDF it is used the root mean square shown in the table II.
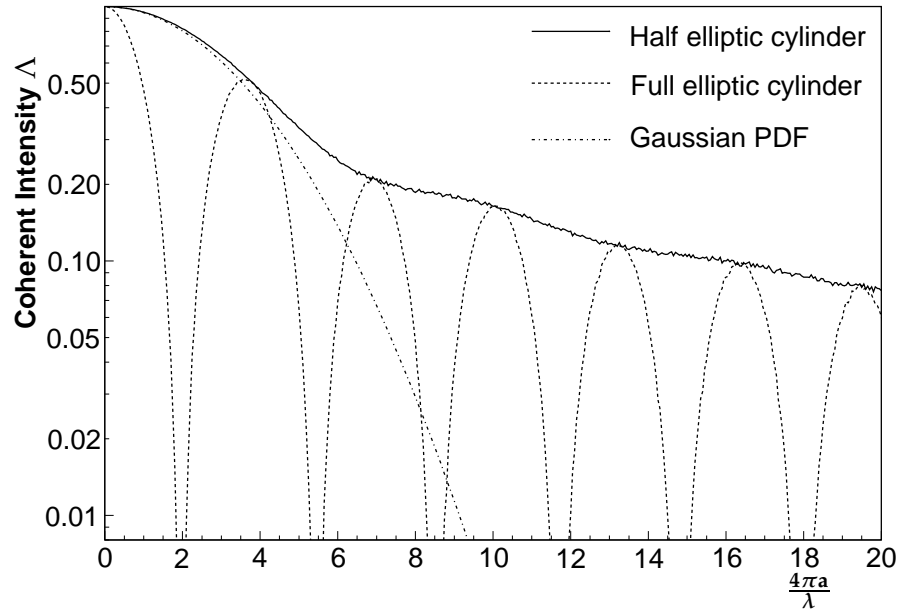
Figure 4.11: Intensity of the specular spike component as function of $4\pi a/\lambda$ for the elliptic cylinder surface. For the gaussian PDF it is used the root mean square shown in the table II.
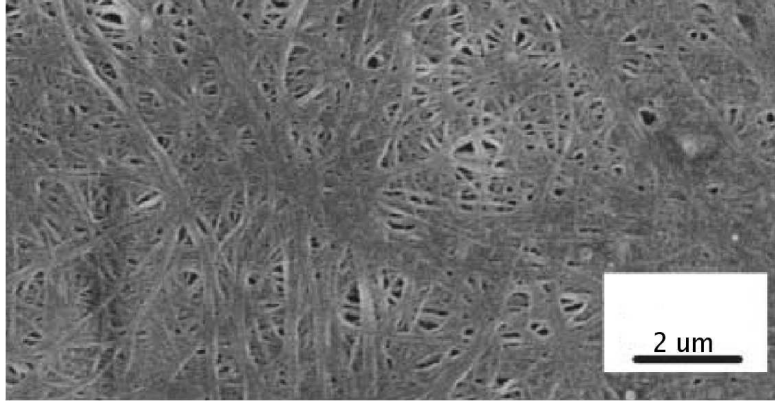
Figure 4.12: SEM Image of a non polished PTFE [188].

we have a larger dispersion for the points of the surface below the average plan. Due to the asymmetry of the height distribution the sine integral in the equation 4.68 is not zero and should also be computed. In fact this term removes the periodicity observed with the equation 4.69.

The intensity of the specular spike for the functions 4.70 is shown in the figure 4.10 and compared with the intensity predicted by the full spheroid. It is also shown the intensity of the specular spike for a gaussian distribution P_h (equation 4.58) with $\sigma_h = 0.235a$ (see table II). The intensity of the specular spike predicted for the gaussian probability distribution function P_h is the same of the hemispheroid for $\Lambda > 0.05$. Below this value the intensity for the hemispheroid decreases slowly with $4\pi a / \lambda$.

The image 4.12 (see section 4.2) shows the surface of the PTFE viewed by a SEM microscope. This image shows that the PTFE has a fibrous nature. This fact suggests that the modelling of the surface by a elliptic cylinder should also be considered. As before, only the upper part of the curve is able to reflect the light, thus the height function with the axis parallel to the surface is given by

$$h(x) = a\sqrt{\left(1 - \frac{x^2}{b^2}\right)} - a\frac{\pi}{4} \tag{4.71}$$

the spherical coordinate r is replaced by x and the integration performed in $\mathrm{d}x$ instead of $r\mathrm{d}r$. The statistical properties of this profile are shown in the table II. This surface profile has a larger negative skewness (i.e. the height function is more assimetric) and a larger kurtosis than the spheroid.

The intensity of the coherent field predicted by the elliptic cylinder and half elliptic cylinder is shown in 4.11. Λ is in general larger for the elliptic cylinder than the spheroid. A significant amount of coherent reflection is observed even for large dimensions of the elliptic cylinder.

The Kirchhoff approximation that was used to obtain these results is only valid when the radius of curvature of the surface r_c is larger than the wavelength of the incident light. In the spheroid and in the elliptic cylinder, the maximum radius of curvature of the surface is obtained at $h(x) = 0$ or $h(r) = 0$ where the radius of curvature is $r_c = a$. Thus the Kirchhoff approximation is not entirely correct for these types of surfaces and to obtain an exact solution it is necessary to compute numerically the scattered electric field 4.35.

4.4 The Geometric Optical Approximation

When the physical dimensions of the surface irregularities are larger than the wavelength of the light ($\sigma_h / \lambda \gg 1$) the problem of calculating the scattering of the light at the surface can be analyzed using a geometric optical approximation (GOA). In doing so, we ignore all wave like effects and for instance the coherent field component. The optical phenomena such as the reflection and transmission are described by the concept of light rays. This so called geometric optical approximation can handle even surfaces with different scales of roughness and include the scattering by multiple reflection effects. The geometric optical approximation is a simpler approach easier to compute and to describe in comparison to the wave theory. However, it fails to predict the specular spike and all wave like effects that can occur at the surface and it is necessary to include then by hand.

In the geometric optical approximation the surface is usually assumed to be composed by an ensemble of micro-facets, curved or planar. The dimensions of these micro-facets are presumably much larger than the wavelength of the incident light. Each micro-facet is defined by a local normal, $\mathbf{n}'$, oriented according to a probability distribution function $P(\alpha)$ (section 4.2). The probability distribution function is presumed to depend of the angle $\alpha = \arccos(\mathbf{n} \cdot \mathbf{n}')$.

The incident flux of radiation impinging at an element δA of the surface is

$$d\Phi_i = L_i \cos\theta_i \, \delta A \, d\Omega_i \tag{4.72}$$

where L_i is the radiance of the source and $d\Omega_i$ is the solid angle subtended by the incident beam. Let the surface have some randomness. The number of normals $\mathbf{n}'$ pointing within a solid angle $d\Omega'$ is $P\,d\Omega'$ and the effective area of the micro-facets whose normal is within the solid angle $d\Omega'$ is $Pd\Omega'\,\delta A$. We assume that the micro-facets have no preferred direction, in which case $P = P(\alpha)$. Thus the incident flux at a micro-facet is

$$d\Phi_i' = L_i \cos\theta_i' \, \delta A \, d\Omega_i P d\Omega' \tag{4.73}$$

Therefore, the specular radiated flux by the area δA into a direction $\mathbf{r}$ is given by

$$d\Phi_r^{(S)} = FG \, d\Phi_i' = FG \, d\Phi_i \frac{\cos\theta_i'}{\cos\theta_i} P d\Omega' \tag{4.74}$$
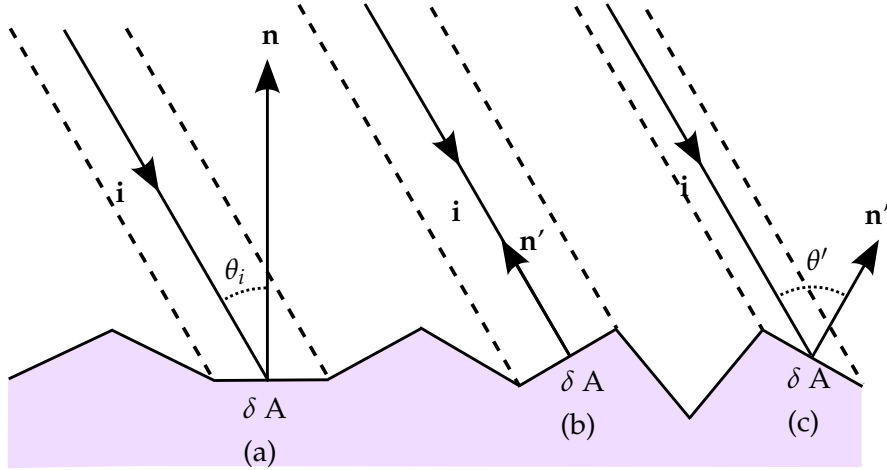
Figure 4.13: Illumination of a rough surface with flat facets with the same area δA by a distant source. The micro-facet (b) whose normal is aligned with the incident direction receives more light comparatively to (a) and (c).
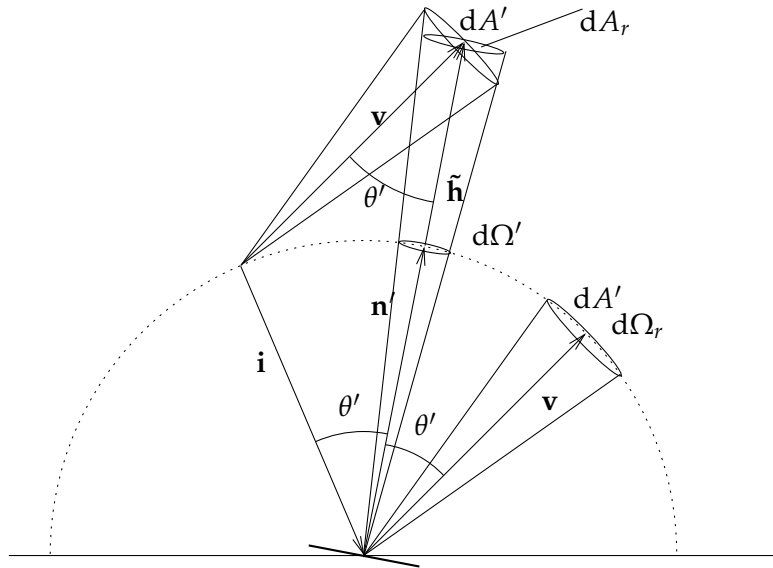
Figure 4.14: Relation between the solid angle subtended by the micro-facet $d\Omega'$ and the viewing solid angle $d\Omega'$. In specular reflection, the micro-surfaces whose normals point within a solid angle $d\Omega'$ radiate towards $\mathbf{v}$, within the solid angle $d\Omega_r$. In this case a simple relation holds. Since $d\Omega' = \frac{d\Omega_r \cos\theta'}{h^2}$, and $h^2 = (\mathbf{v} - \mathbf{i})^2$, consequently, $d\Omega_r = 4\cos\theta' \, d\Omega'$.

where the geometrical attenuation factor G accounts for shadowing and masking between micro-surfaces [189] and the Fresnel coefficient, F, expresses the fraction of light that is reflected at the surface with normal $\mathbf{n}'$ (thus it is computed for the local angle θ'). The ratio $\cos\theta_i' / \cos\theta_i$ expresses the fact that the micro-facets which normal is oriented towards the direction of incidence receive a larger fraction of the incident flux of radiation. Figure 4.13 shows that for the same illumination conditions the micro-facets with smaller local angle of incidence (θ_i') receive more light in comparison to those more inclined.

In the specular reflection, the local angle of incidence θ_i' is the same of the local angle of reflectance θ_r' and we have $\theta_i' = \theta_r' = \theta'$

The relation between $\mathrm{d}\Omega'$ and $\mathrm{d}\Omega_r$ is obtained assuming that the source is at a great distance from the micro-facet, such that the rays that arrive to the micro-facet are nearly parallel between each other. In 4.14 we observe that only the normals $\mathbf{n}'$ that lie within the solid angle $\mathrm{d}\Omega'$ are able to reflect into the solid angle Ω_r. The vector $\tilde{\mathbf{h}} = \mathbf{r} - \mathbf{i}$ is such that $|\mathbf{h}| = 2\cos\theta'$ and the respective solid angle is given by $\mathrm{d}\Omega' = \frac{\mathrm{d}\Omega_r \cos\theta'}{|\mathbf{h}|^2}$. Thus the following relation holds

$$\mathrm{d}\Omega' = \frac{\mathrm{d}\Omega_r}{4\cos\theta'} \tag{4.75}$$

The BRIDF function is defined as $\varrho(\theta_i, \phi_i, \theta_r, \phi_r) = \frac{d\Phi_r/d\Omega_r}{\Phi_i}$ (see appendix A), therefore we have

$$\varrho_S\left(\theta_i, \phi_i, \theta_r, \phi_r\right) = \frac{1}{4\cos\theta_i}PFG \tag{4.76}$$

The geometric attenuation coefficient

In general, in a rough surface there are areas that are shadowed by neighbor protruding tips. This shadowing effect occurs mainly when the surface is illuminated at large angles of incidence, θ_i. Similarly there is also a masking effect when part of the flux reflected from a fully illuminated facet is intercepted by an adjoining micro-facet (see fig. 4.15). These effects are proportional to the roughness of the surface and increase with increasing the angles, either the angle of incidence or the angle of reflection. Therefore, it is necessary to account with this factor in the description of the reflectance distribution.

The geometric attenuation factor G which takes into account these effects, describes the fraction of light from a specific incoming direction $\mathbf{i}$ that is effectively reflected in a specific direction $\mathbf{v}$. Hence G describes the fraction of the micro-facets that contributes to the reflected flux at a given angle θ_r and for a given angle θ_i.

In figure 4.15 the surface is described as a collection of flat micro-facets as prescribed by the Torrance-Sparrow [7]. However, shadowing and masking effects are obviously not exclusive of this model and should be considered regardless of how the rough surfaces is described.
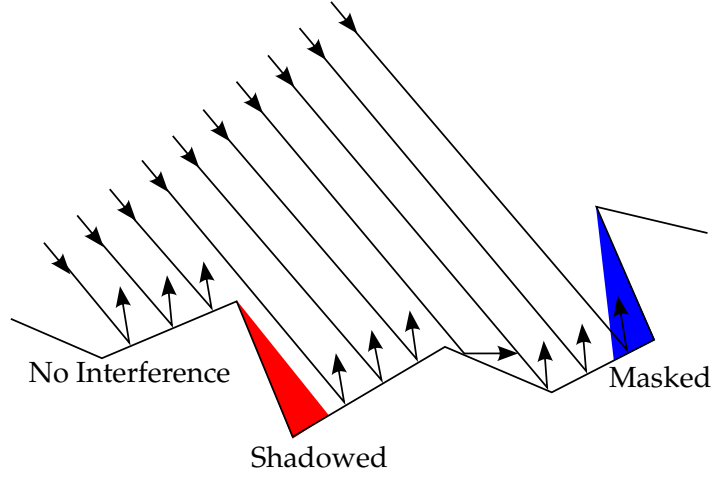
Figure 4.15: Shadowing and masking effects in a rough surface. The light reflected in the masked microarea is intersected by another part of the surface and is not able to reflect specularly the light.

Below we describe two approaches that lead to explicit forms of the factor G: i) the Torrance-Sparrow approach developed in the framework of a model of a set of micro-facets and ii) the general approach due to Smith to tackle shadowing in general grounds [189].

The Torrance-Sparrow geometric attenuation factor

The Torrance and Sparrow model describes the specular reflection by a set of plane specular reflecting micro-facets. Symmetric V-groove all lying on the same plane where considered to account for the masking and shadowing effects (figure 4.16). The upper edges of the cavity lie in the same plane. Only the light that is reflected once in the cavity is added to the specular lobe, the light that is multi-reflected win the cavity is assumed to be reflected diffusely. Thus the geometric factor is given by the fraction of the micro-facets that contributes to the specular lobe,

$$G = 1 - (m/l) \tag{4.77}$$

where m/l is the fraction of the micro-facet with a specific local normal $\mathbf{n}'$ that is shadowed or masked. Torrance and Sparrow computed the two effects separately and concluded that [7]

$$G(\theta_i, \theta_r, \phi_r) = \min(1, G_{\mathrm{msk}}, G_{\mathrm{shd}}) \tag{4.78}$$
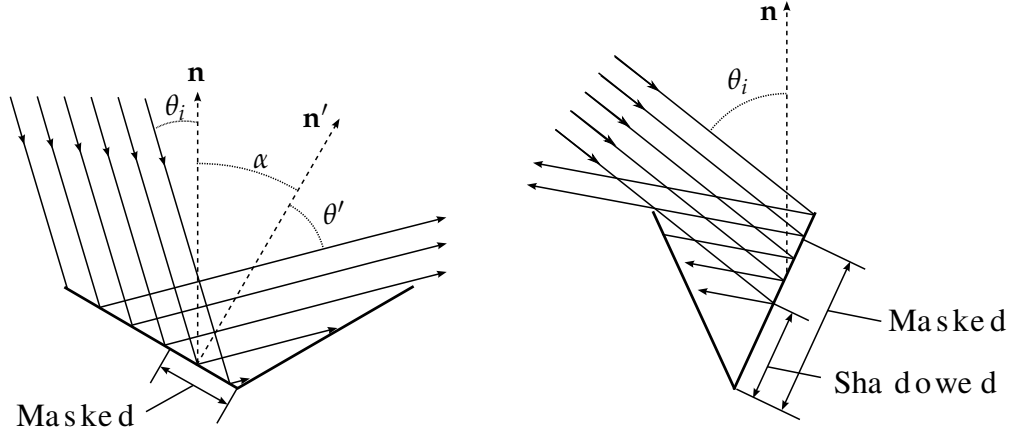
Figure 4.16: Shadowing and masking in the micro-facets with the model of Torrance-Sparrow (adapted from [7]).

where G_{msk} is the fraction of light that is blocked by adjacent micro-surfaces and G_{shdw} is the fraction of the surface that is shadowed by the micro-facets neighbors,

$$G_{msk} = \frac{2\cos\alpha\cos\theta_r}{\cos\theta'}$$
$$G_{shd} = \frac{2\cos\alpha\cos\theta_i}{\cos\theta'}$$

α and θ' are computed using the equations 4.16a and 4.16b.

This computation is however very restricted to this type of micro-facets and cannot be applied for example to the Trowbridge-Reitz model. This formulation is also independent of the surface roughness which is not realistic.

Smith shadowing theory

Models for shadowing and masking using a height distribution model for the surface roughness are usually more realistic. Expressions for the geometric approximation factors were derived by Wagner [190] Beckmann or Smith [189]. Both the Wagner and Beckmann factors assume a gaussian correlation function. However many surfaces do not show a gaussian behaviour. The Smith model has no such restriction and it can be applied to other distributions of slopes such as the Trowbridge-Reitz model. According to Sadiku and Nelatury [191] the Smith model give the best results when compared with the Wagner and Beckmann descriptions.

The Smith shadowing theory considers a smooth surface upon which are superimposed positive and negative undulations of height generated by a stationary random
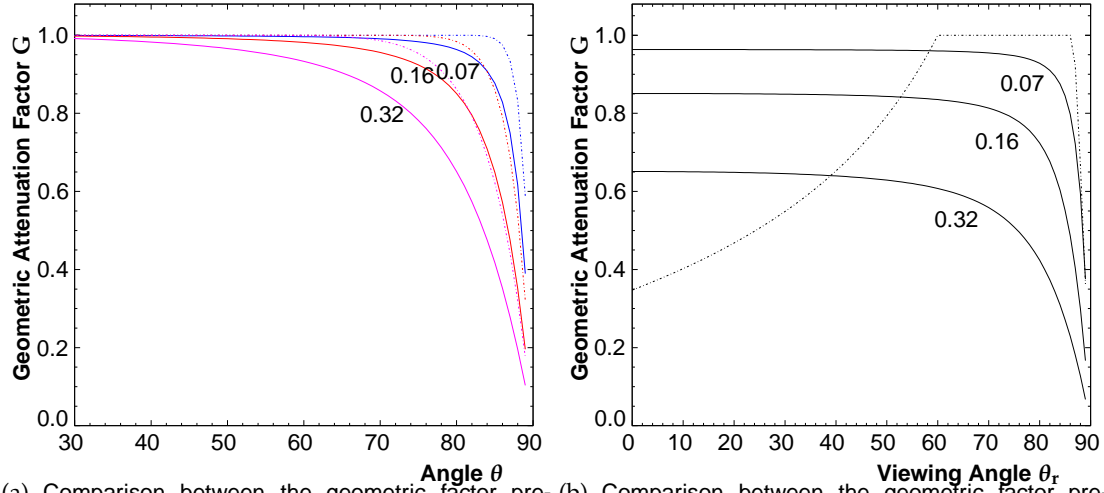
(a) Comparison between the geometric factor predicted by Smith with the Trowbridge-Reitz distribution (solid lines) and the Cook-Torrance distribution (dotted lines) for three different roughnesses 0.07 (blue), 0.16 (red) and 0.32 (magenta)

(b) Comparison between the geometric factor predicted by the Smith model with the Trowbridge-Reitz distribution (solid lines) and the Torrance-Sparrow (dotted lines) for the three different surface roughnesses. The angle of incidence is $\theta_i = 80°$ and the $\phi_r = 0°$
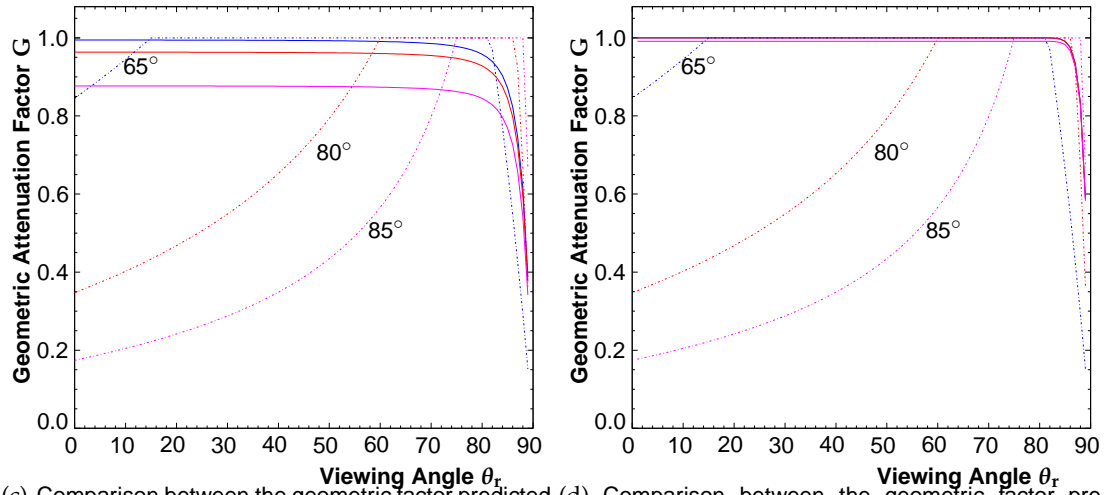
(c) Comparison between the geometric factor predicted by Smith with the Trowbridge-Reitz distribution with $\gamma = 0.07$ (solid lines) and the Torrance-Sparrow (dotted lines) for three different angles of incidence shown. The azimuthal angle is $\phi_r = 0°$

(d) Comparison between the geometric factor predicted by Smith with a gaussian distribution (solid lines) the Torrance-Sparrow (dotted lines) with $m = \gamma = 0.07$ for three different angles of incidence shown in the graphic and $\phi_r = 0°$

Figure 4.17: Comparison between the different models for the geometrical attenuation functions, G (see text).

process described by the probability function $P(z)$, which represents the average planar surface and the actual points of the surface along z (see section 4.2).

The probability that a point in the surface could reflect incident light with an angle of incidence θ_i into the direction θ_r is given by:

$$G\left(\theta_i, \theta_r, \phi_r\right) = H\left(\theta_i' - \frac{\pi}{2}\right) H\left(\theta_r' - \frac{\pi}{2}\right) G'\left(\theta_i\right) G'\left(\theta_r\right) \tag{4.79}$$

where H is the Heaviside step function and accounts for the fact that no light can be reflected if the local angle is above $\pi/2$. For the specular lobe $\theta_i' = \theta_r' = \theta'$. $G'\left(\theta_i\right)$ and $G'\left(\theta_r\right)$ are monodirectional terms and give the probability that no part of the surface intersect the incident or reflected rays. To compute this factor is necessary to describe statistically the surface. Usually it is assumed that the surface heights are statistically uncorrelated with the slopes of the surface [192], thus G' is only dependent of the distribution of slopes $P\left(\alpha\right)$.

For the Cook-Torrance distribution (equation 4.20) this term was found to be given by[1] [193]

$$G'\left(\theta\right) = \frac{2}{1 + \text{erf}\left(\tilde{m}\right) + \frac{1}{\tilde{m}\sqrt{\pi}}e^{-\tilde{m}^2}} \tag{4.80}$$

where

$$\tilde{m} = 1/\left(m \tan\theta_r\right)$$

For the Trowbridge-Reitz distribution (eq. 4.23) the mono-directional term is given by

$$G'\left(\theta\right) = \frac{2}{1 + \sqrt{1 + \gamma^2 \tan^2\theta}} \tag{4.81}$$

These two mono-directional terms 4.80 and 4.81 are compared in the figure 4.17(a) for three different roughness parameters. The attenuation observed for the Trowbridge-Reitz is generally higher than for the Cook-Torrance distribution. For example the shadowing predicted for the Trowbridge-Reitz distribution for $\gamma = 0.07$ is similar to the shadowing predicted for the Cook-Torrance distribution for $m = 0.14$. This is caused by the greater likelihood of the larger slopes in the Trowbridge-Reitz distribution (see figure 4.8) which are more likely affected by shadowing and masking.

For low values of roughness ($\gamma < 0.07$ or $m < 0.07$) the shadowing and masking effects are small, in fact $G' > 0.99$ for $\theta < 85°$ in the Cook-Torrance distribution and $\theta < 70°$ in the Trowbridge-Reitz distribution.

The figures 4.17(a) to 4.17(d) compare the geometrical attenuation factors predicted by the Smith theory (eq. 4.80 and 4.81) with the geometrical attenuation factors of the Torrance-Sparrow model (eq. 4.79) for different roughnesses and angles of incidence. As shown in fig. 4.17(b) the intensity of G predicted by Torrance-Sparrow does not change with the roughness of the surface, unlike the Smith shadowing term. It has a

Figure 4.18: Limitations of the shadowing-masking factor. Left: the shadowing will not reduce the intensity of the specular lobe. Right: the masking effect does not take into account that the light can be reflected or refracted again in the surface.

maximum in the direction of incidence which is not observed with the Smith formulation.

The current formulation of the shadowing and masking effects has an important limitation. The light that is reflected (or refracted) is not considered any further in the reflection distribution. However, the shadowing of the micro-facets does not reduce the intensity of the incident beam, instead the light will be reflected by other micro-facet and will be eventually end up be reflected by somewhere else (see figure 4.18). Therefore, a normalization of the function P is necessary

$$2\pi \int_0^{\frac{\pi}{2}} P(\alpha) \, G(\theta_i) \cos\alpha \sin\alpha \mathrm{d}\alpha = 1 \tag{4.82}$$

However this normalization is dependent of the angle θ_i, thus increasing the complexity of the distribution function.

The masking reduces the intensity of the specular reflection because the light has already been reflected by the micro-facet, however the light at the surface can be double reflected or it will be refracted. The refracted light will increase the intensity of the transmitted components or when the internal scattering is dominant in the new medium the light will be part of the diffuse lobe.

4.5   Reflection from Diffuse Materials

Early attempts to explain the diffuse reflection phenomenon of a surface attributed the effect to the reflection of countless small mirrors (Bouguer hypothesis), however this hypothesis could not explain how perfectly smooth surfaces can also exhibit diffuse

---

[1]with $\mathrm{erf}(z) = \frac{2}{\sqrt{\pi}} \int_0^z \exp\left(-t^2\right) \mathrm{d}t$

reflection [194]. In fact the origin of the diffuse reflection can be traced to two different phenomena.

In dielectrics the diffuse reflectance is normally associated with the "internal reflectance" that occurs in the subsurface of a material that is inhomogeneous, whose inhomogeneities serve as scatters centers in a otherwise uniform dielectric medium with index of refraction n. Examples of such materials include rubber, ceramics and plastics (e.g. PTFE). The light that refracted to the inhomogeneous dielectric will be scattered many times before it returns to the first medium; due to the multi-scattering nature of this reflection the direction of the photons will be quite random and usually well described by the Lambertian model [195].

If the reflection occurs at a surface of a conductor material this reflection mechanism is not present, because the light is absorbed within some nanometers of the surface, killing any internal scattering. Nevertheless diffuse reflection can occur in this case originated from multiple reflections that occur in a rough surface. Conductors have a reflectance which is in general higher than in a dielectric. Hence, even at normal incidence multiple reflection can be important. However this phenomenon is of different nature and cannot be confused with the phenomenon of body reflectance mentioned above. Here we will discuss in detail the diffuse reflection by a dielectric.

Lambertian model

The first empirical description of the diffuse reflection was made by Johann Heinrich Lambert. He observed in the eighteenth century that some materials appear equally bright independently of the viewing angle. He published this result in his work *Photometria* in 1760, thus establishing the Lambert law [196]. According to this law the surface's radiance is constant, i.e. the radiated intensity distribution of specular surfaces has the form

$$\varrho_D\left(\theta_r\right) = \frac{\rho_l}{\pi}\cos\theta_r \tag{4.83}$$

where ρ_l is the albedo defined as the ratio between the light flux which is diffusely reflected relative to the light incident at the surface.

The factor $\frac{1}{\pi}$ is a normalization coefficient such that the integral over the hemisphere is one

$$\int_\pi^{-\pi}\int_0^{+\frac{\pi}{2}}\frac{\varrho_D\left(\theta_r\right)}{\rho_l}\sin\theta_r\mathrm{d}\theta_r\mathrm{d}\phi = \frac{1}{\pi}2\pi\int_0^{+\frac{\pi}{2}}\cos\theta_r\sin\theta_r\mathrm{d}\theta_r = 1 \tag{4.84}$$

The albedo ρ_l is an important parameter in climatology because it controls the amount of energy absorbed by the Earth thus affecting the temperature of the environment. Table III shows the value for the albedo of some typical surfaces. As shown, ice and snow have the highest albedo and soil the lowest.

The Lambertian model is a purely phenomenological model and sometimes it is an inaccurate approximation to describe a body reflectance. In fact a pure Lambertian

Table III: Typical values for the albedo for some materials illuminated by incident solar radiation.

Fresh deep snow	0.9 [197]	Dry sand	0.35 [198]
Snow in the antartic plateau	0.8 [199]	Asphalt	0.15 [198]
Frozen white ice	0.7 [200]	Wet dark soil	0.08 [198]

reflection do not exist between two media with different indices of refraction because part of the light will be always specularly reflected.

The radiative transfer theory

The phenomenon of the internal scattering of the light caused by the inhomogeneities of the dielectric constant (body reflectance) is similar to the scattering of incident light upon stellar and planetary atmosphere caused by the gaseous molecules [201]. The scattering in the atmosphere is described by the radiative transfer theory of multiple scattering and the same theory can be applied to the internal scattering in a dielectric. The scatter particles in the medium are assumed to be located randomly in the medium, thus the phase correlation between the the incident and scattered waves is zero. In a medium without sources of radiation the light can be absorbed or scattered by particles of the medium, thus the intensity of the light (I) inside these scattering medium obeys to the following equation of transport (figure 4.19) (for a detailed derivation see
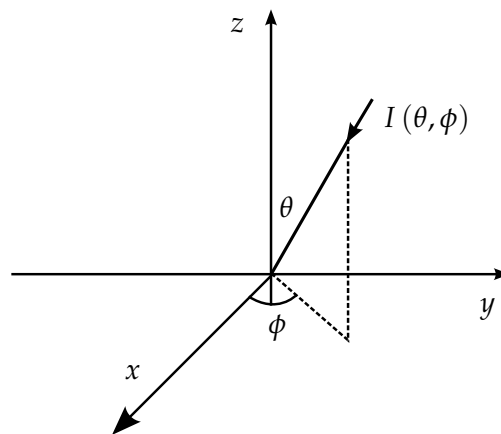
Figure 4.19: Definition of the angles used in the equation of transport of light in a scattering media.

4. MODELLING THE REFLECTION
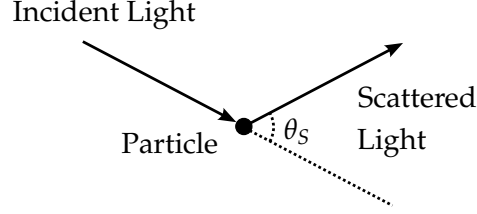
Figure 4.20: Definition of the scatter angle

[202, 203, 204])

$$\cos\theta \frac{\mathrm{d}I\left(z,\cos\theta,\phi\right)}{\mathrm{d}z} = -\left(\alpha^{\mathrm{abs}} + \alpha^{\mathrm{scat}}\right) I\left(z,\cos\theta,\phi\right)$$
$$+ \frac{\alpha^{\mathrm{scat}}}{4\pi} \int_0^{2\pi} \int_{-\pi/2}^{+\pi/2} I\left(z,\cos\theta_S,\phi_S\right) \chi\left(\theta_S\right) \sin\theta_S \mathrm{d}\theta_S \mathrm{d}\phi_S \qquad (4.85)$$

where α^{abs} and α^{scat} are the absorption and scattering lengths respectively. The phase function $\chi\left(\theta_S\right)$ (also called scattering indicatrix function or scattering diagram) is a probability density function which characterizes the angular distribution of the light in the medium, it is dependent of the angle of scattering θ_S defined in the figure 4.20. This function is normalized such that

$$\frac{1}{4\pi} \int_{4\pi} \chi\left(\theta_S\right) \mathrm{d}\Omega = 1 \qquad (4.86)$$

For the Rayleigh scattering this indicatrix function is given by $\chi = \frac{3}{4}\left(1 + \cos^2\theta_S\right)$ which corresponds basically to the angular part of the Rayleigh cross section. The Rayleigh scattering is only valid for particles of small size comparatively to the wavelength of the light. For larger particles the Mie scattering should be used [205].

The majority of materials have a distribution of particles with different sizes and the phase function of single scattering cannot be applied. For that reason the empirical formula of Henyey-Greenstein[206] is used generally to describe the internal scattering

$$\chi\left(\theta_S\right) = \frac{1}{4\pi} \frac{1 - g^2}{\left(1 + g^2 - 2g\cos\theta_S\right)^{\frac{3}{2}}} \qquad (4.87)$$

where the parameter g is an asymmetric parameter that controls the distribution of the light. When $g = 0$ the scattering is isotropic, if $g > 0$ it is predominantly emitted forward and for $g < 0$ it is predominantly backward [204].

Using the Henyey-Greenstein empirical formula the modelling of the internal scattering (eq. 4.85) usually requires the evaluation of three parameters: the cross section of absorption, the cross section of scattering and the asymmetry parameter g. These three parameters change with the wavelength of the incident light, this fact is responsible

Table IV: Scattering length α^{scat}, absorption length α^{abs} and asymmetric factor g for the PTFE.

Wavelength λ nm	Scattering Length α^{scat} cm^{-1}	Absorption Length α^{abs} cm^{-1}	Asymmetric Factor g
300	119 ± 9.5	2.31	0.591 ± 0.0396
488	44 ± 1.8	3.96 ± 0.16	0.836 ± 0.0057
633	26 ± 1.5	3.64 ± 0.12	0.8895 ± 0.0276

for the colored appearance of many dielectrics. An estimative of these parameters for the PTFE was made by Hueber *et al* [207]. The results show that the anisotropy factor is positive, thus the scattering is mainly in the forward direction and it increases with the wavelength of the light. On the contrary, the scattering length increases with the wavelength.

The light that is scattered inside the material returns eventually to the first medium. Thus it is also necessary to describe the reflections and refractions that occur at this transition of medium.

The Wolff model for diffuse reflection

Given that diffuse reflection of light is associated to multiple scattering underneath the surface it means that the light enters and exits the interface and as such it should satisfy the Fresnel equations both at the entrance and at the exit (see fig. 4.21).

Below the surface of the dielectric light is presumably scattered isotropically ($\chi(\theta_S) = 1$) thus the reflection distribution is azimuth independent relatively to the normal of the surface and regardless of the direction of the incident light. With such approximation the scattering of the light can be calculated using the Chandrasekhar diffuse law (details about this function can be found here [208]). As we have previously discussed, the isotropic behaviour was not observed for the PTFE, however we are mainly interested in describing the boundary effect.

The first order contribution to the diffuse reflection corresponds to the light that is refracted into the material surface, scatters among the surface inhomogeneities and return back to the original medium making an angle of θ_r with the normal to the interface. (figure 4.21). Given the Fresnel equations only the fraction $\left\{ 1 - F\left(\theta_i, \frac{n}{n_0}\right) \right\}$ will be refracted into the material and only the quantity will be able to exit to the first medium $\left\{ 1 - F\left(\sin^{-1}\left[\frac{n_0}{n}\sin\theta_r\right], \frac{n_0}{n}\right) \right\}$. Thus the BRIDF is given by

$$\varrho_D = \frac{1}{\pi}\cos\theta_r \rho_1 W \qquad (4.88)$$

4. MODELLING THE REFLECTION
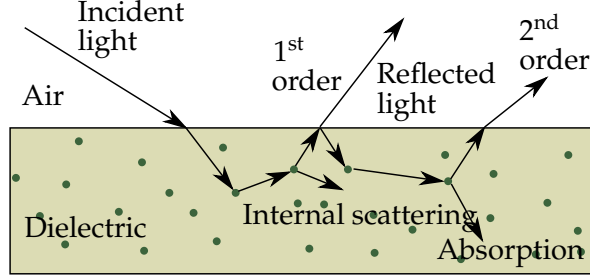
Figure 4.21: Diffuse reflection in result of internal scattering of the light in a dielectric-air interface [6]. The light can be reflected at the interface dielectric/air leading to more subsurface scattering.

The term W is the Wolff Fresnel term given by

$$W = \left[1 - F\left(\theta_i, \frac{n}{n_0}\right)\right] \times \left[1 - F\left(\sin^{-1}\left(\frac{n_0}{n}\sin\theta_r\right), \frac{n_0}{n}\right)\right] \tag{4.89}$$

ρ_1 corresponds to the first-order diffuse albedo, calculated using the diffuse law. This quantity is nearly constant for the majority of the angles of incidence [6].

However, the light can be reflected in the interface dielectric-air returning back to the dielectric and producing more subsurface scattering. This can eventually occur multiple times until the light is absorbed by the dielectric or refracted out in which case it returns to the original medium (fig. 4.21). The total diffuse albedo is given by the sum of all contributions

$$\varrho_D = \frac{1}{\pi}\cos\theta_r\left\{\rho_1 + \rho_1^2 K + \rho_1^3 K^2 + ...\right\} \tag{4.90}$$

the term K accounts for the all the internal reflections, it is nearly constant for significant values of ρ_1. A detailed description of this factor is described in the original paper by Wolff [6].

The geometric series shown in the equation 4.90 can be replaced by

$$\rho_l = \frac{\rho_1}{1 - K} \tag{4.91}$$

ρ_l is called the multiple-diffuse albedo.

The BRIDF for diffuse reflection is then given by

$$\varrho_D = \frac{1}{\pi}\cos\theta_r\rho_l W \tag{4.92}$$

This equation is a modified Lambert Law. The factor W changes the dependency of the reflection function; specially whenever θ_i or θ_r approaches to 90°. Therefore ϱ_D goes to zero much faster than predicted by the Lambert law.
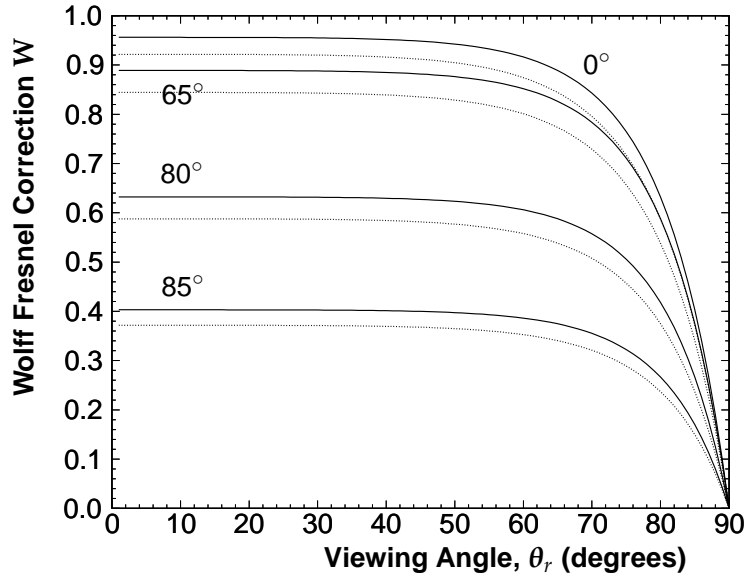
Figure 4.22: Dependence of the Wolff Fresnel correction (equation 4.88) as a function of the reflection angle θ_r for the angles of incidence θ_i indicated. These curves are for an interface air-dielectric if $n = 1.35$ (full lines) and $n = 1.50$ (dotted lines).

The factor W is represented in the figure 4.22 for an interface air-dielectric ($n_0 = 1$, $n_1 = 1.35$ and 1.50, which are common in dielectrics) as function of θ_r. For a given angle of incident this factor is almost constant until 60°, after that it decreases to zero. The factor W for $\theta_r = 0$ decreases from about 0.96 at normal incidence to about 0.4 at $\theta_i = 85°$.

The factor $F\left(\theta_i, \frac{n}{n_0}\right)$ (equation 4.89) is dependent of the polarization of the incident light. However after several scatterings in the interior of the material the light will be in principle unpolarized and $F\left(\theta_r, n_o/n\right)$ should be computed always for unpolarized light.

The diffuse reflection at a rough surface

The roughness of the surface affects the distribution of the diffused light, increasing the observed radiance when the viewing direction approaches to the incident direction [209]. This effect is caused by the foreshortening of the microsurfaces, the microsurfaces whose normal is aligned with the direction of the incident light receive a larger amount of light. To take into account for this effect we used the model proposed by Oren and Nayar ([144]). This model showed to successfully describe the reflectance distribution observed from various materials [209].

In the Oren-Nayar model the roughness of the surface is described by micro-facets.

115

4. MODELLING THE REFLECTION

Each micro-facet is assumed to be Lambertian reflecting the light according to the Lambert law. These micro-facets are described by the local variables (α, ϕ_α) measured relatively to the global normal (see section 4.2). The orientation distribution of the micro-facets is described again by the function $P(\alpha, \sigma_\alpha)$, (see section 4.2).

Due the roughness of the surface radiometric phenomena such as masking, shadowing and also inter-reflections between the surfaces (section 4.4) and need to be accounted with the shadowing-masking factor.

The intensity of the reflected light by a smooth surface is given by the Lambertian law to be

$$\frac{d\Phi_r}{d\Omega_r} = \frac{\rho_l}{\pi}\Phi_i \cos\theta_r \tag{4.93}$$

where Φ_r is the reflected flux, Φ_i the incident flux and ρ_l the albedo of the surface.

Considering that the rough surface is composed by a multitude of lambertian micro-facets then the diffuse reflected intensity should be given by the integral over the micro-facets as

$$\frac{d\Phi_r}{d\Omega_r} = \frac{\rho_l}{\pi}\int \Phi_i' \frac{\cos\theta_r' GP d\Omega_\alpha}{\cos\alpha} \tag{4.94}$$

where, as before, the factor $P d\Omega_\alpha$ is the fraction of micro-facets whose normal point within the solid angle $d\Omega_\alpha$. The flux Φ_i' is the flux incident in each micro-facet. Taking into account that $\Phi_i' = (\cos\theta_i')/(\cos\theta_i)\Phi_i$ (equation 4.74) then

$$\frac{d\Phi_r}{d\Omega_r} = \frac{\rho_l}{\pi\cos\theta_i}\Phi_i \int \frac{\cos\theta_i'\cos\theta_r'}{\cos\alpha} GP d\Omega_\alpha \tag{4.95}$$

Thus the BRIDF ($\varrho = \frac{d\Phi_r}{d\Omega_r}/\Phi_i$) due the direct illumination by the source along the direction (θ_r, ϕ_r) is given by

$$\varrho_1 = \varrho_L \frac{1}{\cos\theta_i\cos\theta_r}\int \frac{\cos\theta_i'\cos\theta_r'}{\cos\alpha} GP d\Omega_\alpha \tag{4.96}$$

where ϱ_L corresponds to the BRIDF given by the Lambertian law, $\varrho_L = \frac{\rho_l}{\pi}\cos\theta_r$. The local angles of incidence, θ_i', and reflectance, θ_r', are given by

$$\begin{align}
\theta_i' &= -\sin\alpha\cos\phi_\alpha\sin\theta_i + \cos\alpha\cos\theta_i \tag{4.97a}\\
\theta_r' &= \sin\theta_r\sin\phi_r\sin\alpha\sin\phi_\alpha + \sin\theta_r\cos\phi_r\sin\alpha\cos\phi_\alpha + \cos\alpha\cos\theta_r \tag{4.97b}
\end{align}$$

The case in which light is multiple reflected at different micro-facets is ignored. If those are considered we have an additional term ϱ_2 which is proportional to ρ_l^2. This factor is also accounted for in the original article of Oren-Nayar [144].

Oren and Nayar have used the normal distribution for the function P. The shadowing-masking factor is described using the Torrance-Sparrow model of the V-groove symmetric micro-facets. With such functions these integrals are too complex which discourage any analytical approach. Therefore, Oren and Nayar parametrized numerically the

integrals ϱ_1 and ϱ_2 in the form [144]

$$\varrho_D = \varrho_1 + \varrho_2 = \frac{\rho_l}{\pi} N = \frac{\rho_l}{\pi} \left(1 - \mathcal{A} + \mathcal{B} + \rho_l \mathcal{C}\right) \cos \theta_r \tag{4.98}$$

where

$$\mathcal{A} = 0.50 \frac{\sigma_\alpha^2}{\sigma_\alpha^2 + 0.33}$$

$$\mathcal{B} = -0.45 \frac{\sigma_\alpha^2}{\sigma_\alpha^2 + 0.09} H(-\cos \phi_r) \cos \phi_r \sin \alpha \tan \beta \tag{4.99}$$

$$\mathcal{C} = 0.17 \frac{\sigma_\alpha^2}{\sigma_\alpha^2 + 0.13} \left[1 - \left(\frac{2\theta_m}{\pi}\right)^2 \cos \phi_r\right] \tag{4.100}$$

and σ_α is the width of the distribution $P(\alpha)$ given by the Torrance-Sparrow distribution; $H(x)$ is the Heaviside step function; $\theta_m = \min(\theta_i, \theta_r)$, and $\theta_M = \max(\theta_i, \theta_r)$. In a perfect smooth surface ($\sigma_\alpha = 0$) the equation 4.98 reduces to the Lambert law.

Figure 4.23 shows the intensity of the Oren-Nayar correction factor $(1 - \mathcal{A} + \mathcal{B} + \rho_l \mathcal{C})$ as function of the viewing direction, for four angles of incidence. In the figure 4.24 it is shown the relative contribution of each term of the Oren-Nayar factor for an angle of incidence $\theta_i = 65°$. When $\phi_r < 90°$ the term $\mathcal{B}$ is zero and the correction ϱ_1 is only dependent of the surfaces' roughness being smaller than the respective Lambertian reflection. For $\phi_r > 90°$ this correction term $\mathcal{B}$ is dependent of the viewing and incident angles. This factor gradually increases with the viewing angle and becomes larger than one for angles larger than the angle of incidence. The curves shown in 4.23 and in 4.24 are azimuthal dependent and are maximal for $\phi_r = 180°$.

The main drawback of the parameterization developed by Oren-Nayar (equation 4.98) is that it cannot be directly applied to other distribution of micro-facets or shadowing function. Thus to compute this effect for the Trowbridge-Reitz distribution is necessary to compute the integral 4.96 again. The solution was not found anywhere in the literature, thus we have computed ourselves the result.

The shadowing-masking factor is given by the Smith model which for the Trowbridge-Reitz model is given by the equation 4.81. In contrast with the work of Oren-Nayar it was found an analytical solution for the integral when the following approximation is used.

$$G \simeq G'(\theta_i) G'(\theta_r) \tag{4.101}$$

the Heaviside function was left out therefore this function does not depend of the local angles and does not need to be integrated.

Then the equations for the local angles 4.97a and 4.97b are introduced explicitly in
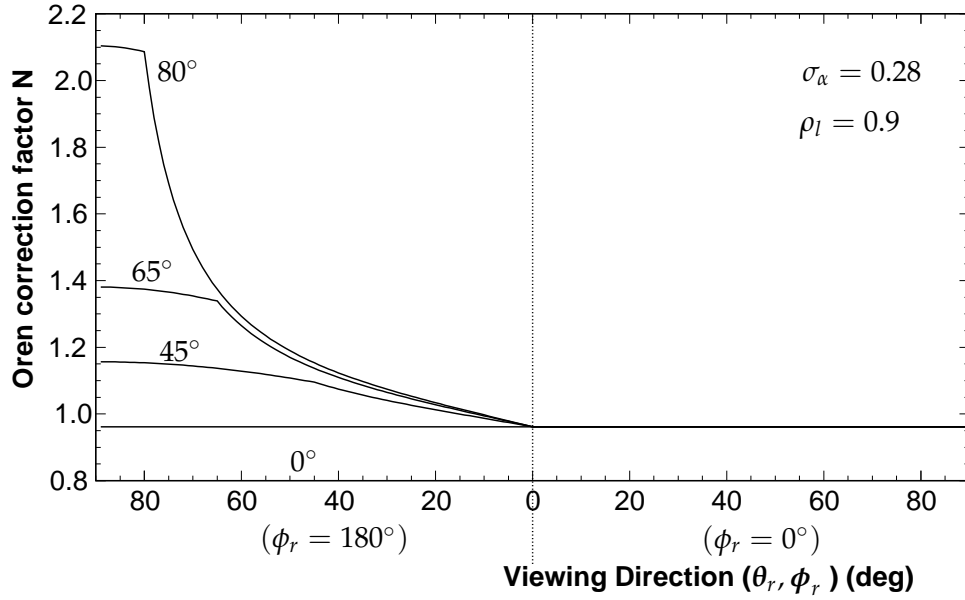
Figure 4.23: Oren-Nayar correction factor for the Torrance-Sparrow distribution and for various angles of incidence and a roughness of σ_α=0.28.
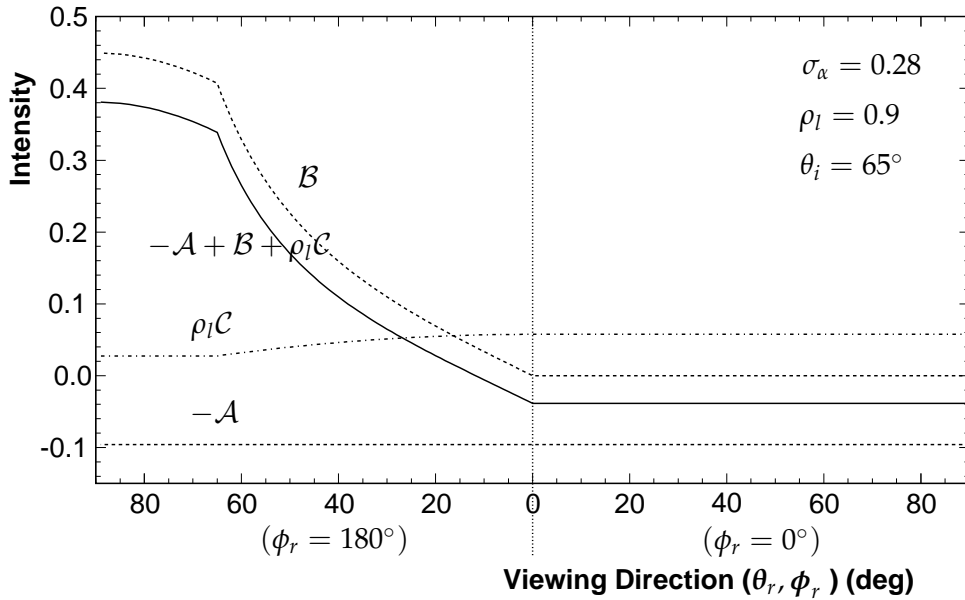
Figure 4.24: Correction introduced by each term of the factor given by the equation 4.98 for an angle of incidence $\theta_i = 65°$, $\sigma_\alpha = 0.28$ and ρ_l=0.9.

the integral 4.96 resulting in the following six double integrals

$$
\begin{aligned}
\varrho_1 \;=\; & \varrho_L G'\left(\theta_i\right) G'\left(\theta_r\right) \left\{ -\tan\theta_i \tan\theta_r \sin\phi_r \int_{-\pi}^{+\pi} \cos\phi_\alpha \sin\phi_\alpha \mathrm{d}\phi_\alpha \int_0^{\frac{\pi}{2}} P \sin^3\alpha \mathrm{d}\alpha \right. \\
& -\tan\theta_i \tan\theta_r \cos\phi_r \int_{-\pi}^{+\pi} \cos^2\phi_\alpha \mathrm{d}\phi_\alpha \int_0^{\frac{\pi}{2}} P \sin^3\alpha \mathrm{d}\alpha \\
& -\tan\theta_i \int_{-\pi}^{+\pi} \cos\phi_\alpha \mathrm{d}\phi_\alpha \int_0^{\frac{\pi}{2}} P \cos\alpha \sin^2\alpha \mathrm{d}\alpha \\
& +\tan\theta_r \sin\phi_r \int_{-\pi}^{+\pi} \sin\phi_\alpha \mathrm{d}\phi_\alpha \int_0^{\frac{\pi}{2}} P \cos\alpha \sin^2\alpha \mathrm{d}\alpha + \int_{-\pi}^{+\pi} \mathrm{d}\phi_\alpha \int_0^{\frac{\pi}{2}} P \cos^2\alpha \sin\alpha \mathrm{d}\alpha \\
& \left. +\tan\theta_r \cos\phi_r \int_{-\pi}^{+\pi} \cos\phi_\alpha \mathrm{d}\phi_\alpha \int_0^{\frac{\pi}{2}} P \cos\alpha \sin^2\alpha \mathrm{d}\alpha \right\}
\end{aligned}
\tag{4.102}
$$

where $\varrho_L = \frac{\varrho_l}{\pi}\cos\theta_r$.

The micro-facet distribution, P, is now given by the Trowbridge-Reitz distribution 4.23. Due the integration in ϕ_α only the second and fifth integrals are different from zero. The computation of these two integrals gives the following result for ϱ_1

$$
\varrho_1 = \varrho_L N = \varrho_L G'\left(\theta_i\right) G'\left(\theta_r\right) \left\{ \mathcal{N}_0 - \tan\theta_i \tan\theta_r \cos\phi_r \mathcal{N} \right\}
\tag{4.103}
$$

The $\mathcal{N}$ is an angular term dependent of the incident and viewing directions and $\mathcal{N}_0$ a constant term independent of those directions. They are given by

$$
\mathcal{N}_0 \;=\; \frac{1}{1-\gamma^2} - \frac{\gamma^2}{1-\gamma^2} \frac{\operatorname{arctanh}\left(\sqrt{1-\gamma^2}\right)}{\sqrt{1-\gamma^2}}
\tag{4.104}
$$

$$
\mathcal{N} \;=\; \frac{\gamma^2}{2\left(1-\gamma^2\right)} - \frac{\gamma^2\left(2-\gamma^2\right)}{1-\gamma^2} \frac{\operatorname{arctanh}\left(\sqrt{1-\gamma^2}\right)}{\sqrt{1-\gamma^2}}
\tag{4.105}
$$

arctanh, the inverse hyperbolic tangent, is defined as

$$
\operatorname{arctanh}\left(z\right) = \frac{1}{2}\left[\log\left(1+z\right) + \log\left(1-z\right)\right]
\tag{4.106}
$$

The intensity of these two terms is shown in the figure 4.25 as function of γ, as shown the angular term increases with the roughness of the surface at the expenses of the constant term.

The correction factor $N = \varrho_1/\varrho_L$ for the Trowbridge-Reitz distribution is shown in the figure 4.26 for different angles of incidence and reflectance and for $\phi_r = 0$ and $\phi_r = 180°$. Like in the normal distribution it is also observed an asymmetry in the angle ϕ_r.

The Heaviside term in the shadowing-masking term is not accounted in the equation 4.105. However, it should be introduced to describe the ϱ_1 at large angles of incidence and reflectance.
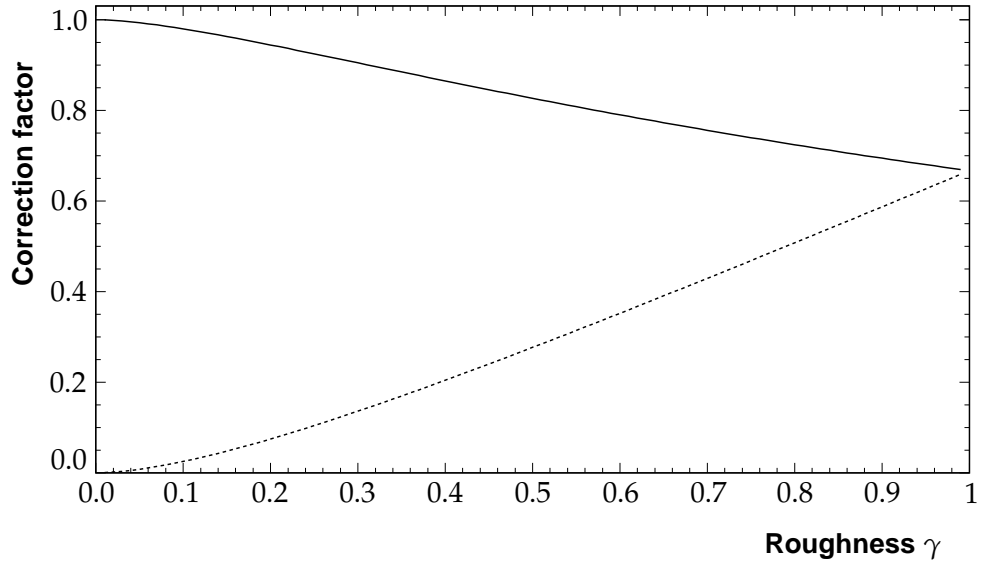
Figure 4.25: Correction introduced by the constant term $\mathcal{N}_0$ (solid line) and the angular term $\mathcal{N}$ (dashed line) of the equation 4.105.
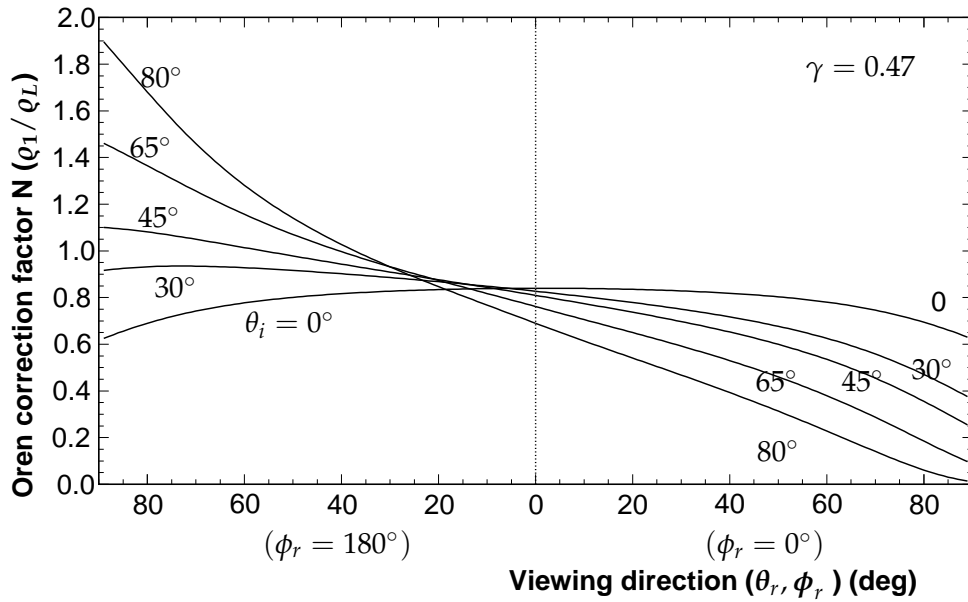
Figure 4.26: Roughness correction for the Trowbridge-Reitz distribution

The Wolff-Oren-Nayar model

The effect introduced by the Fresnel factors in the two refractions of the light in equation 4.89 should also be included in the Oren-Nayar model. Now each micro-facet is assumed to reflect the light according to the Wolff model, and the respective correction term, W, should be included in the integral 4.96,

$$\varrho_1 = \varrho_L \frac{1}{\cos\theta_r \cos\theta_i} \int W\left(\theta_i', \theta_r'\right) \frac{\cos\theta_i' \cos\theta_r'}{\cos\alpha} GP d\Omega_\alpha \tag{4.107}$$

Nevertheless for the majority of the angles of incidence the factor W remains almost constant when the surface is only slightly rough and can be taken out of the integral. Thus the reflectance function has the form

$$\varrho_D \simeq \frac{\rho_l}{\pi} W(\theta_i, \theta_r) N \cos\theta_r \tag{4.108}$$

where N is the correction factor introduced by the Oren-Nayar model[1] It is given by the equation 4.98 for the Torrance-Sparrow distribution and by 4.105 for the Trowbridge-Reitz distribution. The equation 4.108 is usually used for intermediate levels of roughnesses, for higher roughness the Oren term is dominant and the computation of the factor W using the global angles instead of the local angles is not correct.

4.6 A Semi-Empirical Model for the Reflection

In the previous sections the different physical processes that are involved in the reflection by a rough dielectric surface were described. The specular reflection at a rough surface was described using a scattering model and a geometrical optical approximation (GOA). The diffuse lobe was associated to the internal scattering and described by the Wolff-Oren-Nayar combined model. The specular lobe described by the GOA model is easier to describe and compute, however, as previously mentioned, the specular spike cannot be predicted by the GOA. Therefore, to describe the experimental observations we used a mixed model approach, with the specular lobe described by the GOA and the specular spike described by the wave scattering Kirchhoff approximation. Using such approach the ϱ function is given by

$$\varrho = \varrho_D + \varrho_S + \varrho_C \tag{4.109}$$

with

$$\varrho_D = \frac{\rho_l}{\pi} NW \cos\theta_r \tag{4.110a}$$

$$\varrho_S = (1 - \Lambda) \frac{1}{4\cos\theta_i} FPG \tag{4.110b}$$

$$\varrho_C = \Lambda FG\delta\left(\mathbf{r} - \mathbf{i}'\right) \tag{4.110c}$$

---

[1]In the original paper of Wolff *et al* (1998, [210]) the correction factor is slightly different from 4.108 because only $\mathcal{A}$ of the Oren-Nayar correction term is considered.

4. MODELLING THE REFLECTION

ϱ_D, ϱ_S and ϱ_C correspond to the diffuse lobe, specular lobe and specular spike.

The coherent contribution ϱ_C was obtained using the physical model described in the section 4.3 and is weighted by the factor Λ which describes the fraction of light that undergoes coherent reflection. This factor is given by the integrals in the equation 4.47. This component is dependent of the distribution of the heights on the surface (section 4.2).

The specular lobe ϱ_S is described by the geometrical optical approximation described in detail in the section 4.4. It is weighted by the factor $(1 - \Lambda)$ and dependent of the micro-facet distribution $P(\alpha)$. The surface structure is characterized by the probability distribution functions P_z and P_h both dependent of the roughness of the surface.

The BRIDF is dependent of five parameters, namely $\rho_l, \kappa, n, \sigma_h, \sigma_\alpha$, the wavelength λ is usually known but occasionally it can be also included in the parameters. The three contributions mentioned above are dependent of the Fresnel equations, thus they are dependent of the optical constants n and κ. Both σ_h and σ_α (γ if using the Trowbridge-Reitz distribution) characterize the roughness of the surface. The optical constants and the multi-scattering albedo are dependent of the material itself and change with wavelength of the light. The five parameters are reduced to four whenever the material have a significant attenuation coefficient κ and does not undergo diffuse reflectance.

The main advantages of this description of the reflectance are:

a) The parameters of the model are all physically motivated and can be obtained by different experimental procedures [211].

b) In most cases the way light is reflected depends of the surface treatment and the material properties. The functions Λ, P and G can be adapted accordingly to accommodate different cases;

c) This approach can be applied irrespectively to either metals or dielectrics whatever are their levels of roughness.

In this study the specular lobe is described by the GOA model only. However, if the wavelength of the incident light decreases the observed roughness of the surface increases given that the light is able to inspect more details of the surface.

In the GOA model the attenuation factor can be approximated to $\Lambda \simeq 0$. Therefore, the coherent reflection disappears and we have for ϱ only two components

$$\varrho = \frac{\rho_l}{\pi} WN \cos\theta_r + \frac{1}{4\cos\theta_i} FPG \tag{4.111}$$

This approximation uses only three parameters (or four if extinction coefficient is included) n, γ and ρ_l.

In the next chapter we will use this model to describe quite a bunch of experimental data and show that these three or four parameters are sufficient to describe the observations.

Reflectance Measurements in the VUV and Analysis

In this chapter we report the reflection measurements made for the PTFE and other materials. These reflectance distributions were obtained using the goniometer mounted in our laboratory and described in the chapter 2. The measurement procedure of the different radiometric quantities, e.g. the conical reflectance, is described in chapter 3. The data are interpreted using a reflectance model dependent of specific parameters suffice to describe the reflectance in the hemisphere of reflectance, as detailed in the (chapter 4).

The experimental results cannot be compared directly to predicted values because both the incident and viewing directions are not unidirectional as it is required by the BRIDF definition. Thus we have to perform a transformation of variables and an integration over the incident and viewing solid angles (section 5.1). The parameters of the BRIDF are then fitted to the experimental observations and the best fitted values extracted. For the fit minimization we implemented a genetic algorithm which revealed to be quite suitable for this optimisation.

The experimental methods were tested measuring the reflectance of copper, glass, gold and quartz (section 5.2). These materials show only a specular spike and the hemispherical reflectance can be directly obtained by the ratio between incident and reflected fluxes, both of which can be measured in a similar manner. These results are fitted using the Fresnel equations which are sufficient to describe the reflectance distribution of the surface.

Reflectance measurements of various surfaces of PTFE and for the copolymers FEP, ETFE and PFA were carried out. For the PTFE various samples were measured, either polished and unpolished samples with different levels of roughness and manufactured by different methods (skived, molded and extruded, etc.) and from different manufacturers. These results were fitted using a geometrical optical approximation (GOA)

model mentioned above. The samples with less specular reflection are successfully described by the BRIDF ($\varrho = \varrho_D + \varrho_S$) neglecting the coherent peak of reflection. But the samples showing a smoother look require the additional consideration of a coherent reflection contribution.

The fitted BRIDF obtained for each sample is integrated in the hemisphere to obtain the directional hemispherical reflectance factor and the bi-hemispherical reflectance factor (see appendix A). These reflectances can be compared with the results obtained using a total integrating sphere.

The reflectance of the PTFE is well studied in the visible specially because this material is the standard reflector in equipments used in reflection measurements (section 1.4). Therefore a sample of molded PTFE was also measured at larger wavelengths and the results compared with the published values (section 5.7).

Part of the results shown in this chapter are published in the Nuclear Instruments and Methods A [212] and in the Journal of Applied Physics [213].

5.1 Estimation of the Reflectance Parameters

The transformation of variables

To interpret and understand the reflection of the surfaces, the measured quantities were compared against the predictions of the BRIDF, ϱ. This means the fitting the free parameters of the model to the data to extract the values of these that describe the data best. However, the reflectance obtained with the goniometer, equation 3.15, corresponds to a conical reflectance which is different from the BRIDF. The BRIDF is a bidirectional quantity and requires the incident and viewing directions to be unidirectional. When the bidirectional reflectance of a surface is known in all the hemisphere the directional-conical reflectance (measured) is obtained through the integration

$$\varrho^{DC}\left(\Omega_i, \Omega_r\right) = \varrho\left(\nu_i, \nu_r, \psi\right) = \frac{1}{\Omega_r} \int_{\Omega_r} \varrho\left(\theta_i, \theta_r, \phi_r\right) d\Omega_r \tag{5.1}$$

For simplicity this quantity is represented with the same symbol of the BRIDF, however dependent of the experimental angles $\{\nu_i, \nu_r, \psi\}$ These angles represent the position of the sample and of the PMT relative to the incident light beam. These angles comprise several incident and viewing directions inside the viewing, Ω_r, and incident, Ω_i, solid angles. If the solid angles of the detector Ω_r and of the incident beam Ω_i can be considered infinitesimal the angles $(\theta_i, \theta_r, \phi_r)$ are given by (see figure 5.1)

$$\cos\theta_i = \cos\nu_i \cos\psi \tag{5.2a}$$

$$\cos\theta_r = \cos\nu_r \cos\psi \tag{5.2b}$$

$$\cos\phi_r = \frac{\cos\theta_i \cos\theta_r - \cos\left(\nu_i - \nu_r\right)}{\sin\theta_i \sin\theta_r} \tag{5.2c}$$

Figure 5.1: Relation between the angles $\{\nu_i, \nu_r, \psi\}$ and $\{\theta_i, \theta_r, \phi_r\}$.

We considered the samples used to be isotropic, therefore we have $\phi_i = 0$. However, the solid angles, especially Ω_r are too large and the BRIDF function can change significantly within both Ω_i and Ω_r. Therefore, we use a Monte-Carlo simulation to reproduce the experimental conditions when fitting the BRIDF function to the data. This Monte-Carlo simulation is described in detail in the appendix B. Here we outline only the main steps of the simulation.

The Monte-Carlo minimization

In the Monte-Carlo simulation the photons from the proportional counter are generated inside a cone with an apex angle (ϵ) obtained in the fit to the incident beam. These photons strike at a specific point S in the sample which is well defined for each direction. A random position in the slit in front of the PMT is sampled and the viewing direction is defined relative to this position of the point S. With these directions in hand it is possible to obtain the global ($\theta_i, \theta_r, \phi_r$) and local angles ($\theta'$ and α). The BRIDF $\varrho(\theta_i, \theta_r, \phi_r)$ can now be calculated upon a set of parameters. Several directions inside Ω_i and in the slit (that is inside Ω_r) are generated and the reflectance is computed taking the average of these directions of incidence **i** and viewing **v**

$$\varrho(\nu_i, \nu_r, \psi) = \frac{1}{N} \sum_{j=1}^{N} \varrho_j(\mathbf{i}, \mathbf{v}) \tag{5.3}$$

where N represents the number of directions **i** and **v** sampled. This number is dependent of the variation of the bidirectional reflectance within the solid angles Ω_i and Ω_r.

5. REFLECTANCE MEASUREMENTS IN THE VUV AND ANALYSIS

The diffuse lobe does not change strongly with both θ_i and θ_r. In this case it is not necessary to sample a high number of directions (N is usually between 10 and 25). However, both the specular spike and specular lobe are both very sensitive to the direction of the photons and the number of directions needed is much higher, $N \simeq 250$.

The parameters of $\varrho\,(\theta_i, \theta_r, \phi_r)$, whose value are unknown, are extracted by fitting the function to the experimental data to find the best values of the parameters that describe the results. As discussed before the parameters of the reflectance function ϱ are

a) n, the index of refraction of the material, and the attenuation coefficient κ (specially for metallic surfaces);

b) the roughness parameter, γ for the Trowbridge-Reitz distribution and m for the Cook-Torrance distribution;

c) the multiple diffuse albedo of the surface ρ_l;

d) a parameter which controls the amount of coherent reflection K (specially when the surface is shiny);

the above parameters are put in a form of a vector $\mathbf{p} = \{n, \kappa, \gamma, \rho_l, K\}$. The number of parameters can be changed however the analysis of the data remain the same.

Each measurement can be represented by a generic vector $\mathbf{r} = \{v_i, v_r, \psi\}$ in the coordinates of the laboratory's system (see chapter 2). As usual the best set of parameters is the one which minimizes the χ^2 quantity

$$\chi^2\,(\mathbf{p}) = \sum_{i=1}^{N} \frac{\left(\varrho_i^I\,(\mathbf{r}) - \varrho_i^E\,(\mathbf{r}, \mathbf{p})\right)^2}{\left(\sigma_{\varrho_i^I}\right)^2} \tag{5.4}$$

where $\varrho_i^I\,(\mathbf{r})$ is the observed reflectance and $\varrho_i^E\,(\mathbf{r}, \mathbf{p})$ is the estimated reflectance given by the equation 5.3. $\sigma_{\varrho_i^I}$ corresponds to the uncertainty in the reflection measurement and is given by the equation 3.17. The index i runs over all data points measured, for every angles of incidence and of observation set for a given sample (in this work $N \simeq 1000$-3000 data points).

There are well known several minimization algorithms to find the best parameters of a fit, notably, the Levenberg Marquardt algorithm (LMA) [214], the partial linear methods (PLM) [215] and the genetic algorithms (GA) [216]. We implemented and optimised a genetic algorithm to carry out the χ^2 minimization of the problem at hand. This genetic algorithm is described in detail in appendix C. The genetic algorithm does not require the calculation of any derivatives of the minimizing function unlike the more classic methods. Thus modifications to the model of reflectance can be introduced without having to change the minimization code. Furthermore, the method is very robust to local minima, which is a very important issue given the complexity of the function

ϱ. While the conventional methods search from a single point, the GA operates with a population of points, this increases the chance of reaching the global minimum and reduces the possibility to be trapped in a local minimum. Thus these type of algorithms are more efficient to find a minimum when the space is poorly understood, the noise signal ratio is large or the search space has many local minima.

The GA shows however some disadvantages relative to the other methods of minimization. The main drawback is its speed, it can be considered a slow method comparatively to LMA or PLM. As usually the user needs to specify the search space, i.e. the range of values which the different parameters can assume, when the minimum is outside this search space the fit will fail or it will converge slowly to the global minimum. It is dependent of a set of internal variables (including the crossing rate, breeding rate etc.) that affect the algorithm behaviour. However, these variables are problem dependent and should be evaluated and fined tuned for the problem at hand.

Evaluation of the uncertainties in the parameters

The reduced chi-square obtained in the minimization is usually large because it is not possible to describe all the details of the reflection distribution of the surface with the simple model discussed above, thus the standard procedures to compute the errors of the parameters are not adequate in this case.

To evaluate the uncertainties of the parameters we have followed the following procedure. First, separately for each angle of incidence, θ_i, the observed reflection distribution is fitted with one variable parameter only keeping the others parameters fixed at the values of χ^2 minimum, obtained in the global fit to all data. The root mean square is computed for the parameters obtained this way for all measured angles, using as average the value obtained in the global fit. The uncertainty of each parameter is taken as the respective root mean square. This technique is repeated for all other parameters of the model. Moreover, it is also necessary to consider the uncertainty intrinsic of the minimization method. This is obtained by repeating the χ^2 minimization of the same data set for at least five times. The r.m.s. of the values of the parameters obtained is computed. This relative error is normally below 2%. It is propagated in quadrature to the final uncertainty of the parameters.

5.2   The Reflectance of Smooth Surfaces

This section concerns tests of the experimental methods and data analysis methods using different smooth samples.

The reflectance of quartz

Quartz is a crystalline material, usually very smooth, whose reflectance is peaked at the specular direction. It does not absorb significantly the xenon scintillation light, thus the Fresnel equations are only dependent of the index of refraction. The simplicity of this characterization makes the quartz a good candidate to test the experimental procedure and the alignment of our experimental system.

The reflection measurements were made using a sample of quartz 5 mm thick, for different angles of incidence. The observations were fitted with the Fresnel equations (eq 4.8a and 4.8b), with $\kappa = 0$. The results are shown in table I along with the prediction of the Sellmeier equations for quartz [217]. Although we do not know any fit to the Sellmeier equations for wavelengths below 180 nm, we extrapolated the value of the index of refraction to 175 nm.

These measurements are shown in the figure 5.2 together with the fitted curve, for
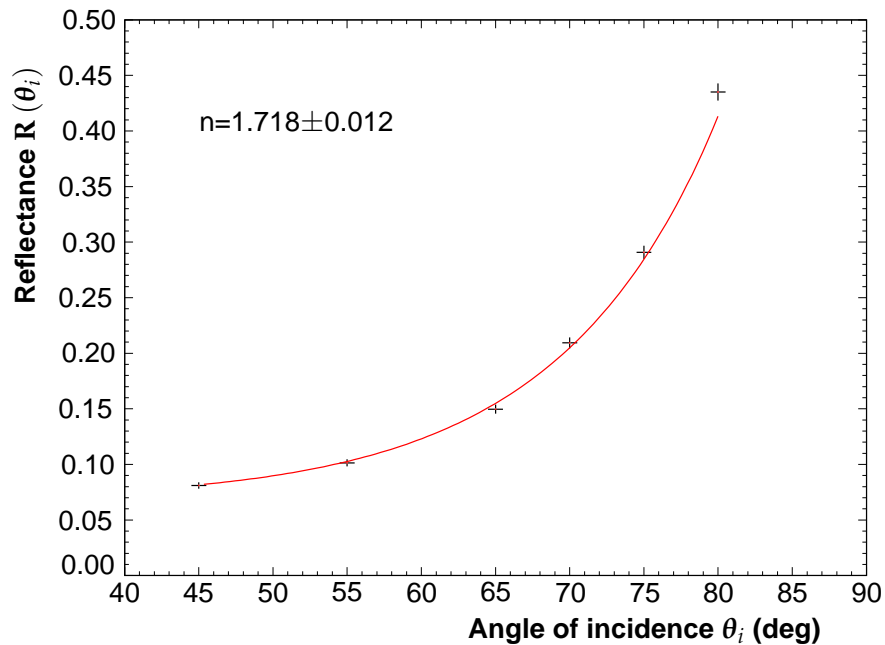
Figure 5.2: The reflectance of the quartz for different angles of incidence. The curve is the best fit of equations 4.8a and 4.8b, to data.

Table I: Index of refraction and reflectance of quartz at normal incidence for the xenon scintillation light

	n	$R\,(\theta_i = 0°)$	χ^2_ν
$F\,(\theta_i, n)^{\dagger}$	1.718±0.012	0.0698±0.0017	2.3
Sellmeier Equations [217]	1.710±0.008	0.0687±0.0012	

† Fresnel equations, eq. 4.8a and 4.8b with $\kappa = 0$

angles of incidence higher than 40° The refraction index obtained is comparable with the extrapolated value and within the experimental uncertainty. We measured the reflectance also for $\theta_i < 40°$, but given that the light is refracted into the quartz and is partially reflected in the back surface of the quartz block and refracted again into the original medium these data are difficult to analyse and were not included in the fit.

The attenuation length of quartz was directly measured introducing the sample of quartz between the VUV source and the photomultiplier. The experimental method is similar to the one used to measure the incident beam but from the fact that the sample is now lowered (see section 3.1). The reduction of the photon flux at the two quartz interfaces due the reflection was taken into account for,

$$I = I_0\,(1 - F)^2 \exp\,(-z/\zeta) = I_0 \frac{16n^2}{(n+1)^4} \exp\,(-z/\zeta) \tag{5.5}$$

where ζ is the attenuation length of the material From the analysis of these data we obtained a VUV attenuation length, ζ of $13.48 \pm 0.4\,\text{mm}$. This attenuation length corresponds to a coefficient of extinction of

$$\kappa = \frac{\lambda}{4\pi\zeta} = 1.07 \times 10^{-6} \tag{5.6}$$

Reflectance of glass

Light of wavelength smaller than 300 nm is usually absorbed in the glass. Thus, the xenon scintillation light is highly absorbed and when measuring the reflectance of the glass we should include the extinction coefficient, κ, in the fit.

The reflectance of a glass as a function of the angle of incidence is shown in fig. 5.3. The curves represent the best fits of the Fresnel equations, with $\kappa = 0$ (dashed line) and with $\kappa \neq 0$ a free parameter (solid line). The fitted values are both shown in the table II.

The reflectance at $\theta_i = 0°$ for a pure SiO_4 glass is known to be between 5-6% for light of wavelength in the region 170-180 nm [219]. However, we measured the reflection of a piece of glass whose specific type is unknown. Nonetheless, the observed reflectance at the normal incidence is consistent with the value of pure silica.
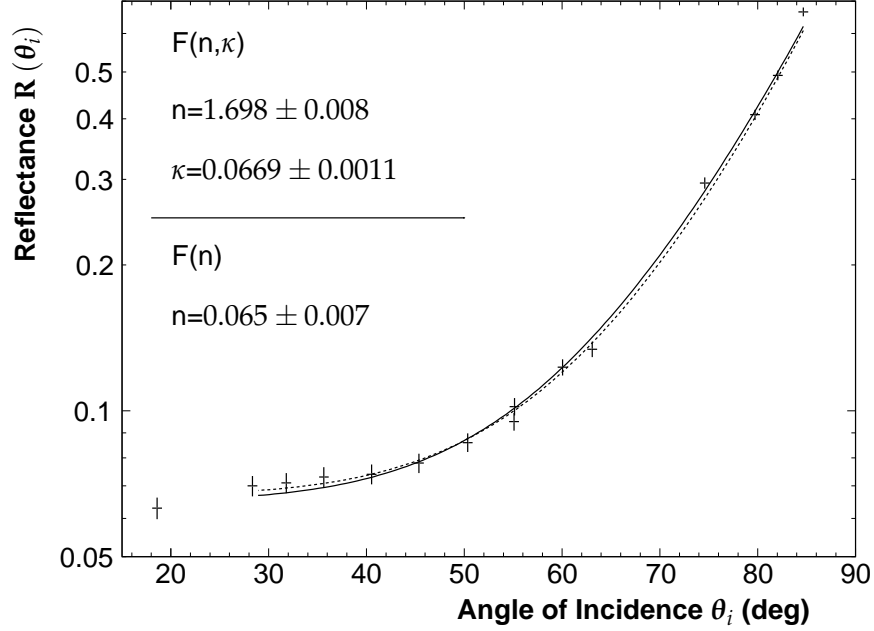
Figure 5.3: Reflectance of glass as function of the incident angle for light of wavelength $\lambda =175$ nm. The dashed line is the best fit setting $\kappa = 0$ in the Fresnel equations (eq. 4.8a and 4.8b); the solid line is the fit with the Fresnel equations for absorbing media (equations 4.5a and 4.5b).

s

Table II: Optical constants and reflectance at the normal incidence for the glass at light of wavelength 175 nm

n	κ	$R\,(\theta_i = 0°)$	χ^2_ν
1.698 ± 0.008	—	0.0669 ± 0.0011	1.7
1.58 ± 0.05	0.20 ± 0.04	0.065 ± 0.007	2.2

Reflectance of copper

A high purity copper is used in the Zeplin III detector to achieve a low level of radioactive background [60]. Therefore the reflectance of copper was measured with the xenon scintillation light. Two samples of copper were measured, one polished and another unpolished. The directional-hemispherical reflectances obtained for these two samples are shown in figure 5.4.
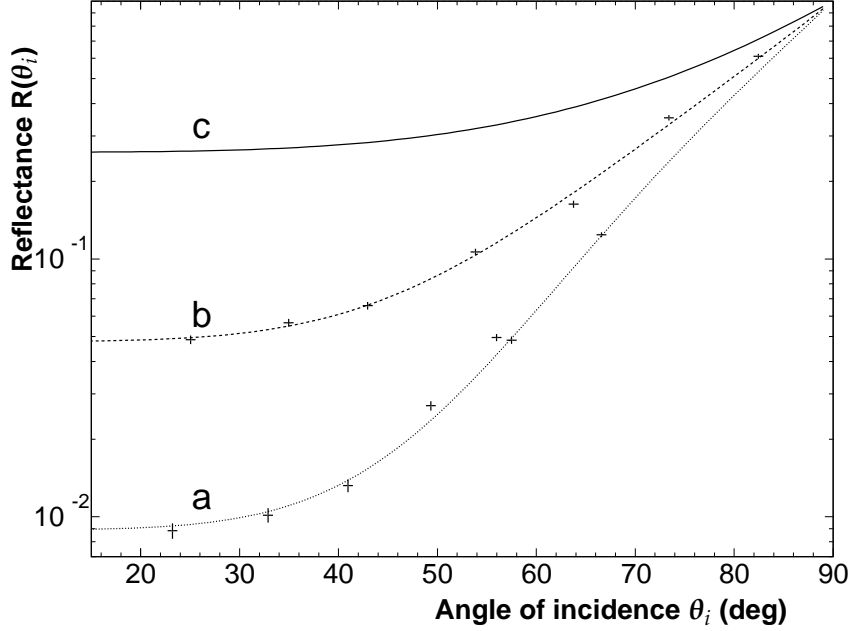
Figure 5.4: Dependence of the reflectance of copper with the incident angle, θ_i for a) unpolished copper b) polished copper and c) expected value for the pure copper, [217]. The fitted parameters are shown in the table III.

The two samples of copper are from the very same piece that was carved to build the Zeplin III detector used for dark matter search [60]. Contrary to the unpolished sample, the other sample was polished and cleaned with a special chemical product to remove the oxide layer.

The observation results are well fitted using the Fresnel equations for absorbing media (eqs. 4.5a and 4.5b). The optical constants of the two samples (polished and unpolished) obtained from the fit are shown in table III together with the published values of these quantities ([217], [220]). The indices of refraction obtained are similar in both cases. The fitted κ is different for the polished and unpolished surfaces, 0.191 and 0.439 respectively, and smaller than the published value of 1.36 [217]. Consequently the observed reflectance for the normal incidence is only 5% for the polished sample, a value which is much lower than the predicted value of 30% [217].

The difference between these values can be explained by the presence of an oxide layer deposited over the copper surface, respectively cuprous oxides Cu_2O, CuO. The oxide is a semi-conductor, thus it will decrease the conductivity of the material, decreasing the coefficient of extinction κ. A lower value for κ reduces substantially the reflectance of the surface specially for lower wavelengths. When the surface is polished and cleaned the oxide layer is at least partially removed. Nevertheless, in this case the

5. REFLECTANCE MEASUREMENTS IN THE VUV AND ANALYSIS

Table III: Optical constants and the reflectance for copper at 175 nm

	n	κ	χ_ν^2	$R\,(\theta_i = 0°)^\dagger$	$R\,(2\pi)^\ddagger$
Non-Polished	0.964 ± 0.005	0.191 ± 0.004	5	0.00905	0.07
Polished	1.036 ± 0.018	0.439 ± 0.004	4	0.0480	0.13
(191 nm) [217]	0.96	1.36		0.3076	0.37
(188 nm) [220]	0.94	1.337		0.296	0.37
(177 nm) [221]	0.972	1.20		0.226	0.33

The obtained values are compared with the results obtained by different authors

† Directional-hemispherical reflectance at the normal incidence

‡ Bi-hemispherical reflectance white-sky albedo (section A)

sample was not kept in vacuum and it was partially oxidized between preparation and measurement. In fact, the accumulation of the oxide is faster in the first minutes after the removal of the oxide layer because the thickness of the oxide layer in the surface of copper follows a logarithmic law of the type $a \ln{(bt + 1)}$ where t is the time of exposition, both a and b increase with humidity and temperature [218]. Thus, we need to be much more careful in handling the copper, avoiding contact of the sample with air, both during and after cleaning the surface.

The presence of oxide layers increases the level of impurities in scintillation detectors, particularly OH^- and decreases significantly the reflectance of the material. To remove completely this oxide layer, the sample needs to be polished, annealed at about $450°$ and kept in a high quality vacuum (10^{-7} bar) [222]. However, the scintillation detectors are not usually heated at these temperatures. Thus the reflectance of the copper will be generally lower than expected.

In the simulation of the reflectance of the Zeplin III detector it is assumed a reflectance of 15% independent of the angle of incidence. Nevertheless, as is clearly seen from the figure 5.4, this assumption is wrong given that the reflectance is highly dependent of the angle of incidence, being much smaller than 15% at the normal incidence.

Reflectance of gold

As part of this work we also measured the reflectance of gold for light with wavelength $\lambda = 255\,\text{nm}$. These measurements were not part of the bunch tests that were carried out to test and validate the empirical set up and methods and are shown here. for completeness and because of their similitude with those mentioned above.

These reflectance measurements were asked by the LISA collaboration and are needed for the charge management system of the LISA pathfinder detector [223]. The measure-
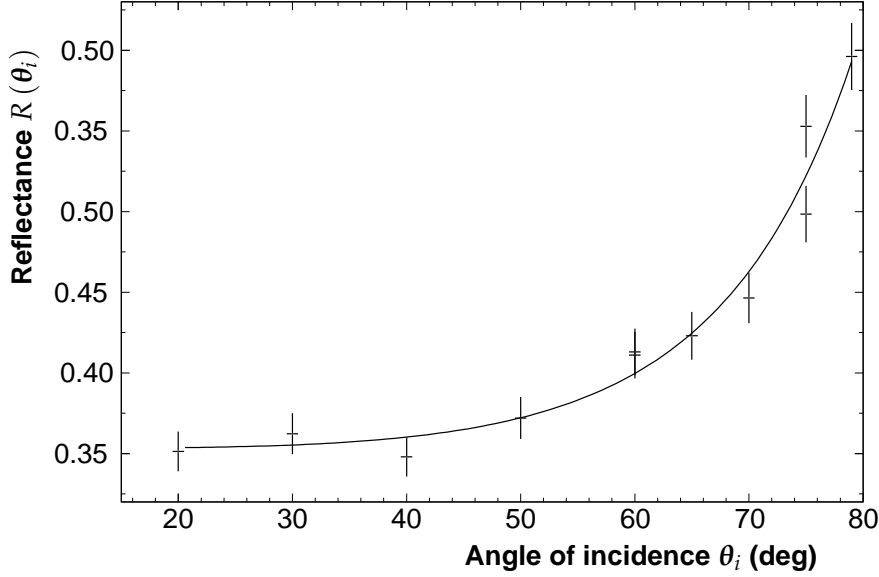
Figure 5.5: The reflectance of the gold as function of the incident angle for light of $\lambda = 255$ nm. The curve is a fit of equations 4.5a and 4.5b, to data with two free parameters. This yields for the index of refraction n=1.33±0.08 and for the attenuation coefficient κ=1.67±0.05 .

ments were made with the collaboration of David Hollington, PhD student from the Imperial College. LISA Pathfinder mission is designed to test the working principle of a future a Laser Interferometer Space Antenna (LISA) for gravitational wave detection in space [224] .

The gold is a noble metal and does not suffer corrosion or oxidation contrary to the copper, thus its optical constants are well known. Nevertheless, the reflectance of the gold can be altered due the roughness of the surface and each specific surface should be measured whenever a detailed analysis is required.

The sample of gold used has a diameter of 25 mm and is deposited upon a glass substrate. The sample used proved to be very shiny and with only a specular spike, even for incident angles near the normal. Thus it is only necessary to use the Fresnel equations to fully describe the reflectance distribution, as discussed before. The reflectance (ratio between the reflected and incident fluxes) is shown in the figure 5.5, the values of the parameters obtained are shown in the table IV. The value of the parameters obtained are compatible with the experimental values published in [225], which are also shown in the table IV for comparison.

Table IV: Optical constants and the reflectance at normal incidence for the gold at 255 nm.

	n	κ	χ_ν^2	$R\,(\theta_i = 0°)^\dagger$
Gold in glass substrate‡	1.33±0.08	1.67±0.054	0.92	0.351±0.008
(255 nm) [225]	1.33±0.02	1.688±0.007		0.357±0.002

    The results for the gold deposited in a glass substrata are compared with Johnson and Christy [225]

† Directional-hemispherical reflectance at the normal incidence

‡ sample from the LISA pathfinder detector

Reflectance for Rough Fluoropolymer Surfaces

The study for the reflectance of the PTFE is necessary for a better understanding of the scintillation chambers that use this material in their interior walls (see chapter 1). The PTFE is an efficient diffuser for wavelengths larger than 200 nm. At the xenon scintillation wavelength a relevant contribution from the diffuse component is expected given that we are still placed above the absorption edge (figure 1.13). Thus the study of this material involves the measurement of at least two components of reflection: the specular and diffuse lobe. These components are first described by an optical model as described in chapter 4, involving the minimization of at least three parameters: the index of refraction, the albedo and the width of the specular lobe.

5.3 The Characterization of the Samples

The reflectance distribution was measured for samples with different manufacturing processes (molding, skiving, extrusion and expansion), different manufacturers and with different surface finishings. The manufacture processes of PTFE is outlined in the section 1.3. The physical and chemical characteristics of these materials is shown in the table III of the chapter 1. The physical dimensions of the samples used is shown in the table V. As shown the samples used in this work have a rectangular shape with 20 to 30 mm height and 30 to 40 mm width and a thicknesses ranging from 0.5 mm (ETFE sample) to 7 mm (molded extruded and expanded samples).

The polishing and cleaning process

The polished samples were finished with sandpaper from 3M$^®$ with ultrafine grain (2000), then they were polished with a soft tissue. All the samples were cleaned with
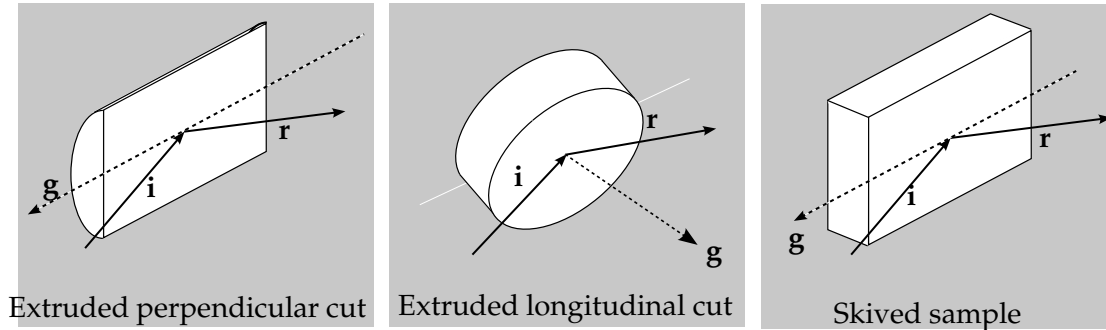
Figure 5.6: Representation of the measurement with the extruded longitudinal (a) and transversal (b) cuts and with the skived sample. The vector **g** corresponds to the direction of extrusion and skiving, respectively.

acetone in an ultrasound bath during about 10 min with the exception of the PTFE sample 5 mm thick. To reduce the water content in the samples they were heated in an oven at 50°C during about 1 hour. Then they were transfered to the chamber and kept in vacuum, during at least one day, before measurement.

Two samples were carved from a PTFE molded sheet from the Fluoroseals®. One sample was polished, the other was not, thus it is possible to establish the effect of the polishing in the reflectance distribution.

The two extruded samples were taken from an extruded rod with 20 mm diameter. They were cut along and transversally to the direction of extrusion respectively. The transversal cut is such that the direction of extrusion is parallel to the plane of incidence (figure 5.6).

The expanded PTFE should be handled carefully and should not be squeezed or pressed as this may alter its reflectance properties, thus it cannot be polished.

In the surface of the skived sample the scratches made by the cutting tool of the manufacturing machine (section 1.3) are visible at naked eye. This sample was polished up to the point that these scratches disappear. The measurements were performed in such a way that the direction of cutting is coplanar with the optical plane as shown in figure 5.6.

The copolymers of the tetrafluoroethyelene share many mechanical, electric and thermal characteristics of the PTFE (section 1.3), thus they can be used as an alternative to the PTFE in scintillation detectors. We measured the copolymers FEP, ETFE and PFA. The samples of these materials where kindly offered by the DuPount® de Nemours. They are originally sheets A4 paper size; their references and thicknesses are shown in the table V. The two surfaces of the sheets used have different optical properties which can be distinguished clearly to the naked eye. One surface is clearly shiny and the specular spike is visible even at the normal incidence. The opposite surface is rougher. The measurements were performed using the smoother surface.

5. REFLECTANCE MEASUREMENTS IN THE VUV AND ANALYSIS

Table V: Characterization of the samples used in the reflection measurements.

	Manufacturer	Reference/ polishing	Thickness (mm)	Dimensions (mm^2)
PTFE Molded	Unknown	Not polished	5.0	30×20
PTFE Molded	Goodfellow[®]	Not polished	2.0	30×20
PTFE Molded	Dongyang[®]	Not polished	7.0	30×20
PTFE Molded	Fluoroseals[®]	Not polished	7.0	35×25
PTFE Molded	Fluoroseals[®]	Polished	7.0	35×25
PTFE skived	Fluoroseals[®]	Polished	2.0	35×24
PTFE extruded ‖	Fluoroseals[®]	Polished	7.0	∅20
PTFE extruded ⊥	Fluoroseals[®]	Polished	7.0	25×20
PTFE expanded	Fluoroseals[®]		7.0	30×21
PTFE 25% glass filled	Fluoroseals[®]		1.000	
ETFE	DuPont[®]	200LZ	0.508	35×25
FEP	DuPont[®]	4500L	1.143	35×25
PFA	DuPont[®]	6000LP	1.524	35×25

A rectangular sample with 35×25 mm^2 was cut from each sheet of the copolymers, they were not polished and were cleaned as above. These samples showed to be transparent to visible light, but proved to be opaque at 175 nm, as concluded from the fact that no light was detected by the PMT when the goniometer is in the configuration of the measurement of the transmitted light (see figure 3.1 c)).

Observations with an optical microscope

The extruded and skived samples of PTFE were observed in a optical microscope with different resolutions. The images obtained are shown in the figures 5.7 and 5.8 for two different amplifications. As shown, scratches are clearly seen in the surface. These scratches are more intense in the skived sample than on the extruded samples. In the extruded longitudinal cut the larger scratches have about 10 μm width and are clearly visible at naked eye. The scratches are still visible at larger amplifications although the majority of the surface is occupied by other type of roughness.

(a) Extruded longitudinal cut

(b) Extruded perpendicular cut
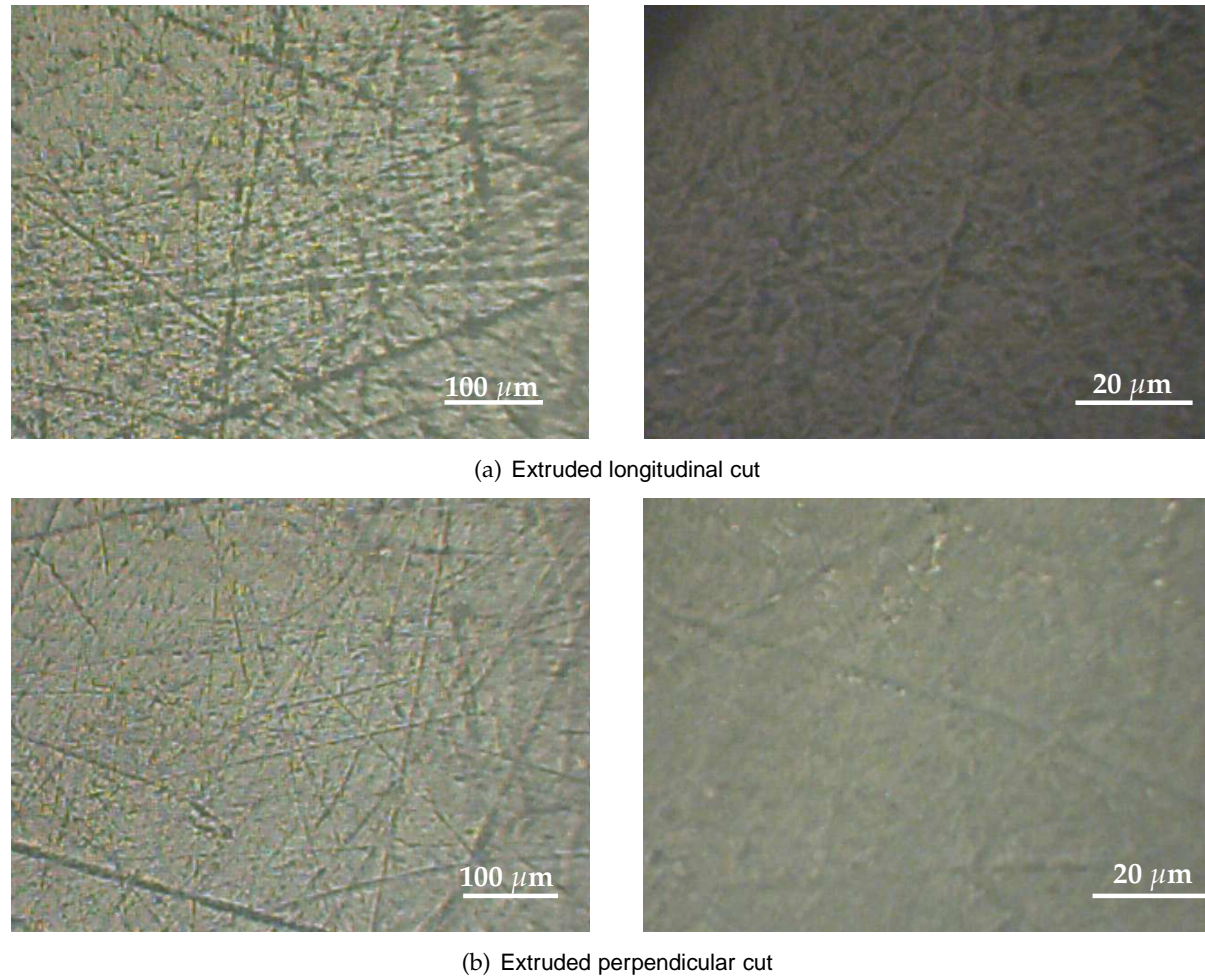
Figure 5.7: Microscopic images obtained by an optical microscope. a) for the extruded transversal and b) extruded longitudinal samples. Two different amplifications are shown.

5. REFLECTANCE MEASUREMENTS IN THE VUV AND ANALYSIS
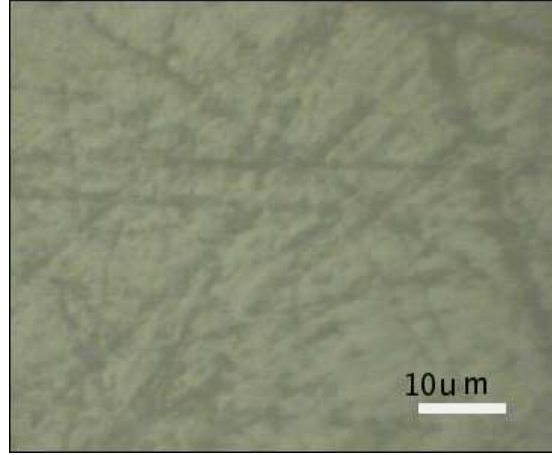
Figure 5.8: Microscopic image obtained by an optical microscope for the skived sample.

PTFE is a soft material with a high viscosity which is difficult to polish without leaving any scratches. As observed in the optical microscope the finishing with sand paper is insufficient to polish the PTFE surfaces. Nevertheless, good results can be obtained when a laser technique is used. Gumpenberger *et al* [188] polished the surface of PTFE with a F_2 laser irradiating at 157 nm, near the absorption edge of the PTFE. He showed that when observed in a SEM microscope the sample showed to be featureless. This could be a good solution to achieve a better polishing of the PTFE surfaces.

The inclination of the samples relative to the plane of measurement was always set to $\phi_i = 0°$, measurements were produced for about seven angles of incidence

Table VI: The apertures ϵ used as controlled by the iris diaphragm placed near the sample.

	Small opening (deg)	Wide opening (deg)
Extruded Longitudinal PTFE	0.343 ± 0.004	0.4776 ± 0.0031
Extruded Transversal PTFE	0.3771 ± 0.0026	0.4778 ± 0.0024
Skived PTFE	0.316 ± 0.005	0.4774 ± 0.0019
Molded PTFE	0.265 ± 0.006	0.3407 ± 0.0012
FEP	0.3165 ± 0.0005	0.4004 ± 0.0018
ETFE	0.3075 ± 0.0009	-

[†] The apertures angles shown are an average for several measurements performed to the incident beam with the same aperture in the iris diaphragm. The errors correspond to the root mean square of the average value.

$\theta_i \in \{0°, 20°, 30°, 45°, 55°, 65°, 80°\}$ as shown in figures 5.13. The light beam set for the measurements are shown in the table VI.

Each angle of incidence was measured for two different apertures of the iris diaphragm placed near the sample: i) a small aperture for the viewing angles near the specular direction (typically $|\nu_r - \nu_i| < 20°$), thus ensuring a good angular definition of the specular lobe and ii) a larger aperture to measure all the viewing angles, thus increasing the photon flux and reducing the statistical errors, specially far from the specular angle. Therefore the specular lobe is measured twice. In each case we verified that the intensity and shape of the specular lobe is always similar, thus ensuring the quality of the experimental data and possible avoiding systematic errors. The aperture angle ϵ was measured by fitting the incident beam (section 3.1) and the values for some samples are listed in the table VI.

Probability distributions of micro-surfaces

The measured light reflected by different kinds of PTFE surfaces, illuminated with xenon scintillation light are shown in the figures 5.10, 5.11 and 5.12. The reflectance distributions show both the presence of specular light and diffused light.

The shape of the specular lobe observed in the data is related with the surface structure function. The surface is modeled by an ensemble of micro-surfaces distributed according to some (usually unknown) probability distribution function $P(\alpha)$ (see section 4.2).

We compared the predictions based on two possible probability distribution func-
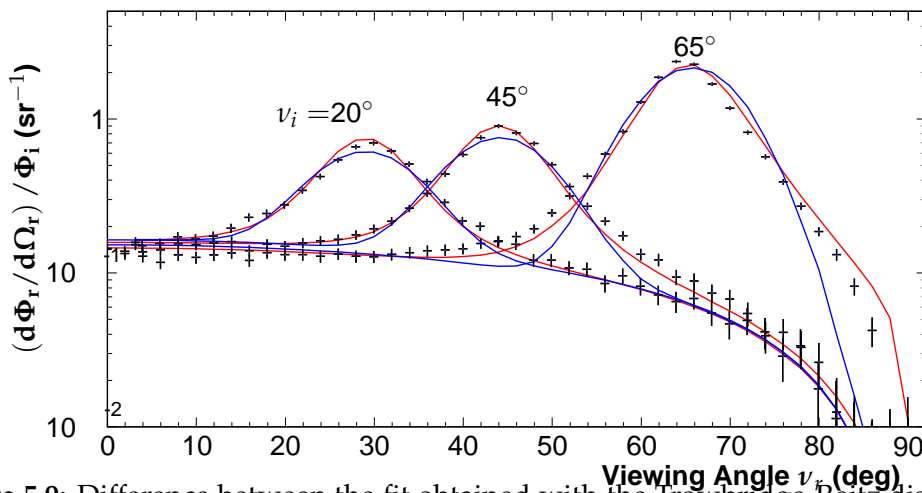
Figure 5.9: Difference between the fit obtained with the Trowbridge-Reitz distribution (red curves) and the Cook-Torrance distribution (blue curves).

5. REFLECTANCE MEASUREMENTS IN THE VUV AND ANALYSIS

Table VII: Values of the fitted for skived PTFE, using two different probability distribution functions, as indicated

Probability Distribution Function	n	ρ_l		χ^2
Trowbridge-Reitz	1.51	0.58	$\gamma = 0.064$	3.4
Cook-Torrance	1.43	0.59	$m = 0.069$	5.5

tions: i) the Cook-Torrance function for V shaped micro-surfaces, P_{CT}, which is approximately gaussian for small roughness (section 4.2), and ii) the function deduced by Trowbridge-Reitz for ellipsoidal shaped micro-surfaces [164], P_{TR} (section 4.2).

In the figure 5.9 we compare two fits of the BRIDF to the experimental data of skived PTFE for the angles $\theta_i = (30°, 45°, 65°)$. The only difference between the two functions is the probability distribution of normals, the P_{CT} in one case and the P_{TR} in other, for the angles of incidence not shown in this figure the comparison is similar. The values of the parameters obtained in the fit are shown in the table VII. Clearly the Trowbridge-Reitz distribution describes the data much better[1]. It has a significantly lower χ^2 compared to the Cook-Torrance distribution. The tails are underestimated by the Cook-Torrance distribution, a difference that is more pronounced for larger angles of incidence. Consequently the index of refraction fitted assuming the Cook-Torrance distribution is artificially low.

The same comparison can be established for the data shown in the figures 5.10, 5.11 and 5.12. Therefore, we adopted this probability distribution function of Trowbridge-Reitz in all what follows unless otherwise stated.

Reflectance distributions for the fluoropolymers

The reflectance distributions of the fluoropolymers obtained by different manufacturing methods are shown in figures 5.10, 5.11 and 5.12 along with the fitted curves. In all cases we interpret the data in the framework of geometric optical approximation and fitted the BRIDF function $\varrho(\theta_i, \theta_r, \phi_r)$ (equation 4.111) with free three parameters. The value of these parameters are shown in table VIII for the various PTFE surfaces.

The reflectance distributions show a similar behaviour in all measured types of PTFE (extruded, skived and molded), with the notable exception of the expanded and glass filled PTFE. In fact the reflectance of expanded PTFE appears to be quite different from the rest, with less diffuse reflected light and a much broader specular lobe. The PTFE glass filled does not exhibit diffuse reflection, which might be caused by the

---

[1]In [226] the specular component was described using a Cauchy-Lorentz distribution $P(\alpha) = \frac{1}{\pi}\frac{\gamma}{(\alpha^2+\gamma^2)}$ which has a shape similar to the Trowbridge-Reitz distribution.

absorption by glass content of this material.

Usually the non-polished samples showed a smaller albedo relatively to the polished samples. The albedo of the PTFE not polished (Fluoroseals® samples) is $\rho_l \simeq 0.36$. It increased to $\rho_l = 0.82$ for the molded polished sample. The lowest value for the albedo was obtained for the expanded sample $\rho_l \simeq 0.14$ and the glass filled PTFE has an albedo ρ_l consistent with zero.

As expected, the non-polished samples of PTFE showed a larger value of roughness comparatively to the polished samples. The molded unpolished sample 5 mm thick has the broadest lobe of all the measured samples with $\gamma = 0.154 \pm 0.018$. For the polished samples the roughness obtained was between 0.014 and 0.064 for the molded and skived surfaces, respectively. The expanded PTFE sample has also a broad lobe with $\gamma = 0.146 \pm 0.011$.

The reflectance distributions obtained for three different fluoropolymer surfaces (ETFE, FEP and PFA) are shown in figure 5.13. The values of the fitted parameters are included in table VIII. The reflection distribution of the PFA is similar to the PTFE samples, these two materials are chemically very similar (see figure 1.6) and it is no surprise that they showed similar reflection distributions at 175 nm. The FEP showed a lower value for the diffuse lobe $\rho_l = 0.24$. The ETFE diffuse lobe is very small $\rho_l = 0.07$, which possibly is caused by the low levels of fluorination and the presence of the C-H bound in the material.

The index of refraction obtained is between 1.30 ± 0.09 for the molded sample and 1.49 ± 0.07 for the expanded sample. For the copolymers the index of refraction is between 1.25 (FEP sample) and 1.33 (ETFE sample). Thus the samples with narrower lobes will have a lower index of refraction. In these samples the fit clearly fails to fully describe the tails of the specular lobe. This suggests that the contribution from coherent reflection should also be considered, and cannot be neglected in these cases. Hence, the indices of refraction obtained for these fluoropolymers are under-estimated (table VIII). We will address this issue in a forthcoming section.

Table VIII: Fitted values of n, ρ_l and γ for the samples measured at 175 nm

Fluoropolymer	Manufacturing Method	Data Points	Fitted Parameters			
			n	ρ_l	γ	χ^2_ν
PTFE	Extruded $\perp$ cut [†‡]	570	1.35 ± 0.03	0.73 ± 0.07	0.019 ± 0.010	26
PTFE	Extruded $\parallel$ cut [†‡]	304	1.32 ± 0.06	0.65 ± 0.04	0.033 ± 0.012	19
PTFE	Skived[‡]	618	1.49 ± 0.07	0.580 ± 0.013	0.064 ± 0.006	14
PTFE	Molded[‡]	622	1.30 ± 0.09	0.82 ± 0.09	0.014 ± 0.005	32
PTFE	Molded not polished	238	1.52 ± 0.04	0.36 ± 0.04	0.076 ± 0.003	4
PTFE	Molded (Dongyang®) [††]	2223	1.51 ± 0.07	0.52 ± 0.06	0.057 ± 0.008	10
PTFE	Molded 5 mm	413	1.47 ± 0.04	0.30 ± 0.06	0.154 ± 0.008	4.7
PTFE	Molded 2 mm (Goodfellow®)	577	1.41 ± 0.04	0.42 ± 0.03	0.094 ± 0.014	3.7
PTFE	Expanded	239	1.56 ± 0.05	0.14 ± 0.03	0.146 ± 0.011	1.9
PTFE	Filled 25% Glass	477	1.61 ± 0.06	$-^*$	0.050 ± 0.010	16
PFA		525	1.30 ± 0.06	0.69 ± 0.05	0.012 ± 0.007	26
FEP		350	1.25 ± 0.10	0.24 ± 0.02	0.0092 ± 0.015	45
ETFE		252	1.33 ± 0.12	0.07 ± 0.07	0.007 ± 0.003	46

[†] The "Extruded $\perp$" and "Extruded $\parallel$" refer to cuts perpendicular and parallel to the extrusion direction.

[‡] These samples were polished before the measurement.

[††] These measurements were taken for different surface inclinations.

[‡‡] The filled sample was not fitted with a diffuse lobe.

[*] In this sample it was not observed a diffuse lobe.

Figure 5.10: Reflectance distribution of PTFE produced by the methods indicated, as a function of the viewing angle, for various angles of incidence. The curves are predictions of $\varrho\left(\theta_i, \theta_r, \phi_r\right)$ (eq 4.111) obtained from a global fit to all data points measured for each sample (that is one sample, one fit). The best values of the three parameters n, ρ_l, γ are shown.

143
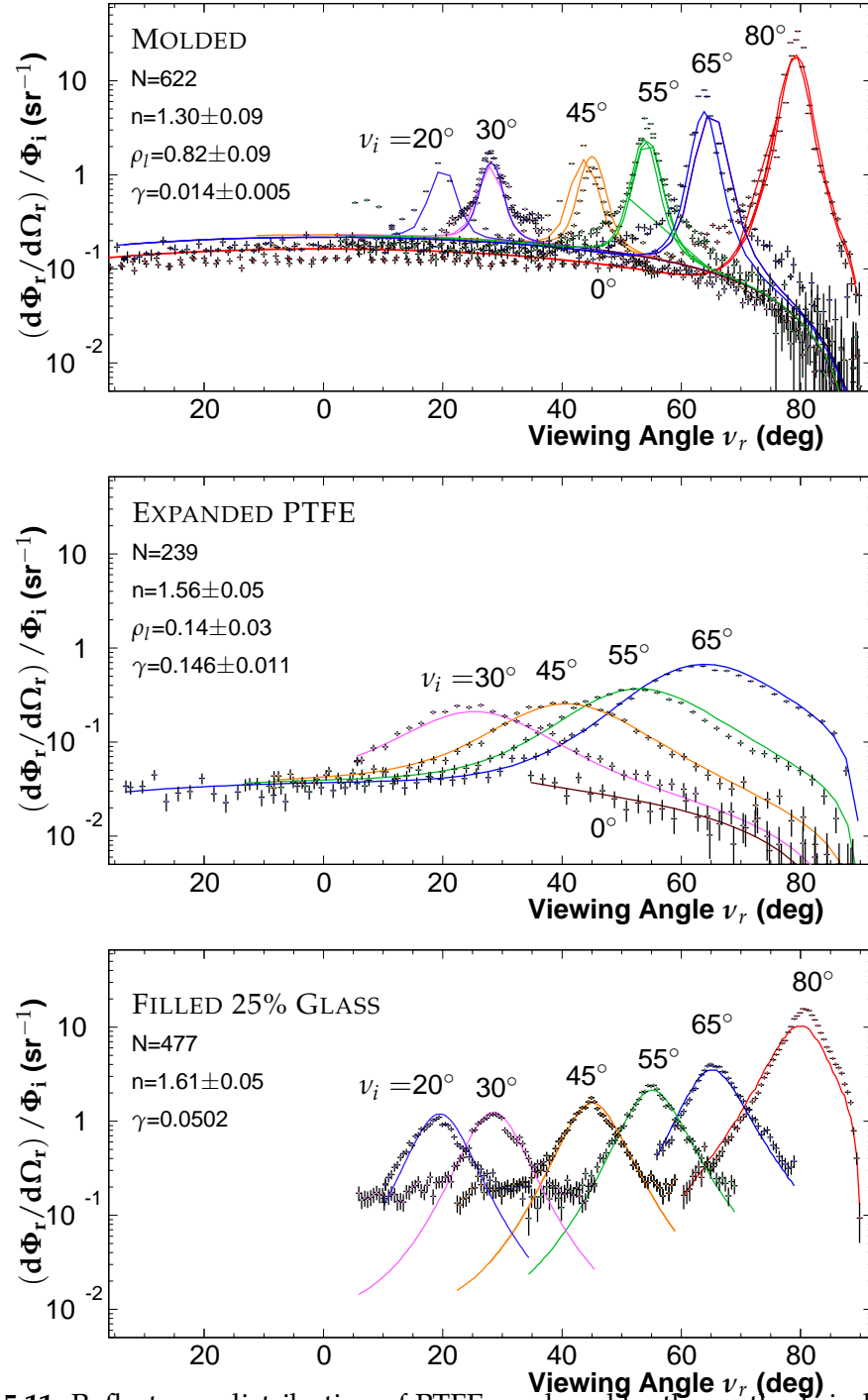
Figure 5.11: Reflectance distribution of PTFE produced by the methods indicated, as a function of the viewing angle, for various angles of incidence. The curves are predictions of $\varrho\left(\theta_i, \theta_r, \phi_r\right)$ (eq 4.111) obtained from a global fit to all data points measured for each sample (that is one sample, one fit). The best values of the three parameters n, ρ_l, γ are shown.

Figure 5.12: Reflectance distribution of PTFE produced by the methods indicated, as a function of the viewing angle, for various angles of incidence. The curves are predictions of $\varrho\left(\theta_i, \theta_r, \phi\right)$ (eq 4.111) after a global fit to all data points measured for each sample, to the best values of the three parameters n, ρ_l, γ.
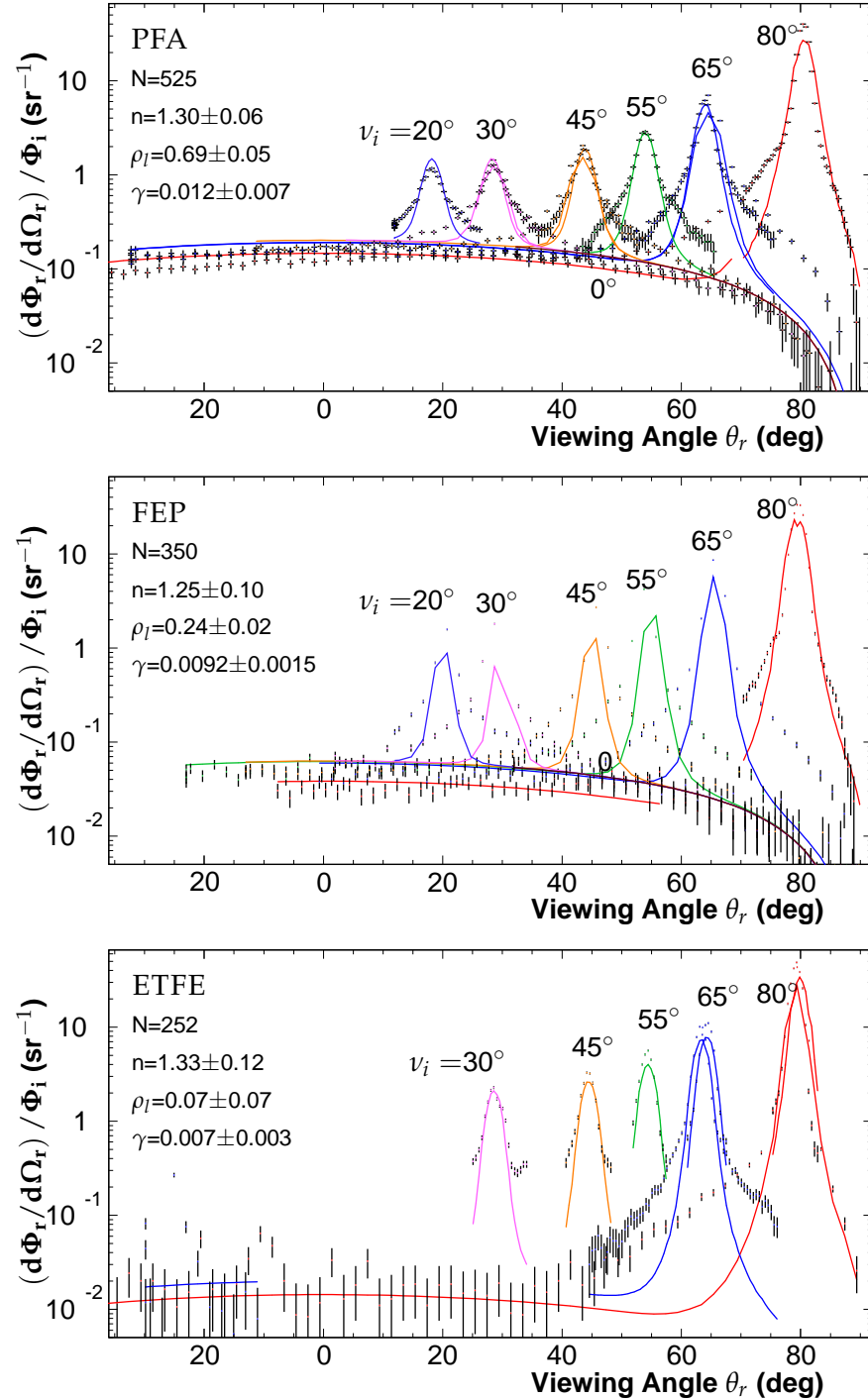
Figure 5.13: Reflectance distribution for the fluoropolymers PFA, FEP and ETFE as a function of the angle of incidence, measured in the plane of incidence $\psi = 0°$. The curves are predictions of $\varrho\left(\theta_i, \theta_r, \phi\right)$ (eq 4.111) after a global fit to all data points measured for each sample, to the best values of the three parameters n, ρ_l, γ.

Measurement of the reflectance out of the plane of incidence

In the previous sections we discussed the measurements made in the plane of incidence, for an inclination of $\psi = 0°$. Nevertheless, it is important to measure the reflectance outside the plane of reflectance to verify the consistency of the results obtained.

The samples used for this measurement were all taken from an unpolished sheet of molded PTFE sheet from Fluoroseals$^{®}$, with a thickness of 5 mm. Each sample was set to a specific inclination relative to the plane of incidence. The aperture of the incident beam used is 0.450±0.007° for the following directions of incidence ν_i and for the surface inclinations, ψ indicated

$$\nu_i \in \{0°, 20°, 30°, 45°, 55°, 65°, 80°\} \otimes \psi \in \{0°, 3°, 11°, 20°\}$$

The BRIDF function ϱ was fitted to the entire data set with all combination of angles (2223 points in total), with three free parameters, yielding for unpolished molded-PTFE: $n = 1.51 \pm 0.07$, $\rho_l = 0.52 \pm 0.06$ and $\gamma = 0.057 \pm 0.08$. A subset of these results is shown in Fig. 5.14, for the angles indicated. The curves represent the reflectances predicted by the overall fit to all data points measured, including the measurements out of the plane of incidence. The model that is behind ϱ seems to reproduce the main features observed in the data, despite the fact that data at high angles of incidence are included in the fit. The last point should be emphasized since in many other studies of the problem of describing the reflectance the models used cannot be used for angles larger than 60°.

These results show that for $\psi_i \geq 10°$ the specular lobe is highly suppressed, whereas the intensity of the diffuse component does not change significantly, as would be expected for a consistent data set. Moreover, these results were obtained with different samples showing that the results are reproducible.

The index of refraction for this sample is compatible with the index of refraction obtained for the skived sample. In both situations the specular lobe is not underestimated meaning that the index of refraction is not underestimated.
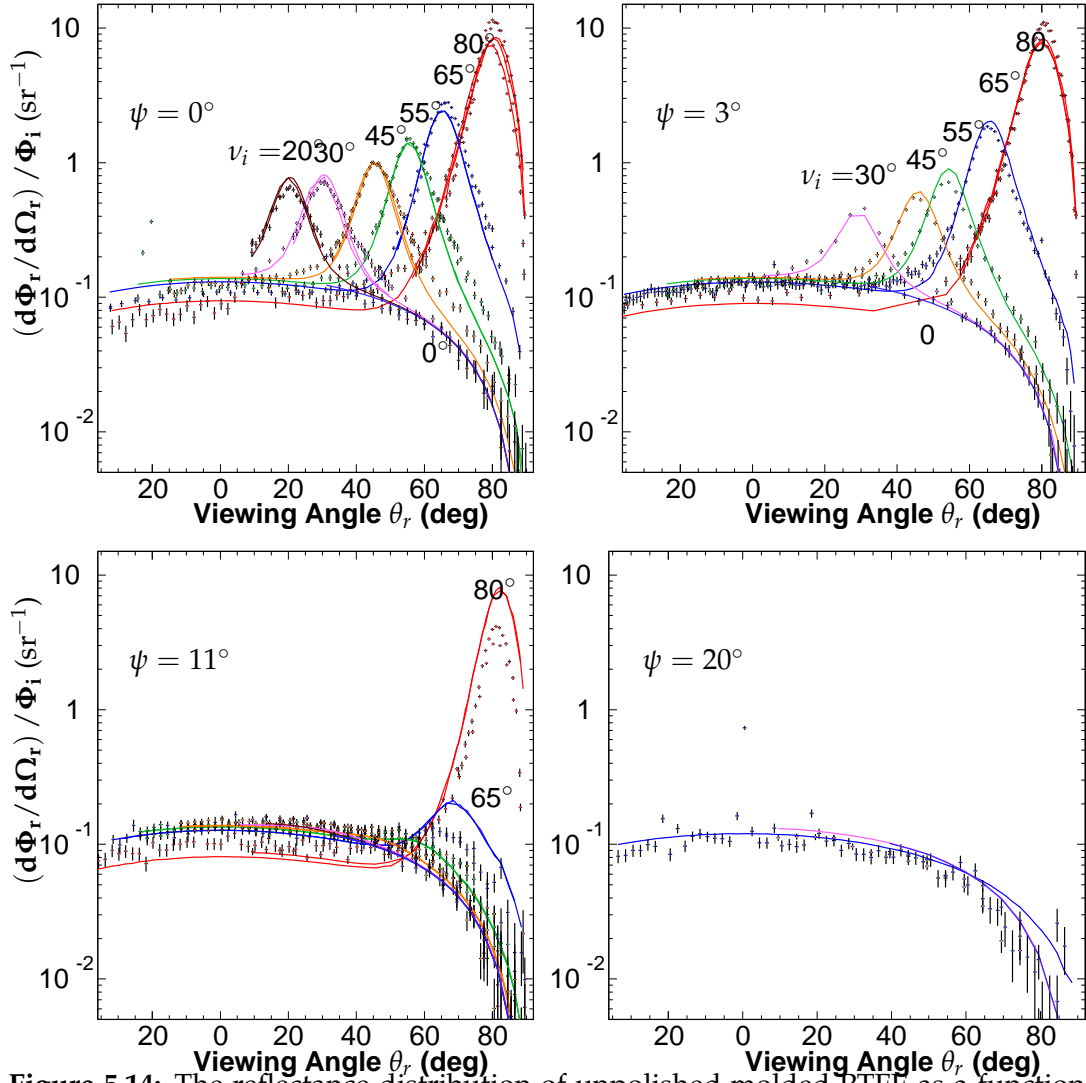
Figure 5.14: The reflectance distribution of unpolished molded PTFE as a function of the viewing angle (in degrees) and for the surface inclinations shown in the graphic. The curves represent the predicted reflection upon an overall fit of the function ρ to the entire data set (2223 data points in total), with three free parameters. The fitted parameters have values: $n = 1.51 \pm 0.07$, $\rho_l = 0.52 \pm 0.06$, $\gamma = 0.057 \pm 0.008$.

5.4 The Coherent Reflection

The observed reflectance distributions for smoother samples show clearly the presence of a specular spike, corresponding to the coherent reflection. This is especially notorious at large angles of incidence $\theta_i > 80°$. Thus it is necessary to include this component in the description of these reflection distributions.

Analysis of the specular spike contribution with the angle of incidence

As discussed in the section 4.6, we parameterize the importance of the coherent reflection applying a factor Λ. This parameterization has been suggested by some authors to be independent of the direction of incidence and is as such currently implemented in the Geant4 simulation package (see chapter 6 and [227]). However, as it is possible to assert from the figure 5.15, this parameterization does not describe the results obtained and contradicts the theory of reflection (see section 4.3). The intensity of the specular spike is overestimated for low angles of incidence and underestimated at the higher angles. Thus the data show as expected that the intensity of the coherent reflection increases with the angle of incidence and the approximation to a fixed ratio is not correct.

Given that relative intensity of the specular lobe $\Lambda = \varrho_C / (\varrho_C + \varrho_S)$ changes with the angle of incidence, we should write (see equation 4.109)

$$\varrho = \varrho_D + \Lambda(\theta_i) FG\delta \left(\mathbf{v} - \mathbf{i}' \right) + (1 - \Lambda(\theta_i)) \frac{PFG}{4\cos\theta_i} \tag{5.7}$$

The dependence of Λ with the angle of incidence and roughness of the surface can be obtained with the equation 4.47 which is dependent of the height distribution function P_z of the surface. This function is not known *a priori* for a particular surface. Therefore, to study the dependence of Λ with the angle of incidence we need to perform a fit for each angle of incidence individually, with three parameters (n, γ, Λ). The parameter ρ_l is already known from the previous fit (it is related with the diffuse reflection not with the specular), thus this parameter was fixed and n, γ and Λ minimized individually for each angle of incidence. The standard deviation is evaluated for each parameter.

The dependence of the parameters $n\,(\theta_i)$ and $\gamma\,(\theta_i)$ with the angle of incidence is consistent with a constant, as expected. Therefore, both the n and γ that characterize the samples are obtained using a weighted mean[1]. These results, shown in the table IX, place the refraction index of the PTFE at $\lambda = 175$ nm between 1.47 and 1.50 (except for the cases of expanded and fiberglass sample PTFE). The index of refraction of the ETFE is then 1.467 a value close to that of PTFE. Both the PFA and FEP have indices of refraction of about 1.41, significantly lower than the PTFE samples. The roughness parameter

---

[1]The weighted mean is obtained using $\langle n \rangle = \frac{\sum_{i=1}^{N}\left(n_i/\sigma_i^2\right)}{\sum_{i=1}^{N}\left(1/\sigma_i^2\right)}$ where i corresponds to each angle of incidence. The same procedure was applied to γ.
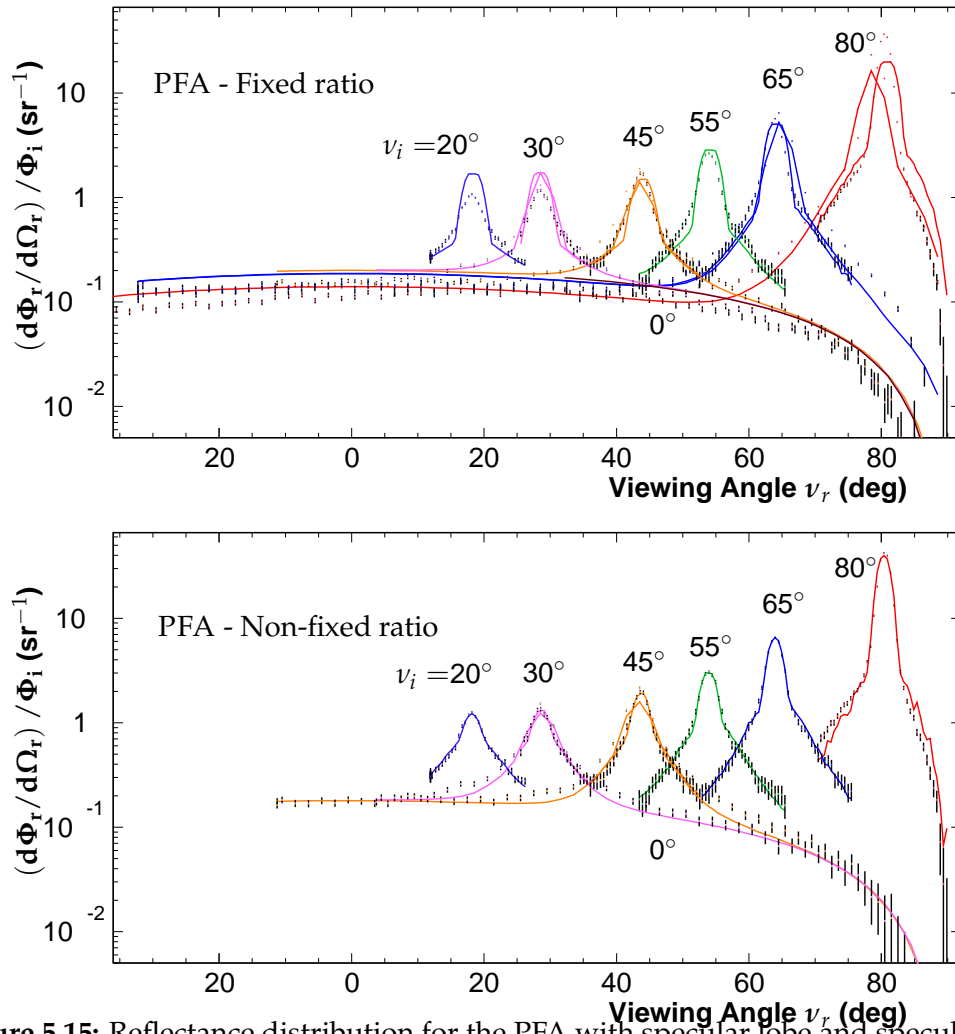
Figure 5.15: Reflectance distribution for the PFA with specular lobe and specular spike with fixed a ratio (a) and non-fixed ratio (b).
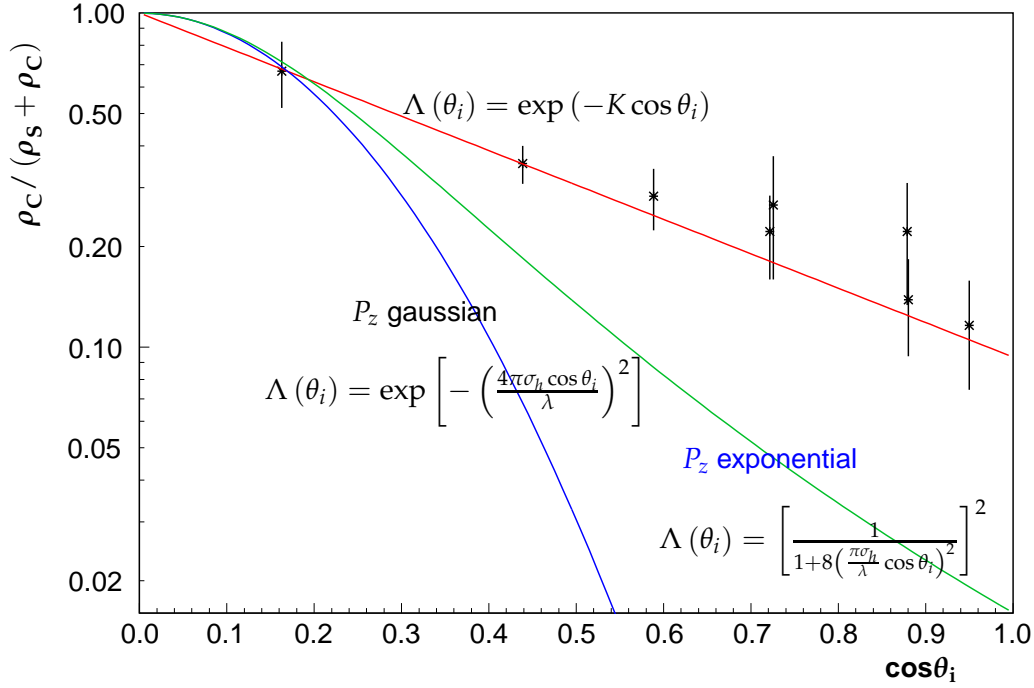
Figure 5.16: Relative intensity of the coherent reflection as function of $\cos\theta_i$ for the PFA. The points shown correspond to the intensity of the coherent reflection obtained in the fits to each angle of incidence. The curves were computed using different functions for $\Lambda(\theta_i)$, gaussian, exponential and the empirical function $\exp(-K\cos\theta_i)$. The parameters σ_h or K were obtained using a global fit with all angles of incidence.

γ has increased significantly relative to the fit if the coherent reflection is neglected and now is close to the values obtained to the rougher samples (skived and unpolished samples). On the other hand, it was observed that Λ, the relative intensity of the specular spike ($\varrho = \varrho_C / (\varrho_C + \varrho_S)$), varies significantly with the angle of incidence as shown in the figure 5.16 for a sample of PFA.

From this analysis we can try to obtain empirically a possible dependency of $\Lambda(\theta_i)$ on the angle of incidence. To find this dependence, a global fit is performed to all angles of incidence measured with a specific dependence for the function $\Lambda(\theta_i)$. The results of this analysis are shown in table X for different realizations of $\Lambda(\theta_i)$. The dependences were calculated for a gaussian and an exponential height distribution of the surface irregularities. The predicted relative intensity of the specular spike Λ for these two distributions is discussed in the chapter 4.3. The curves predicting the Λ dependency are compared with the values of $\Lambda(\theta_i)$ obtained previously in the fit for each angle of incidence (see figure 5.16). However, as it is possible to assert from figure 5.16 these

5. REFLECTANCE MEASUREMENTS IN THE VUV AND ANALYSIS

Table IX: Average values of n and γ. These results are obtained by fitting each angle of incidence with three parameters (n, γ and Λ), then a weighted mean is performed for each sample with the values obtained in each angle of incidence.

Sample	n	γ
PTFE Extruded $_\perp$	1.473±0.025	0.0517±0.0012
PTFE Extruded $_\parallel$	1.470±0.016	0.0693±0.0030
PTFE Molded	1.502±0.022	0.0622±0.0032
PFA	1.413±0.010	0.0475±0.0012
FEP	1.4087±0.0024	0.0594±0.0020
ETFE	1.467±0.031	

Table X: Fitted Parameters for reflection distribution of PFA using different attenuation functions.

P_z	$\Lambda\left(\theta_i\right)$	n	ρ_l	γ	σ_h/λ or K	χ^2
GOA model	0	1.30	0.69	0.012	-	27
Gaussian	$\exp\left(-g^2\right)$	1.392	0.653	0.0373	0.30	7.9
Exponential	$\left[1/\left(1+g^2/2\right)\right]^2$	1.424	0.653	0.0411	0.417	8.6
Empirical	$\exp\left(-K\cos\theta_i\right)$	1.438	0.641	0.0551	0.422	3.4

The function g, also called the optical roughness is given by $g = \left(4\pi n_1\sigma_h/\lambda\right)\cos\theta_i$.

two distributions do not describe the results obtained because they fall faster with $\cos\theta_i$ than it is observed in the data.

The data of the figure 5.16, clearly suggests that $\Lambda\left(\theta_i\right)$ decreases exponentially with $\cos\theta_i$. Therefore, let's assume empirically that

$$\Lambda = \exp\left(-K\cos\theta_i\right) \tag{5.8}$$

K is an empirical function that controls the intensity of the specular spike. The χ_ν^2 of the fir largely improves if this equation is used (to 3.3, see table X). This dependency is however empirical and is not possible to infer immediately the dimensions and distribution of the roughness of the surface.

The reflectance distributions with the empirical model

The analysis described before was applied for the other smooth surfaces that were measured, considering a function Λ given by the equation 5.8. The values of the parameters obtained in the global fit using all the angles of incidence are shown in the table XI. The χ^2_ν decreased significantly in all cases relative to the results obtained in the model with a diffuse plus a specular lobe. The χ^2_ν of the molded PTFE decreased from 32 to 7.4, the χ^2_ν of the FEP sample decreased from 45 to 5.7. Thus the introduction of this contribution is essential for a correct description of the observed reflectance distributions.

The intensity of the specular spike predicted by the equation 5.8 is shown in figure 5.17 as a function of $\cos\theta_i$. The value for the parameter K was obtained in a global fit using all angles of incidence. These curves are compared with the intensity of the specular spike obtained in the fits for each angle of incidence. The dependency $\Lambda = \exp\left(-K\cos\theta_i\right)$ seems to be well supported by the data from all surfaces measured.

These samples have different levels of intensity of the specular spike, with K ranging from 1.0 to 4.3. They have also different treatments of the surface, the PTFE samples were polished and the copolymers FEP, PFA and ETFE were not polished, yet all exhibit a similar form for $\Lambda\left(\theta_i\right)$. Thus, the function of eq. 5.8 is not restricted to a specific type of surface.

The observed width of the specular spike is merely instrumental due to the aperture of the incident beam and of the aperture of the photo-detector used in the experiment. Both in the fit and in the data the specular spike has a certain width. The coincidence between the width of the specular spike observed in the data and in the fit shows that

Table XI: Fitted values of n, ρ_l, γ and K for the samples indicated measured with light of 175 nm and with the relative intensity of the specular spike given by $\Lambda = \exp\left(-K\cos\theta_i\right)$.

Sample	Fitted Parameters				
	n	ρ_L	γ	K	χ^2_ν
Extruded ($\perp$) PTFE	1.50±0.03	0.69±0.07	0.055±0.007	3.0±0.3	8.4
Extruded ($\parallel$) PTFE	1.46±0.04	0.63±0.07	0.066±0.008	4.3±0.5	8.5
Molded PTFE	1.45±0.04	0.74±0.07	0.049±0.015	1.7±0.2	7.4
PFA	1.44±0.04	0.69±0.05	0.057±0.006	2.4±0.4	3.3
FEP	1.41±0.02	0.22±0.04	0.052±0.009	1.2±0.4	5.7
ETFE	1.44±0.03	0.13±0.01	0.040±0.010	1.0±0.2	11
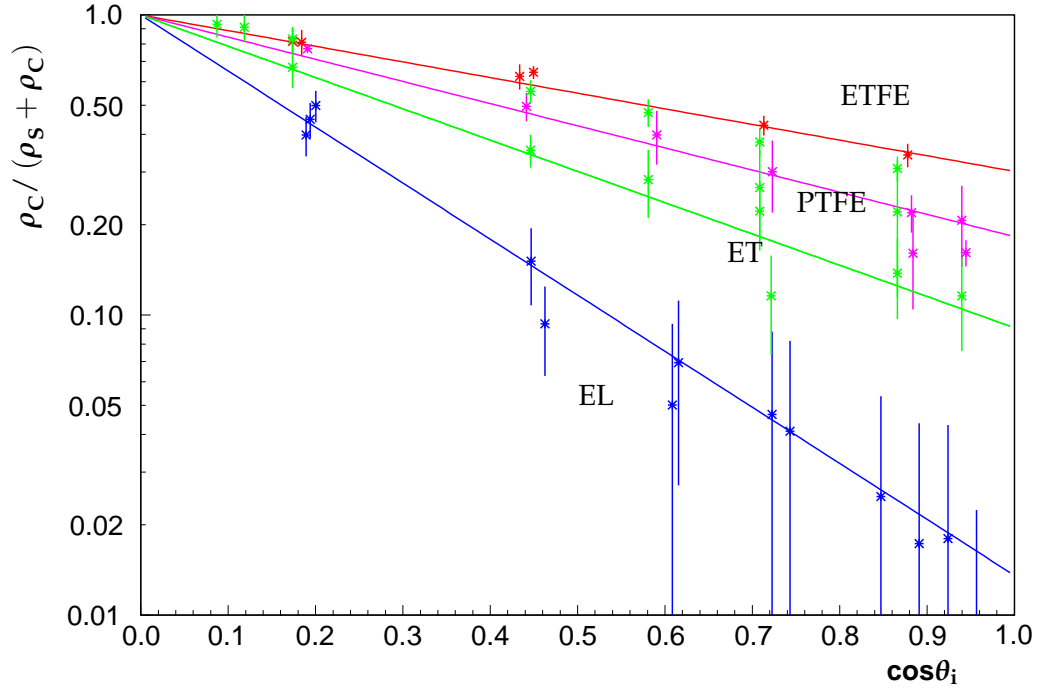
Figure 5.17: Relative intensity of the coherent reflection as function of $\cos\theta_i$ for the different samples measured. The points shown correspond to the intensity of the coherent reflection obtained in the fits to each angle of incidence. The curves were computed using the equation 4.109 with the K obtained in the fit using all the angles of incidence measured. EL and ET indicate the measurements performed to the extruded longitudinal and transversal cuts respectively. The PTFE shown corresponds to the molded polished PTFE.

the geometric features of the experiment are well described.

The values for the index of refraction are placed between 1.44 and 1.50 for the PTFE. These values are similar to the ones obtained in the fits to each angle of incidence and are consistent with the values obtained for the rougher samples.

The two extruded samples show different reflection parameters. The longitudinal surface cut has a wider specular lobe and less diffuse light than the transversal surface. The index of refraction is similar and contained within the error. It is however not possible from this analysis to assert that these differences are caused by the internal disposition of the PTFE grains.

The values obtained for the albedo are smaller comparatively to the results obtained with the model with only two contributions (the albedo decreased about -0.08 for the extruded $\perp$ PTFE and -0.12 for the molded PTFE). In the GOA model the intensity of
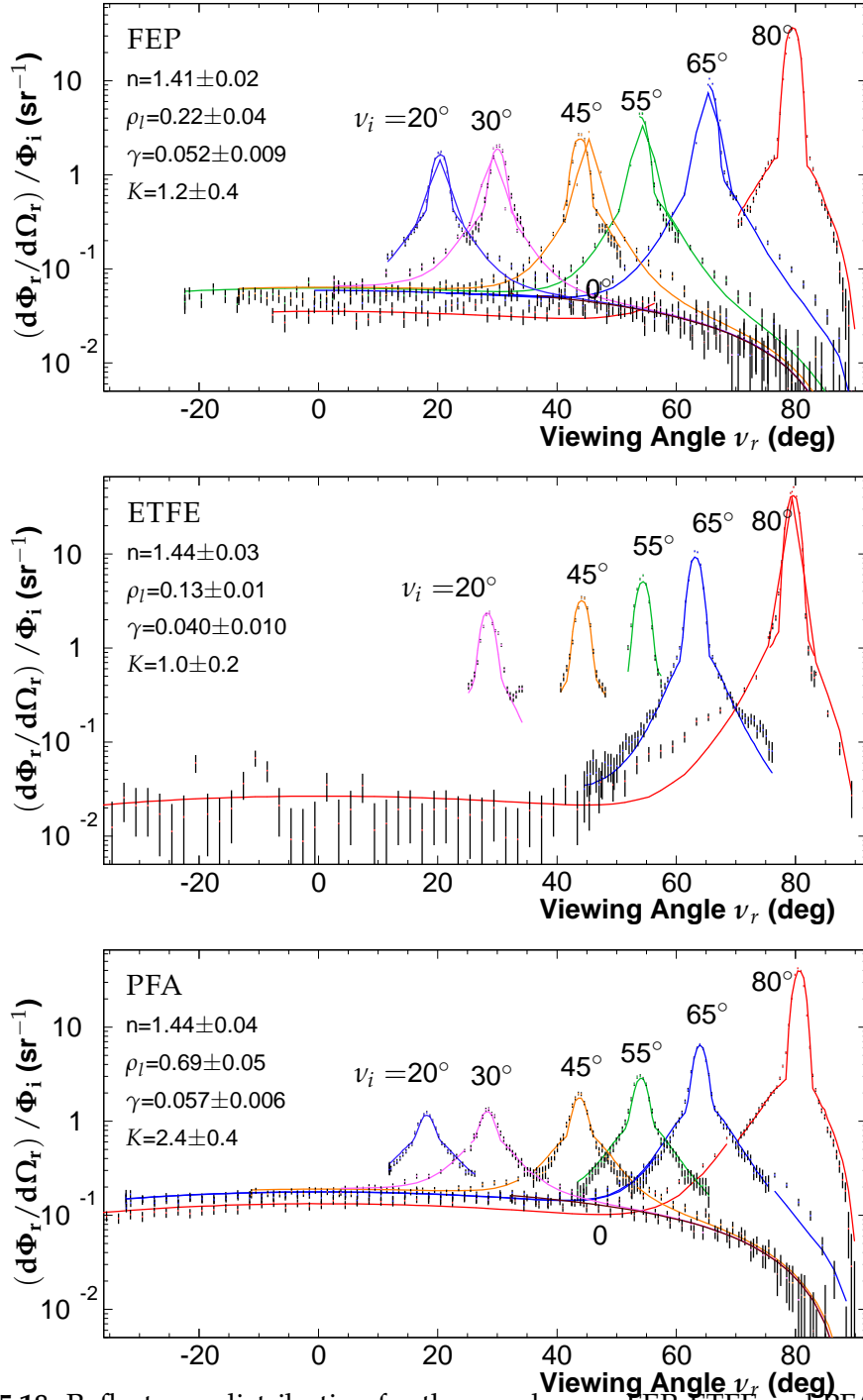
Figure 5.18: Reflectance distribution for the copolymers FEP, ETFE and PFA as a function of the viewing angle, for various angles of incidence. The curves are a global fit obtained with the equation 4.110c for the Trowbridge-Reitz function, assuming a dependency of $\Lambda(\theta_i) = \exp\{-K\cos\theta_i\}$.
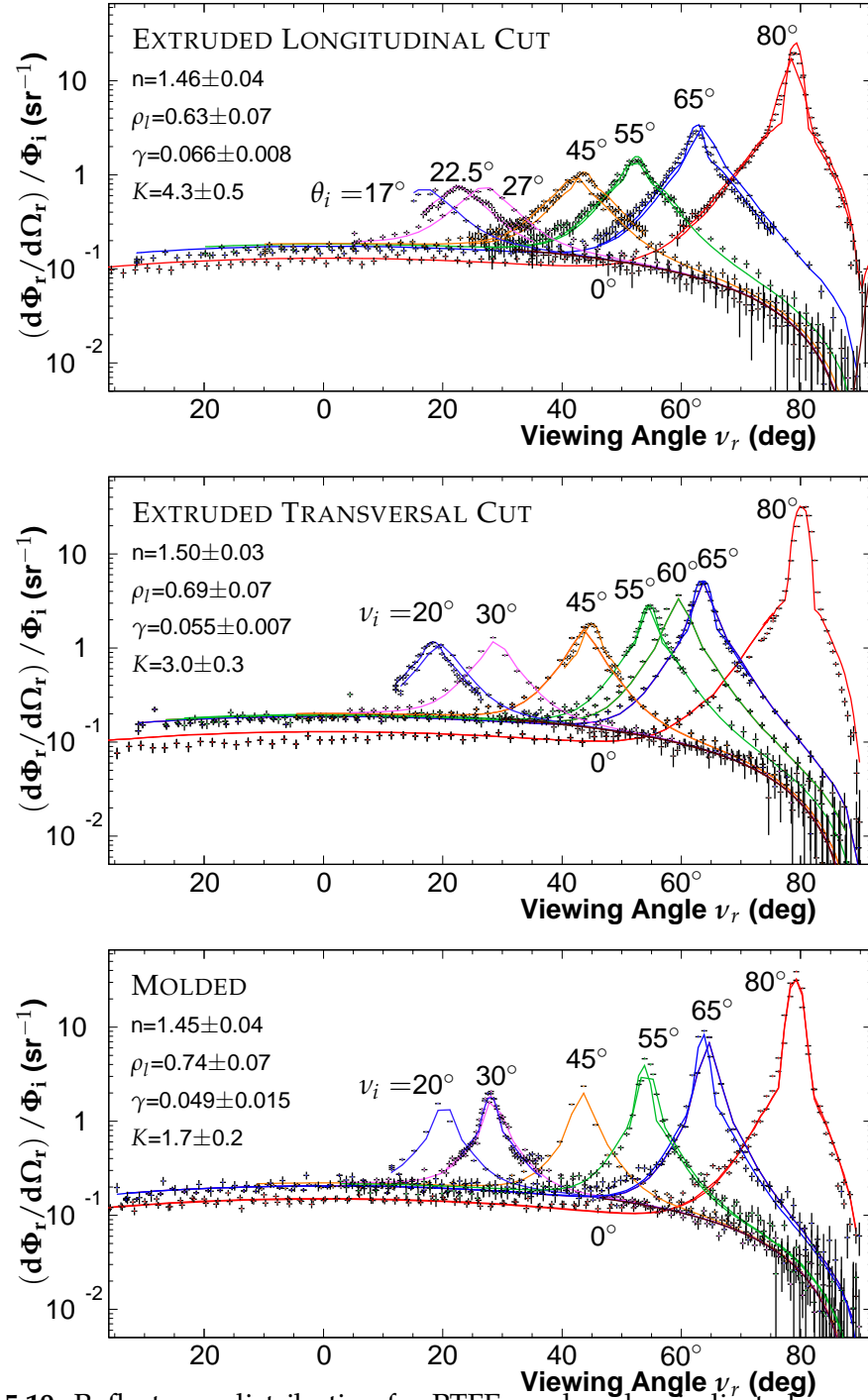
Figure 5.19: Reflectance distribution for PTFE produced as indicated, as a function of the viewing angle, for various angles of incidence. The curves are a global fit obtained with the equation 4.110c for the Trowbridge-Reitz function, assuming a dependency of $\Lambda\left(\theta_i\right) = \exp\left(-K\cos\theta_i\right)$.

the diffuse lobe is artificially increased to better describe the specular lobe. Thus the results obtained for the albedo in the smoother samples are more similar to the ones of rougher samples if the coherent contribution is included.

The roughness and the albedo
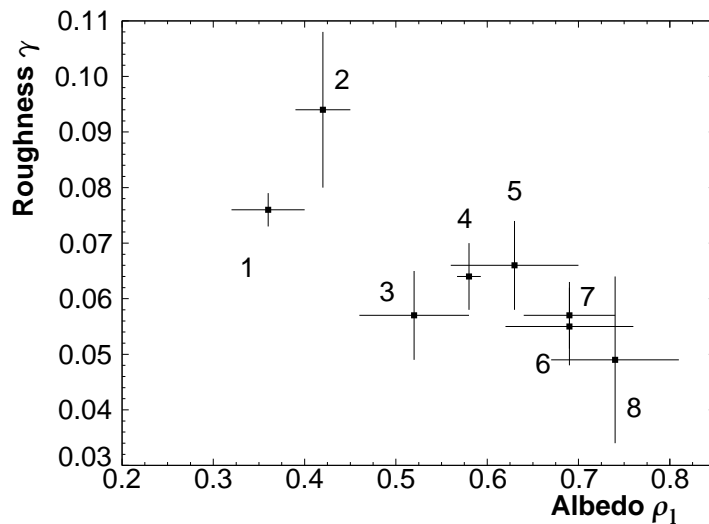
Figure 5.20: Correlation between the roughness parameter γ and the albedo ρ_l of the surface for different surfaces of PTFE/PFA. The samples included in this plot are: 1: Molded PTFE Fluoroseals® not polished, 2: Molded PTFE 1 mm thickness (Goodfellow®), 3:Molded PTFE Fluoroseals®, 4: Skived PTFE, 5:Extruded Perpendicular cut, 6:Extruded Transversal cut, 7 Molded PTFE Polished, 8: PFA

In figure 5.20 it is shown the correlation between the albedo of the surface and the roughness. The samples with the lower values of the roughness appear to have a higher value for the total diffuse albedo. In fact, the samples of PTFE with the highest values for the albedo (samples 4-7) were all polished.

The increase of the reflectance observed by polishing the surfaces may be caused by removal of asperities in the surface or the removal of contaminants that existed in the surface or possibly due to the fact that the surface material transforms from a crystalline to a glassy state when polished. A similar effect was observed by [188] for PTFE surfaces polished using the F_2 laser. They observed this effect for wavelengths between 200 nm and 800 nm and being more intense at lower wavelengths.

5.5 Reflectance Distributions for Different Models of Reflectance

In the previous section we analysed data and its interpretation based on the application of a BRIDF function that incorporates three components of reflection, in this chapter we analyse some aspects of the surface modelling.

Analysis of the model of diffuse reflection

According to the Lambert law the reflectance of the diffused light is independent of the angle of reflection (section 4.5). However the Fresnel correction term of Wolff (section 4.5) introduces a dependence of this component with the angle of incidence. In fact, the intensity of the diffuse lobe is proportional to the light transmitted beyond the surface, thus when the angle of incidence increases the intensity of the diffuse lobe decreases. This effect is well noticed in the experimental data (figures 5.10, 5.11, 5.13, 5.25). To appreciate fully this effect we show in the figure 5.21 the reflection distribution of a surface molded of PTFE illuminated with light of $\lambda = 560$ nm. As shown, the fit follows closely the data and the reflectance decreases with the increasing of the angle of incidence in a non-linear way. If illuminated from $\nu_i = 65°$, the surface has a reflectance of $\varrho = 0.3$ sr^{-1} towards the normal direction. This value decreases to $\varrho = 0.26$ sr^{-1} at $\nu_i = 72.5°$ and 0.21 sr^{-1} at $\nu_i = 80°$, respectively.

The second effect that can be observed is the rapid decreasing of the reflectance
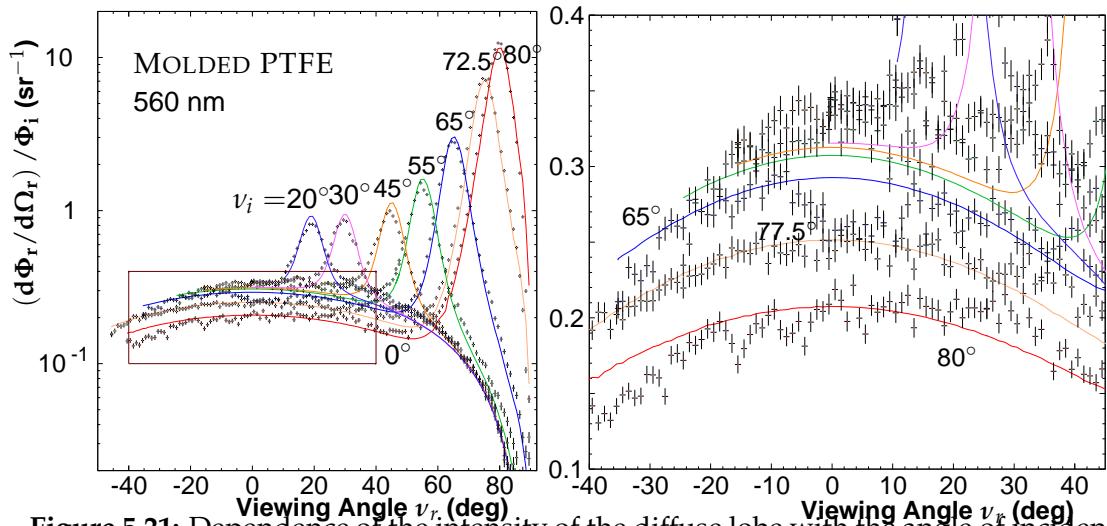
Figure 5.21: Dependence of the intensity of the diffuse lobe with the angle of incidence. The figure in the left shows the reflectance distribution for a sample of molded PTFE measured at $\lambda = 560$ nm for different angles of incidence. The reflectance distribution inside the box was amplified and shown in the right figure. As shown the fit agrees with the Wolff Fresnel correction.

Table XII: Correction of the diffuse law due the roughness of the surface for different values of the roughness of the surface (γ). Two different functions $P(\alpha)$ are used, the Torrance-Sparrow distribution (equation 4.98 with $\sigma = 0.6\gamma$) and the Trowbridge-Reitz distribution (equation 4.105).

| Sample | γ | Torrance-Sparrow $\rho_L (1 - \mathcal{A} + \mathcal{B})$ | | Trowbridge-Reitz $\rho_L G (\mathcal{N}_0 - \tan\theta_i \tan\theta_r \cos\phi\mathcal{N})$ | |
		$\mathcal{A}$	$\mathcal{B}$	$\mathcal{N}_0$	$\mathcal{N}$
Expanded PTFE	0.146	0.011	0.035	0.964	0.046
Skived PTFE	0.064	0.0022	0.0072	0.990	0.012
Extruded PTFE	0.033	0.00059	0.0020	0.997	0.0039
PFA	0.009	0.000046	0.00015	0.9996	0.00040

with ν_r comparatively to the Lambertian law. However, it is not possible to observe this effect from the data because the PTFE has larger index of refraction than the air and the term $F\left(\sin^{-1}\left[\frac{n_0}{n}\sin\theta_r\right], \frac{n_0}{n}\right)$ is almost constant with θ_r

We have computed the correction introduced by the roughness of the surface for two different micro-facet distributions, the Torrance and Sparrow distribution (eq. 4.18) described using the parametrization developed by Oren-Nayar (eq 4.98) and also the Trowbridge-Reitz distribution (eq. 4.23) with a correction factor given by the equation 4.105. In both cases the correction due the roughness of the surface given by the Oren-Nayar model is very small for the values of roughness (γ) observed. Table XII shows the values of the factors $\mathcal{A}$ and $\mathcal{B}$ for the Oren-Nayar parametrization and the angular $\mathcal{N}(\gamma)$ and constant term $\mathcal{N}_0(\gamma)$ of the equation[1] 4.105 for the different fluoropolymers surfaces using the value of γ extracted from the respective fit In the parameter $\mathcal{B}$ of the Oren-Nayar parametrization we have set $H(\cos\phi_r)\cos\phi_r\sin\alpha\tan\beta = 1$, thus we show the maximum value of this parameter for a specific roughness. The highest values of $\mathcal{A}$ and $\mathcal{B}$ are for the expanded PTFE, which is also the sample that has the highest value of γ corresponding to the roughest surface. For the Torrance-Sparrow distribution the highest values of the factors $\mathcal{A}$ and $\mathcal{B}$ is 0.011 and 0.035, respectively which means that at least in these cases the correction is very small indeed. A larger effect of the surface roughness is observed if we use the Trowbridge-Reitz distribution. The correction[2] to the lambertian law is significant for the expanded sample, nevertheless for the majority of the surfaces measured the correction introduced is still very small.

---

[1]These terms were defined as $\varrho_1 = \rho_L G'(\theta_i) G'(\theta_r) (\mathcal{N}_0(\gamma) - \tan\theta_i \tan\theta_r \cos\phi_r \mathcal{N}(\gamma))$

[2]The effect of the shadowing-masking is not fully described in the equation 4.105 due to the approximation $G \simeq G'(\theta_i) G'(\theta_r)$

5. REFLECTANCE MEASUREMENTS IN THE VUV AND ANALYSIS

The optical constants

Table XIII: Coefficient of extinction, penetration depth of PTFE for light at various wavelengths. Measurements taken by several authors.

Wavelength (nm)	Penetration depth (nm)	Coefficient of extinction	Ref
125	0.1	99.50	[229]
157	161	0.078	[229]
193	666	0.023	[229]
633	2.8×10^6	3.8×10^{-5}	[230]

Table XIV: Comparison between the fitted values of the reflectance of PTFE and PFA obtained in the fits with and without the extinction coefficient κ.

Sample	n	κ	$\zeta^{\dagger}$ (nm)	ρ_l	γ	K	χ^2_ν
Without κ							
Skived PTFE	1.49±0.07	-	-	0.580±0.013	0.064±0.006		13.9
Molded PTFE	1.45±0.04	-	-	0.74±0.07	0.049±0.015	1.7±0.2	7.4
PFA	1.44±0.04	-	-	0.69±0.05	0.057±0.006	2.4±0.4	3.3
With κ							
Skived PTFE	1.48±0.04	< 0.12	> 116	0.600±0.034	0.060±0.005		14.5
Molded PTFE	1.44±0.029	< 0.17	> 82	0.75±0.06	0.046±0.006	1.8±0.2	8.2
PFA	1.42±0.06	< 0.16	> 87	0.66±0.05	0.054±0.008	2.4±0.4	3.4

† Attenuation length (or penetration depth) it can be obtained using the relation $\zeta = \lambda/(4\pi\kappa)$.

The results shown for the fluoropolymers were fitted assuming that the extinction coefficient, κ is negligible in the computation of the Fresnel equations. However, in general, the Fresnel equations depend of the extinction coefficient κ (eq. 4.5a and 4.5b). For the dielectrics κ is usually very low in the visible spectra, $\kappa \simeq 0$ and $F(n,\kappa) \simeq F(n)$ holds. Nevertheless, in the VUV region of the spectra the coefficient κ can be significant even for dielectrics.

Table XIII lists some published values of the extinction coefficient and attenuation length for the PTFE for various wavelengths. This suggests that, as shown, for the xenon scintillation light the penetration depth in the PTFE should be placed between 161 nm and 666 nm which results in a coefficient of extinction placed between 0.023 and

0.078.

To test if our results are consistent with these measurements the dependence with the extinction coefficient was explicitly introduced in the Fresnel equations. Given the values of the table XIV that indicate that the extinction coefficient increases at the VUV, we added the parameter κ to the fits, specifically to the Fresnel equations, to check the consistency of the analysis and extract the value of κ at 175 nm. The results of these fits are shown in the table XIV. The fitted values of the extinction coefficient show that $\kappa < 0.2$ for the samples analysed, but the uncertainties are compatible with $\kappa \simeq 0$ The other parameters do not change significantly with it in result of κ, meaning that the correlation is certainly small, namely with n. Hence, it can be concluded that for these samples the absorption length is larger than 200 nm in agreement with what can be expected from the values of the table XIV.

The geometrical attenuation factor

As was discussed in the section 4.4, the geometrical effects leading to masking and shadowing are increasingly important at grazing angles. In fact, the effect of the geometrical shadowing-masking factor, G, is only visible for large angles of incidence, $\nu_i \gtrsim 80°$.
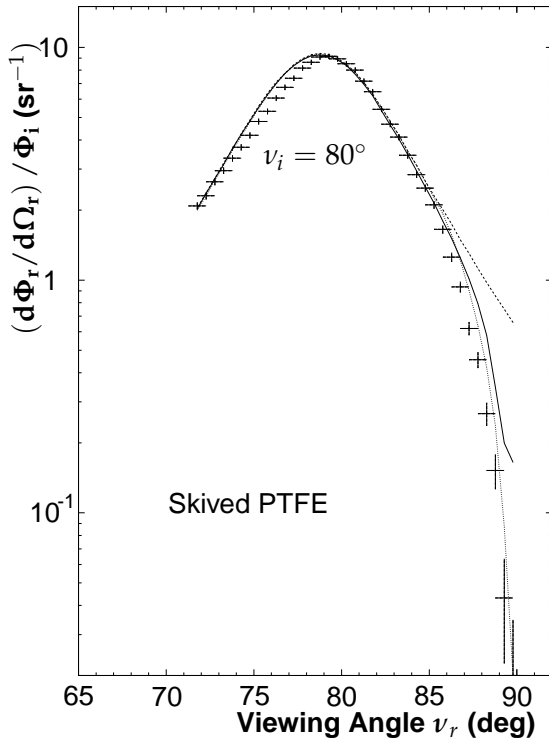
Figure 5.22: The reflectance distribution of the skived PTFE illuminated with an angle $\nu_i \simeq 80°$. The fits simple out the effect of the masking and shadowing factors on the reflectance. Three different fits are superimposed for comparison: a) without any shadowing-masking correction (dashed line); b) with the Torrance-Sparrow correction (dotted line); c) with the correction of the Smith theory applied to the Trowbridge-Reitz probability distribution that is standard in this work (solid line).

The measured data were fitted considering the following geometrical attenuation factors: i) the *de facto* attenuation factor adopted in this work using the Smith function and the Trowbridge-Reitz distribution of slopes (eq. 4.81), ii) the factor predicted by Torrance-Sparrow model and iii) a fit considering no shadowing/masking. These fits are shown in the figure shown below. As observed in this figure above $v_r > 85°$ the curve without the shadowing factor diverges clearly from the data whereas the curves with the shadowing-masking factor follow more closely the data. The Smith and Torrance-Sparrow model corrections are small however.

5.6   The Hemispherical Reflectances

The parameters shown in the tables VIII and XI are sufficient to fully describe the function ϱ in the hemisphere. With this function, the reflectance can be obtained for any beam geometry. Here we are mainly interested in the directional-hemispherical and bi-hemispherical reflectances (defined in the appendix A).

The directional-hemispherical reflectance

The directional-hemispherical reflectance factor $R(\theta_i)$ is obtained for a specific angle of incidence by integration of the BRIDF for all possible viewing directions (equation A.18). The shadowing-masking function introduced in the BRIDF function does not decrease the amount of reflected light. Therefore, the reflectance is computed through the following integration

$$R(\theta_i, \phi_i) = \int \frac{1}{G} \varrho(\theta_i, \phi_i, \theta_r, \phi_r) \sin \theta_r d\theta_r d\phi_r \qquad (5.9)$$

when the factor $1/G$ is not removed from the specular lobe and diffuse lobe it is observed an unexpected decreasing in the reflectance of the specular components at very small grazing angles.

The directional-hemispherical reflectance of skived PTFE given by the previous integral is represented in Fig. 5.23 in solid lines as a function of the angle of incidence, for the specular and diffuse reflection components separately. The results show that the reflectance in the PTFE/gas interface is nearly constant up to about 60° where the value of the reflectance is about +5% above its value at normal incidence. Then it increases rapidly and at low grazing angles the reflectance approaches one. The behaviour of the diffuse reflectance contribution can be understood to closely follow the Fresnel equations for the refracted wave, multiplied by the albedo of the surface. The diffuse lobe is dominant for the majority of the angles of incidence. However, the specular lobe increases gradually with θ_i and becomes dominant for $\theta_i \gtrsim 80°$.

Figure 5.24 shows the reflectance of polished molded PTFE sample using the parameters used in ϱ shown in table XI, separately for the different components of the reflection. As above, the three reflection components that are shown remain constant up

to $\theta_i \sim 60°$. For the normal incidence the diffuse reflection dominates all along with a hemispherical reflectance of 68%, whereas the specular lobe and specular spike amount to only 2.8% and 0.5% respectively. The two specular components become more intense than the diffuse lobe only for angles larger than 80°. The specular lobe dominates over the specular coherent peak at low angles of incidence. For angles larger than 70° the coherent spike becomes the main component of the specular reflection in vacuum.

The same exercise was made for all samples whose reflectance distributions were measured using the BRIDF fitted. These values for the directional hemispherical reflectances are summarized in table XV for $\theta_i = 0$ and $\theta_i = 65°$. The uncertainties indicated for the directional-hemispherical reflectance result from error propagation of K, ρ_l and n. The parameter γ has a small effect in the computation of the hemispherical reflectances. It has only a signable effect for angles of incidence larger than 80°, for $\gamma < 0.1$. For these angles the γ decreases the intensity of the specular components. Almost in all cases the reflectance is dominated by the diffuse component, with the diffuse lobe accounting for more than 90% of the reflection at $\theta_i = 0°$, for all materials with the exception of expanded PTFE (70%) and the glass filled sample. At $\theta_i = 65°$ the diffuse lobe still accounts for more than 80% of the reflection (48% for expanded PTFE).

The expanded PTFE shows the lowest reflectance of all measured (17% at normal incidence). This fact might suggest that VUV light is being absorbed by oxygen molecules trapped in the pores of the material, underneath the surface [231]. Although this topic
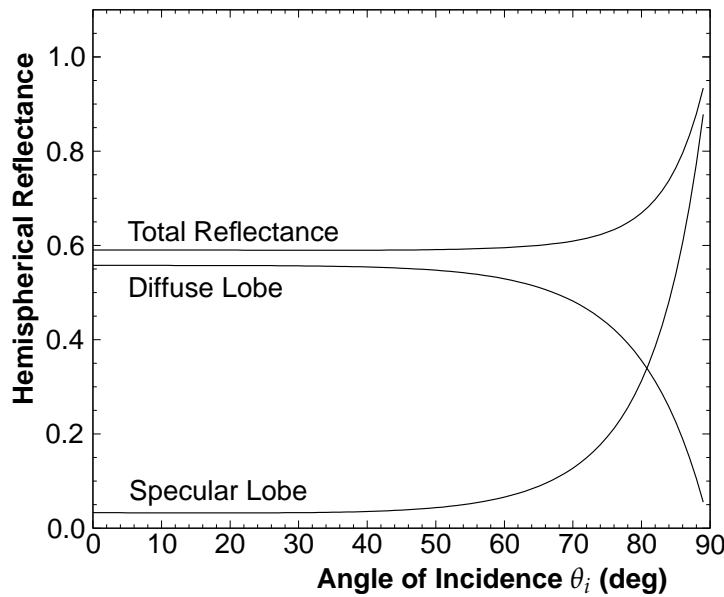
Figure 5.23: The directional-hemispherical reflectance of the skived PTFE sample as a function of the angle of incidence θ_i (in degrees), for light of λ=175 nm, in vacuum.

Table XV: Directional-hemispherical reflectance of various types of PTFE, manufactured as indicated, for two angles of incidence $\theta = 0°$ and $\theta = 65°$.

	$R_{diffuse}$	$R_{specular}$	R_{spike}	R_{total}
		$\theta_i = 0°$		
Molded PTFE (Dongyang®) ‡	0.45 ± 0.05	0.041 ± 0.009	-	0.49 ± 0.04
Molded PTFE 5 mm	0.26 ± 0.07	0.035 ± 0.004	-	0.29 ± 0.07
Molded PTFE (Goodfellow®)	0.38 ± 0.02	0.031 ± 0.005	-	0.41 ± 0.02
Expanded PTFE	0.11 ± 0.03	0.048 ± 0.007	-	0.16 ± 0.03
Glass Filled PTFE	-	0.053 ± 0.008	-	0.053 ± 0.008
Skived PTFE	0.507 ± 0.014	0.040 ± 0.007	-	0.543 ± 0.010
Extruded $\perp$ PTFE †	0.60 ± 0.07	0.038 ± 0.004	0.0024 ± 0.0008	0.64 ± 0.07
Extruded $\parallel$ PTFE†	0.59 ± 0.06	0.034 ± 0.005	0.0005 ± 0.0003	0.62 ± 0.07
Molded Polished PTFE	0.69 ± 0.05	0.028 ± 0.005	0.0062 ± 0.0015	0.72 ± 0.07
PFA††	0.62 ± 0.05	0.030 ± 0.005	0.0020 ± 0.0013	0.66 ± 0.05
FEP	0.20 ± 0.03	0.020 ± 0.004	0.009 ± 0.003	0.23 ± 0.03
ETFE	0.118 ± 0.010	0.020 ± 0.003	0.012 ± 0.003	0.15 ± 0.009
		$\theta_i = 65°$		
Molded PTFE (Dongyang®)‡	0.41 ± 0.02	0.115 ± 0.012	-	0.53 ± 0.02
Molded PTFE (5 mm)	0.24 ± 0.06	0.113 ± 0.005	-	0.35 ± 0.06
Molded PTFE (Goodfellow®)	0.35 ± 0.02	0.106 ± 0.009	-	0.46 ± 0.02
Molded Expanded	0.10 ± 0.03	0.111 ± 0.009	-	0.21 ± 0.03
Glass Filled PTFE	-	0.136 ± 0.009	-	0.136 ± 0.009
Skived PTFE	0.465 ± 0.013	0.120 ± 0.009	-	0.585 ± 0.010
Extruded $\perp$† PTFE	0.55 ± 0.06	0.085 ± 0.006	0.036 ± 0.005	0.67 ± 0.06
Extruded $\parallel$† PTFE	0.53 ± 0.05	0.093 ± 0.008	0.018 ± 0.004	0.64 ± 0.05
Molded Polished PTFE	0.61 ± 0.05	0.055 ± 0.005	0.056 ± 0.007	0.73 ± 0.05
PFA††	0.57 ± 0.05	0.065 ± 0.007	0.041 ± 0.007	0.68 ± 0.05
FEP	0.19 ± 0.03	0.04 ± 0.008	0.064 ± 0.008	0.29 ± 0.03
ETFE	0.109 ± 0.009	0.037 ± 0.006	0.072 ± 0.007	0.219 ± 0.009

† *Extruded$_\perp$ and Extruded$_\parallel$ refer to surfaces cut perpendicular and parallel to the extrusion direction, respectively.*

‡ *Also shown in the figure 5.23 for all the angles of incidence.*

†† *Also shown in the figure 5.24 for all the angles of incidence.*
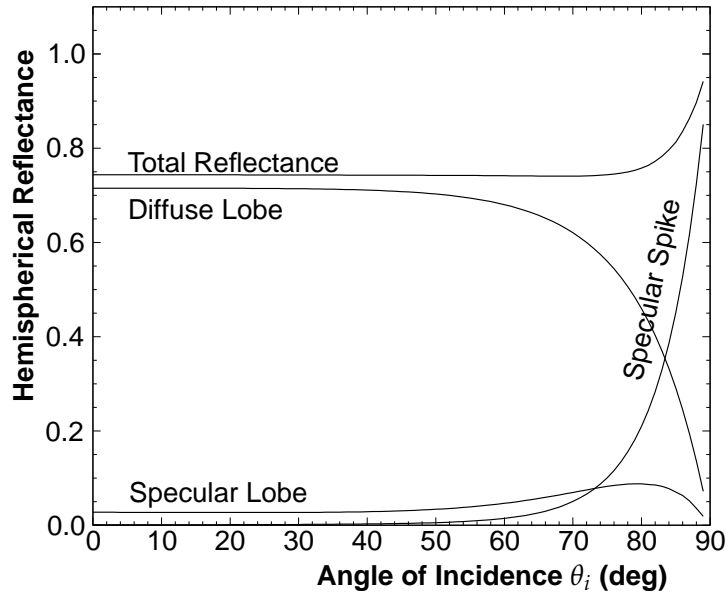
Figure 5.24: The directional-hemispherical reflectance of molded polished PTFE as a function of the angle of incidence θ_i for light of $\lambda = 175$ nm.

needs a further study. It can be concluded from these results that the reflectance of polished-molded-PTFE is about 72% ($\theta_i = 0°$), whereas the corresponding non polished surface has a reflectance of only 49%. Both are dominated by diffuse reflection.

At the normal incidence, the reflectance of the specular spike is below 1% of the total integrated reflectance in all cases studied, with the exception of the ETFE. The specular lobe represents between 2% and 4% of the total reflectance and the intensity of the diffuse lobe is dominant in all cases.

Both the FEP and ETFE have low reflectance due their low diffuse component. Nevertheless, in both materials the diffuse component is still dominant at $\theta_i = 0°$ representing 95% of the total reflectance for the FEP and 76% of the total reflectance for the ETFE.

The bi-hemispherical reflectance

The bi-hemispherical reflectance (defined in the appendix A) for the samples measured is shown in the table XVI. The contribution of the different components of reflection (specular lobe, specular spike and diffuse lobe) is also shown. The reflectance of polished PTFE samples is between 60% and 71% and that of non-polished is between 34% and 58%. Polished surfaces of PTFE have 86% to 88% of the reflected light in the diffuse component. In the surfaces with a higher roughness this value decreases to 73%-85%. Therefore, when the sample is polished the increasing in the reflectance is mainly associated to the increasing of the diffuse component.

Table XVI: Bi-hemispherical reflectance (white-sky albedo) for the measured surfaces. The analysis of the data considered the three contributions to the reflection: the diffuse, the specular lobe and the coherent spike, the later was neglected in the analysis of the rough surfaces.

	R_{diffuse}	R_{lobe}	R_{spike}	R_{total}	$R_{\text{diffuse}}/R_{\text{total}}$ (%)
Skived PTFE[†]	0.488±0.009	0.089±0.008	-	0.577±0.007	85
Molded PTFE (Dongyang®)	0.429±0.038	0.095±0.006	-	0.52±0.05	82
Molded PTFE (5 mm Thick)	0.251±0.029	0.089±0.005	-	0.34±0.04	73
Molded PTFE (Goodfellow®)	0.364±0.014	0.079±0.005	-	0.443±0.016	82
Expanded PTFE	0.117±0.014	0.102±0.005	-	0.219±0.016	54
Filled PTFE 25% Glass	-	0.108±0.005	-	0.108±0.006	0
Extruded ⊥ PTFE[†]	0.55±0.04	0.059±0.003	0.0311±0.0020	0.64±0.05	86
Extruded ∥ PTFE[†]	0.52±0.05	0.063±0.003	0.0225±0.0017	0.60±0.06	86
Molded PTFE [†]	0.625±0.034	0.040±0.004	0.0438±0.024	0.71±0.04	88
PFA	0.570±0.030	0.050±0.003	0.0357 ±0.0033	0.66 ±0.04	87
FEP	0.185±0.017	0.028±0.006	0.0503 ±0.0054	0.263±0.022	70
ETFE	0.110±0.007	0.028±0.003	0.0570±0.0028	0.194 ±0.008	56

These results are obtained by the integration of ϱ for all the incident and viewing directions assuming a diffuse illumination (eq. XVI).

[†] Polished samples

5.7   Reflectance Distribution for Larger Wavelengths

PTFE is considered a good diffuser with a reflectance greater than 98% for visible light [3]. The values published indicate that the reflectance decreases significantly for smaller wavelengths [115] (section 1.4). In the VUV the data are scarce and limited to hemispherical reflectances [4]. Therefore, the reflectance distribution of the PTFE was measured for various wavelengths to study how it changes as the wavelength varies and fill the gap between the VUV and the near visible. This also contributes to check the consistency of our results.

The light is obtained from three light emitting diodes (LED's) emitting at different wavelengths, one in the visible spectra (a green LED), other in the Near Ultraviolet (315±7.5 nm), and the other in the ultra-violet B region (255±7.5 nm). The UV LEDs used in the experiment are from the Roithner LaserTechnik$^®$, their characteristics are shown in the table XVII.

Each LED was introduced in front of the view port of the proportional counter and aligned with the needle. The trigger system was turned off because the light produced by the LED's is continuous. The air does not absorb these wavelengths, thus the chamber did not had to be filled with argon and these measurements can be performed in air. The incident flux observed with these LED's is typically 6×10^6 photons/s within the regime of validity of the photon counting mode.

The reflectance distributions of molded PTFE unpolished (Fluoroseals$^®$) measured with light of wavelengths λ =255, 310 and 560 are represented in figure 5.25. The values of the fitted parameters are shown in table XVIII. The variation of the these parameters with λ is shown in the figure 5.26 together with the directional-hemispherical reflectance at $\theta_i = 0°$. These results show that the albedo of the surface increases with increasing wavelength (figure 5.26(a)), from 0.52 at $\lambda = 175$ nm to 1.06 at $\lambda = 560$ nm, dropping at low wavelengths. This can be explained by the decreasing of the penetration depth with the wavelength, given that the probability of the absorption of the light increases. However, this issue needs further study to understand to what extend the penetration depth is related with the albedo.

Table XVII: Properties of the LED's Used

Manufacturer	Ref.	Emission wavelength	Spectrum half width nm	View angle deg	Optical power output μW
Roithner LaserTechnik$^®$	T9B25*	255	15	10	50
Roithner LaserTechnik$^®$	T9B31*	310	15	10	150
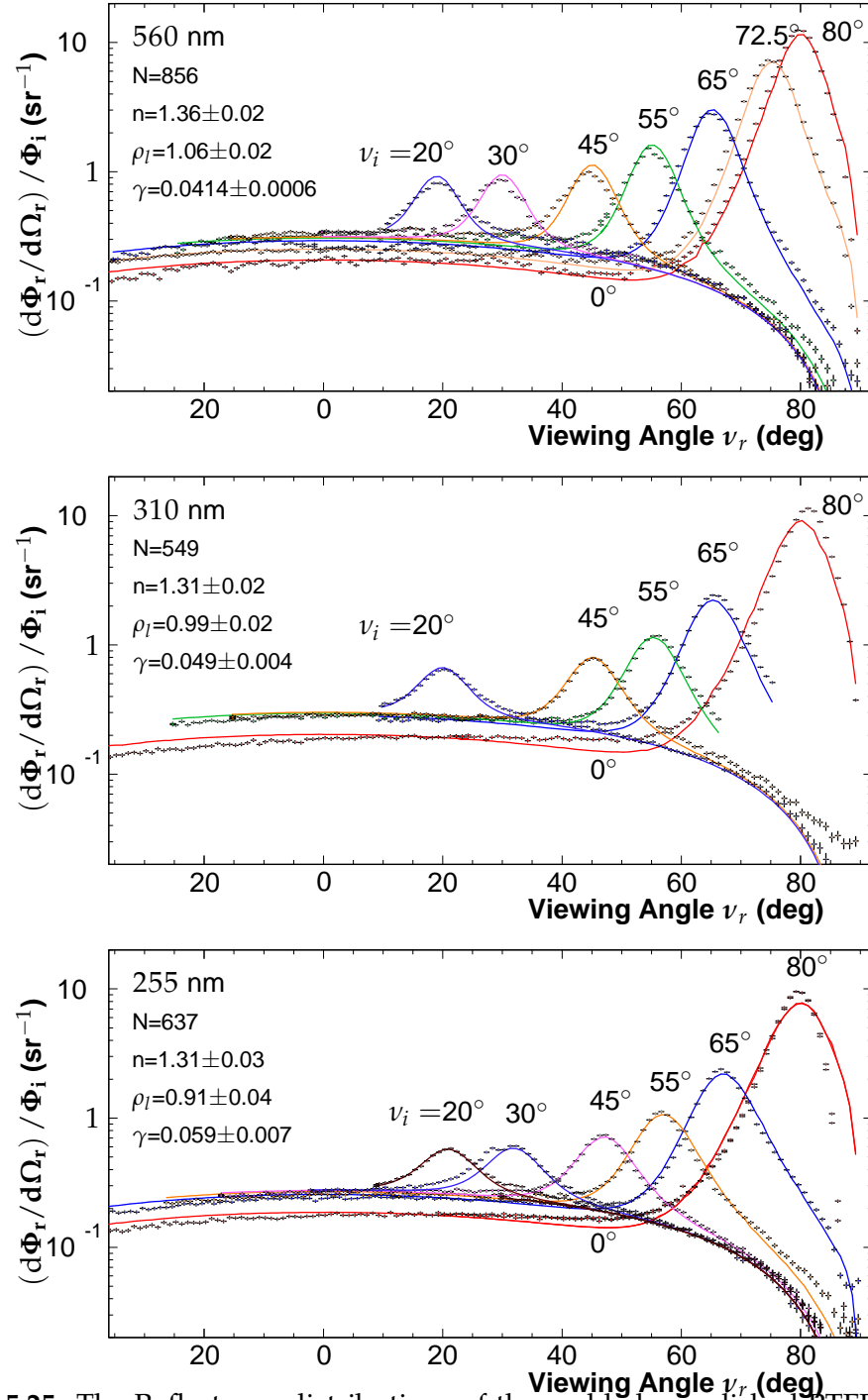
Figure 5.25: The Reflectance distributions of the molded unpolished PTFE measured with the LED's emitting at the wavelengths indicated. The curves show the predictions. The number of data points, N, is also indicated in each plot.

(a) Albedo ρ_l

(b) Index of Refraction n the curve represents a fit with the Lorentz-Lorenz dispersion formula assuming only the absorption edge at 161 nm.

(c) Roughness γ

(d) Directional-hemispherical reflectance R for the normal incidence $\theta_i = 0°$

Figure 5.26: Variation of the parameters of reflection of the molded PTFE unpolished sample with the wavelength. The evolution of the directional-reflectance at the normal incidence is also shown.

5. REFLECTANCE MEASUREMENTS IN THE VUV AND ANALYSIS

Table XVIII: Fitted values of n, ρ_l and γ obtained for a sample of molded PTFE unpolished (Fluoroseals®) for the different wavelengths measured.

Wavelength (nm)	Data Points	n	ρ_l	γ	χ^2
175	2223	1.51 ± 0.07	0.52 ± 0.06	0.057 ± 0.008	10
255	637	1.31 ± 0.03	0.91 ± 0.04	0.059 ± 0.007	5
310	549	1.31 ± 0.02	0.99 ± 0.02	0.049 ± 0.004	12
560	856	1.36 ± 0.02	1.06 ± 0.02	0.0414 ± 0.0006	27

The variation of the index of refraction with the wavelength (i.e. the dispersion curve) is shown in the figure 5.26(b). The index of refraction of the molded PTFE obtained at 560 nm (n=1.361) agrees with published values, which are placed between 1.3 and 1.4 (see section 1.4) which is a good indication of the consistency of the results obtained in this work. The index of refraction drops to 1.31 at 255-310 nm and goes up to about 1.5 at 175 nm. It is expected that the index of refraction increases monotonically with the frequency (normal dispersion, [233]) with the increasing being more intense near the absorption edge. However the uncertainties of the index of refraction values are still high and do not allow a definitive conclusion.

The width of the specular lobe seems to be increasing slightly for smaller wavelengths, but the uncertainties are too high for any definitive conclusion. However in general terms this makes sense, since small wavelengths probe smaller scales of the roughness. Nonetheless any wavelength dependency cannot be understood in the framework of a geometric model of reflection. To do so, a wave base model is required in which the wave nature of the light is taken into account (see section 4.3).

The values for the directional-hemispherical reflectance factor and bi-hemispherical reflectance factor for the various wavelengths measured are shown in the table XIX. For the visible light the directional-hemispherical reflectance of the molded PTFE is about 99% at $\theta_i = 0°$. This is in good agreement with the results published by the National Bureau of Standards [3] and [115]. However, for 255 nm the difference between the values is about 10% and not within the error bars.

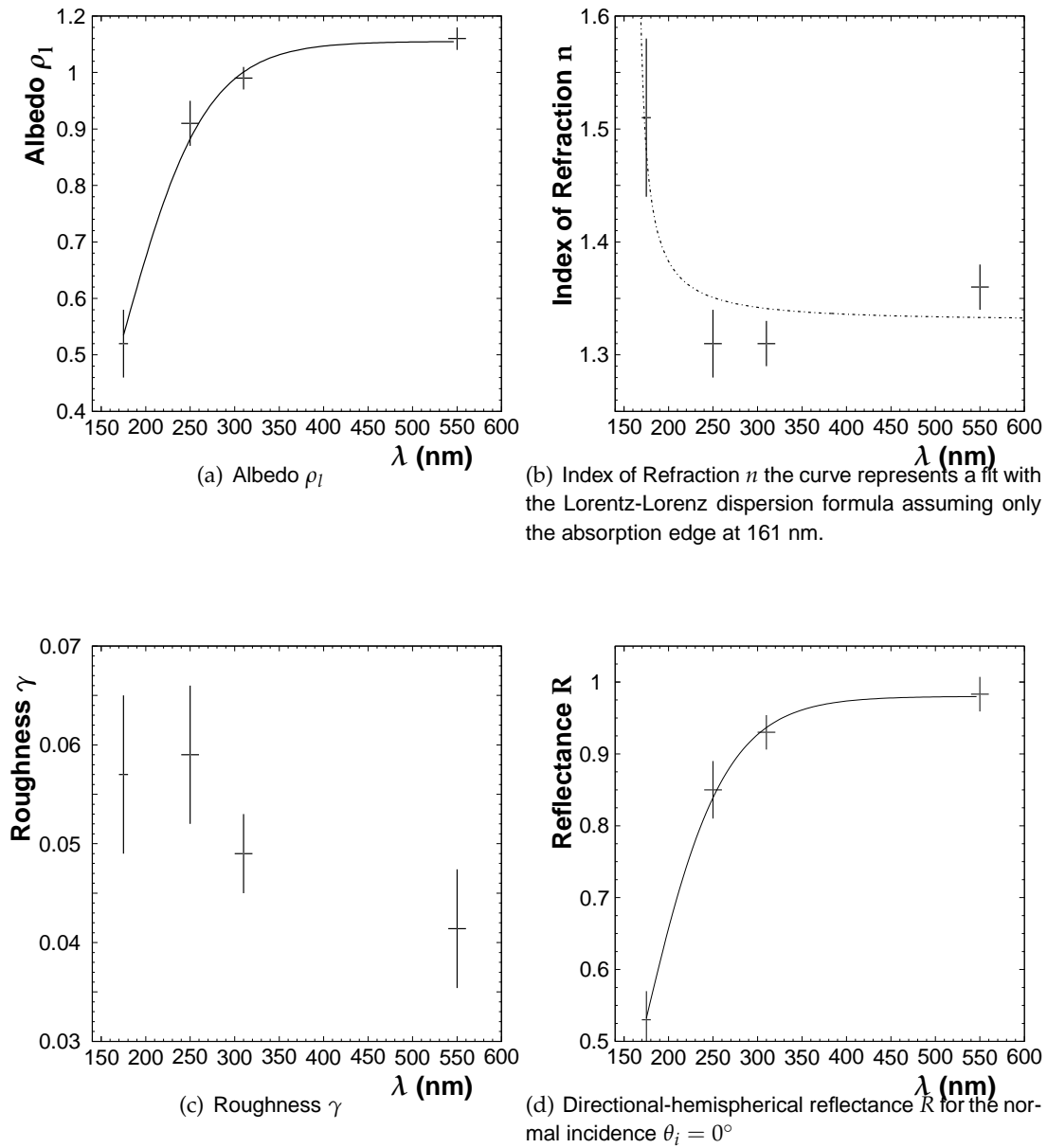The reflectance is mainly diffuse, at λ =560 nm, for $\theta_i = 0°$ we find that 98% of the light observed comes from the diffuse component. When considering the bi-hemispherical reflectance results we concluded that more than 91% of all the reflected light for the wavelengths larger than 200 nm comes from the diffuse component. In fact, PTFE is considered to be a perfect diffuser for visible light and is used as reference standard for other reflectance measurements in the visible [115]. However, the diffuse characteristics of PTFE decrease in the VUV (figure 5.26(d)). At 175 nm and for $\theta_i = 0°$

Table XIX: Directional-hemispherical reflectance at $\theta_i = 0°$ and bi-hemispherical reflectance of the molded polished PTFE for the wavelengths indicated. The reflectance results are compared with the results published by the US National Bureau of Standards (NBS), currently known as NIST, for pressed powder of PTFE [115], when available.

λ (nm)	$R_{diffuse}$	$R_{specular}$	R_{total}	NBS
DIRECTIONAL-HEMISPHERICAL REFLECTANCE θ_i=0°				
175	0.42±0.05	0.039±0.009	0.46±0.04	
255	0.84±0.02	0.018±0.004	0.86±0.02	0.9576±0.0020 (255 nm)
310	0.92±0.02	0.018±0.002	0.93±0.02	0.9792±0.0063 (300 nm)
560	0.96±0.02	0.023±0.002	0.99±0.02	0.9929±0.0020 (500 nm)
BI-HEMISPHERICAL REFLECTANCE				
				$R_{diffuse}/R_{total}$ (%)
175	0.429±0.038	0.095±0.006	0.52±0.05	82
255	0.808±0.012	0.0641±0.0031	0.873±0.014	92
310	0.876±0.016	0.0630±0.0024	0.940±0.02	93
560	0.926±0.015	0.0714±0.0024	1.001±0.017	93

for the PTFE molded sample about 94% of the light reflected belongs to the diffuse lobe, and for a diffuse illumination (bi-hemispherical reflectance) about 82% of the reflected light comes from the diffuse component. The decreasing of the diffuse behaviour of the material is caused by the decreasing in the multiple diffuse albedo and the increase in the index of refraction which also increases the specular component. Thus at these wavelengths the PTFE cannot be approximated to a perfectly diffuse material.

We observed that the fluoropolymers have a complex reflectance distributions that can be associated to three main reflection components, a diffuse lobe, a specular lobe and a specular spike. The reflectance model explained in the chapter 4 was used successfully to describe these three components at the xenon scintillation light, for different manufactures of the material and finishing of the surface. We observed that three or four parameters are sufficient to describe the reflectance in the hemisphere. The BRIDF function whose parameters are fitted to the data can be integrated to yield the hemispherical reflectances of the surface.

5. REFLECTANCE MEASUREMENTS IN THE VUV AND ANALYSIS

CHAPTER 6

Monte Carlo Simulation of the Reflection by Rough Surfaces in Geant4

The results obtained in the last chapter show that the proposed model comprising three reflection components: a specular lobe, a specular spike and a diffuse lobe (section 4.4) is ad equated to describe the experimental observations. We studied various materials, either with rough or smooth surfaces, having or not internal body scattering and we could interpret all data with a minimal number of physically motivated parameters. Therefore, having proved the concept, we are now interested in building a Monte Carlo simulation of the light that embodies the aforementioned model of reflection. There is all interest to include this model in the simulation of detectors, particularly the scintillation detectors.

There are various simulation toolkits that have been used in the Monte Carlo simulations of detectors, Geant4 which is developed at CERN is possibly at the present most used toolkit [227]. The simulation of the reflection of light, in particular the transport of light through a medium, that is currently build in Geant4 does not agree in many ways with our experimental observations and description of the reflection processes. Thus a new reflectance simulation was added to the Geant4 toolkit. Here, instead of pursuing an analytical model of the BRIDF, $\varrho\left(\theta_i, \theta_r, \phi_r\right)$, a Monte Carlo method generates the function ϱ. The new simulation can describe the reflectance of surfaces with different roughness and correctly include the dependence of the coherent spike and diffuse lobe with the angle of incidence. The optical model of simulation can handle the reflection at any interface, with roughness, irrespective of the optical properties of the new medium, be it either a dielectric or a conductor, with or without internal body scattering.

6.1   The Optical Simulations in Geant4 - the Current Unified Model

The experimental measurements described in the chapter 5 will be first simulated
using the version[1] of Geant4 4.9.3. For this description we will use the so called `unified
model` of simulation implemented in the toolkit.

The photons are treated, in Geant4, by two distinct classes, namely `G4Gamma` and
`G4OpticalPhoton`. The photons from the class `G4OpticalPhoton` are supposed
to have a wavelength, λ, much larger than the atomic spacing, contrary to `G4Gamma`
which is thought to simulate high energy photons and their interaction with the matter.
There is no communication between these two classes, the use of one or another is sole
dependent of the simulation purpose in view.

The photons defined in class `G4OpticalPhoton` are supposedly optical photons
(a loosely concept) and can be associated to the following list of processes which are
implemented

Process	Geant4 Class
Refraction and reflection at medium boundaries	`G4OpBoundaryProcess`
Rayleigh scattering	`G4OpRayleigh`
Bulk absorption	`G4OpAbsorption`
Wavelength shift	`G4OpWLS`

The reflection and refraction at the medium boundary surfaces is delegated to the
`G4OpticalBoundaryProcess` class. In this class, the user needs to choose the model
of reflection, the physical characteristics of the surface and the optical characteristics of
the materials that meet at the boundary surface

Model	Glisur
	Unified
Surface Tye	Dielectric-Dielectric
	Dielectric-Metal
Surface Finnish	Polished
	Ground

When the surface finishing is set to `polished`, the reflection processes are treated
in the same manner in both the `Glisur` and `Unified` models, nevertheless it is depen-
dent of the surface type chosen by the user. The reflectance for the `dielectric-metal`
surface type can be introduced in two different ways; either i) issuing a constant which
gives the probability of reflection, independent of the angle of incidence, or ii) introduc-
ing the optical constants of material and use the equations 4.5a and 4.5b to compute the

---

[1]In this chapter we always refer to the version 4.9.3 of Geant4 unless stated otherwise.

reflectance. The first option[1] is not exact and should be used only when the reflectance of the metal at the normal direction is larger than 0.70 and the respective optical constants are not known[2].

If the interface is dielectric-dielectric and the surface finish is set to polished the reflection is specular only. The index of refraction of both materials is used to compute the fraction of light that undergoes reflection or refraction. But these equations are sole dependent of the index of refraction, thus ignoring completely the attenuation function.

The reflection from a diffuse material or from a rough surface can be implemented through two different models, the `Unified` and the `Glisur` models. In both models there is no clear distinction between reflection caused by internal scattering and the reflection caused by the roughness of the surface. In the `Glisur` model these two processes are described using only one variable, P the polishing degree of the surface, that is introduced by the user. P is placed between 0 and 1 with the surface perfectly polished for $P = 1$. Then, a random vector $\mathbf{b}$ is generated in a sphere of radius $1 - P$, and the local normal $\mathbf{n}'$ given by

$$\mathbf{n}' = \frac{\mathbf{n} + \mathbf{b}}{||\mathbf{n} + \mathbf{b}||}$$

is generated.

The `Unified` model aims to reproduce the reflection distribution in a more detailed way, including both specular and diffuse components. A detailed description of the `Unified` simulation is represented schematically in figure 6.1.

In the `Unified` model the program starts by generating the micro-facet normal $\mathbf{n}'$ to describe the roughness of the surface. This normal is generated by sampling a normal distribution (with width σ_α representing the roughness of the surface). The refraction angle θ_t is obtained using the Snell-Descartes law and the probability of reflection/refraction calculated with Fresnel equations applied to the local angle.

If the probability says that the photon is going to be reflected, it is now necessary to choose the type of reflection. The user is supposed to have introduced several weights for each type of reflection: w_d for the diffuse reflection, w_s for the specular lobe, w_r for the specular spike and w_b for the backscattered lobe[3]. The probability of each type of reflection is proportional to these weights.

---

[1]Until 2006 this was the only method to describe the reflectance in a metal. Therefore it has been used extensively in the detector's simulations (see 5.2).

[2]The optical constants of the metals are well known for pure metals and for a wide range of wavelengths, however, the metals are affected by corrosion and oxidation which alters their optical constants and decreases the reflectance of the metal.

[3]This is also called retroflection, the light is reflected back toward the source (therefore $\mathbf{r}=\mathbf{-i}$) and spreaded in a lobe. There are some mechanisms responsible for retroflection, some are exposed in [228].

MICRO-FACET NORMAL $\mathbf{n}'$

$$P\left(\alpha, \sigma_\alpha\right) = \frac{1}{\sigma_\alpha \sqrt{2\pi}} \exp\left(-\frac{\alpha^2}{2\sigma_\alpha^2}\right)$$

test if $\mathbf{i} \cdot \mathbf{n}' > 0$

$n_1 \sin\theta_r = n_2 \sin\theta_t$

$\sin\theta_t > 1$
Total Internal
Reflection

$\sin\theta_t < 1$
Amplitude $F\left(\theta', n\right)$

$\xi < F$
Reflection

$\xi > F$
Refraction

$\xi < w_s$
Specular Lobe
$\mathbf{r}$

$\xi > w_s$ and $\xi < w_s + w_r$
Specular Spike
$\theta_i = \theta_r$

$\xi > w_s + w_r$
Diffuse Lobe
Lambertian
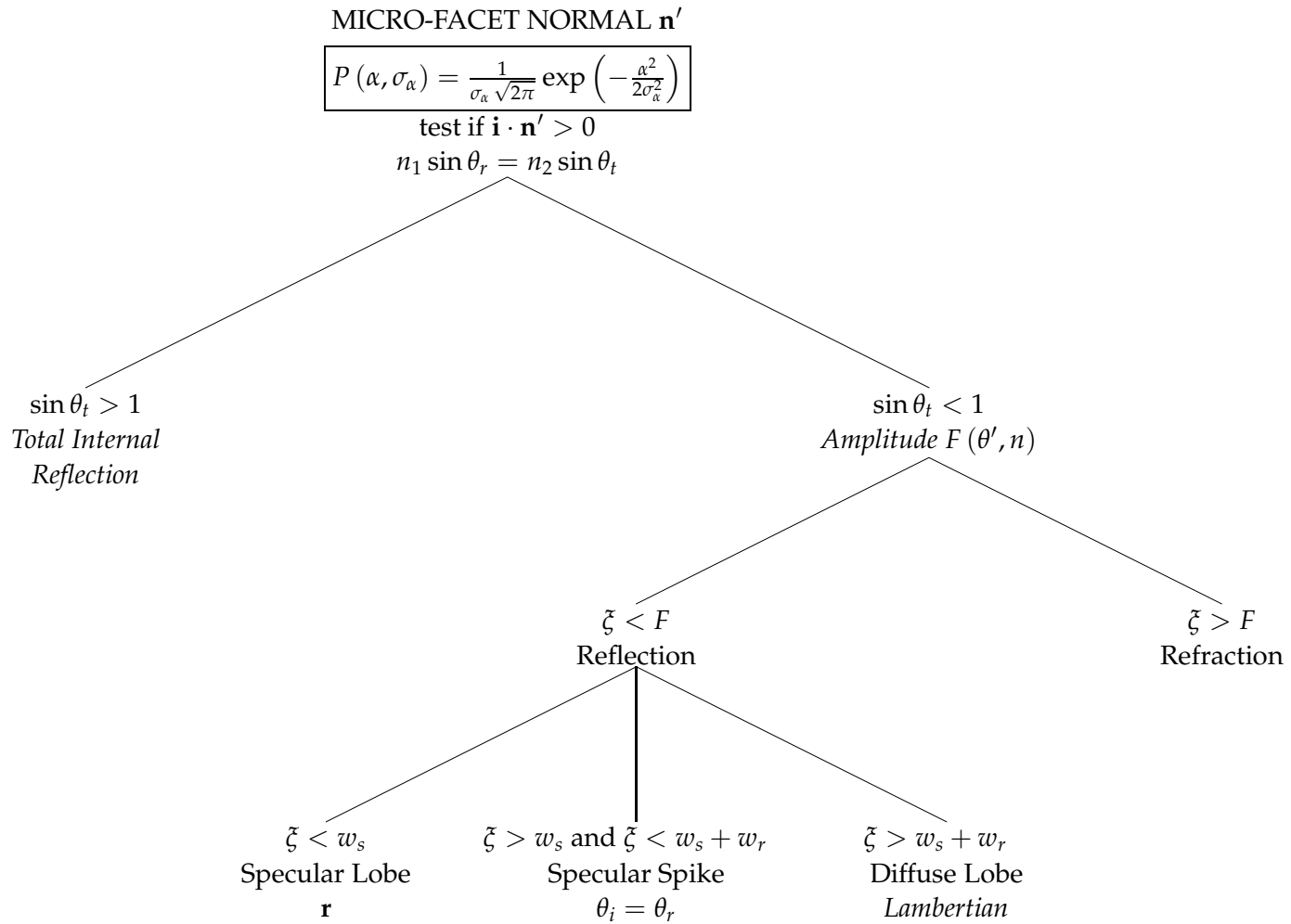
Figure 6.1: The algorithm of the Geant4 Unified model of reflection at rough dielectric surfaces ($\xi \in [0,1]$ is a random number)
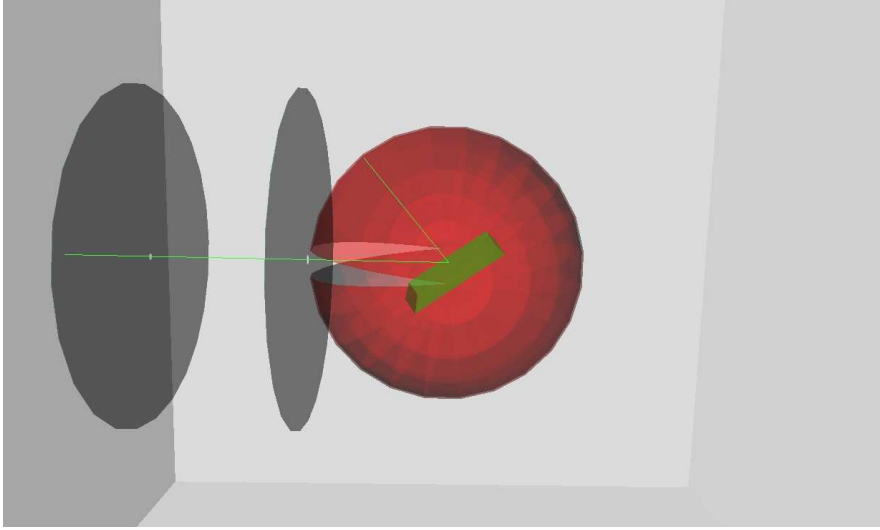
Figure 6.2: Geometry of the simulation of the reflection measurements implemented in Geant4 (see text for details).

The reflection direction, **r**, is dependent of the type of reflection. For the diffuse reflection, a vector is randomly generated according to the law of Lambert. The direction of the specular spike is computed from the global normal **n**. The photon direction that belongs to the specular lobe is calculated relative to the local normal **n′**.

The direction of the backscattered lobe will be generated relative to the direction **n′** and around the direction of incidence.

The reader is referred to the Geant4 documentation for more details about this toolkit[1]. A schematic overview of the reflection processes is depicted in the figure 6.1.

Simulation of the reflection measurements with the Unified model

The experiments described in the chapters 2 and 3 were simulated using the Geant4 package. Figure 6.2 shows the geometry used in that simulation and that closely follows the goniometer used. The reflecting surface (shown in green) is placed at the centre of the detector. Two iris diaphragms are placed between the surface and the point of origin of the photons and are placed in the same positions and with the same apertures of the experiment (see chapter 2). The surface is oriented according to a certain angle θ_i, relative to the direction defined by the iris diaphragms. The photons are generated at a fixed position to a random direction and at a distance of 220.6 from the photomultiplier. Most of the photons are absorbed by the iris-diaphragm, save a fraction of photons that strike the surface inside a cone beam similar to the experiment. At the surface

---

[1]In the last release of Geant4 v. 4.9.3 the user can also issue a look-up-table containing the measured optical reflectances [234].

6. MONTE CARLO SIMULATION OF THE REFLECTION BY ROUGH SURFACES IN GEANT4

these photons will be either reflected or refracted or eventually absorbed. The reflected photons are *detected* by a sensitive sphere (shown in red in the figure 6.2) placed at about 66.4 mm from the centre of the reflecting surface and the hit positions defined by the angles θ and ϕ_r of this sphere are recorded. For each position v_r of the photomultiplier, the corresponding area of detection in the semi-sphere of reflection is determined and the number of photons that were detected in this area is counted. This number can then compared with our experimental measurements.

The reflection in the sample is simulated using the unified model of the Geant4, thus it is necessary to introduce the parameters σ_α, w_d, w_s and the index of refraction of the material. Several combinations of these parameters were tested in search for the best fitted combination of parameters which gave a reflection profile closest to the experimental data. The results are shown in figure 6.3. As shown, the results obtained with the Geant4 simulation are very different from the data and cannot be, at least with the current implementation, improved.

The main problem with the unified model of the Geant4 toolkit is that the type of reflection is chosen after the Fresnel equations are applied at the surface. Then the diffuse component is proportional to the specular component. This causes the intensity of the diffuse lobe to increase with the angle of increase. However, the observed data (section 5.5) shows an opposite behaviour with the diffuse component decreasing with the angle of incidence. In fact, only the photons that are transmitted to the subsurface are able to reflect diffusely.

We noticed that if the index of refraction is assigned to a realistic value, the diffuse component will be very low. Thus in the figure 6.3(a) the index of refraction of PTFE had to be artificially increased to an unrealistic value ($n_2 = 100$) to reproduce the diffuse lobe reflection. Thus, even if the diffuse lobe is somehow reproduced it is done at the expenses of the specular lobe which becomes exaggerated and independent of the angle of incidence.

If the diffuse reflection component is ignored in the simulation and the index of refraction is set to the value measured in the chapter 5 it is possible to fit roughly the specular lobes. However, the shape of these lobes differ from the data in many respects as can be seen in figure 6.3(b). This should be not unrelated to the fact that the micro-facet distribution is restricted to a gaussian distribution contrary to our argument that is better described by a Trowbridge-Reitz probability distribution (see section 5.3).

Another problem with the current model implemented in Geant4 simulation is the fact that it requires us to define both a weight factors for the diffuse lobe, specular lobe and specular spike. These three factors are independent of the angle of incidence and the sum of these factors cannot be larger than 1. The weight factor attributed to the diffuse lobe can be related directly with the albedo of the surface which does not depend strongly of the angle of incidence. However, the factors assigned to the specular lobe and to the specular spike do not represent the reality because, in real surfaces, the intensities of the specular lobe and specular spike are highly dependent of the angle of

(a) Simulation profile obtained with $n_{\mathrm{PTFE}} = 100$, w_d=0.54, $w_s = 0.46$ and $\sigma_\alpha = 2.75°$

(b) Simulation profile obtained with $n_{\mathrm{PTFE}} = 1.41$, w_d=0.0, $w_s = 1.00$ and $\sigma_\alpha = 2.75°$

Figure 6.3: Comparison between the measured reflectance of skived PTFE and the Geant4 simulation predictions using the standard Unified model of this package. Two best combinations of parameters are shown. The simulation can be made closed to either the reflection observed ar specular angles or at off-specular angles, but not both.

incidence and viewing, being the specular spike much more intense at lower grazing angles than at the normal direction.

The Geant4 only checks for non-physical scenarios such as $\mathbf{i} \cdot \mathbf{n}' > 0$ [1]. The geometrical attenuation factor is not included yielding large deviations from the observed data at low grazing angles.

In brief, the Geant4 simulation model is not able to describe the reflection distributions of surfaces that have both specular and diffuse reflectances. To address the above issues the model of simulation of the optical processes of reflection of light needs to be improved. In the next section we propose a new implementation.

6.2 A New Method to Simulate the Reflection in Geant4

We developed a new method of simulation of the reflection by rough surfaces in Geant4. It is based in the phenomenological model discussed in chapter 4, which has been applied successfully to the reflectance distributions of the fluoropolymers (chapter 5). For such a purpose we coded a new software class in Geant4 which interacts with the other classes in the hierarchy of Geant4 and can be called to handle specifically

---

[1]These vectors were defined in the figure 4.6,

6. MONTE CARLO SIMULATION OF THE REFLECTION BY ROUGH SURFACES IN GEANT4

the reflection at any surface of the simulated system. This has been introduced in the simulation framework using the instruction `SetModel(trowreitz)` for any surface defined as an object of the class `G4OpticalSurface` of Geant4.

The surface is defined at the boundary between two media with a global normal **n**. The first medium, in which the photons with wavelength λ are being propagated, has an index of refraction n_1 and coefficient of extinction $\kappa \simeq 0$ by hypothesis, the second medium has optical constants n_2 and κ and can yield mate reflection with an intensity given by the multiple-diffuse albedo ρ_l. The relative index of refraction of the interface n is given by $n = n_2/n_1$.

The way the reflection is processed is dependent of the type of material of the second medium. Three different situations are considered differing in the way the transmitted light is processed: a dielectric-metal interface, a dielectric-dielectric dispersive interface and a dielectric-dielectric non-dispersive interface[1]. These three situations differ the way the light transmitted to the new medium is processed.

The algorithm implemented in the geant4 simulation is represented in the flowchart of the figure 6.4. As shown, three different situations are considered according to the roughness constants of the surface, the r.m.s. of the surface slopes[2], σ_α, and the r.m.s. of the height function[3], σ_h:

$\sigma_\alpha/\gamma/m$ and σ_h/K both defined	Moderate roughness	Specular lobe plus specular spike
$\sigma_\alpha/\gamma/m$ defined and σ_h/K not defined	Rough	Specular lobe
$\sigma_\alpha/\gamma/m$ and σ_h/K both not defined	Smooth	Specular spike

In a smooth surface the light is scattered (transmitted or reflected) according to the global normal to the surface **n**; in a rough surface the light is scattered according to a local normal **n′**. If the surface has a moderate roughness the light can be scattered either according to **n** or **n′**, depending of which process occurs at the surface. This situation is the more general and accurate being necessary to introduce the constants σ_α/γ and σ_h/K of the surface to characterize the roughness. The probability that the light is scattered according to a global normal **n** or a local normal **n′** is not dependent of the viewing angle and is given by the function Λ. As discussed in the section 4.3 this function is dependent of the height distribution $z = h(x,y)$ of the surface and can be obtained from the equation 4.47, therefore Λ is dependent of the roughness type of the surface. In the Geant4 simulation we have assumed, as usually, a gaussian distribution

---

[1]The dielectric-dielectric non dispersive interface has not been implemented in the code, therefore it will not be discussed in this chapter.

[2]The Trowbridge-Reitz function is expressed directly in terms of the parameter γ and the Cook-Torrance is expressed in terms of m. Nevertheless both parameters are related with the r.m.s. of the surface slopes $\sigma_h \simeq 0.6\gamma \simeq 0.6m$

[3]K can be used instead of σ_h when the surface is described by the empiric function defined by the equation 5.8.
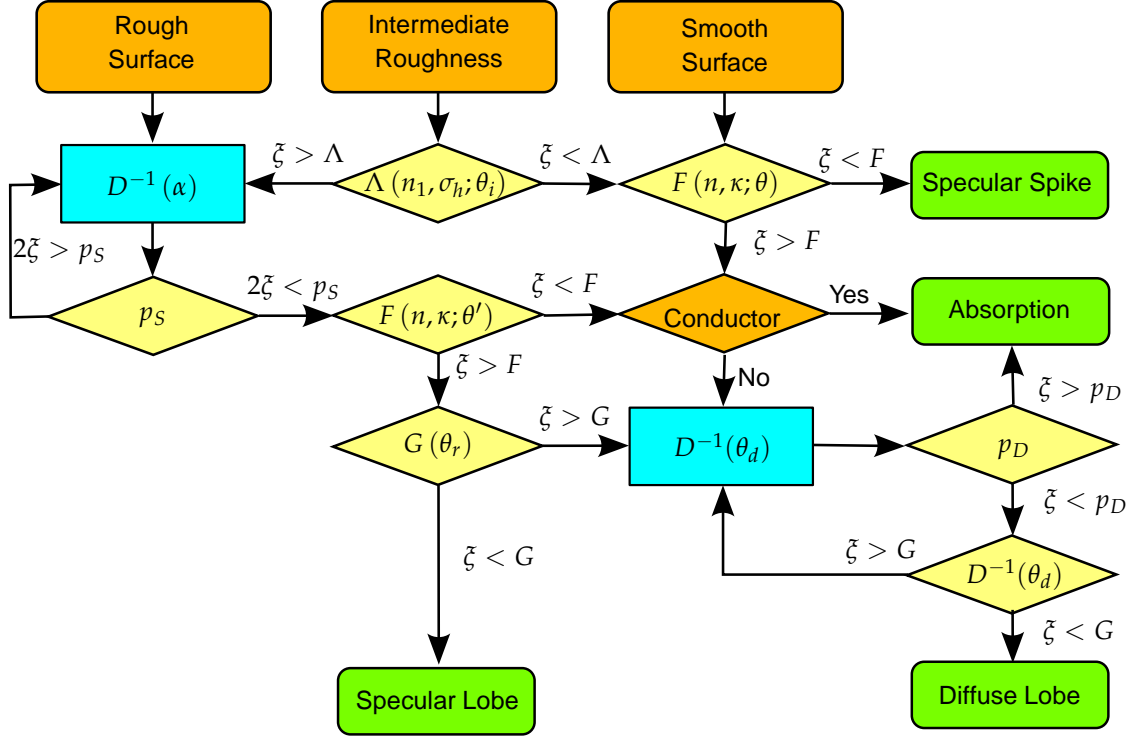
Figure 6.4: Monte Carlo simulation of the reflection of light at an interface dielectric-dielectric. Different branches are considered according to the degree of roughness of the surface, the character of the materials (whether it is conductor or not), and the nature of the physical processes at work. In each rhombus the quantity shown is evaluated and compared with a random number $\xi \in [0, 1]$. Λ is the probability of reflection according to a specular spike, F the Fresnel equations, G the shadowing-masking function and D^{-1} the inverse cumulative function that generates both α and θ_d.

for the probability distribution of heights P_z. For this distribution the function Λ is given by the equation

$$\Lambda (\theta_i; \sigma_h) = \exp\left[-\left(\frac{4\pi\sigma_h n_1}{\lambda} \cos\theta_i \right)^2 \right] \tag{6.1}$$

This function is dependent solely of the angle of incidence θ_i, the angle between the global normal, **n**, and the directions of incidence of the photons, **i**. Nevertheless, this function can be replaced by other function that describes better the reflectance of the material. For example, we have concluded in the chapter 5 that the fluoropolymers are better described by the empirical function $\Lambda = \exp(-K\cos\theta_i)$, this function can be introduced in the code by replacing 6.1.

To choose between the two normals **n** and **n'** a random number ξ, between 0 and 1,
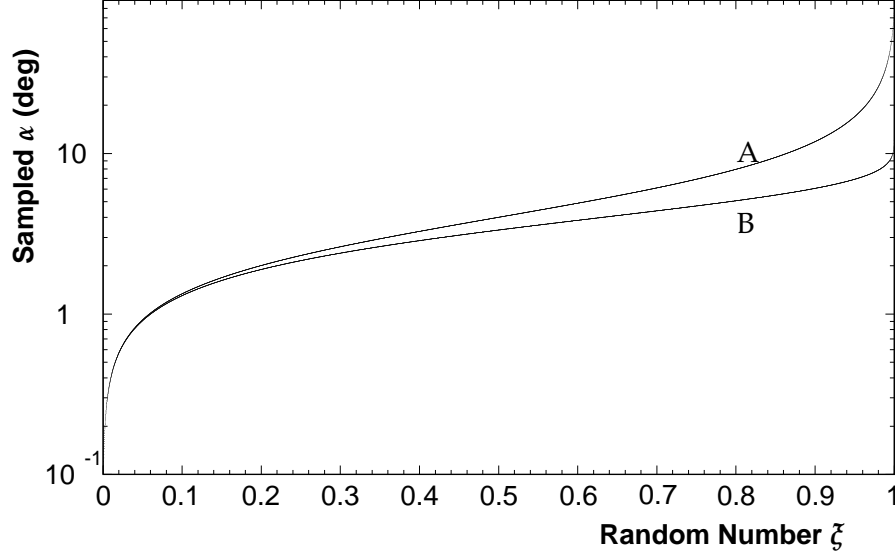
Figure 6.5: Comparison between the sampling of a Trowbridge-Reitz distribution (curve A, equation 6.4) and the Cook-Torrance distribution (curve B, equation 6.5) with γ=m=0.07.

is generated and compared with the function $\Lambda\left(\theta_i; n_1, \sigma_h, \lambda\right)$. When $\xi < A$ the light will be scattered according to the global normal $\mathbf{n}$, when $\xi > A$ the light scatters according to the local normal $\mathbf{n}'$.

When $\xi < \Lambda$, the light scatters according to the global normal and the Fresnel equations are computed using the angle θ_i. A random number determines if the photon undergoes transmission or reflection. When the light is reflected it emerges at the reflecting direction given by

$$\mathbf{r} = 2\cos\theta_i\mathbf{n} + \mathbf{i} \qquad (6.2)$$

these photons can be identified with the specular spike.

When $\xi > \Lambda$ the incident light scatters according to the local normal $\mathbf{n}' = \mathbf{n}\left(\alpha, \phi_\alpha\right)$ given by

$$\mathbf{n}' = \sin\alpha\sin\phi_\alpha\hat{\mathbf{e}}_\mathbf{x} + \sin\alpha\cos\phi_\alpha\hat{\mathbf{e}}_\mathbf{y} + \cos\alpha\hat{\mathbf{e}}_\mathbf{z} \qquad (6.3)$$

$\mathbf{n}'$ is determined by sampling the local angles α and ϕ_α of the micro-surface slope according to the distribution of the micro-facets $P\left(\alpha\right)\cos\alpha$ of the surface (see section 4.2). In general this function is not dependent of the azimuthal angle, thus ϕ_α is generated uniformly between 0 and 2π. The angle α is obtained using the micro-facet distribution function $P\left(\alpha\right)$. When the integral is defined it is possible to find the inverse cumulative function D^{-1} (quantile function) which generates the the α distributed according to probability distribution function $P\left(\alpha\right)\cos\alpha$. For the Trowbridge-Reitz function (eq.

4.23) the α are generated with the function

$$\alpha = \arctan\left(\frac{\gamma\sqrt{\xi}}{\sqrt{1-\xi}}\right) \tag{6.4}$$

again $\xi \in [0,1]$ is a random number between, γ corresponds to the oblateness, the parameter that controls the roughness of the surface.

For the Cook-Torrance distribution function (eq. 4.20) the quantile function is given by

$$\alpha = \arctan\left(\sqrt{-m^2\log(1-\xi)}\right) \tag{6.5}$$

The two functions D^{-1} above (equations 6.4 and 6.5) are compared in the figure 6.5 for a level of roughness corresponding to γ=m=0.07. As observed in this figure, the equation 6.4 generates larger angles of scattering than equation 6.5. The probability distribution functions and the respective inverse cumulative functions are summarized in the table I.

With the sampled α it is possible to compute the local angle θ' (angle between the local normal **n**' and the direction of incidence **i**) which is given by

$$\theta' = \cos\alpha\cos\theta_i - \sin\theta_i\sin\alpha\cos\phi_\alpha \tag{6.6}$$

The sampled α is tested using a weighting factor given by

$$p_S = \frac{\cos\theta'}{\cos\theta_i}\frac{G(\theta_i)}{\cos\alpha} \tag{6.7}$$

The weighting factor introduces the shadowing-masking factor $G(\theta_i)$ and the geometrical factor ($\cos\theta'/\cos\theta_i$) (see section 4.4). A random number is compared with p_S. If $\xi < p_S$ the photon is propagated along the generated direction. Otherwise ($\xi > p_S$) the micro-facet is discarded and a new angle α is computed. Though the factor p_S can be larger than 1, computer simulations showed that only occasionally is it larger than 2. Thus, this random number ξ is generated between 0 and 2. This reduces the speed of the simulation because the function D^{-1} needs to be computed in average twice. This issue should be addressed further.

The Fresnel equations are computed for the local angle θ' giving the probability that the light is transmitted, thus undergoing internal scattering, or if it is reflected, contributing to the specular lobe.

The light that is reflected at the surface is passed through the shadowing probability $G(\theta_r)$. If the light is shadowed it means that it is double scattered at the surface. In a second scattering it can be transmitted to the material or be double reflected. For the majority of the dielectrics and angles of incidence we have $F(1-F) \gg F^2$ being a good approximation to consider this light diffusely reflected, so it is given to the diffuse component.

6. MONTE CARLO SIMULATION OF THE REFLECTION BY ROUGH SURFACES IN GEANT4

The light that is reflected according to the local normal and not shadowed follows the direction given by

$$\mathbf{r} = 2\cos\theta'\mathbf{n}' + \mathbf{i} \qquad (6.8)$$

which corresponds to the reflected lobe.

Simulation of the transmitted light

The simulation of the light transmitted into the new medium depends obviously of its properties. The type of the material is set using the instruction `SetType`. In what concerns the transmitted light the following definitions are possible

`dielectric_amorphous`	Diffuse reflection/absorption
`dielectric_metalic`	Absorption
`dielectric_dielectric`	Transmitted spike/transmitted lobe

At a dielectric-metallic interface the absorption is so strong that no light is observed for films thicker than a few wavelengths, thus the transmitted light is considered to be absorbed at once.

When the photon is transmitted to an inhomogeneous medium scattering of the light can return to the first medium after several interactions in the bulk of the material or otherwise absorbed. It is assumed that after several interactions the direction of the light is isotropic and obeying to the lambertian law.

Let us assume that the direction of the diffused reflected photons is given by the

Table I: Summary of the probability distribution functions used in the analytical description of the reflectance and its correspondent inverse cumulative functions used in the Monte Carlo description of the reflectance to sample the directions of the reflected photons.

	$P\cos\alpha$ or $P\cos\theta_d$	$D(\alpha)$ or $D(\theta_d)$	$\alpha = D^{-1}$ or $\theta_d = D^{-1}$
Cook-Torrance	$\frac{1}{\pi m^2 \cos^4\alpha}\exp\left(-\frac{\tan^2\alpha}{m^2}\right)$	$1 - \exp\left(-\frac{\tan^2\alpha}{m^2}\right)$	$\arctan\sqrt{-m^2\log(1-\xi)}$
Trowbridge-Reitz	$\frac{\gamma^2}{\pi\left(\gamma^2\cos^2\alpha + \sin^2\alpha\right)^2}$	$1 - \frac{\gamma^2}{\gamma^2 + \tan^2\alpha}$	$\arctan\left(\frac{\gamma\sqrt{\xi}}{\sqrt{1-\xi}}\right)$
Lambertian Law	$\frac{\rho_l}{\pi}$	$\frac{\rho_l}{2\pi}\sin^2\theta_d$	$\arcsin\sqrt{\xi}$

The azimuthal angles are generated between 0 and 2π for the functions shown.
ξ is a random number between 0 and 1.

following vector, expressed in spherical coordinates

$$\mathbf{r} = \sin\theta_d \sin\phi_d \hat{\mathbf{e}}_{\mathbf{x}} + \sin\theta_d \cos\phi_d \hat{\mathbf{e}}_{\mathbf{y}} + \cos\theta_d \hat{\mathbf{e}}_{\mathbf{z}} \tag{6.9}$$

where θ_d, the polar angle, corresponds to the angle between $\mathbf{r}$ and $\hat{\mathbf{e}}_{\mathbf{z}}$, ϕ_d is the azimuthal angle. When the photons are scattered according to the global normal we have $\hat{\mathbf{e}}_{\mathbf{z}} = \mathbf{n}$ and $\hat{\mathbf{e}}_{\mathbf{z}} = \mathbf{n}'$ when they are scattered according to the local normal.

To sample the vector $\mathbf{r}$ in such a way that the reflected photons follow the Lambertian's law of reflection the angles θ_d and ϕ_d are generated by [235]

$$\sin\theta_d = \sqrt{\xi} \tag{6.10a}$$

$$\phi_d = 2\pi\xi \tag{6.10b}$$

ξ is a random number generated uniformly in [0,1].

The Geant4 package includes a specific function that generates the direction of the reflected photons according to the Lambertian law. This function can be called using `G4LambertianRand(theGlobalNormal)`. However, it is computationally more expensive than the method shown above.

The masking probability $G(\theta_r)$ is computed to the sampled direction. When the diffused light is masked, the program will generate a new direction of the diffused photons (eqs. 6.10a and 6.10b) different direction of reflection $\mathbf{r}$. Then the following weighting factor is computed

$$p_D = \rho_l \left(1 - F\left(\theta_t, \frac{n}{n_0}\right)\right) \tag{6.11}$$

where ρ_l is the multiple-diffuse albedo and θ_t the transmission angle, given by $\theta_t = \arcsin\left(\frac{n_1}{n_2}\sin\theta_d\right)$. The Fresnel factor accounts for the light that is reflected in the interface between the medium which undergoes diffuse reflection and the first medium. A random number between 0 and 1 is generated and compared with the weighting factor 6.11. When the random number is larger than p_D the photon is absorbed, otherwise it is refracted back into the original medium, along the direction defined by the angles (θ_d, ϕ_d).

The effect introduced by the roughness of the surface which described by the Oren-Nayar correction term in the analytical description of the reflectance (section 4.5) is already being accounted with the Monte Carlo method. In fact, the angle θ_d is measured relative to the local normal $\mathbf{n}'$ and the shadowing-masking term is evaluated in the equation 6.7.

Simulation Results

The model described above was implemented in the Geant4 simulation. We run the simulation with the values of the reflectance parameters that we measured in the chapter 5 (see table VIII) and plot both the experimental data and the results of this Monte
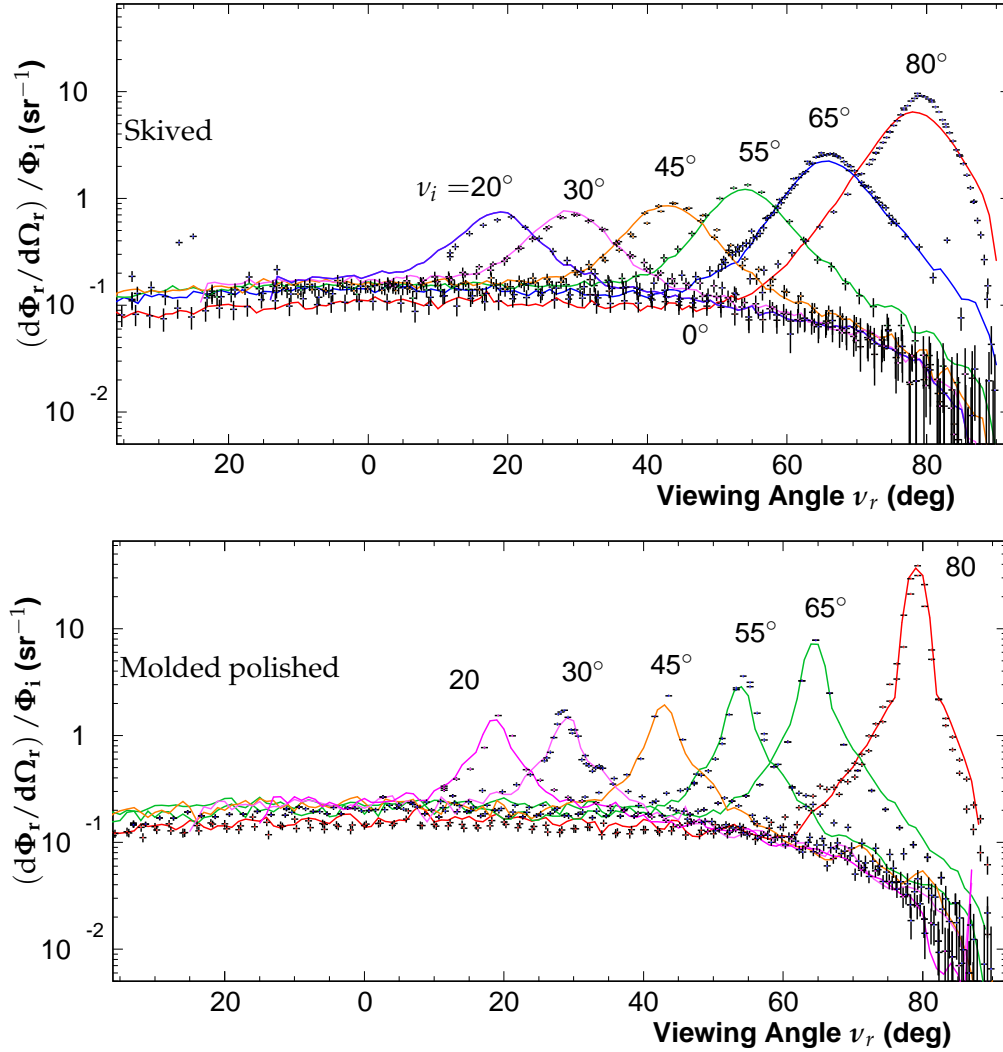
Figure 6.6: Comparison between the results obtained for the skived sample (chapter 5) and the simulation of the experiment using the model introduced in the Geant4 and the parameters obtained in the fit.

Carlo simulation in figure 6.6 for a surface of skived PTFE and the molded polished PTFE. As discussed in the previous chapter the first sample is described using only a specular lobe and a diffuse lobe, in the polished sample it is also introduced the effect of the coherent reflection. As can be seen, the simulation results describe very closely the empirical measurements for all angles of incidence and of reflection. Even at the grazing angles where the test is more stringent the simulation agree with the data. This new simulation model shows a much better agreement than the current most complete

model of Geant4, as can be judge by plotting side by side figures 6.3(b) and 6.6.

A new model for the light reflection was introduced in the Geant4. It comprises three different contributions: a specular lobe, a specular spike and a diffuse lobe, and can be applied to both dielectric and diffuse reflectors. These components are described using a Monte-Carlo method in contrast with the analytical methods used in the previous chapters.

This new description of the reflection was successful to describe the data on the reflectance distributions of fluoropolymers. Thus, it can be used to describe the reflection in the interior surfaces of scintillation detectors, in particular whenever a diffuse reflector such as PTFE is used.

6. MONTE CARLO SIMULATION OF THE REFLECTION BY ROUGH SURFACES IN GEANT4

Reflection in Liquid Xenon Detectors

Various experiments, notably experiments that search for dark matter rely on the scintillation of the liquid xenon (LXe). In some cases, the projected detectors have larger dimensions, which requires a much detailed knowledge of the light propagation in such light volumes. The use of large areas of PTFE in contact with the liquid xenon is a foreseeable possibility. Therefore, it is of utmost importance to study the reflection of light in xenon detectors, namely the reflectance of PTFE in direct contact with the liquid.

The published values of the index of refraction of liquid xenon are between 1.55 and 1.70. The reflectance at the interface liquid-PTFE is expected to be highly dependent of the refraction indices of both materials. As we have seen in the chapter 5, the PTFE has an index of refraction of 1.5 at the room temperature. Hence, assuming the same index of refraction, there are possibly angles for which the reflection is total. In such a case the amount of specular reflection should become highly increased, at expenses of the diffuse reflection. On the other hand, given that the indices of the two media, the liquid and the PTFE, are much closer now, comparatively to the gas-PTFE interface, then the specular reflectance should be much smaller before, unless there is total reflectance.

The two mentioned mechanisms above are basically dependent of the relation of the indices of refraction and can change completely the reflectance of the PTFE in the liquid xenon as compared to the vacuum/gas. The PTFE itself can be different at low temperatures ($\sim -100°C$, see 1). Not only, the index of refraction can change with the temperature, also the internal scattering can be different.

To carry out this study of the PTFE-liquid xenon interface we applied the Geant-4 Monte Carlo simulation discussed before to the case of this interface. The model of simulation is detailed in chapter 6. We also applied the simulation to the study of the light collected during the calibration of a liquid xenon detector with gamma rays. A

fairly good agreement with the data was obtained.

7.1 Reflection of VUV light at a liquid xenon-PTFE interface

The index of refraction of the liquid xenon

The index of refraction of liquid xenon n_{LXe} is important here since it determines through the Fresnel equations the fraction of light that is reflected or transmitted into the PTFE and out of it as diffuse light. The value of the index of refraction is not well known though. The measured values range from 1.5655±0.0024 measured by Barkov *et al* [236] (at the triple point of the liquid xenon) and 1.69 ± 0.002 measured by Solovov *et al* [25] at -103° C. These two values of index of refraction were obtained by measuring the refraction at the interface liquid-gas and are inconsistent. The index of refraction was also estimated by Seidel (2001) [23] using the data available of the index of refraction of gaseous xenon. He arrived to a value of 1.69, similar to the value published in [25].

Estimates of the reflectance of PTFE-LXe

The total reflectance of PTFE immersed in liquid xenon detectors has been estimated indirectly from the amount of light collected in scintillation detectors having PTFE inside. The light collection of such detectors is computed by Monte Carlo simulation. From this calculation it is possible to get insight about the average reflectance of PTFE. However, the PTFE surfaces are always assumed to be pure lambertian[1] planes and tuned so that the simulation reproduces the detected light. The specular lobe and the specular spike are neglected.

The first evaluation of the reflectance of the PTFE in contact with liquid xenon that we know was obtained by Barabanov *et al* [237]. They measured the scintillation observed in a detector with a PTFE reflector placed inside the chamber and compared the results with the scintillation obtained with the same detector without PTFE. Using Monte Carlo simulation they concluded that the reflection coefficient of PTFE (i.e. the albedo of the surface) is about 60%. However, more recent data showed that the reflectance of the PTFE should be much higher than the Barabanov figure. Miyajima *et al* (1992) [35] also used two reflectors, a white box made of PTFE and a black box made of black rough aluminum, to measure this reflection coefficient. From the comparison between the values of the two setups they obtained a reflectance of about 82.5%. Miyajima attributed the low value obtained by Barabanov due the poor PTFE used.

More recently, Yamashita *et al* (2004) [238] published an even higher figure for the average reflectance of the liquid xenon-PTFE interface in comparison to previous esti-

---

[1]Since the PTFE is assumed to be a *pure* lambertian material the directional-hemispherical reflectance is equal to the bi-hemispherical reflectance and these two quantities could be treated indistinctly. The BRIDF, $\varrho = \frac{\varrho_l}{\pi} \cos \theta_r$, therefore the reflectance is equal to the multiple-diffuse albedo.

mations. The reflection was measured in a double phase liquid-gas chamber. A Monte Carlo simulation was used to compute the light collection. The reflectance obtained is dependent of the attenuation length in xenon. Their figure are (0.95,1.0); (0.92,1.5) and (0.88, ∞) for the various binomials (reflectance, attenuation length in metres) they have considered. These parameters are clearly anti-correlated and cannot be easily disentangled. Using a similar procedure Chepel *et al* (2004) [242] concluded that the reflectance of the PTFE should be not smaller than 0.87.

The above results point to an average reflection of PTFE in liquid xenon of at least 80%. This value is much higher than has been obtained in this work for PTFE in gas. However, as mentioned above, the reflectance showed to increase in contact with the liquid if the index of refraction of the liquid xenon is higher than the refraction index of PTFE as we measured (chapter 5) at room temperature.

A similar effect was observed with a sheet of Spectralon® submerged in liquid water with visible light. The reflectance increased 2% relative to the reflectance measured in vacuum with visible light, for viewing angles below 55° [239].

The effect of the temperature effects on the properties of the polytetrafluoroethylene (PTFE)

It is known that the structure of PTFE changes with the temperature. Thus at the operating temperature of the xenon detectors ($\simeq -110°$C)[1] the optical characteristics of the PTFE are in principle different from those measured at the room temperature.

PTFE has a phase transition at 19° C. Above this temperature, the PTFE has an helicoidal structure with thirteen groups of carbon-fluorine bound for about five 180° twists (see section 1.3). Below 19° C the helice unfolds slightly and is observed about fifteen carbon-fluorine groups for seven 180° twists [240]. This phase transition alters the optical properties of the PTFE, namely the index of refraction, the albedo and the extinction coefficient.

The measurements that we have discussed in the chapter 4 and chapter 5 were carried out at room temperature. The temperature in the laboratory is always between 22°C and 25°C. That means that the experimental data was obtained above the temperature of the phase transition. The temperature of working of a liquid xenon detector, at 1 bar, is about $\simeq -110°$C, well below the phase transition. However, there is no exhaustive study of the variation of the optical characteristics of the PTFE with the temperature. The only results that we have acknowledgment are for the transmittance of a PTFE sheet 2.5 mm thick, illuminated with incident light of 400 nm. These results showed a significant dependence of the transmittance with the temperature [241]. Above the phase transition, the transmittance of PTFE decreases with the increasing of temperature (at about $\simeq -0.1\%/°$C). At the phase transition at 19°C a sudden change is observed, the transmittance decreases about 3% at once. At lower temperatures

---

[1]At 1 bar the melting point of the xenon is -111.9°C and the boiling point is -107.1°C

($T < 15°$), the transmittance increases again with decreasing of the temperature. The transmittance is a diffuse material is dependent of both the scattering and absorption lengths, therefore this quantity is connected with the albedo of the surface (see section 4.5).

The specular components for the liquid/PTFE interface

The intensity of the specular components is proportional to the Fresnel equations for the reflectance (equations 4.8a and 4.8b) which are dependent of the ratio between the indices of refraction of the two media that met at the surface. When the PTFE is immersed in liquid xenon, the intensity of the specular components change. The index of refraction of PTFE is about 1.5 for VUV light at room temperature (see chapter 5). Assuming that the same value at the temperature of the liquid xenon ($n_{LXe} = 1.7$) then the liquid xenon is optically harder than the fluoropolymer surface.

For $n_{LXe} = 1.5655$ (Barkov measurement) the critical angle is 73.4° and for $L_{LXe} = 1.69$ (Solovov measurement) is 62.6°. The reflectance above the critical angle is 100%, no light crosses the boundary and the diffuse lobe falls to zero and the reflectance is totally concentrated in the specular lobe. Obviously, given that the surface is rough this condition is never met completely, but a high suppression of the diffuse lobe should be expected. The difference between the indices of refraction of the liquid and PTFE is smaller than between the gas and the PTFE, for that reason we will have a smaller inten-

(a) Reflectance for the gas-to-PTFE interface (full line) and the LXe-to-PTFE interface (dashed line)

(b) Reflectance for the PTFE-to-gas interface (full line) and the PTFE-to-LXe interface (dashed line)
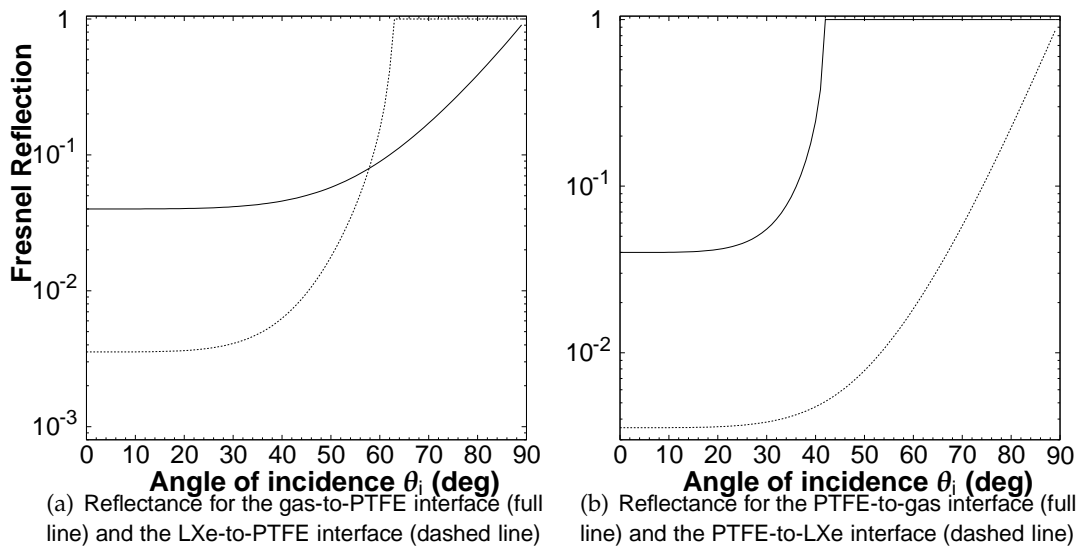
Figure 7.1: Fresnel equations computed for the different interfaces between the liquid or gas and the PTFE. We have assumed $n_{PTFE} = 1.50$ and $n_{LXe} = 1.69$.

sity of the specular components at the normal direction[1] The probabilities of reflection at the interface gas-to-PTFE and LXe-to-PTFE interface are compared in the figure 7.1(a) assuming n_{PTFE}=1.5 and n_{LXe}=1.69.

The diffuse reflection at LXe-to-PTFE
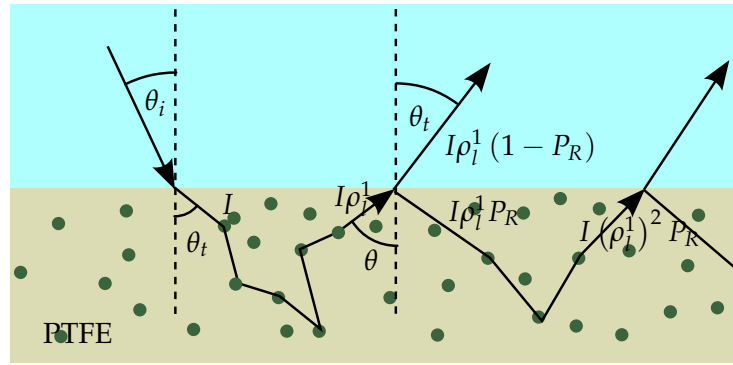
Figure 7.2: The internal scattering process in the PTFE. *I* corresponds to the intensity of the light after the refraction to the bulk of the PTFE. The angles used in the computation of P_R and P_T are also shown.

In the diffuse reflection, the light is refracted into the PTFE, scattered in the bulk of the material and refracted again to the first medium. The light can also be reflected in the interface PTFE and the original medium returning to bulk of the material where it undergoes additional scattering. The probability of reflection or refraction is affected by the index of refraction of the first medium, therefore the diffuse reflection will be different in the liquid and in the gas.

The light scattered in the bulk of the PTFE has a probability of $1 - \rho_l^1$ to be absorbed, where ρ_l^1 corresponds to the multiple-scattering albedo[2]. ρ_l^1 is only dependent of the physical properties of the PTFE (absorption and scattering cross sections).

If the light is not absorbed during the scattering process it eventually returns to the interface PTFE-to-LXe or PTFE-to-gas. We assume that the direction of light that arrives to this interface follows the Lambertian law[3] ($\cos \theta$). Therefore, the probability that the

---

[1]For $n_{\text{PTFE}} = 1.5$ we have an intensity of the specular components of 11%, when it is placed in the liquid the intensity of the specular components ranges from 0.05% to 0.35%, depending of the value assumed for the index of refraction of the liquid.

[2]This parameter is different from the single-diffuse albedo and multiple-diffuse albedo defined in the Wolff model (see section 4.5).

[3]The distributions of the light that arrives to the interface is connected with the diffuse process *per se*.

Table I: Probability of reflection P_R (given by the equation 7.1) in the interface PTFE-to-other, as indicated and the probability of refraction P_T for the same interface (given by the equation 7.4).

	n_2 (PTFE)	n_1	P_R (%)	P_T (%)
PTFE-to-gas (visible light)	1.35	1.00 (air)	49	91
PTFE immersed in water (visible light)	1.35	1.33 (water)	2	99
PTFE-to-gas (light of λ=175 nm)	1.50	1.00 (air)	59	90
PTFE-to-LXe (light of λ=175 nm)	1.50	1.5565 (LXe)	1.1	97
PTFE-to-LXe (light of λ=175 nm)	1.50	1.69 (LXe)	3	94

light is reflected or refracted in the interface between the diffuser (PTFE) and the first medium (a liquid or a gas) is given by the following integral

$$P_R = 2 \int_0^{\pi/2} F\left(n_1/n_2, \theta\right) \cos\theta \sin\theta \mathrm{d}\theta \tag{7.1}$$

where θ is angle between the incident photon and the normal to the interface PTFE-to-gas or liquid (defined in the figure 7.2). F corresponds to the Fresnel equations, with n_2 the index of refraction of the diffuser (PTFE) and n_1 is the index of refraction of the first medium. The value of F as function of the angle of incidence θ_i is shown in the figure 7.1(b) for the PTFE-to-gas and PTFE-to-LXe interfaces. From this figure we conclude that the probability of reflection is larger in the interface PTFE-to-gas than in the interface PTFE-to-LXe for any angle of incidence. With $n_{\mathrm{PTFE}} = 1.5$ it is observed total internal reflection in the interface PTFE-to-gas for $\theta_i > 42°$. The internal reflection is not observed in the interface PTFE-to-LXe ($n_{\mathrm{LXe}} > n_{\mathrm{PTFE}}$) and the Fresnel reflection is very small ($F < 0.01$ for $\theta_i < 50°$).

The integral 7.1 was computed for different interfaces with the PTFE, the results are shown in the table I for different interfaces of PTFE, as indicated. As shown, the probability of specular reflection, P_R, in the interface PTFE gas is about 60% for the xenon scintillation. However if PTFE is in contact with liquid xenon P_R decreases to about 1.1% ($n_{\mathrm{LXe}} = 1.56$) and 3% ($n_{\mathrm{LXe}} = 1.69$).

The amount of light refracted to the original medium corresponds to $\rho_l^1 (1 - P_R)$. The quantity $\rho_l^1 P_R$ is reflected returning back to the bulk of material, going through more internal scattering. These phenomena occur successively until all the light is absorbed or refracted to the original medium. At the end, the probability that the light

---

The Wolff model uses the Chandrasekhar diffuse law [208] to describe this process. Nevertheless, due the complexity of this law and some doubts about its validity (it is assumed an isotropic law for the indicatrix function, see section 4.5) we have opted by the Lambert's law.
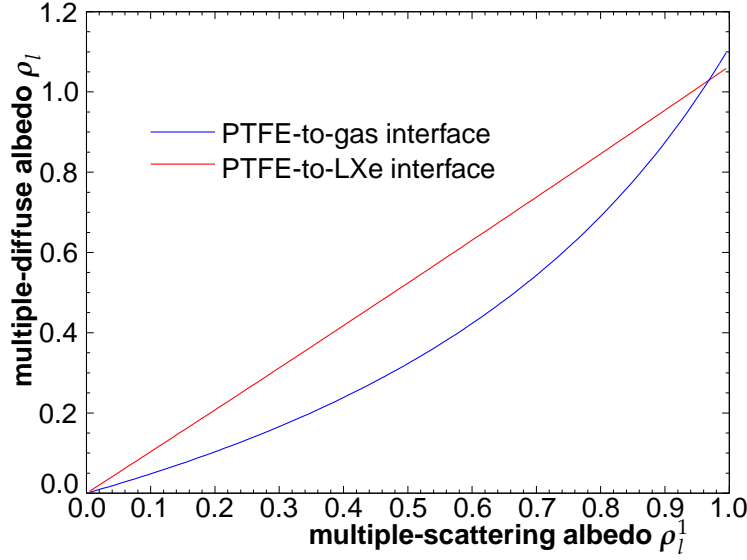
Figure 7.3: Prediction of multiple-diffuse albedo as function of the multiple-scattering albedo for the liquid/PTFE and for the gas/PTFE ($n_{\mathrm{PTFE}} = 1.5$ and $n_{\mathrm{LXe}} = 1.69$).

Table II: Prediction of the multiple-scattering albedo and the multiple-diffuse albedo for the liquid using the surfaces measured

Sample	n (PTFE) [measured]	ρ_l (gas) [measured]	ρ_l^1 [predicted]	ρ_l (LXe) [predicted]
				n=1.69
Skived PTFE	1.49	0.58	0.73	0.75
Molded PTFE (Dongyang®)	1.51	0.52	0.69	0.71
Molded polished	1.45	0.74	0.83	0.86
PFA	1.44	0.69	0.80	0.82

goes out of PTFE and returns back into the original medium is given by the following geometric series

$$
\begin{aligned}
\rho_l^T &= \rho_l^1 (1 - P_R) + \left(\rho_l^1\right)^2 P_R (1 - P_R) + \left(\rho_l^1\right)^3 P_R (1 - P_R)^2 \dots \\
&= \sum_{j=0}^{\infty} \rho_l^1 (1 - P_R) \left(\rho_l^1 P_R\right)^N = 1 - \frac{1 - \rho_l^1}{1 - \rho_l^1 P_R}
\end{aligned}
\tag{7.2}
$$

ρ_l^T is the probability that the light which was refracted into the PTFE returns back to the first medium, i.e. it is not absorbed by the media. However at the exit, the light that is observed will follow a Lambertian multiplied by the refraction probability (see section 4.5). Therefore we have

$$\rho_l^T = 2\rho_l \int_0^{\pi/2} \left\{ 1 - F\left(\sin^{-1}\left[\frac{n_0}{n}\sin\theta_r\right], \frac{n_0}{n}\right) \right\} \cos\theta_r \sin\theta_r \mathrm{d}\theta_r \tag{7.3}$$

where θ_r corresponds to the viewing angle (defined in the figure 7.2). We will define the probability given by P_T which corresponds to the above integral and relates ρ_l^T with ρ_l

$$P_T = \frac{\rho_l^T}{\rho_l} \tag{7.4}$$

We do not have $P_R + P_T = 1$ because the angles of integration are different. The value for P_T for the different interfaces is shown in the table I.

At the end, the multiple-diffuse albedo should be given by the expression

$$\rho_l = \frac{1}{P_T}\left\{ 1 - \frac{1 - \rho_l^1}{1 - \rho_l^1 P_R} \right\} \tag{7.5}$$

In the table II we have computed the multiple-diffuse albedo for three different PTFE surfaces. We have assumed that the multiple-scattering albedo is the same in the liquid and in the gas. It is observed that the multiple diffuse albedo increased between 16% and 40% when the material is immersed in the liquid. This increasing is larger for the smaller values of ρ_l obtained in the gas.

Table II shows the predictions of single-diffuse albedo for various PTFE surfaces (as discussed in the chapter 5) and the multiple-diffuse albedo for the PTFE-to-LXe interface. The values obtained for the multiple-diffuse albedo are larger for the liquid comparatively to the gas for the same multiple-diffuse albedo. This increasing is larger for the smaller values of ρ_l obtained in the gas.

In the figure 7.4 we contrast the reflectances distributions obtained in the liquid (solid lines) and in the gas (dashed lines). Both the index of refraction and the multiple-scattering albedo of the PTFE are considered to be the same in the liquid and in the gas. Specular and diffuse lobes have a very distinct behaviour in the liquid and in the gas

We can observe off-specular peaks in the specular component, for the angles of incidence around the critical angle. These peaks are caused by the abrupt increasing of the Fresnel equations when the local angle of incidence approaches the critical angle.

The hemispherical reflectances at the LXe-to-PTFE interface

The directional-hemispherical reflectances of the three components of the reflection as function of the angle of incidence is represented in the figure 7.5. In this figure we observe that he intensity of the diffuse lobe remains almost constant until an angle of
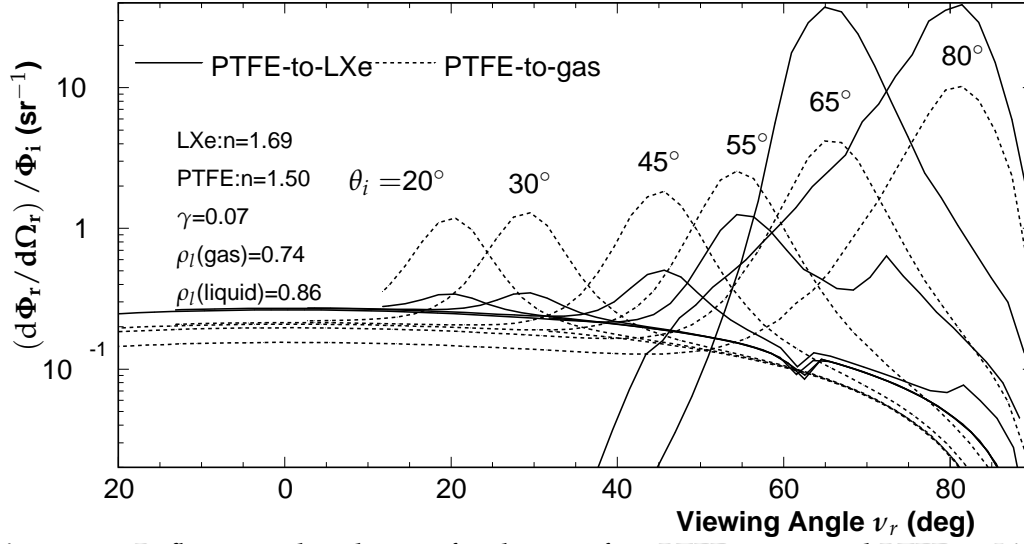
Figure 7.4: Reflectance distribution for the interface PTFE-to-gas and PTFE-to-LXe, the same parameters for the reflectance are used in both situations. For the angles $65°$ and $80°$ we do not observe a diffuse lobe because they are placed above the critical angle for total internal scattering.

$\theta_i = 52°$, then it decreases rapidly to 0 at $59°$. For angles of incidence above $60°$ most of the light goes into the specular spike and specular lobe. Therefore, the PTFE immersed in the liquid can be approximated[1] to a perfect diffuser below the critical angle and to a perfect reflector above the critical angle. The decreasing in the reflectance around the critical angle is caused by the roughness of the surface.

Table III contains the values of the directional-hemispherical reflectance at normal incidence and of the bi-hemispherical reflectance, of three different samples of PTFE and a sample of PFA with $n_{LXe} = 1.69$. The values of the index of refraction correspond to those obtained in the chapter 5. At normal incidence almost all the light reflected by the PTFE immersed in liquid xenon comes from the diffuse component. The ratio between the directional-hemispherical reflectance of the diffuse component at normal direction and the specular components in the skived sample increases from 13 in the gas to 185 in LXe.

The total bi-hemispherical reflectances of PTFE in contact with LXe are all above 75% and can be as high as 89% The increasing in the reflectance is impressive, specially in the samples that show low reflectance in the gas. These values are in agreement with the figures that have published on the PTFE immersed in LXe. These values are

---

[1]The Wolff correction factor $W \simeq 1$ due the lower difference between the index of refraction of the PTFE and of the liquid.
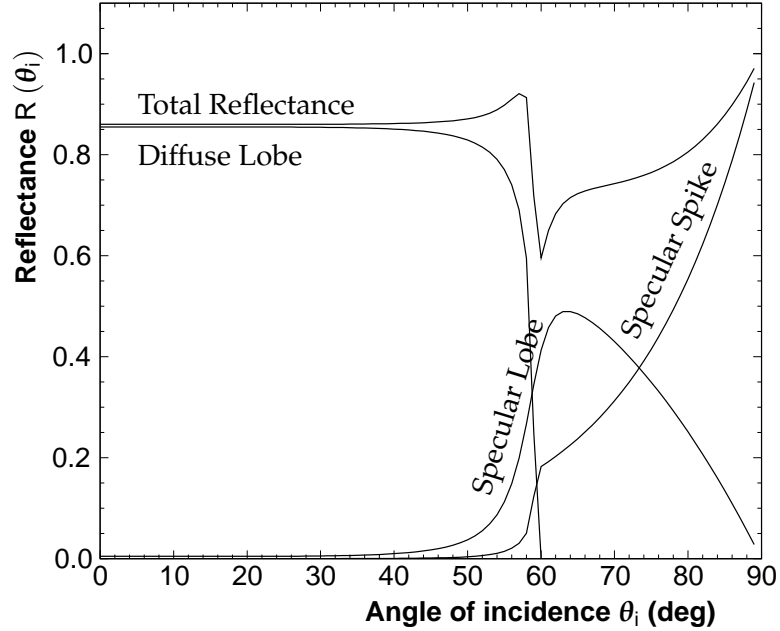
Figure 7.5: The expected reflectance of pressed polished molded PTFE in contact with liquid xenon as a function of the angle of incidence θ_i for light of $=$ 175 nm ($n_{\text{LXe}} =$ 1.69[25]), $n_{\text{PTFE}} = 1.45$ and $\rho_l = 0.72$.

very similar to the values of reflectance previewed in the liquid xenon detectors. Nevertheless, even if the average value agrees there is a serious flaw in the Monte-Carlo simulations that predict the light collection on those detectors. Contrary to the belief that PTFE is a pure diffuser we conclude otherwise that PTFE immersed in LXe behaves as shiny surface at angles of incidence over 60°. This ought change dramatically, the light propagation inside a scintillation chamber and the collecting of light.

The results above show that PTFE is a good reflector in the VUV, specially when in direct contact with liquid xenon. But it cannot be considered a good diffuser because the specular reflectance is dominant in such a case.

Table III: Comparison between the directional-hemispherical reflectances and the bi-hemispherical reflectances in LXe and in the gas for some of the samples of PTFE measured.

	Diffuse Lobe		Specular Lobe		Specular Spike		Total Reflect.		$\frac{R^{\text{diffuse}}}{R^{\text{total}}}$† (%)	
	gas	LXe	gas	LXe	gas	LXe	gas	LXe	gas	LXe
DIRECTIONAL-HEMISPHERICAL REFLECTANCE ($\theta_i = 0°$)										
Skived PTFE	0.51	0.72	0.040	0.0039	0.0	0.0	0.54	0.73	92.9	99.5
PTFE (Dongyang®)	0.45	0.69	0.041	0.0031	0.0	0.0	0.52	0.69	91.2	99.6
Molded polished PTFE	0.59	0.83	0.028	0.0048	0.0024	0.0011	0.72	0.83	95.0	99.3
PFA	0.62	0.79	0.030	0.0060	0.0020	0.0007	0.66	0.79	95.0	99.2
BI-HEMISPHERICAL REFLECTANCE										
Skived PTFE	0.49	0.55	0.089	0.25	0.0	0.0	0.58	0.80	84.2	69
PTFE (Dongyang®)	0.43	0.54	0.095	0.22	0.0	0.0	0.52	0.76	81.6	71
Molded polished PTFE	0.63	0.59	0.040	0.13	0.044	0.16	0.71	0.89	87.8	67
PFA	0.57	0.56	0.050	0.17	0.036	0.13	0.66	0.86	87.7	64

These samples were characterized in the chapter 5.

† Ratio between the diffuse component and the total reflectance (directional-hemispherical or bi-hemispherical)

7.2 Application of the Reflection Model to a Liquid Xenon Chamber

The model of reflectance discussed in the last chapter in Geant4 is here applied to a simulation of a real liquid xenon chamber. The chamber was designed and used to the study the scintillation efficiency and decay time of the scintillation due to nuclear recoils produced by neutron collisions [242]. The chamber and the experiments done are described in [44],[2] and [243].

This chamber has an active volume of liquid xenon of about 1.2 litre, this is read by a set of 7 PMT's with 163 mm diameter each. The walls of the chamber are made of pressed PTFE 1 mm thick (walls and top) and 4 mm thick (bottom).

In the calibration of the liquid chamber it was used a radioactive source of ^{57}Co with an activity of 94 μCu, emitting γ-rays with 122 keV (83.4%) and 136 keV (16.6%). The γ-rays of 122 keV and 136 keV are highly attenuated in the liquid xenon (attenuation length is about 3 mm) thus its energy is immediately converted into photons through
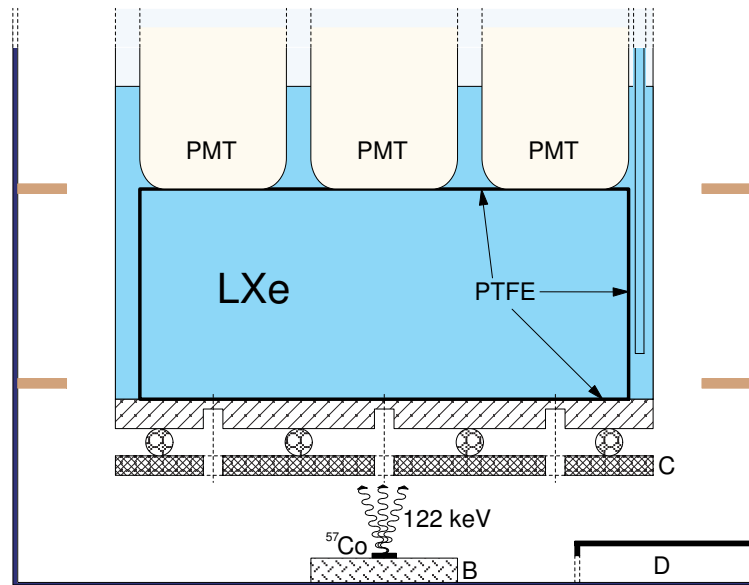

Figure 7.6: Gamma-ray calibration of the liquid xenon chamber. The gamma-ray source is placed at each hole using a magnet placed below the chamber. After the measurements the source is placed in the fender D (from the PhD thesis of Francisco Neves [243]). The sheet C is made of leader.

Figure 7.7: Map showing the position of the PMT's (transverse view). The grey circles represent the holes positioned underneath the bottom of the chamber. The crosses show the center of the PMT. The angular distance between the center of the PMT 1 and the collimators of each photomultiplier is shown in degrees.

photoabsorption[1].

The cobalt source was placed under the chamber's bottom in the vacuum cryostat. The source was placed at every one of seven 12 mm diameter holes carved in a sheet placed under the chamber (see fig. 7.6). One hole is aligned with the centre of the central PMT, the other six holes are misaligned, $12°$ relative, to the PMT's above. The signal of each PMT was read for all positions of the source. The positions of the PMT's and of the holes are shown in the figure 7.7.

When the cobalt source is placed at the central hole, all the PMTs receive the same amount of light (but the central). Hence any differences among the observed signal should be do to differences in the quantum efficiencies and intrinsic resolution of the PMTs.

If the source is housed at any outer hole the amount of light is asymmetric, the PMTs further away should receive less light. The amount of light that reaches each PMT is dependent of the angle between the direction of the hole and the centre of the PMT window. For the different positions of the source the same angles are measured at different positions of the PMTs. Thus an average and standard deviation can be calculated upon six positions of the source. However due the fact that the quantum efficiency of the PMT's is not known they need to be normalized using the data collected with the PMT

---

[1]For gammas of these energies the cross section of the photoabsorption/photoelectric effect is about 20 times larger than the Compton scattering.

in the central position. Thus the normalized amplitude E_i^j of PMT i when the source at the position j is given by:

$$A'_{ij} = \frac{A_i^j / A_0^j}{A_i^0 / A_0^0} \quad \text{with} \quad i = 1, 2, ..., 6 \quad \text{and} \quad j = 1, 2, ..., 6 \tag{7.6}$$

A_i^j is the amplitude of the signal of the single PMT i when the source is at position j.

The amount of light received by each PMT is dependent of the distance between the source and the PMT. E.g., the amount of light that reaches the second photomultiplier when the source is below the first hole is the same of the amount of light that reaches the third PMT when the source is placed in the second hole and so on. Therefore, we can cluster the A'_{ij} in six different groups, that are at the same distance and receive the same amount of light. The average over the this groups results in

$$B_k = \frac{1}{6} \sum_{i=1}^{6} A'_{i\alpha} \quad \text{with} \quad \alpha = (i + k) \bmod 6 \tag{7.7}$$

The r.m.s., σ_{B_k}, is readily computed for each average.

A Geant4 simulation of the chamber, including the gamma ray calibration, was developed. The program was based in a early code due to A. Lindote. The details of this simulation, namely the geometric specifications, are in [244]. The early simulation assumed that the reflection of PTFE walls was purely Lambertian with an albedo of 0.95. We changed the reflection model to include the results of the analysis discussed in chapter 5 and chapter 6. We have not considered the specular spike component because this component was only observed in the PTFE that was polished and the PTFE placed in the chamber was not polished. The gamma rays of 122 keV and 136 keV are generated isotropically in a circle with the same dimensions of the source. The lead sheet and holes are correctly simulated as the gamma rays can scatter at the hole boundaries.

The simulation of the collection of light can be used to gather some insight about the reflectance of the PTFE immersed in liquid and eventually check the overall consistency of the reflectance model. The simulation is performed for several sets of the parameters $\{n_{PTFE}/n_{LXe}, \rho_l, \gamma, L_{ab}, L_r\}$ where n_{PTFE}/n_{LXe} corresponds to the relative index of refraction between the liquid xenon and the PTFE. As discussed in the previous section, n_{LXe} and n_{PTFE} are not well known and the relative index of refraction can range values from 0.86 to 0.97 (with n_{PTFE} between 1.45-1.52 and n_{LXe} between 1.56-1.69). We observed that the results did not changed significantly with the roughness, γ, therefore we have considered a constant value for this parameter of 0.07.

Due the normalization introduced in the equation 7.6, this analysis is not dependent of the scintillation yield of the liquid xenon and of the efficiencies of the PMTs. It is however dependent of the absorption length, L_{ab}, and of the Rayleigh scattering length, L_r of the VUV light in liquid xenon (see 1). These values are not known and need to be also fitted to the data, nevertheless, although both L_{ab} and L_r are not known, the
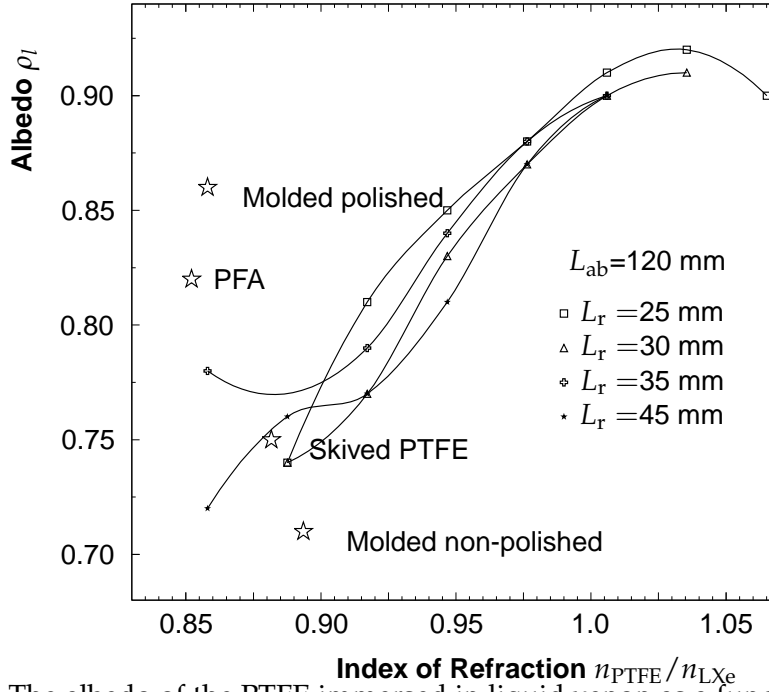
Figure 7.8: The albedo of the PTFE immersed in liquid xenon as a function of the ratio of indices of refraction $n_{\mathrm{PTFE}}/n_{\mathrm{LXe}}$. The various curves are eye guides for the different values of the Rayleigh scattering length in the liquid xenon. The absorption length was set to 120 mm in all the points. The stars represents the values predicted for the three samples of PTFE (with n_{LXe}=1.69) are also shown in this figure.
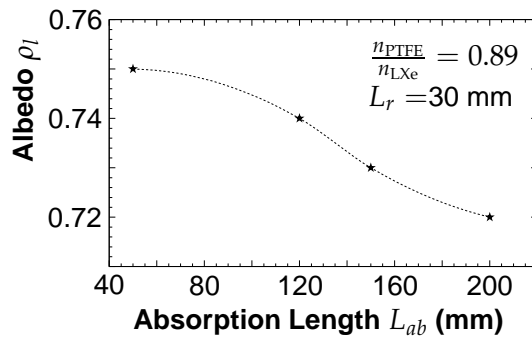
Figure 7.9: Correlation between the absorption length and the multiple-diffuse albedo ρ_l, the relative index of refraction $n_{\mathrm{PTFE}}/n_{\mathrm{LXe}} = 0.89$ and the Rayleigh scattering length L_r are constants.

attenuation length (defined in chapter 1) should be comprised between 25 mm and 40 mm.

For each set of parameters the source is placed below the central PMT and the intensity of light that reaches each PMT is registered. The simulation is repeated placing the source below one of the outer's PMTs with the same set of parameters. The values of A'_{ij} are calculated using the same relation 7.6 and are compared with the experimental data with a χ^2 test

$$\chi^2 = \sum_{i=1}^{N} \frac{B_k^{\text{measured}} - B_k^{\text{simulated}}}{\sigma_{B_k^{\text{measured}}}} \tag{7.8}$$

For a specific set of parameters $\{n, \gamma, L_{\text{ab}}, L_{\text{r}}\}$ we kept the albedo which gave the lowest value for χ^2.

Figure 7.8 shows the albedo obtained as function of the relative index of refraction and for several values of the Rayleigh scattering lengths. We have assumed a constant absorption length of 120 mm. We observe that the albedo increases when the relative index of refraction increases. From the range of $n_{\text{PTFE}}/n_{\text{LXe}}$ (0.85-0.97) the albedo increased from 0.73 to 0.89. This increasing is due the fact that when the relative index of refraction approaches to 1, less light is specularly reflected. This decreasing is compensated by an increasing in the diffuse component. In the figure it is also represented the predictions for the multiple-diffuse albedo and relative index of refraction (with $n_{\text{LXe}} = 1.69$) for some samples measured (see chapter 5).

For $\frac{n_{\text{PTFE}}}{\text{LXe}} = 1$ (perfect diffuser) the multiple-diffuse albedo of the surface is $\simeq 0.92$ which is compatible with the albedo predicted by [242].

The behaviour of the albedo obtained for the minimum of the χ^2 as function of the absorption length and Rayleigh scattering length is represented in the figure 7.9. From this figure we conclude that the albedo decreases monotonically with the absorption length. However, this decreasing is small, when L_{ab} increased from 50 mm to 200 mm the albedo decreased only 0.03.

Although these results are compatible with the predictions made in the section 7.1, we still have too many free parameters and some uncertainties about the modelling used to describe the diffuse reflection in LXe. Therefore, no definitive conclusions can be made without a direct measurement of the reflection distribution of the PTFE in the liquid xenon.

Conclusion

The reflectance of PTFE and other materials with interest to scintillation detectors was studied in detail in this thesis. The study was performed using a goniometer specifically designed and constructed to measure the reflectance in the vacuum ultra-violet region (VUV). This goniometer is placed inside a vacuum air tight chamber filled with argon gas. To produce the VUV light we constructed a gaseous xenon proportional counter that could be operated in trigger mode with a photomultiplier to detect the light. The light emitted by this source is collimated and strikes the reflecting surface, being measured along a specific angle of incidence, that can be changed at will. The light is detected by a photomultiplier placed at a specific viewing angle. Both the position and orientation of the sample surface and the position of the photomultiplier can be changed to set different values of the angle of incidence and reflectance, thus measuring the reflectance distribution of the PTFE.

The experimental procedure was tested by measuring the reflectance of metallic and crystalline samples, namely quartz, glass, gold and two samples of copper. The first three materials showed values similar to the expected values that are known. The copper samples were affected by oxidation in air and we could observe the variation of the reflectance with the oxidation of the sample.

The reflectance of PTFE was measured in samples prepared by different manufacturing processes and polishing. The reflectance distributions showed to be composed by three different reflection components, a diffuse lobe, a specular lobe and a specular/coherent spike. The origin of these components is described in detail in this thesis. The diffuse lobe corresponds to internal scattering of the light in the volume of the material underneath the surface and yields a reflection distribution which is mostly independent of the direction of the incident light. The specular lobe is centered along the specular reflection direction and has a width and distribution which are proportional to the roughness of the surface. Finally, the specular spike corresponds to mirror like reflection which can be attributed to a coherent reflection at the mean plane of the

(irregular) surface.

The reflectance from these components can be fully described for each wavelength using only four free parameters: the total diffuse albedo of the surface, the index of refraction of the reflector material, the width of the specular lobe and the fraction or relative intensity of the specular spike. The attenuation coefficient and the index of refraction of the medium above the surface can also be included in a fit. This description reproduces fairly well the details of the reflectance distributions that we measured. If the rough surface is very rough only three parameters are necessary because the specular spike can be neglected. However, it might not be the case if the total reflection takes place (see fig. 7.4). The data show that the specular lobe is best reproduced if the reflecting surface is modeled by a characteristic ellipsoid of reflection, whose oblateness embodies the features of the surface, notably its roughness. In this case the reflected surface is governed by a Trowbridge-Reitz probability distribution function. This conclusion comes at no surprise though, since these materials are granular by nature.

The index of refraction of PTFE is about 1.5 at the wavelength of scintillation of the xenon, larger than in the visible, thus the amount of specularly reflected light is also larger. The fit to the data using the extinction coefficient leads to a value that is compatible with zero, whose upper limit agrees with published values.

The relative intensity of the coherent/specular spike appears experimentally to vary exponentially with the cosine of the angle of incidence, $\cos \theta_i$ in all cases studied. This is in contrast to the prediction of the Beckmann-Spizzichino model of an exponential dependency in $\cos^2 \theta_i$. Such a dependence can be caused by the ellipsoid-shaped nature of the micro-facets or the polishing scratches visible on the surface, which might correspond to a combination of different scale roughness or both effects. We have studied the intensity of the specular spike using the Kirchhoff approximation for both ellipsoid-shaped and cylindric-shaped surfaces. However, this issue deserves more study, specifically the measurement of the samples that was observed a specular spike for different wavelengths to study the behaviour of the intensity of the specular spike with the wavelength of the incident light.

The reflectance distribution of the copolymers PFA, FEP and ETFE was also measured. The reflectance of PFA and PTFE are similar, but not ETFE which reflection is dominantly specular with only a very small diffuse component. The FEP showed a reflectance distribution which is somehow intermediate between PFA and ETFE.

The directional-hemispherical reflectance at the normal incidence is placed between 40% and 72% depending of the manufacturing process and surface finishing of the PTFE. The diffuse lobe accounts for about 90% of the total reflectance when the surface is illuminated from above ($\theta_i = 0°$). These values agree with the measurements made at the Alvensleben Laser Zentrum ([4], see section 1.3). The bi-hemispherical reflectance of PTFE obtained is between 42% and 71% for the PTFE and PFA. The larger values of the reflectance were observed for the smoother samples. The diffuse lobe amount to 86% of the total reflectance in the non-polished samples and 82-85 % of the

total reflectance of the polished surfaces of contact with gas/vacuum.

One finds that the reflectance of the PTFE increase with the wavelength. This increasing appears to come basically from the diffuse component of the reflection, which increases for wavelengths near the visible. The index of refraction decreases from about 1.5 at 175 nm to 1.35 in the visible, leading to a decrease of the intensity of the specular components. Hence, PTFE can be considered a *perfect* diffuser in the visible. However, when illuminated with UV light, a significant part of the reflected light is specular. It was also observed that the width of the specular lobe, γ decreases with the wavelength, this effect can only be understood using a physical based model.

The effect of the roughness of the surface in the diffuse lobe is accounted by the Oren-Nayar model. This description uses a parameterization restricted to a gaussian distribution of micro-facets to describe the correction of the Lambertian reflectance. We have extended the Oren-Nayar model to the Trowbridge-Reitz distribution and obtained, with some approximations, an algebraic solution for this correction factor.

The experiments were simulated using the Geant4 Monte Carlo simulation package. We concluded that the reflection models implemented in Geant4 are unable to describe effectively the reflectance distributions that we observe, even if unrealistic parameters are considered. Therefore, we implemented and coded a new class in Geant4 that embodies the analysis model of reflection that is proposed in this thesis. The new model successfully describes the reflection of the surfaces that we measured.

The reflectance of PTFE immersed in liquid xenon are often announced to be much higher than above (about 90%). Assuming that the same optical properties of PTFE still apply at $-100°$C then in such case the indices of refraction at either side of the interface are much closer than before. Moreover, the liquid has a highest index of refraction, which means that there are total internal reflection for all range of angles above the critical angle. This favours the internal reflection in the LXe-to-PTFE interface and the transmission probability in the PTFE-to-LXe interface. These two factors increase both the intensity of the specular lobe and the intensity of the diffuse lobe resulting in an bi-hemispherical reflectance in the liquid of 76-90% depending of the surface and manufacture.

The direct measurement of the reflectance of PTFE immersed in liquid xenon is the natural follow up of this work. However, this measurement has significant technical difficulties that are not easily overcomes. Some fundamental properties of the liquid xenon such as its index of refraction, attenuation length and Rayleigh scattering length are not well known. These quantities have all to be measured, and it will be very difficult to measure one without knowing the others as well. These effects are strongly correlated and the main difficulty will be to disentangle them.

Another forthcome of this work is to measure the reflectance distributions of PTFE and like with the scintillation light of the krypton, argon and neon, all of which are not well known. The wavelength of the scintillation of these rare gases is smaller than the absorption edge of the PTFE (2). Thus, PTFE is expected to have almost no diffuse

reflection at those wavelengths.

Some results exposed in this thesis were published in the NIM-A [226], [212] and in the Journal of Applied Physics [213].

Principles of Radiometry

Radiometry is the measurement of the energy content of the electromagnetic radiation field and how the energy Q is transferred from a source, through a medium, into a detector. Thus, the radiometric measurements are usually expressed in unites of energy but can be also given in number of photons (the later case is referred as actiometric).

These concepts are too well known and can be found in many specialized publications. They are introduced here for completeness purposes and to fix the notation and the definition of relevant quantities. The definitions exposed here are based in [113] and [114].

The Radiant Flux and Radiant Intensity

The radiant flux is defined as the amount of electromagnetic energy Q received, transferred or emitted per unit of time by a given object,

$$\Phi = \frac{dQ}{dt} \qquad [W] \tag{A.1}$$

This quantity can also be expressed as the number of photons N_{ph} per unit of time that are emitted received or transverse a certain area,

$$\Phi = \frac{dN_{ph}}{dt} \qquad [N_{ph}s^{-1}] \tag{A.2}$$

Usually we distinguish between incident flux Φ_i, emitted/reflected flux Φ_r and transmitted flux, Φ_t, according as the radiation is received, emitted or transmitted.

The radiant intensity or photon flux intensity is defined as the ratio between the flux emitted towards a specific direction per unit of solid angle $d\Omega$,

$$I = \frac{d\Phi_r}{d\Omega} \tag{A.3}$$

A. PRINCIPLES OF RADIOMETRY
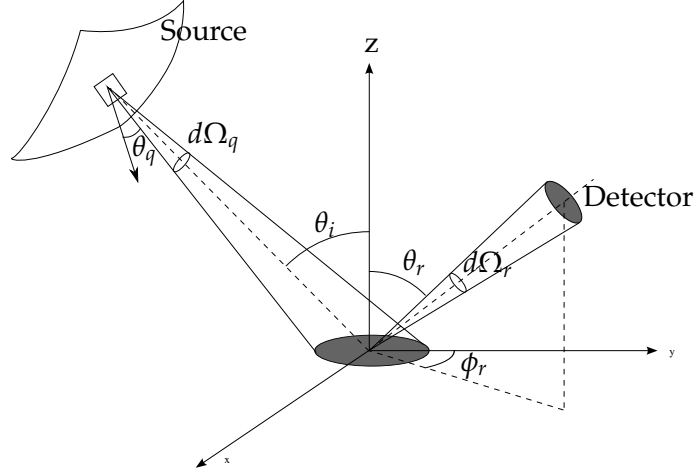
Figure A.1: Definition of the angles and solid angles relevant to radiometry.

and is in general dependent of the angles θ and ϕ of the direction of the radiation.

The Irradiance and Radiance of a Surface

All incident and reflected directions associated to a particular scattering point, S, are inside a hemi-sphere with an origin at S.

Two different light sources that produce the same illuminated area in this hemi-sphere will produce the same illuminated area in the surface. Specifically a big source viewed at a grazing angle will produce the same result as a small source viewed frontally. Thus it will be the foreshortening area $A_f = A_{\text{source}} \cdot \cos\theta_q$ (figure A.1) that needs to be considered. $\cos\theta_q$ is the angle between the direction of the photons and the vector defined between the source and the scattered point. Similarly a detector placed at a low grazing angles probe larger area of the radiating surface in comparison to the same detector if facing the surface from above at the perpendicular to the surface. The effective radiating area is $A\cos\theta_r$ (see figure A.1). Both the irradiance and radiance use of this concept of foreshortening area.

The irradiance measures the incident flux of radiation per unit of irradiated area, $\text{d}A$,

$$E = \frac{\text{d}\Phi_i}{\text{d}A} \tag{A.4}$$

and decreases with increasing the angle of incidence.

The radiance at a given point is defined as the flux emitted along a certain direction per unit of solid angle per unit of foreshortened area:

$$L = \frac{\text{d}^2\Phi_r}{\text{d}A \cos\theta_r \text{d}\Omega_r} \tag{A.5}$$
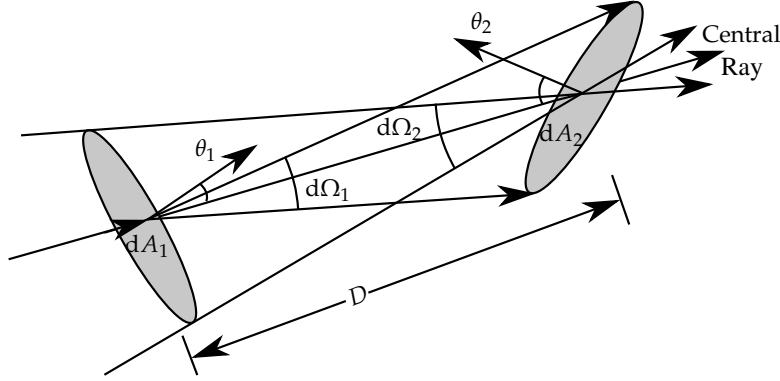
Figure A.2: Conservation of the radiance along a tube of rays (adapted from [113])

.

where $\cos \theta_r$ is the angle between the normal of the element of area dA and the direction of the emitted light.

The radiance is related intrinsically with visual sensation of brightness [245]. One important characteristic of this quantity is given by the radiance conservation theorem which states that the the radiance is conserved along any tube of rays propagating through an optical system .

Proof:

If dA_1 and dA_2 are infinitesimal elements of area and are at a distance D from each other then (see A.2)

$$d\Omega_1 = \cos \theta_1 \frac{dA_1}{D^2}$$

$$d\Omega_2 = \cos \theta_2 \frac{dA_2}{D^2}$$

thus,

$$d\Omega_1 \cos \theta_2 dA_2 = d\Omega_2 \cos \theta_1 dA_1 \tag{A.6}$$

Since the flux is conserved (in the absence of absorption) $d\Phi_1 = d\Phi_2$, therefore the radiance of the two surfaces dA_1 and dA_2 is conserved, $L_1 = L_2$.

In a boundary between two isotropic homogeneous media with two different indexes of refraction n and n' the power of the beam is the same in both sides of the surface thus,

$$L \cos \theta dA d\Omega = L' \cos \theta' dA d\Omega' \tag{A.7}$$

an since $d\Omega = \sin \theta d\theta d\phi$ and $d\Omega' = \sin \theta' d'\theta d'\phi$ then $n' \sin \theta' = n \sin \theta$ (Snell-Descartes law) then

$$\frac{L'}{n'^2} = \frac{L}{n^2} \tag{A.8}$$

A. PRINCIPLES OF RADIOMETRY

The Bidirectional Reflectance

Let the incident beam comes from the direction (θ_i, ϕ_i) within a solid angle $d\Omega_i$. The portion of the flux which strikes the element of area dA_i centred at (x_i, y_i) is given by $d\Phi_i$. The reflected radiance towards the direction (θ_i, ϕ_r) at the point (x_r, y_r) should be proportional to

$$dL = S\left(\theta_i, \phi_i, x_i, y_i, \theta_r, \phi_r, x_r, y_r\right) d\Phi_i \qquad (A.9)$$

where S is a scattering function known as the **bidirectional scattering-surface reflectance function** BSSRDF. This is a function of the middle point of the incident flux, (x_i, y_i), the point from where the reflected flux emerges (x_r, y_r) and the directions of incidence and reflectance. These two points can be different due effects such as sub-surface scattering and multi-scattering.

This is a generic function dependent of 8 parameters and is in general of no practical use. However it can be assumed that the surface element is uniformly irradiated and the radiance is only dependent of the incident direction, in which case the incident flux is

$$d\Phi_i = L_i \cos\theta_i d\Omega_i dA_i \qquad [W] \qquad (A.10)$$

Moreover, in general the scattering properties of the sample are uniform and isotropic across the reference plane, so that the scattering function does not depend on the location of the point (x_r, y_r), but it still depends on the distance between (x_i, y_i) and (x_r, y_r). In such a case the radiance is written as

$$dL_r = \varrho_r\left(\theta_i, \phi_i, \theta_r, \phi_r\right) \frac{d\Phi_i}{dA_i} \qquad [\text{Wm}^{-2}\text{sr}^{-1}] \qquad (A.11)$$

The function $\varrho_r\left(\theta_i, \phi_i; \theta_r, \phi_r\right)$ is called the **bidirectional reflected distribution function** (BRDF). This function is in fact the ratio between the differential radiance and the irradiance of the surface,

$$\varrho_r\left(\theta_i, \phi_i, \theta_r, \phi_r\right) = \frac{dL_r\left(\theta_i, \phi_i, \theta_r, \phi_r\right)}{L_i\left(\theta_i, \phi_i\right)\cos\theta_i d\Omega_i} \qquad (A.12)$$

In a similar way it is possible to define the **bidirectional transmission-distribution function** defined by:

$$\varrho_t\left(\theta_i, \phi_i, \theta_t, \phi_t\right) = \frac{dL_t\left(\theta_i, \phi_i, \theta_t, \phi_t\right)}{L_i\left(\theta_i, \phi_i\right)\cos\theta_i d\Omega_i} \qquad (A.13)$$

These functions, ϱ_r and ϱ_r, cannot be measured precisely since the solid angles involved are infinitesimal.

In case the reflecting surface is viewed by the detector from a great distance, then it appears for all practical purposes as it was a point source. Then the radiance can be replaced by the intensity, $I = \int L_r \cos\theta_r dA_r$.

The *BRDF*, the **bidirectional reflected-radiance-distribution function** *BRIDF* is defined as ratio of the radiant intensity I_r in a direction (θ_r, ϕ_r) to the incident flux Φ_i.

$$\varrho\,(\theta_i, \phi_i, \theta_r, \phi_r) = \frac{\mathrm{d}I_r\,(\theta_i, \phi_i, \theta_r, \phi_r)}{\mathrm{d}\Phi_i\,(\theta_i, \phi_i)} \tag{A.14}$$

When the element of area $\mathrm{d}A_i$ is small enough so that the radiance L_r can be considered constant in $\mathrm{d}A_r$, the functions *BRIDF* and *BRDF* are related by the relation

$$\varrho_{rl}\,(\theta_i, \phi_i, \theta_r, \phi_r) = \varrho_r\,(\theta_i, \phi_i, \theta_r, \phi_r)\cos\theta_r \tag{A.15}$$

In either case the bidirectional reflectance functions relate the incoming and outcoming directions.

Reflectance Geometry Definitions

The bidirectional reflectance is a conceptual quantity and cannot be measured directly due the fact that it corresponds to infinitesimal solid angles. In real life the solid angles can be made small, but are still finite. Real experiments involve radiation that goes some specific solid angle. Hence, this as to be taken into account when measuring this reflectance functions.

BIDIRECTIONAL   DIRECTIONAL-HEMISPHERICAL

BI-CONICAL   BI-HEMISPHERICAL

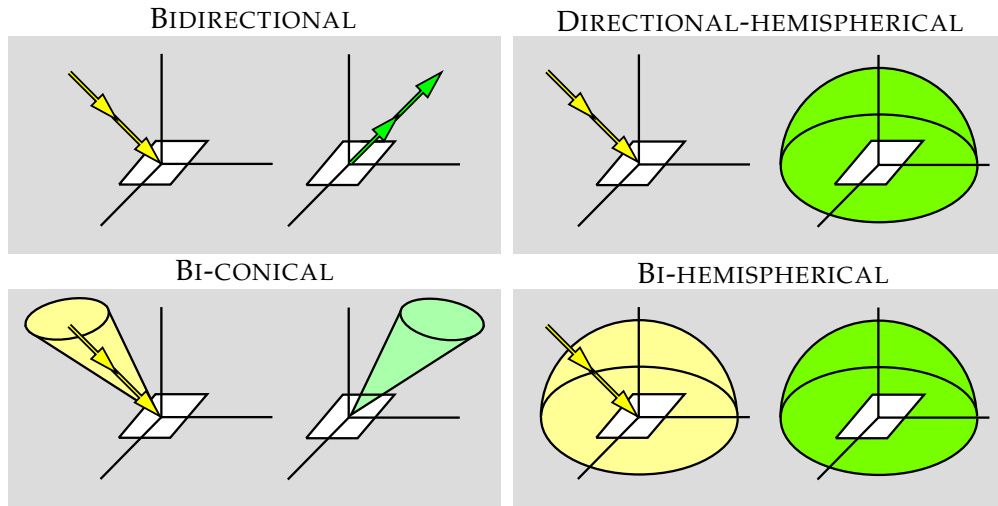**Figure A.3:** Definition of the reflectances that are used through out the text. Actually only the bi-hemispherical and bi-conical reflectances can be measured, the directional reflectances are conceptual only (adapted from [246]).

The reflectance R is defined as the ratio between the reflectance flux and the incident flux,

$$R\,(\Omega_i, \Omega_r, \Phi_i) = \frac{\Phi_r}{\Phi_i} \tag{A.16}$$

However, a more correct expression usually requires the definition of the beam geometry. We are interested in specifically three different geometries; i) directional-conical reflectance, ii) directional-hemispherical reflectance and ii) the bi-hemispherical reflectance (see figure A.3). All of these reflectances can be measured directly or obtained from the $BRIDF$ when it is known.

The **directional-conical reflectance** applies to a reflected solid angles that is far from infinitesimal. The direction of the incident light is supposed to be unidirectional and the reflected light is assumed to be within the cone Ω_r. This factor is obtained from the BRIDF integrating over Ω_r,

$$\varrho^{DC}\left(\theta_i, \phi_i; \Omega_r\right) = \int_{\Omega_r} \varrho\left(\theta_i, \phi_i, \theta_r, \phi_r\right) d\Omega_r \tag{A.17}$$

where ϱ corresponds to the bidirectional reflectance function.

The **directional-hemispherical reflectance** is characterized for a surface which receives incident radiation that comes from an incident direction (θ_i, ϕ_i). The reflected flux is measured in hemisphere of all possible viewing directions. Thus, it is given by the integral of $BRIDF$ for all the viewing directions,

$$R^{DH}\left(\theta_i, \phi_i; 2\pi\right) = \int_{2\pi} \varrho\left(\theta_i, \phi_i, \theta_r, \phi_r\right) d\Omega_r \tag{A.18}$$

This function can also be called *black-sky albedo*.

The **bi-hemispherical reflectance** is by definition the ratio between the reflected flux and the incident flux, both measured over the whole hemisphere above the surface (see fig. A.3). For the BHRF is necessary to specify the specific illumination conditions. When the surface is illuminated under diffuse light, thus the incident photons have a random incident direction BHRF is given by the integral of the $BRIDF$ over the hemisphere for the incident and reflectant direction

$$R^{BH}\left(2\pi; 2\pi\right) = \frac{1}{\pi} \int_{2\pi} \int_{2\pi} \varrho\left(\theta_i, \phi_i, \theta_r, \phi_r\right) d\Omega_r \cos\theta_i d\Omega_i \tag{A.19}$$

This function is also called the *white-sky albedo*.

However under normal ambient conditions there is also a directional component which can be introduced in the above integral, this is called the *blue-sky albedo*.

The Data Analysis Program

The differential reflectance functions, in particular the BRIDF function, are defined for infinitesimal solid angles. In practice we cannot measure such angles. In fact, the experimental data measured with the goniometer described in the chapter 2 corresponds to the ratio between the intensity observed in the field of view of the PMT defined by the solid angle Ω_r and the flux incident in the surface within a cone with solid angle Ω_i. To fit the data is necessary to compare these two quantities, therefore it was necessary to develop a data analysis program that relates both quantities. In the fitting process the BRIDF is assumed to be described by a function ϱ dependent of a specific set of parameters (e.g. index of refraction n, albedo ρ_l). A Monte Carlo simulation is used to obtain the experimental quantity. In this program various directions of incidence, **i**, and reflectance, **r**, are generated within the solid angles Ω_i and Ω_r. These two directions are geometrically connected to a hit taken randomly position or the reflecting surface. The BRIDF function is calculated for many directions within these two solid angles, so that its value could be compared with the experimental data.

The system of coordinates is represented in the figure B.1. The point $\mathscr{O}(0,0,0)$ is at the centre of the reflecting surface. The plan $x\mathscr{O}y$ is the plan of the movement of the PMT where both ν_i and ν_r are defined. The angle ψ is the angle defined between the normal of the sample and the plan $x\mathscr{O}y$.

Direction of Incidence

We have considered that the photons are generated at fixed point $\mathscr{P}(p_s, 0, 0)$, where p_s is the distance between the window of the proportional counter and $\mathscr{O}$ the centre of the reflecting surface (see table I for the definition of the geometrical parameters). A direction of incidence is randomly generated inside the incident cone Ω_i. The polar (ϑ)
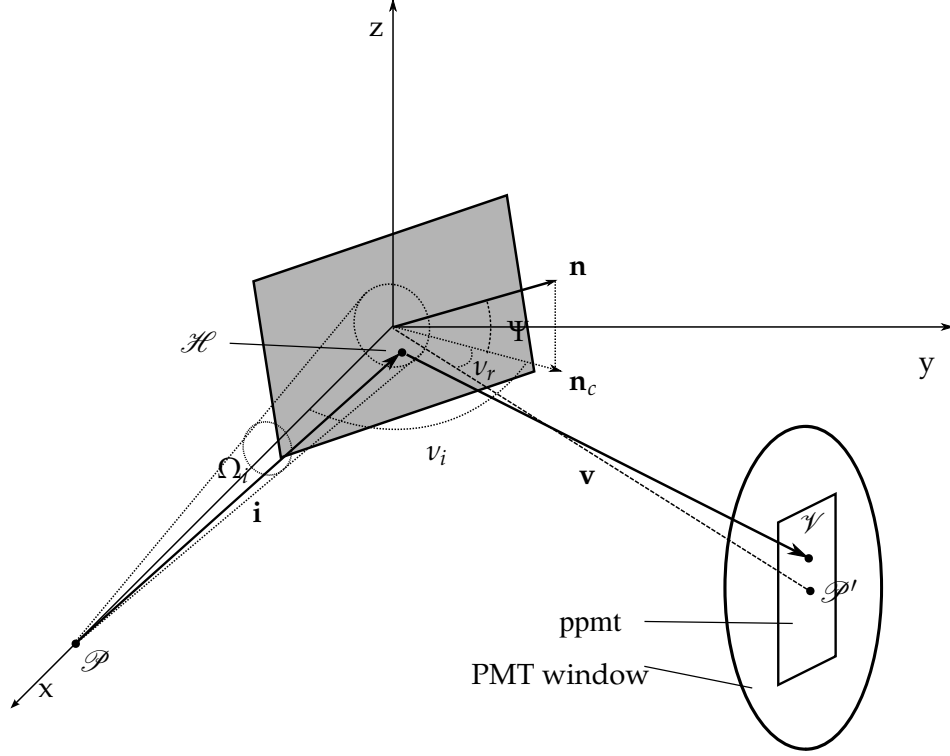
Figure B.1: The system of coordinates. Relation between the variables $\{v_i, v_r, \psi\}$, in the plan *xoy*, and the variables $\{\theta_i, \theta_r, \phi_r\}$. The point $\mathcal{H}$ is the scattering point, $\mathcal{V}$ is the viewing point at the PMT window and $\mathcal{P}$ is where the photons are generated (the source).

and azimuthal (φ) angles are generated with the following functions

$$\vartheta = \arccos\left[\cos\epsilon + \xi \cdot (1 - \cos\epsilon)\right] \tag{B.1a}$$

$$\varphi = 2\pi\xi \tag{B.1b}$$

where $\xi \in [0, 1]$ are random numbers, ϵ is the semi-apex angle of incident cone Ω_i

The direction of incidence **i** is given by

$$\mathbf{i} = \cos\vartheta\,\hat{\mathbf{e}}_\mathbf{x} + \sin\vartheta\cos\varphi\,\hat{\mathbf{e}}_\mathbf{y} + \sin\vartheta\sin\varphi\,\hat{\mathbf{e}}_\mathbf{z} \tag{B.2}$$

where $\hat{e}_x$, $\hat{e}_y$ and $\hat{e}_z$ are unitary vectors along the axis x, y and z.

It should be noted that the direction of the photons is actually $-\mathbf{i}$ and not $\mathbf{i}$ but the latter is chosen by convenience that $\mathbf{i} \cdot \mathbf{v}$, $\mathbf{i} \cdot \mathbf{r}$, $\mathbf{i} \cdot \mathbf{n}$ are all positive. The global normal of the surface, $\mathbf{n}$, is computed using the angular positions of the PMT, v_r, and of the sample, v_i, and ψ,

$$\mathbf{n} = \cos v_i \cos\psi\,\hat{\mathbf{e}}_\mathbf{x} + \sin v_i \cos\psi\,\hat{\mathbf{e}}_\mathbf{y} + \sin\psi\,\hat{\mathbf{e}}_\mathbf{z} \tag{B.3}$$

Table I: Definition of the geometric parameters used

p_s	Distance between the proportional counter and and the centre of the reflecting surface	220.6 mm
p_o	Distance from the PMT and centre of the surface	66.4 mm
V	Height of the slit in front of the PMT	13.4 mm or 12.0 mm
H	Width of the slit in front of the PMT	2.0 mm or 1.0 mm

The angle of incidence θ_i is as usually the angle between the normal **n** and the direction of incidence **i**

$$\cos \theta_i = \cos \vartheta \cos \nu_i \cos \psi + \sin \vartheta \cos \varphi \sin \nu_i \cos \psi + \sin \vartheta \sin \varphi \sin \psi \qquad (\text{B.4})$$

Hit Position

A photon going along the direction **i** hits the surface at the point $\mathscr{H}$. This point can be calculated now The equation of the surface, which contains the point $\mathscr{O}$ and with a normal **n** (see figure B.1) is given by

$$\cos \nu_i \cos \psi x + \sin \nu_i \cos \psi y + \sin \psi z = 0 \qquad (\text{B.5})$$

where (x, y, z) is a point in the surface. The equation of the line with direction **i** and containing the point $\mathscr{P}$ is given by

$$\frac{x - d_{po}}{\cos \vartheta} = \frac{y}{\sin \vartheta \cos \varphi} = \frac{z}{\sin \vartheta \sin \varphi} \qquad (\text{B.6})$$

The intersection between this line and the surface gives the position of the photon hit, $\mathscr{H}$ (figure B.1). After some algebraic manipulation $\mathscr{H}$ is given by the coordinates

$$\mathscr{H} = \frac{d_{po}}{\cos \theta_i} \left\{ \left(\mathbf{i}_y \cdot \mathbf{n}_y + \mathbf{i}_z \cdot \mathbf{n}_z \right), -\mathbf{i}_x \cdot \mathbf{n}_y, -\mathbf{i}_x \cdot \mathbf{n}_z \right\} \qquad (\text{B.7})$$

Viewing Direction

The position of the centre of the PMT window, $\mathscr{P}'$ (see figure B.1) is given by

$$\mathscr{P}'\left(\nu_i, \nu_r\right) = d_{vo} \sin\left(\nu_i + \nu_r - \frac{\pi}{2}\right) \mathbf{\hat{e}_x} + d_{vo} \sin\left(\nu_i + \nu_r - \frac{\pi}{2}\right) \mathbf{\hat{e}_y} \qquad (\text{B.8})$$

d_{vo} is the distance between the PMT and the position $\mathscr{O}$ in the sample.

B. THE DATA ANALYSIS PROGRAM

The slit placed in front of the PMT window can have dimensions $HV = 2.0 \times 13.40\,\mathrm{mm}^2$ or $HV = 1.0 \times 12.00\,\mathrm{mm}^2$. A point within this slit (x', y') is randomly generated by equations

$$x' = \frac{1}{2}H(2\xi - 1) \tag{B.9}$$

$$y' = \frac{1}{2}L(2\xi - 1) \tag{B.10}$$

where $\xi \in [0, 1]$ are random numbers. This is the point where presumably the photon hit the PMT window. Thus the viewer point $\mathscr{V}$ has the following coordinates

$$\mathscr{V} = \left(p_o \cos v^* - x' \sin v^*, p_o \sin v^* + x' \sin v^*, y'\right) \qquad \text{with} \quad v^* = v_i + v_r \tag{B.11}$$

The viewing direction $\mathbf{v}$ is defined by this point $\mathscr{V}$ and the hit position $\mathscr{H}$ (see figure B.1). The viewing angle, θ_r, is the angle between the direction, $\mathbf{v}$, and the global normal to the surface, is given by

$$\cos \theta_r = \mathbf{v} \cdot \mathbf{n} \tag{B.12}$$

Local Angles

The physical quantities, notably the micro-facet probability distribution function, etc ..., are all expressed relative to the local angles, θ_i', θ_r' and α (see section 4.2). If the reflection is specular these angles are $\theta_i' = \theta_r' = \theta'$ and is given by

$$\cos 2\theta' = \mathbf{v} \cdot \mathbf{i} \tag{B.13}$$

The local normal, $\mathbf{n}'$, is defined by the expression

$$\mathbf{n}' = \frac{\mathbf{i} + \mathbf{v}}{2 \cos \theta'} \tag{B.14}$$

The angle α is the angle between the global normal and the local normal thus we have

$$\cos \alpha = \mathbf{n} \cdot \mathbf{n}' \tag{B.15}$$

Both the diffuse lobe and specular spike do not make use of the local angles. The specular spike is only dependent of the global angle θ_i.

The directional-conical reflectance

The BRIDF is calculated for each the angle of incidence (eq. B.4), viewing direction (eqs. B.12) and the local angles (eqs. B.13 and B.15). The function is computed N times, for directions of incidence and reflectance within the solid angles Ω_i and Ω_r for each

pair of angles $\{\nu_i, \nu_r\}$. The directional-conical reflectance (see chapter A) is taken as the average of this N values,

$$\varrho^{DC}(\Omega_i, \Omega_r) = \frac{1}{N} \sum_N \varrho(\mathbf{i}, \mathbf{v}) \qquad \text{with } \mathbf{i} \in \Omega_i \text{ and } \mathbf{v} \in \Omega_r \qquad \text{(B.16)}$$

This function ϱ^{DC} can finally be compared with the experimental data at each angular positions of both the source and photo-detector. This function is feed into the genetic algorithm and the unknown parameters of ϱ are fitted to the data.

B. THE DATA ANALYSIS PROGRAM

The Genetic Algorithm of Simulation

The genetic algorithm GA is a heuristic search algorithm which adapts some concepts of natural selection and of genetics to problems of computational optimization. These algorithms are efficient when the search space is large, complex and poorly understood. Moreover, it does not require the evaluation of any derivatives. An overview of these methods can be found elsewhere [247], [248] and [249]. Here we describe the genetic algorithm used to find the best parameters of reflectance by minimization of a χ^2 function. The schematics of the implemented genetic algorithm is shown in the flowchart C.1.

All genetic algorithms start by the definition of an initial population of rows of parameters. Each individual, the parameter row, is described by a phenotype which contains the coded information. Each phenotype is composed by a specific number of genes. These genes correspond to the parameters of the function ϱ implemented. Hence, for example three genes/parameters for the geometrical optical approximation (ρ_l, n, γ), four genes/parameters in the case of the model with a specular spike (ρ_l, n, γ, K) and so on. The genes are introduced in a form of a vector $\mathbf{p} = \{g_1, g_2, ..., g_n\}$, specific for each individual and where g_i corresponds to the value of the gene/parameter.

The values of the parameters for each individual row are generated randomly uniform inside the interval $[g_m, ..., g_M]$ where g_m and g_M are the minimum and maximum values that this parameter can have. These limits are introduced at the beginning of the program and actually define the search space during the minimization. The values of the genes are introduced through a real value encoding. This type of encoding was chosen over the more common binary encoding because the parameters used in ϱ are real numbers.

The number of individuals in the population is critical for the performance of the genetic algorithm. The minimization was tested for different population sizes. It was
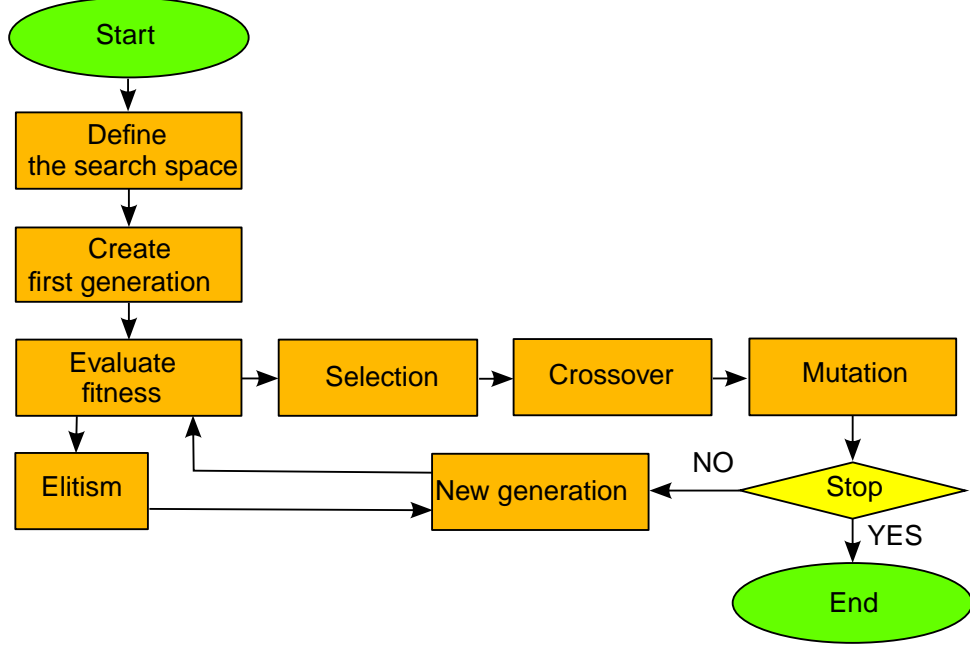
C. THE GENETIC ALGORITHM OF SIMULATION

Figure C.1: Schematics of the genetic algorithm implemented in the minimization code. The algorithm starts by defining the search space and by creating the first generation. Then the fitness of this generation is evaluated using a χ^2 distribution. The new generation is formed through selection, crossover and mutation (see text). When the stop condition is achieved the minimization ends, when it is not achieved the fitness is evaluated for this new generation.

found that in our case the optimum population size is between 100 and 1000, for a minimization speed almost constant within this interval.

The reflectance measured (see section 3.15) corresponds to a directional-hemispherical reflectance. However, $\mathbf{p}$ is used to evaluate the BRIDF function. The transformation between these two quantities was discussed in the appendix B.

The measured directional-conical reflectance, ϱ^O, is obtained for a specific position of the PMT and the sample, $\mathbf{v} = \{\nu_i, \nu_r, \psi\}$. The results are compared with the predicted reflectance using a fitness function, we used χ^2 function

$$\chi^2(\mathbf{p}) = \sum_{i=1}^{N} \frac{\left(\varrho_i^O(\mathbf{v}) - \varrho_i(\mathbf{v}, \mathbf{p})\right)^2}{\left(\sigma_{\varrho_i^I}^2\right)} \tag{C.1}$$

where ϱ^I is the experimental value measured at the angular position $\mathbf{v}$ and ϱ is the reflectance predicted for the very same point in space $\mathbf{v}$ with the vector of parameters $\mathbf{p}$.

Table I: Parameters of the genetic algorithm.

Number of genes	3-5
Population size (number of individuals)	100-200
Crossing rate	0.80
Whole arithmetical crossover rate	0.32
Simple arithmetical crossover rate	0.16
Heuristic crossover rate	0.32
hard mutation rate	0.01
soft mutation rate	0.02
Elitism (number of individuals)	5
Intensity of small mutation	0.05

The sum of the crossover rates is such that $0.32 + 0.16 + 0.32 = 0.80$, the remain individuals are copied exactly to the next generation.

The value of the fitness function is used to generate the next generation of parameters. The two processes that create the next generation are reproduction and mutation as explained below.

Selection and crossover

The idea is to create new solutions through evolution of the actual population. The individuals that lead to better solutions (smaller values of χ^2), i.e. the most fitted individuals ought to be given preference in shaping the new generation. Thus, only the selected individuals are able to breed (through crossover and mutation) the new generation. The individuals are selected according to their fitness in a process that mimics the principles of natural selection.

The individuals are chosen using method of roulette wheel or the *Wheel of Fortune*. In this method the individuals are mapped in a wheel proportionally to their fitness. The probability that the individuals are selected to crossover is proportional to the mapped area in the *Wheel of Fortune*.

Two individuals, the parents, are selected using the *Wheel of Fortune* to breed the next generations (the offspring). This process is called crossover. We used four different types of crossover that are chosen aleatory with a pre-defined probability. Each individual can be selected more than once to crossover because they are not destroyed in this process. The processes implemented are

a) Whole arithmetic crossover: The crossover is performed for each specific chromosome of the individual parents $\mathbf{p}_i$ and $\mathbf{p}_j$. A random number $\xi \in [0, 1]$ is

generated. The value of the offspring chromosome $\mathbf{p}_k$ is given by

$$\mathbf{p}_k = \xi \mathbf{p}_i + (1 - \xi)\, \mathbf{p}_j \tag{C.2}$$

b) Simple arithmetical crossover: The offspring receives the genes from both parents without any change in their values. An integer random number $a \in [0, n]$ is randomly chosen. If the parent chromosomes are given by the $\mathbf{p}_1 = (x_1, ..., x_n)$ and $\mathbf{p}_2 = (y_1, ..., y_n)$ the resulting offspring are

$$\mathbf{p}'_1\, (x_1, ..., x_k, y_{k+1}, ..., y_n) \tag{C.3a}$$
$$\mathbf{p}'_2 = (y_1, ..., y_k, x_{k+1}, ..., x_n) \tag{C.3b}$$

c) Heuristic Crossover: The resulting offspring is generated from two parents $\mathbf{p}_1$ and $\mathbf{p}_2$ with $\chi^2(\mathbf{p}_2) > \chi^2(\mathbf{p}_1)$. For each chromosome k a random number ξ between 0 and 1 is generated

$$\mathbf{p}'_{k1} = \xi\, (\mathbf{p}_{k1} - \mathbf{p}_{k2}) + \mathbf{p}_{k1} \tag{C.4a}$$
$$\mathbf{p}'_{k2} = \mathbf{p}_{k1} \tag{C.4b}$$

d) No Crossover: The crossover between the two individuals do not always occur, with a certain probability (about 20%) the selected individuals are copied directly to the next generation.

At the end of this process only the offspring individuals are kept.

Mutation

The mutation implemented in the genetic algorithm mimics the corresponding process that exists in the nature. The mutation is essential to enrich the genetic pool and prevent the algorithm of falling in local minima. A chromosome is chosen at random to mutate from an individual also chosen at random. These probabilities are uniform and not dependent of the fitness of the individual.

Two different types of mutations are considered: a *large mutation* and a *soft mutation*. If it is a *hard mutation* the new value of the chromosome is chosen from an individual of the initial population. In case of a soft mutation only a small variation of the value of the gene of this chromosome is introduced. If g_0 is the value of the gene and ξ a random number between -1 and 1, we set the new gene g_n as

$$g_n = g_0 + \mathcal{I}\xi\, (g_M - g_m) \tag{C.5}$$

where $\mathcal{I}$ is the intensity of soft mutation, the value used is 0.05.

We introduced the probability of hard mutation P_h and a probability of soft mutation P_s. These probabilities are defined by the number of mutations respectively to the total number of genes.

The probability that a specific chromosome mutates is given by $P_s + P_h$ where P_s corresponds to the probability of *small mutation* and P_h the probability of *hard mutation*.

The probabilities P_s and P_h should be low because because if these probabilities are too large the genetic algorithm becomes a random search algorithm. These probabilities were set the value of $P_s = 0.02$ and $P_h = 0.01$.

Elitism

This is a random algorithm and therefore during the process we risk loosing some of the best individuals and to go straight to after crossover and mutation. A way to avoid this is by *elitism* - The five individuals with the highest fitness are chosen to remain unaltered and to go straight to the next generation.

Next generations

After the reproduction and mutation the χ_ν^2 function is computed for each individual of the entire population. Their chi-square is evaluated again and a new generation is created through crossover and mutation. The minimization stops when the five best individual remain the same after five successive generations.

The values of the genes obtained with the genetic algorithm are a good solution of for the minimization problem. The predicted reflectance needs to be compared with the results to test the fairness of the result obtained.

C. THE GENETIC ALGORITHM OF SIMULATION

Bibliography

[1] M. I. Lopes and V. Chepel. Liquid rare gas detectors: recent developments and applications. *Dielectrics and Electrical Insulation, IEEE Transactions on*, 10:994, 2003. 1

[2] V. Chepel, V. Solovov, F. Neves, A. Pereira, et al. Scintillation efficiency of liquid xenon for nuclear recoils with the energy down to 5 keV. *Astroparticle Physics*, 26(1):58 – 63, 2006. 1, 200

[3] Victor R. Weidner and Jack J. Hsia. Reflection properties of pressed polytetrafluoroethylene powder. *Journal of the Optical Society of America*, 71(7):856–861, 1981. 1, 28, 29, 167, 170

[4] Puja Kadkhoda, Detlev Ristau, and Ferdinand von Alvensleben. Total scatter measurements in the DUV/VUV. volume 3578, pages 544–554. SPIE, 1999. 1, 30, 67, 167, 206

[5] Y. Seo, H. Wang, and D. B. Cline. Simulation results with Zeplin II. *Nuclear Physics B - Proceedings Supplements*, 124:221 – 224, 2003. Proceedings of the 5th International UCLA Symposium on Sources and Detection of Dark Matter and Dark Energy in the Universe. 2, 15

[6] Lawrence B. Wolff. Diffuse-reflectance model for smooth dielectric surfaces. *Journal of the Optical Society of America A*, 11(11):2956–2968, 1994. 3, 76, 114

[7] K. E. Torrance and E. M. Sparrow. Theory for off-specular reflection from roughened surfaces. *Journal of the Optical Society of America*, 57(9):1105–1112, 1967. 3, 86, 104, 105, 106

[8] Bernard Sadoulet. Deciphering the nature of dark matter. *Reviews of Modern Physics*, 71(2):S197–S204, Mar 1999. 5, 14

BIBLIOGRAPHY

[9] H. V. Klapdor-Kleingrothaus, A. Dietz, I. V. Krivosheina, Ch. DĄörr, et al. Support of evidence for neutrinoless double beta decay. *Physics Letters B*, 578(1-2):54 – 62, 2004. 5, 16

[10] F. Cei. Lepton flavour violation: present and future experiments. *Nuclear Physics B - Proceedings Supplements*, 154(1):62 – 79, 2006. Proceedings of the High Intensity Frontier Workshop. 5, 18

[11] M. J. Terry, J. T. Lynch, M. Bunclark, K. R. Mansell, et al. The densities of liquid argon, krypton xenon, oxygen, nitrogen, carbon monoxide methane, and carbon tetrafluoride along the orthobaric liquid curve. *The Journal of Chemical Thermodynamics*, 1(4):413 – 424, 1969. 6

[12] D. Cline, A. Curioni, A. Lamarina, G. Mannocchi, et al. A WIMP detector with two-phase xenon. *Astroparticle Physics*, 12(4):373 – 377, 2000. 6

[13] A. Braem, A. Gonidc, D. Schinzel, W. Seidl, et al. Observation of the UV scintillation light from high energy electron showers in liquid xenon. *Nuclear Instruments and Methods in Physics Research Section A: Accelerators, Spectrometers, Detectors and Associated Equipment*, 320(1-2):228 – 237, 1992. 6

[14] Elena Aprile, Aleksey E. Bolotnikov, Alexander I. Bolozdynya, and Tadayoshi Doke. *Noble Gas Detectors*. Wiley Verlag, 2006. 6

[15] G.J. Davies. Liquid xenon and argon, dark matter detectors with background rejection. *Il Nuovo Cimento*, 112:1455–1471, 1997. 7, 10

[16] Tadayoshi Doke. Fundamental properties of liquid argon, krypton and xenon as radiation detector media. *Portugal Physica*, 12:9–48, 1981. 7

[17] G Ledru, F Marchal, N Merbahi, J P Gardou, et al. Study of the formation and decay of KrXe* excimers at room temperature following selective excitation of the xenon 6s states. *Journal of Physics B: Atomic, Molecular and Optical Physics*, 40(10):1651, 2007. 8

[18] Pierre Millet. *Etude Spectroscopique et Cinétique des Emissions du Xénon e des Mélanges XeO$_2$*. PhD thesis, L'Université Paul Sabatier de Toulose, 1979. 8, 73

[19] J. W. Keto, R. E. Gleason, and G. K. Walters. Production mechanisms and radiative lifetimes of argon and xenon molecules emitting in the ultraviolet. *Physical Review Letters*, 33(23):1365–1368, Dec 1974. 8, 10

[20] Werner F. Schmidt. *Electronic excitations in liquified rare gases*. American Scientific Publishers, 2005. 8

[21] Joshua Jortner, Lothar Meyer, Stuart A. Rice, and E. G. Wilson. Localized excitations in condensed Ne, Ar, Kr, and Xe. *The Journal of Chemical Physics*, 42(12):4250–4253, 1965. 10

[22] A. A. Madej and B. P. Stoicheff. Vacuum-ultraviolet laser spectroscopy: Radiative lifetimes of states of Ar_2, Kr_2, Xe_2, and dependence on internuclear distance. *Physical Review A*, 38(7):3456–3466, Oct 1988. 10

[23] G. M. Seidel, R. E. Lanou, and W. Yao. Rayleigh scattering in rare-gas liquids. *Nuclear Instruments and Methods in Physics Research Section A: Accelerators, Spectrometers, Detectors and Associated Equipment*, 489(1-3):189 – 194, 2002. 10, 12, 190

[24] A. Bideau-Mehu, Y. Guern, R. Abjean, and A. Johannin-Gilles. Measurement of refractive indices of neon, argon, krypton and xenon in the 253.7-140.4 nm wavelength range. dispersion relations and estimated oscillator strengths of the resonance lines. *Journal of Quantitative Spectroscopy and Radiative Transfer*, 25(5):395 – 402, 1981. 10

[25] V. N. Solovov, V. Chepel, M. I. Lopes, A. Hitachi, et al. Measurement of the refractive index and attenuation length of liquid xenon for its scintillation light. *Nuclear Instruments and Methods in Physics Research Section A: Accelerators, Spectrometers, Detectors and Associated Equipment*, 516(2-3):462 – 474, 2004. 10, 12, 13, 190, 198

[26] Tadayoshi Doke and Kimiaki Masuda. Present status of liquid rare gas scintillation detectors and their new application to gamma-ray calorimeters. *Nuclear Instruments and Methods in Physics Research Section A: Accelerators, Spectrometers, Detectors and Associated Equipment*, 420(1-2):62 – 80, 1999. 10, 13

[27] Shinzou Kubota et al. Dynamical behaviour of free electrons in the recombination process in liquid argon, krypton and xenon. *Physical Review B*, 20:3486–3496, 1979. 10

[28] Akira Hitachi, Tan Takahashi, Nobutaka Funayama, Kimiaki Masuda, et al. Effect of ionization density on the time dependence of luminescence from liquid argon and xenon. *Physical Review B*, 27(9):5279–5285, May 1983. 9, 10

[29] E. Aprile and R. Mukherjee and M. Suzuki Ionization of liquid xenon by 241Am and 210Po alpha particles *Nuclear Instruments and Methods in Physics Research Section A: Accelerators, Spectrometers, Detectors and Associated Equipment*, 307(1):119–125, 1991. 11

[30] M. Saito, T. Nishikawa, and M. Miyajima. Electric field dependence of luminescence due to alpha particles in gaseous xenon and the energy expended per photon. *Nuclear Science, IEEE Transactions on*, 51(5):2125 – 2130, oct. 2004. 10

BIBLIOGRAPHY

[31] E. Aprile and T. Doke. Liquid xenon detectors for particle physics and astrophysics. Reviews of Modern Physics, 82(3):2053–2097, 2010. 10, 11, 15, 17

[32] Shinzou Kubota, Masayo Suzuki, and Jian-zhi Ruan(Gen). Specific-ionization-density effect on the time dependence of luminescence in liquid xenon. *Physical Review B*, 21(6):2632–2634, Mar 1980. 10

[33] K. Saito, S. Sasaki, H. Tawara, T. Sanami, et al. Simultaneous measurements of absolute numbers of electrons and scintillation photons produced by 5.49 Mev alpha particles in rare gases. *Nuclear Science, IEEE Transactions on*, 50(6):2452 – 2459, dec. 2003.

[34] K. Saito, H. Tawara, T. Sanami, E. Shibamura, et al. Absolute number of scintillation photons emitted by alpha particles in rare gases. *Nuclear Science, IEEE Transactions on*, 49(4):1674 – 1680, aug 2002. 10

[35] Mitsuhiro Miyajima, Shinichi Sasaki, and Eido Shibamura. Absolute number of photons produced by alpha-particles in liquid and gaseous xenon. *Nuclear Instruments and Methods in Physics Research Section B: Beam Interactions with Materials and Atoms*, 63(3):297 – 308, 1992. 10, 40, 190

[36] V. Chepel, M.I. Lopes, and V. Solovov. Primary scintillation yield and α/β ratio in liquid xenon. *Radiation Physics and Chemistry*, 74(3-4):160 – 167, 2005. Professor Robert Schiller's 70th Birthday. 10

[37] Schwentner. Joshua Jortner, N. Schwentner and E.E. Koch. Electronic Excitations in Condensed Rare Gases. *Springer tracks in modern physics*. Springer Verlag, 1985. 9

[38] V. Chepel et al. *Position Sensitive Detection of Gamma Rays with the Coordinate-Electrode Method Ph.D. Thesis*. PhD thesis, Moscow Physics Engineering Institute, 1988. 11

[39] M. Tanaka, T. Doke, A. Hitachi, T. Kato, et al. Let dependence of scintillation yields in liquid xenon. *Nuclear Instruments and Methods in Physics Research Section A: Accelerators, Spectrometers, Detectors and Associated Equipment*, 457(3):454 – 463, 2001. 11

[40] E. Simon, L. Berg̨é, A. Broniatowski, R. Bouvier, et al. Sicane: a detector array for the measurement of nuclear recoil quenching factors using a monoenergetic neutron beam. *Nuclear Instruments and Methods in Physics Research Section A: Accelerators, Spectrometers, Detectors and Associated Equipment*, 507(3):643 – 656, 2003. 11

230

[41] J. Linhard, V. Nielsen, and M. Scharff. Integral equations governing radiation effects (notes on atomic collisions iii). *Matematisk-fysiske Meddelser*, 33(10):1 – 44, 1963. 12

[42] J. Linhard, H. E. Schiott, and M. Scharff. Range concepts and heavy ion ranges (notes on atomic collisions ii). *Matematisk-fysiske Meddelser*, 33(14):1 – 42, 1963. 12

[43] Akira Hitachi. Properties of liquid xenon scintillation for dark matter searches. *Astroparticle Physics*, 24(3):247 – 256, 2005. 12

[44] V. Chepel, V. Solovov, F. Neves, A. Pereira, et al. Scintillation efficiency of liquid xenon for nuclear recoils with the energy down to 5Ǎǎkev. *Astroparticle Physics*, 26(1):58 – 63, 2006. 8, 12, 200

[45] K. Yoshino and D. E. Freeman. Absorption spectrum of xenon in the vacuum-ultraviolet region. *Journal of the Optical Society of America B*, 2(8):1268–1274, 1985. 12

[46] N. Ishida, M. Chen, T. Doke, K. Hasuike, et al. Attenuation length measurements of scintillation light in liquid rare gases and their mixtures using an improved reflection suppresser. *Nuclear Instruments and Methods in Physics Research Section A: Accelerators, Spectrometers, Detectors and Associated Equipment*, 384(2-3):380 – 386, 1997. 12

[47] E. Aprile, K. L. Giboni, P. Majewski, K. Ni, et al. Observation of anticorrelation between scintillation and ionization for mev gamma rays in liquid xenon. *Physical Review B (Condensed Matter and Materials Physics)*, 76(1):014115, 2007. 13

[48] Henrique AraÅújo Performance results from the first science run of ZEPLIN-III Nuclear Instruments and Methods in Physics Research Section A: Accelerators, Spectrometers, Detectors and Associated Equipment, 604(1-2):41 - 44, 2009.

[49] Dmitry Akimov. Detectors for dark matter search (review). *Nuclear Instruments and Methods in Physics Research Section A: Accelerators, Spectrometers, Detectors and Associated Equipment*, 598(1):275 – 281, 2009. Instrumentation for Collding Beam Physics - Proceedings of the 10th International Conference on Instrumentation for Colliding Beam Physics. 15

[50] E. Aprile, A. Curioni, K. L. Giboni, M. Kobayashi, et al. Calibration and in-flight performance of the compton telescope prototype lxegrit. *New Astronomy Reviews*, 48(1-4):257 – 262, 2004. Astronomy with Radioactivities IV and Filling the Sensitivity Gap in MeV Astronomy. 14, 18

[51] Z. Ahmed, D. S. Akerib, S. Arrenberg, M. J. Attisha, et al. Search for weakly interacting massive particles with the first five-tower data from the cryogenic

dark matter search at the Soudan underground laboratory. *Physical Review Letters*, 102(1):011301, 2009. 14

[52] E. Komatsu, J. Dunkley, M. R. Nolta, C. L. Bennett, et al. Five-Year Wilkinson Microwave Anisotropy Probe (WMAP) Observations: Cosmological Interpretation. *The Astrophysical Journal Supplement Series*, 180:330–376, February 2009. 14

[53] Gerard Jungman, Marc Kamionkowski, Arthur Kosowsky, and David N. Spergel. Cosmological-parameter determination with microwave background maps. *Physical Review D*, 54(2):1332–1344, Jul 1996. 14

[54] Kim Griest and Marc Kamionkowski. Supersymmetric dark matter. *Physics Reports*, 333-334:167 – 182, 2000. 14

[55] Gianfranco Bertone, Dan Hooper, and Joseph Silk. Particle dark matter: evidence, candidates and constraints. *Physics Reports*, 405(5-6):279 – 390, 2005. 14

[56] G.J. Alner, H. Araújo, G.J. Arnison, J.C. Barton, et al. Nuclear recoil limits from the Zeplin I liquid xenon WIMP dark matter detector. *New Astronomy Reviews*, 49(2-6):245 – 249, 2005. Sources and Detection of Dark Matter and Dark Energy in the Universe. 14, 15

[57] J. Angle, E. Aprile, F. Arneodo, L. Baudis, et al. Limits on spin-dependent wimp-nucleon cross sections from the XENON10 experiment. *Physical Review Letters*, 101(9):091301, 2008. 15

[58] Aprile, E. and Arisaka, K. and Arneodo, et al. First Dark Matter Results from the XENON100 Experiment. *Physical Review Letters*, 105(13):131302, 2010 15

[59] G.J. Alner, H.M. Araújo, A. Bewick, C. Bungau, et al. Limits on spin-dependent wimp-nucleon cross-sections from the first Zeplin-II data. *Physics Letters B*, 653(2-4):161 – 166, 2007. 15

[60] D.Yu. Akimov, G.J. Alner, H.M. Araújo, A. Bewick, et al. The Zeplin-III dark matter detector: Instrument design, manufacture and commissioning. *Astroparticle Physics*, 27(1):46 – 60, 2007. 15, 16, 130, 131

[61] H.M. Araújo, D.Yu. Akimov, G.J. Alner, A. Bewick, et al. The Zeplin-III dark matter detector: Performance study using an end-to-end simulation tool. *Astroparticle Physics*, 26(2):140 – 153, 2006. 15

[62] V. N. Lebedenko, H. M. Araújo, E. J. Barnes, A. Bewick, et al. Results from the first science run of the zeplin-iii dark matter search experiment. *Physical Review D (Particles and Fields)*, 80(5):052010, 2009. 15

[63] G.J. Alner, H.M. Araújo, A. Bewick, C. Bungau, et al. First limits on wimp nuclear recoil signals in zeplin-ii: A two-phase xenon detector for dark matter detection. *Astroparticle Physics*, 28(3):287 – 302, 2007. 16, 22

[64] J. Angle, E. Aprile, F. Arneodo, L. Baudis, et al. First results from the xenon10 dark matter experiment at the gran sasso national laboratory. *Physical Review Letters*, 100(2):021303, 2008. 15

[65] K. Ueshima, K. Abe, T. Iida, M. Ikeda, et al. Scintillation yield of liquid xenon at room temperature. *Nuclear Instruments and Methods in Physics Research Section A: Accelerators, Spectrometers, Detectors and Associated Equipment*, 594(2):148 – 154, 2008. 16

[66] Matthew Redshaw, Elizabeth Wingfield, Joseph McDaniel, and Edmund G. Myers. Mass and double-beta-decay q value of ^{136}Xe. *Physical Review Letters*, 98(5):053003, 2007. 17

[67] F. LePort, A. Pocar, L. Bartoszek, R. DeVoe, et al. A liquid xenon ionization chamber in an all-fluoropolymer vessel. *Nuclear Instruments and Methods in Physics Research Section A: Accelerators, Spectrometers, Detectors and Associated Equipment*, 578(2):409 – 420, 2007. 17, 22

[68] F. Sanchez. Next: double beta decay experiment. *Nuclear Physics B - Proceedings Supplements*, 188:71 – 73, 2009. Proceedings of the Neutrino Oscillation Workshop. 17

[69] Toshiyuki Iwamoto. Liquid xenon detector for the MEG experiment. *Nuclear Physics B - Proceedings Supplements*, 172:224 – 226, 2007. Proceedings of the 10th Topical Seminar on Innovative Particle and Radiation Detectors, Proceedings of the 10th Topical Seminar on Innovative Particle and Radiation Detectors. 18

[70] T. Iwamoto, R. Sawada, T. Haruyama, S. Mihara, et al. Development of a large volume zero boil-off liquid xenon storage system for muon rare decay experiment (meg). *Cryogenics*, 49(6):254 – 258, 2009. Fourth Asian Conference on Applied Superconductivity and Cryogenics. 18

[71] M. E. G. Collaboration, J. Adam, X. Bai, A. Baldini, et al. A limit for the mu-gamma decay from the MEG experiment. Aug 2009. 18

[72] Uwe Oberlack, Elena Aprile, Alessandro Curioni, and Karl-Ludwig Giboni. Performance of the light trigger system in the liquid xenon gamma ray imaging telescope LXEGRIT. *Nuclear Science, IEEE Transactions on*, 48:1041–1047, 2001. 18

[73] A. Curioni, E. Aprile, T. Doke, K.L. Giboni, et al. A study of the lxegrit detection efficiency for mev gamma-rays during the 2000 balloon flight campaign. *Nuclear*

BIBLIOGRAPHY

Instruments and Methods in Physics Research Section A: Accelerators, Spectrometers, Detectors and Associated Equipment, 576(2-3):350 – 361, 2007. 18

[74] M.-L. Gallin-Martel, L. Gallin-Martel, Y. Grondin, O. Rossetto, et al. A liquid xenon positron emission tomograph for small animal imaging: First experimental results of a prototype cell. *Nuclear Instruments and Methods in Physics Research Section A: Accelerators, Spectrometers, Detectors and Associated Equipment*, 599(2-3):275 – 283, 2009. 19

[75] http://www.3dchem.com/moremolecules.asp?id=200&othername= ptfe. 21

[76] Sina Ebnesajjad. *Melt processible fluoropolymers: the definitive user's guide and databook Vol. 2*. Plastics Design Library, 2003. 19, 26

[77] http://www.astm.org/DIGITAL_LIBRARY/comp_search.htm 20

[78] Liesl K. Massey. *Film properties of plastics and elastomers*. Plastics Design Library, 2 edition, 2005. 20

[79] Chen-Yan Tu et al. Effects of polymers architecture and composition on the adhesion of polytetrafluoroethylene. *ChemPhysChem*, 7:1355–1360, 2006. 20

[80] Joseph C. Salamone. *Polymeric materials encyclopedia, Volume 4*. CRC Press, 1996. 20

[81] H. P. Brack, M. Wyler, G. Peter, and G. G. Scherer. A contact angle investigation of the surface properties of selected proton-conducting radiation-grafted membranes. *Journal of Membrane Science*, 214(1):1 – 19, 2003. 20

[82] V. Saarinen, M. Karesoja, T. Kallio, M. Paronen, et al. Characterization of the novel ETFE-based membrane. *Journal of Membrane Science*, 280(1-2):20 – 28, 2006. 20

[83] Dinghan Xiang and Chuanjin Gu. A study on the friction and wear behavior of PTFE filled with ultra-fine kaolin particulates. *Materials Letters*, 60(5):689 – 692, 2006. 21

[84] Yasuhiro Okuda, Fumihiro Hayashi, Hiroshi Sakurai, and Masaru Shiotani. A spectroscopic study on defluorination of polytetrafluoroethylene by alkyllithium/electron-donating solvents. *Spectrochimica Acta Part A: Molecular and Biomolecular Spectroscopy*, 60(13):3071 – 3077, 2004. 21

[85] Calum J. Drummond and Derek Y. C. Chan. Theoretical analysis of the soiling of nonstick organic materials. *Langmuir*, 12(13):3356–3359, 1996. 22

[86] Autores. Effect of roughness as determined by atomic force microscopy on the wetting properties of ptfe thin films. *Polymer Engineering & Science*, 36:1849–1855, 1996. 22

[87] Art Springsteen. Standards for the measurement of diffuse reflectance - an overview of available materials and measurement laboratories. *Analytica Chimica Acta*, 380(2-3):379 – 390, 1999. 22

[88] Zhu Qunzhi et al. Radiative properties of materials with surface scattering or volume scattering: A review. *Frontiers of Energy and Power Engineering in China*, 3:60–97, 2009. 22

[89] Sheng-Hao Tseng, Alexander Grant, and Anthony J. Durkin. In vivo determination of skin near-infrared optical properties using diffuse optical spectroscopy. *Journal of Biomedical Optics*, 13(1):014016, 2008. 22

[90] Uwe Lappan, Uwe GeiẞSler, and Klaus Lunkwitz. Modification of polytetrafluoroethylene by electron beam irradiation in various atmospheres. *Nuclear Instruments and Methods in Physics Research Section B: Beam Interactions with Materials and Atoms*, 151(1-4):222 – 226, 1999. 22

[91] Jaydeep Khedkar, Ioan Negulescu, and Efstathios I. Meletis. Sliding wear behavior of ptfe composites. *Wear*, 252(5-6):361 – 369, 2002. 23

[92] Gareth Hougham. *Fluoropolymers 2: Properties*. Kluver Academic, 1999. 23, 25, 26

[93] http://pslc.ws/mactest/crystal.htm. 23

[94] Jr. Fred W. Billmeyer. Measurements of the refractive index of films. *Journal of Applied Physics*, 18(5):431–434, 1947. 23

[95] A. Zimmermann W. Groh. What is the lowest refractive index of an organic polymer? *Macromolecules*, 24:6660–6663, 1991. 23

[96] Olagoke Olabisi. *Handbook of Thermoplastics*. Marcel Dekker, 1999. 23

[97] http://www.texloc.com/closet/cl_refractiveindex.html. 23

[98] H. K. Kim and F. G. Shi. Refractive index of polycrystalline submicrometer polymer thin films: Thickness dependence. *Journal of Materials Science: Materials in Electronics*, 12:361–364, 2001. 23, 24

[99] Hans Rytger et. al. *Handbook of Polymer Synthesis*. Marcel Dekker, 2 edition, 2004. 24

[100] http://www.enotes.com. 24

BIBLIOGRAPHY

[101] Laurence W. McKeen. *Fluorinated coatings and finishes handbook*. Plastics Design Library, 2006. 24

[102] Jiri George Drobny. *Technology of Fluoropolymers*. CRC Press, 2001. 24, 25, 26

[103] http://www2.dupont.com/teflon_industrial/en_us/products/ product_by_name/teflon_ptfe/granular.html. 24

[104] Friedhelm Hensen. *Plastics extrusion technology*. Car Hanser Verlag, 2 edition, 1997. 25

[105] http://www.gore.com/en_xx/technology/timeline/applications _eptfe.html. 25

[106] Rena Bizios David A. Puleo. *Biological Interactions on Materials Surfaces*. Springer, 2009. 25

[107] Sina Ebnesajjad and Pradip R. Khaladkar. *Fluoropolymers applications in chemical processing industries*. Plastics Design Library, 2005. 26

[108] http://www.zeusinc.com/technicalservices/technicalbulletins /technicalinformation/uvtransmission.aspx. 26

[109] http://www2.dupont.com/photovoltaics/en_us/assets/downloads /pdf/concentratorpv_poster.pdf. 26

[110] R. Ulbricht. Die bestimmung der mittleren raeumlichen lichtintensitaet durch nur eine messung. *ez*, 29:595–597, 1900. 27

[111] P. Yvonne Barnes and Jack J. Hsia. 45 deg reflectance factors of pressed polytetrafluoroethylene (ptfe) powder. *Nist Technical Report*, 0:1413, 1995. 27

[112] R. W. Ditchburn. *Light*. Blackie and Son Limited, 2 edition, 1963. 27

[113] Franc Grum and Richard J. Becherer. *Optical Radiation Measurements Vol 1 Radiometry*. Academic press, 1979. 27, 28, 209, 211

[114] F. Nicodemus and J. Richmond and J. Hsia and I. Ginsberg and T Limperis *Geometrical Considerations and Nomenclature for Reflectance* National Bureau of Standards, 1977 209

[115] V. R. Weidner, J. J. Hsia, and B. Adams. Laboratory intercomparison study of pressed polytetrafluoro-ethylene powder reflectance standards. *Applied Optics*, 24(14):2225–2230, 1985. 28, 29, 167, 170, 171

[116] http://www.labsphere.com/data/userfiles/opticalgradespectralondatasheet_1.pdf. 29

[117] http://www.aviantechnologies.com/products/coatings/fluorilon.php. 29, 30

[118] Kazuhiko Seki, Hiroshi Tanaka, Toshiaki Ohta, Yuriko Aoki, et al. Electronic structure of poly(tetrafluoroethylene) studied by ups, vuv absorption, and band calculations. *Physica Scripta*, 41(1):167–171, 1990. 30, 31

[119] S. Bricola, A. Menegolli, M. Prata, M.C. Prata, et al. Noble-gas liquid detectors: measurement of light diffusion and reflectivity on commonly adopted inner surface materials. *Nuclear Physics B - Proceedings Supplements*, 172:260 – 262, 2007. Proceedings of the 10th Topical Seminar on Innovative Particle and Radiation Detectors, Proceedings of the 10th Topical Seminar on Innovative Particle and Radiation Detectors. 31

[120] Robert D. Saunders and William R. Ott. Spectral irradiance measurements: effect of uv-produced fluorescence in integrating spheres. *Applied Optics*, 15(4):827–828, 1976. 31

[121] Ping-Shine Shaw, Zhigang Li, Uwe Arp, and Keith R. Lykke. Ultraviolet characterization of integrating spheres. *Applied Optics*, 46(22):5119–5128, 2007. 31

[122] Albert E. Stiegman, Carol J. Bruegge, and Arthur W. Springsteen. Ultraviolet stability and contamination analysis of Spectralon® diffuse reflectance material. *Optical Engineering*, 32(4):799–804, 1993. 32

[123] D R Gibbs, F J Duncan, R P Lambe, and T M Goodman. Ageing of materials under intense ultraviolet radiation. *Metrologia*, 32(6):601, 1995. 32

[124] Guirong Peng, Dezhuang Yang, Jincheng Liu, and Shiyu He. Effects of vacuum ultraviolet on the structure and optical properties of polytetrafluoroethylene films. *Journal of Applied Polymer Science*, 90(1):115–121, 2003. 32

[125] W. MĄöller, K-P Nikolaus and A. HĄöpe. Degradation of the diffuse reflectance of Spectralon under low-level irradiation. *Metrologia*, 40:S212–S215, 2003. 32

[126] C.P. Silva, J. Pinto da Cunha, V. Chepel, A. Pereira, et al. Measuring the angular profile of the reflection of xenon scintillation light. *Nuclear Instruments and Methods in Physics Research Section A: Accelerators, Spectrometers, Detectors and Associated Equipment*, 580(1):322 – 325, 2007. Proceedings of the 10 th International Symposium on Radiation Physics - ISRP 10. 33

[127] T. Matsui, A.S.-C. Cheung, K.W.-S. Leung, K. Yoshino, et al. High resolution absorption cross-section measurements of the schumann-runge bands of O_2 by VUV fourier transform spectroscopy. *Journal of Molecular Spectroscopy*, 219(1):45 – 57, 2003. 34

BIBLIOGRAPHY

[128] K. Minschwaner, G. P. Anderson, L. A. Hall, and K. Yoshino. Polynomial coefficients for calculating O_2 schumann-runge cross sections at 0.5 cm-1 resolution. *Journal of Geophysical Research, Atmospheres*, 97:0, 1992. 34

[129] K. Yoshino, W.H. Parkinson, K. Ito, and T. Matsui. Absolute absorption cross-section measurements of schumann-runge continuum of o2 at 90 and 295Ąăk. *Journal of Molecular Spectroscopy*, 229(2):238 – 243, 2005. 34

[130] http://www.thorlabs.com/catalogpages/v20/1237.pdf. 38

[131] http://www.nndc.bnl.gov/nudat2/decaysearchdirect.jsp?nuc=241am&unc=nds. 39

[132] F.G. Knoll. *Radiation Detection and Measurement*. John Wiley and Son, 3 edition, 1999. 40

[133] A. A. Kruithof. Townsend's ionization coefficients for neon, argon, krypton and xenon. *Physica*, 7:519–540, June 1940. 40

[134] Frederick H. Sanders. Measurement of the townsend coefficients for ionization by collision. *Physical Review*, 44(12):1020–1024, Dec 1933. 40

[135] A. C. Fonseca et al. Study of the secondary scintillation in xenon vapour. *Nuclear Science Symposium Conference Record, 2004 IEEE*, 1:572–576, 2005. 40

[136] C M B Monteiro, L M P Fernandes, J A M Lopes, L C C Coelho, et al. Secondary scintillation yield in pure xenon. *Journal of Instrumentation*, 2(05):P05001, 2007. 40

[137] Akimov D.Yu., Burenkov A.A., Kuzichev V.N., Morgunov V.L., et al. Cylindrical scintillation proportional counter with wls fiber readout. pages 812 –816 vol.1, Nov 1997. 40

[138] C M B Monteiro, L M P Fernandes, J A M Lopes, L C C Coelho, et al. Secondary scintillation yield in pure xenon. *Journal of Instrumentation*, 2(05):P05001, 2007. 41

[139] http://www.neyco.fr/pdf/vacuum_viewports.pdf. 41

[140] Romualdas Kalytis. Photon counting in astrophotometry, fundamentals and some advices for enginners. *Turkish Journal of Physics*, 23:335–346, 1999. 48

[141] http://sales.hamamatsu.com/assets/applications/etd/photoncounting _tpho9001e0448

[142] A. M. Boichenko, Victor F. Tarasenko, and Sergey I. Yakovlenko. Nature of third continua in rare gases. *International Conference on Atomic and Molecular Pulsed Lasers III*, 4071(1):255–270, 2000. 72, 73

[143] E. Robert, A. Khacef, C. Cachoncinlle, and J. M. Pouvesle. Time-resolved spectroscopy of high pressure rare gases excited by an energetic flash X-ray source. *Optics Communications*, 117(1-2):179 – 188, 1995. 72

[144] Michael Oren and Shree K. Nayar. Generalization of Lambert's reflectance model. In *In SIGGRAPH 94*, pages 239–246. ACM Press, 1994. 76, 115, 116, 117

[145] Wolf, Pierre-Etienne and Maret, Georg. Weak Localization and Coherent Backscattering of Photons in Disordered Media. *Physical Review Letters*, 55(24):2696–2699, 1985. 77

[146] J A Ogilvy. Computer simulation of acoustic wave scattering from rough surfaces. *Journal of Physics D: Applied Physics*, 21(2):260, 1988. 79, 91

[147] Enru Liu, Stuart Crampin, and John A. Hudson. Diffraction of seismic waves by cracks with application to hydraulic fracturing. *Geophysics*, 62(1):253–265, 1997. 79

[148] H E Beckett. The measurement of reflection coefficients for oblique incidence. *Proceedings of the Physical Society*, 44(4):439–444, 1932. 79

[149] N. C . Bruce and J. C. Dainty. Multiple scattering from rough dielectric and metal surfaces using the kirchhoff approximation. *Journal of Modern Optics*, 38, 1991. 80

[150] J M Bennett. Recent developments in surface roughness characterization. *Measurement Science and Technology*, 3(12):1119, 1992. 80

[151] Chin Y. Poon and Bharat Bhushan. Comparison of surface roughness measurements by stylus profiler, AFM and non-contact optical profiler. *Wear*, 190(1):76 – 88, 1995. Macro and Micro-Tribology and Mechanics of Magnetic Storage Systems. 81

[152] F. Meli. Roughness measurements according to existing standards with a metrology afm profiler. *Proceedings of the 3rd Int. Euspen Conference, F. L. M. Delbressine et al. (Eds.)*, 2:533–536, 2002. 81

[153] Ivan Ohlídal, Karel Navrátil, Miloslav Ohlídal, and Miloslav Druckmüller. Characterization of the basic statistical properties of very rough surfaces of transparent solids by immersion shearing interferometry. *Applied Optics*, 33(34):7838–7845, 1994. 81

[154] Jean M. Bennett. Measurement of the r.m.s. roughness, autocovariance function and other statistical properties of optical surfaces using a feco scanning interferometer. *Applied Optics*, 15(11):2705–2721, 1976. 81, 84

[155] Franz J. Giessibl. Advances in atomic force microscopy. *Reviews of Modern Physics*, 75(3):949–983, Jul 2003. 81

BIBLIOGRAPHY

[156] N. K. Myshkin, A. Ya. Grigoriev, S. A. Chizhik, K. Y. Choi, et al. Surface roughness and texture analysis in microscale. *Wear*, 254(10):1001 – 1009, 2003. Papers presented at the 3rd International Colloquim Micro-tribology 2001. 82

[157] E. S. Gadelmawla, M. M. Koura, T. M. A. Maksoud, I. M. Elewa, et al. Roughness parameters. *Journal of Materials Processing Technology*, 123(1):133 – 145, 2002. 81, 84

[158] M. Saillard and D. Maystre. Scattering from metallic and dielectric rough surfaces. *Journal of the Optical Society of America A*, 7(6):982–990, 1990. 83, 92

[159] Hannu Karttunen Kari Lumme and William M. Irvine. Roughness of the lunar soil. *Earth, Moon, and Planets*, 33:19–29, 1985. 84

[160] Virginija Jankauskaite, Kristina Zukiene, and Stase Petraitiene. Quantitative description of polychloroprene and piperylene-styrene blend films surface morphology. *Polymer Engineering and Science*, 47(6):824–829, 2007. 84

[161] F. Varnier, M. Rasigni, G. Rasigni, J. P. Palmari, et al. Height and slope distributions for surfaces of rough metallic deposits. *Applied Optics*, 21(20):3681–3684, 1982. 84

[162] J. H. Jang, W. Zhao, J. W. Bae, D. Selvanathan, et al. Direct measurement of nanoscale sidewall roughness of optical waveguides using an atomic force microscope. *Applied Physics Letters*, 83(20):4116–4118, 2003. 84

[163] Gregory J. Ward. Measuring and modeling anisotropic reflection. *SIGGRAPH Computer Graphics*, 26(2):265–272, 1992. 86

[164] T. S. Trowbridge and K. P. Reitz. Average irregularity representation of a rough surface for ray reflection. *Journal of the Optical Society of America*, 65(5):531–536, 1975. 86, 87, 88, 89, 98, 140

[165] Rong-Sheng Lu and Gui Yun Tian. On-line measurement of surface roughness by laser light scattering. *Measurement Science and Technology*, 17(6):1496–1502, 2006. 87

[166] R. L. Cook and K. E. Torrance. A reflectance model for computer graphics. *ACM Trans. Graph.*, 1(1):7–24, 1982. 87

[167] Aravind Krishnaswamy. A study on skin optics. *Technical Report - University of Waterloo, Canada CS-2004-01*, 0:0, 2004. 88

[168] C.X.Liu et al. The accuracy of kirchoff's approximation in describing the far field speckles produced by random self-affine fractal surfaces. *The European Physical Journal D*, 36:105–110, 2005. 90, 91

[169] J. A. Sánchez-Gil and M. Nieto-Vesperinas. Light scattering from random rough dielectric surfaces. *Journal of the Optical Society of America A*, 8(8):1270–1286, 1991. 91, 93

[170] W. Freude and G.K. Grau. Rayleigh-sommerfeld and helmholtz-kirchhoff integrals: application to the scalar and vectorial theory of wave propagation and diffraction. *Lightwave Technology, Journal of*, 13(1):24–32, Jan 1995. 91

[171] JĄérĄôme Caron, Jacques Lafait, and Christine Andraud. Scalar kirchhoff's model for light scattering from dielectric random rough surfaces. *Optics Communications*, 207(1-6):17 – 28, 2002. 91, 93, 97

[172] Roberto Li Voti, Grigore L. Leahu, Simone Gaetani, Concita Sibilia, et al. Light scattering from a rough metal surface: theory and experiment. *Journal of the Optical Society of America B*, 26(8):1585–1593, 2009. 92

[173] Imed Sassi and M. Salah Sifaoui. Comparison of geometric optics approximation and integral method for reflection and transmission from microgeometrical dielectric surfaces. *Journal of the Optical Society of America A*, 24(2):451–462, 2007. 92

[174] J. A. Sánchez-Gil, A. A. Maradudin, and E. R. Méndez. Limits of validity of three perturbation theories of the specular scattering of light from one-dimensional, randomly rough, dielectric surfaces. *Journal of the Optical Society of America A*, 12(7):1547–1558, 1995. 92

[175] Jorge Ripoll, Vasilis Ntziachristos, Remi Carminati, and Manuel Nieto-Vesperinas. Kirchhoff approximation for diffusive waves. *Physical Review E*, 64(5):051917, Oct 2001. 93

[176] Leung Tsang, Jin Au Kong, and Kung-Hau Ding. *Scattering of Electromagnetic Waves: Advanced Topics*. John Wiley & Sons, 2001. 93, 95, 97, 98

[177] Leung Tsang, Jin Au Kong, and Kung-Hau Ding. *Scattering of Electromagnetic Waves: Theories and Applications*. John Wiley & Sons, Inc., 2000. 93, 94

[178] Theodore V. Vorburger, Egon Marx, and Thomas R. Lettieri. Regimes of surface roughness measurable with light scattering. *Applied Optics*, 32(19):3401–3408, 1993. 93, 95

[179] S. I. Hayek. *Advanced Mathematical Methods for Science and Engeneering*. Marcel Decker, 1994. 96

[180] A. A. Maradudin. *Light Scattering and Nanoscale Surface Roughness*. Springer-Verlag, Irvine NY, USA 2007. 97

BIBLIOGRAPHY

[181] J. Rife and J. Osantowski. Extreme ultraviolet optical properties of two SiO_2 based low-expansion materials. *Journal of the Optical Society of America*, 70(12):1513–1518, 1980. 97

[182] Masoomeh Dashtdar and M. Taghi Tavassoly. Determination of height distribution on a rough interface by measuring the coherently transmitted or reflected light intensity. *Journal of the Optical Society of America A*, 25(10):2509–2517, 2008. 97

[183] Petr Beckmann II Scattering of Light by Rough Surfaces *Progress in Optics*, 6:53–69, 1967 98

[184] Sheppard, C. J. R. Imaging of random surfaces and inverse scattering in the Kirchoff approximation. *Waves in Random Media*, 8(1):53–66, 1998. 98

[185] Beckmann, P. Scattering by composite rough surfaces. *Proceedings of the IEEE*, 53(8):1012–1015, 1965. 98

[186] Jan H Rakels. Influence of the surface height distribution on the total integrated scatter (TIS) formula. *Nanotechnology*, 7(1):43, 1996. 97

[187] Xiao D. He, Kenneth E. Torrance, François X. Sillion, and Donald P. Greenberg. A comprehensive physical model for light reflection. *SIGGRAPH Comput. Graph.*, 25(4):175–186, 1991. 98

[188] T. Gumpenberger et al. F_2-laser polishing of polytetrafluoroethylene surfaces. *Europhysics Letters*, 70:831–835, 2005. 101, 138, 157

[189] B. Smith. Geometrical shadowing of a random rough surface. *Antennas and Propagation, IEEE Transactions on*, 15(5):668–671, Sep 1967. 104, 105, 106

[190] R. J. Wagner. Shadowing of randomly rough surfaces. *The Journal of the Acoustical Society of America*, 41(1):138–147, 1967. 106

[191] M.N.O. Sadiku and S.R. Nelatury. A comparison of models for shadowing functions for random rough surfaces. In *SoutheastCon, 2006. Proceedings of the IEEE*, pages 11–15, 31 2005-April 2 2006. 106

[192] G. Brown. Shadowing by non-gaussian random surfaces. *Antennas and Propagation, IEEE Transactions on*, 28(6):788–790, Nov 1980. 108

[193] Bruce Walter et al. Microfacet models for refraction through rough surfaces. *EGSR*, 0:0, 2007. 108

[194] Eugene M. Berry. Diffuse reflection of light from a matt surface. *Journal of the Optical Society of America*, 7(8):627–633, 1923. 110

[195] Hsien-Che Lee. *Introduction to color imaging science*. Cambridge University Press, 2005. 110

[196] Johann Heinrich Lambert. *Photometria sive de mensure et gradibus luminis colorum et umbra*. Eberhard Kletty, 1760. 110

[197] http://www.uni-miskolc.hu/ ecodobos/14334.pdf. 111

[198] http://agsys.cra-cin.it/tools/solarradiation/help/albedo.html. 111

[199] Stephen G. Warren. Optical properties of snow. *Reviews of Geophysics*, 20:67–89, 1982. 111

[200] Christina Alsvik Pedersen. *Optical Properties of Snow and Sea Ice*. PhD thesis, University of Tromso, 2007. 111

[201] James E. Hansen and Larry D. Travis. Light scattering in planetary atmospheres. *Space Science Reviews*, 16:527–610, 1974. 111

[202] G. H. Goedecke. Radiative transfer in closely packed media. *Journal of the Optical Society of America*, 67(10):1339–1348, 1977. 112

[203] Knut Stamnes. The theory of multiple scattering of radiation in plane parallel atmospheres. *Rev. Geophys.*, 24:299–310, 1986. 112

[204] G. Bazalgette Courreges-Lacoste, J. Groote Schaarsberg, R. Sprik, and S. Delwart. Modeling of spectralon diffusers for radiometric calibration in remote sensing. *Optical Engineering*, 42(12):3600–3607, 2003. 112

[205] Mie G. Beitraege zur optik trueber medien, speziell kolloidaler metalloesungen. *Annalen der Physik*, 4:377–445, 1908. 112

[206] Dominique Toublanc. Henyey-greenstein and mie phase functions in monte carlo radiative transfer computations. *Applied Optics*, 35(18):3270–3274, 1996. 112

[207] N. Huber, J. Heitz, and D. Bauerle. Pulsed-laser ablation of polytetrafluoroethylene (PTFE) at various wavelengths. *The European Physical Journal Applied Physics*, 25(1):33–38, jan 2004. 113

[208] Chandrasekhar. *S. Radiative Transfer.* Dover, 1960. 113, 194

[209] Marigo Stavridi, Bram van Ginneken, and Jan J. Koenderink. Surface bidirectional reflection distribution function and the texture of bricks and tiles. *Applied Optics*, 36(16):3717–3725, 1997. 115

[210] Lawrence B. Wolff, Shree K. Nayar, and Michael Oren. Improved diffuse reflection models for computer vision. *International Journal of Computer Vision*, 30(1):55–71, 1998. 121

BIBLIOGRAPHY

[211] Paul J. Caber. Interferometric profiler for rough surfaces. *Applied Optics*, 32(19):3438–3441, 1993. 122

[212] C. Silva, J. Pinto da Cunha, A. Pereira, M.I. Lopes, et al. A model of the reflection distribution in the vacuum ultra violet region. *Nuclear Instruments and Methods in Physics Research Section A: Accelerators, Spectrometers, Detectors and Associated Equipment*, In Press, Corrected Proof:–, 2009. 124, 208

[213] C. Silva, J. Pinto da Cunha, A. Pereira, V. Chepel, et al. Reflectance of polytetrafluoroethylene for xenon scintillation light. *Journal of Applied Physics*, 107(6):064902, 2010. 124, 208

[214] H.D. Tagare and R.J.P. deFigueiredo. A theory of photometric stereo for a class of diffuse non-lambertian surfaces. *IEEE Transactions on Pattern Analysis and Machine Intelligence*, 13:133–152, 1991. 126

[215] Greg Kay and Terry Caelli. Inverting an illumination model from range and intensity maps. *CVGIP: Image Underst.*, 59(2):183–201, 1994. 126

[216] Il Dong Yun and Sang Uk Lee. Reflectance parameter estimation and its application to surface inspection. *Real-Time Imaging*, 4(6):429 – 442, 1998. 126

[217] Michael Bass. *Handbook of Optics – Vol. II*. McGraw Hill, 2 edition, 1995. 128, 129, 131, 132

[218] Z. Feng and C. R. Marks and A. Barkatt Oxidation-Rate Excursions During the Oxidation of Copper in Gaseous Environments at Moderate Temperatures *Oxidation of Metals* 60(5): 393-408, 2003. 132

[219] Bath Neuroth. *The Properties of Optical Glass*. Springer-Verlag, 2 edition, 1998. 129

[220] P. B. Johnson and R. W. Christy. Optical constants of copper and nickel as a function of temperature. *Physical Review B*, 11(4):1315–1323, Feb 1975. 131, 132

[221] Edward D. Palik. *Handbook of Optical Constants of Solids*. Academic Press, 3 edition, 1991. 132

[222] G P Pells and M Shiga. The optical properties of copper and gold as a function of temperature. *Journal of Physics C: Solid State Physics*, 2(10):1835, 1969. 132

[223] T Ziegler, W Fichter, M Schulte, and S Vitale. Principles, operations, and expected performance of the lisa pathfinder charge management system. *Journal of Physics: Conference Series*, 154:012009 (6pp), 2009. 132

[224] P McNamara, S Vitale, and K Danzmann (on behalf of the LISA Pathfinder Science Working Team). Lisa pathfinder. *Classical and Quantum Gravity*, 25(11):114034 (8pp), 2008. 133

[225] P. B. Johnson and R. W. Christy. Optical constants of the noble metals. *Physical Review B*, 6(12):4370–4379, Dec 1972. 133, 134

[226] C.P. Silva, J. Pinto da Cunha, V. Chepel, A. Pereira, et al. Measuring the angular profile of the reflection of xenon scintillation light. *Nuclear Instruments and Methods in Physics Research Section A: Accelerators, Spectrometers, Detectors and Associated Equipment*, 580(1):322 – 325, 2007. Proceedings of the 10 th International Symposium on Radiation Physics - ISRP 10. 140, 208

[227] S. Agostinelli, J. Allison, K. Amako, J. Apostolakis, et al. G4–a simulation toolkit. *Nuclear Instruments and Methods in Physics Research Section A: Accelerators, Spectrometers, Detectors and Associated Equipment*, 506(3):250 – 303, 2003. 149, 173

[228] T. S. Trowbridge Retroreflection from rough surfaces *Journal of the Optical Society of America*, 68(9):1225–1242, 1978. 175

[229] D. Riedel and C. Castex. Effective absorption coefficient measurements in pmma and ptfe by clean ablation process with a coherent vuv source at 125 nm. *Applied Physics A: Materials Science & Processing*, 69:375–380, 1990. 160

[230] W.F. Cheong, S.A. Prahl, and A.J. Welch. A review of the optical properties of biological tissues. *Quantum Electronics, IEEE Journal of*, 26(12):2166–2185, Dec 1990. 160

[231] Huang J.1 et.al. Unk. *Materials Chemistry and Physics*, 68:180–196, 2001. 163

[232] L.Ferry et al. Interaction between uv radiation and filled polytetrafluoroethylene (ptfe). i. degradation processes. *Journal of Polymer Science Part B: Polymer Physics*, 36:2057–2067, 1998.

[233] Max Born and Emil Wolff. *Principles of Optics: Electromagnetic Theory of Propagation Interference and Diffraction of Light*. Pergamon Press, 1959. 170

[234] http://www.geant4.org/geant4/support/releasenotes4.9.3.html. 177

[235] M J Ballico. Modelling of the effective emissivity of a graphite black body. *Metrologia*, 32(4):259, 1995. 185

[236] L. M. Barkov, A. A. Grebenuk, N. M. Ryskulov, P. Yu. Stepanov, et al. Measurement of the refractive index of liquid xenon for intrinsic scintillation light. *Nuclear Instruments and Methods in Physics Research Section A: Accelerators, Spectrometers, Detectors and Associated Equipment*, 379(3):482 – 483, 1996. Proceedings of the Sixth International Conference on Instrumentation for Experiments at e+ e- Colliders. 190

BIBLIOGRAPHY

[237] I.R. Barabanov, V.N. Gavrin, and A.M. Pshukov. Liquid xenon scintillation spectrometer. *Nuclear Instruments and Methods in Physics Research Section A: Accelerators, Spectrometers, Detectors and Associated Equipment*, 254(2):355 – 360, 1987. 190

[238] M. Yamashita, T. Doke, K. Kawasaki, J. Kikuchi, et al. Scintillation response of liquid xe surrounded by ptfe reflector for gamma rays. *Nuclear Instruments and Methods in Physics Research Section A: Accelerators, Spectrometers, Detectors and Associated Equipment*, 535(3):692 – 698, 2004. 190

[239] Kenneth J. Voss and Hao Zhang. Bidirectional reflectance of dry and submerged labsphere spectralon plaque. *Applied Optics*, 45(30):7924–7927, 2006. 191

[240] E. S. Clark. The molecular conformations of polytetrafluoroethylene: forms ii and iv. *Polymer*, 40(16):4659 – 4665, 1999. 191

[241] Lasse Ylianttila and Josef Schreder. Temperature effects of ptfe diffusers. *Optical Materials*, 27(12):1811 – 1814, 2005. 191

[242] V. Chepel, F. Neves, V. Solovov, A. Pereira, et al. Performance of a chamber for studying the liquid xenon response to nuclear recoils. In *Nuclear Science Symposium Conference Record, 2004 IEEE*, volume 1, pages 422–426 Vol. 1, Oct. 2004. 191, 200, 204

[243] Francisco Neves. *Applicacao de Xenon Liquido na Deteccao de Materia Escura*. PhD thesis, Universidade de Coimbra, 2006. 200

[244] A. Lindote. *Estudo da Simulacao de um Detector de Xenon Liquido com Aplicacao a Deteccao de Materia Escura*. PhD thesis, Universidade de Coimbra, 2003. 202

[245] Casimer DeCusatis. *Handbook of applied photometry*. Optical Society of America, 1998. 211

[246] G. Schaepman-Strub, M.E. Schaepman, T.H. Painter, S. Dangel, et al. Reflectance quantities in optical remote sensing–definitions and case studies. *Remote Sensing of Environment*, 103(1):27 – 42, 2006. 213

[247] Bull D.R. Beasley D. and Martin .R. An overview of genetic algorithms part 1 fundamentals. *Technical report, University of Purdue*, 0:0, 1993. 221

[248] Deep Malya Mukhopadhyay *et al*. Genetic algorithm: A tutorial review. *International Journal of of Grid and Distributed Computing*, 2:25–32, 2009. 221

[249] Tarek A. El-Mihoub. Hybrid genetic algorithms: A review. *Engineering Letters*, 13:13211, 2006. 221